MINISTRY OF EDUCATION AND RESEARCH

THE ANNALS OF "DUNAREA DE JOS" UNIVERSITY OF GALATI

Fascicle IX
METALLURGY AND MATERIALS SCIENCE

YEAR XXVI (XXXI),
November 2008, no. 2

ISSN 1453-083X

2008
GALATI UNIVERSITY PRESS

THE ANNALS OF "DUNAREA DE JOS" UNIVERSITY OF GALATI.
FASCICLE IX. METALLURGY AND MATERIALS SCIENCE
N^0. 2 – 2008, ISSN 1453 – 083X

Table of Contents

THE ANNALS OF "DUNAREA DE JOS" UNIVERSITY OF GALATI.
FASCICLE IX. METALLURGY AND MATERIALS SCIENCE
N^0. 2 – 2008, ISSN 1453 – 083X

AN ANALYTICAL PROCEDURE FOR THE PREDICTION OF THE STRESS-STRAIN STATE IN NOTCHES UNDER MULTIAXIAL FATIGUE

Nikolas PITATZIS[1], Alexander SAVAIDIS[2], Georgios SAVAIDIS[1]

[1] Aristotle University of Thessaloniki, Dept. of Mechanical Engineering, Greece
[2] National Technical University of Athens, Department of Mechanics, Greece
e-mail: pitatzis@auth.gr

ABSTRACT

This work presents an analytical procedure for estimating elastic-plastic stresses and strains in notched shafts subjected to synchronous non-proportional torsional and tensile cyclic loading. The specification of the equivalent stress concentration factor is firstly accomplished. Neuber's rule in conjunction with the assumed material law provides the relation between the applied loading and the equivalent stress and strain. Principal stresses and strains yield from the corresponding equivalent values incorporating Hencky's equations. The transformation of the principal stresses and strains to the appropriate coordinate system yields the final result. For the assessment of the analytical procedure, notch stress-strain results from several finite element analyses of an axisymmetric cylindrical shaft with a circumferential groove subjected to multiaxial synchronous fatigue loading are presented. A satisfactory agreement between the analytical and numerical results is observed.

KEYWORDS: Finite elements, Plasticity, Notches, Analytical model, Fatigue

1. Introduction

Engineering components often provide unavoidable local stress concentrations due to notches or other geometrical discontinuities. Such stress concentration sites yield intense cyclic plastic deformation under service loading, which may give rise to a drastic reduction in the operational lifetime of a structure. The understanding of the local stress-strain responses on the failure-critical areas and a thorough cognition into the damage evolution process are ultimate prerequisites to preserve structural safety in conjunction with design optimization.

Nowadays, extensive literature exists concerning approximate methods for computing notch stresses and strains. For the pure elastic case, the quantities of interest are the stress concentration factors, which describe the local stress amplification at a notch-root. Approximate and exact results for stress concentration factors can be found in many reference books [22, 25, 35]. Studies on this subject can be found in [8, 24, 40]. The corresponding elastic–plastic notch problems are, however, much more complex than those for the pure elastic case. For uniaxial loading, approximate methods have been proposed in [5, 9, 11, 17, 23, 27, 35, 36]. Applications of Neuber's rule to notch fatigue analysis have been presented in [34, 37]. Approximate methods for the estimation of multiaxial stress–strain have been developed in [1, 2, 5-7, 9, 10, 12-16, 38].

In our previous works [29-32] basic investigations dealing with the well-known kinematic hardening rule of Prager-Ziegler [26, 39] in conjunction with the von Mises yield criterion [19] were investigated. Prager-Zieler's kinematic hardening rule is capable to describe linear material hardening in a reliable way. Therefore, and due to its simplicity, it is implemented in all common commercial finite element programs. However, neither the material cyclic stress-strain curve, nor the hysteresis loop shapes that arise during the fatigue process can be described with good precision [18].

Especially in low cycle fatigue with high plastic strains, as well as in cases with variable amplitude cyclic loading a linear kinematic hardening model is not capable to provide a realistic transposition of the

yield surface within the whole stress spectrum. To overcome these obstacles, several improvements have been proposed during the last decades. One way to cope with these deficiencies is to apply multilayer [4] or multisurface [21] models. Thus, the curved stress-strain relations can be sufficiently approximated by means of multi-segment lines providing the desired accuracy.

In the present work, an approximate model [28, 32] will be used for computing the complete elastic–plastic notch stresses and strains. In order to verify the model, detailed elastic–plastic FE analyses for a cylindrical shaft with a circumferential notch are performed. The elastic–plastic material properties are described by the von Mises yield criterion [19] and the multilayer material model of Besseling [4]. Synchronous non-proportional cyclic tension/torsion loading with constant and variable amplitudes is applied to validate the accuracy of the results derived from the analytical model comparing them with the corresponding FE results.

2. Problem formulation

Consider an infinite and elastic-plastic cylindrical shaft with a circumferential groove as depicted in fig. 1.

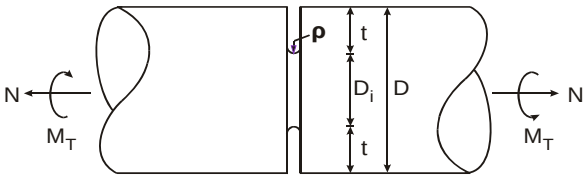

Fig. 1. The infinite notched shaft

Table 1 includes the geometrical dimensions of the cylindrical shaft under investigation.

Table 1. Geometrical parameters in [mm]

Shaft Diameter	Crucial Diameter	Notch Depth	Notch Radius
D	D_i	t	P
140	70	35	3

A tensile force $\boldsymbol{N}$ combined with a torsional moment $\boldsymbol{M_T}$ are applied on the notched shaft. For convenience, the nominal tensile stress $\boldsymbol{S}$ and the nominal shear stress $\boldsymbol{T}$, instead of $\boldsymbol{N}$ and $\boldsymbol{M_T}$ are used as external loads in the analysis, which are related by

$$S = \frac{N}{\pi (D_i/2)^2}, \qquad T = \frac{2M_T}{\pi (D_i/2)^3}. \tag{1}$$

3. Approximation model

The origin of the analytical model goes back to the work of Savaidis et al [28, 32]. The model uses the same input as the well-known model of Hoffmann and Seeger [12-15] for ***proportional*** loading as starting point. Taking the material's stress-strain curve and the notch concentration factors for every individual loading as an input, two steps are performed.

Step 1: Relationship between applied load and equivalent notch stress σ_{eq} and strain ε_{eq}.

The elastic solution is based on the approximate uniaxial stress–strain relation for the equivalent quantities. The material law in conjunction with the elastic solution yields the relation between the applied external load and the equivalent stress, defined by the equation:

$$\varepsilon_{eq} = \frac{\sigma_{eq}}{E} F \quad \frac{\sigma^e_{eq}}{\sigma_{eq}}, K_p \quad \frac{E\varepsilon^*}{S^*}, \tag{2}$$

where the superscript '$\boldsymbol{e}$' denotes the elastic solution, $\boldsymbol{F}$ is a function of the ratio $\sigma^e_{eq}/\sigma_{eq}$ and the plastic limit load factor K_p, while S^* and ε^* are the modified nominal stress and strain respectively. In particular they are defined by

$$K_p = \frac{\sigma_u}{\sigma_y}, \quad S^* = \frac{\sigma^e_{eq}}{K_p}, \quad \varepsilon^* = g^{-1}\left(S^*\right), \tag{3}$$

in which σ_u is the ultimate limit load and σ_y is the load at yield initiation.

Step 2: Derivation of the individual stress and strain components or principal stresses and strains from the equivalent stress σ_{eq} and strain ε_{eq}.

For this, use is made of the yield criterion, flow rule and the boundary as well as the constraint conditions at the notch-root. The Prandtl-Reuss law yields

$$d\varepsilon_i^p = \frac{3}{2h}\frac{d\varepsilon_{eq}^p}{\sigma_{eq}}\sigma_i', \quad i = 1,2,3, \tag{4}$$

with the plastic tangent modulus $h = d\sigma_{eq}/d\varepsilon^p_{eq}$, while the Hencky's law results in

$$\varepsilon_i^p = \frac{3}{2}\frac{\varepsilon^p_{eq}}{\sigma_{eq}}\sigma_i'. \tag{5}$$

Assume that the directions of the principal stresses remain unchanged during loading, i.e., φ_i = const., then the following boundary and constraint conditions hold at the notch-root: σ_3=0, $\varepsilon_2/\varepsilon_1$=const. The output quantities are the notch stresses σ_{ij}=0, notch strains ε_{ij} or ε_i, and the directions of the principal stress axes characterized by the orientation angles φ_i.

The ***non-proportional*** loading can be classified into two different categories as illustrated in fig. 4. In the first loading category, both loading components are cyclic. In the second loading category, one

loading component is cyclic, while the other is kept constant. Three cases are distinguished according to fig. 2:

- Case I: Both components, S and T, are cyclic and $1 \geq S_a/T_a \geq 0.65$. This case corresponds to a large amplitude ratio S_a/T_a.
- Case II: S (or T) is constant while T (or S) is cyclic, and $0.05 \geq S_a/T_a \geq 0$ (or $0.05 \geq T_a/S_a \geq 0$). This case corresponds to a small amplitude ratio S_a/T_a (or T_a/S_a).
- Case III: Both components S and T are cyclic, and $0.65 \geq S_a/T_a \geq 0.05$. This case corresponds to a moderate amplitude ratio S_a/T_a.

With cases I, II and III, the complete range of the amplitude ratio S_a/T_a is covered.

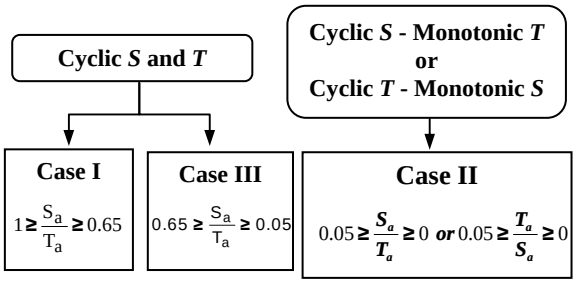

Fig. 2. Load case classification within the framework of the analytical model

Detailed description how to proceed within each case is given in [28, 32].

4. Finite elements

To verify the analytical procedure, various numerical analyses for a multiaxially loaded notched shaft have been performed. For its discretization 13120 solid elements have been applied. Each element consists of 20 nodes and 14 Gaussian points. The total number of nodes is 51677. The shaft has been divided up to 40 cylindrical segments, each having an angle θ=9^o. In the non-linear analysis, a full Newton-Raphson procedure [3] for all degrees of freedom has been applied. A section of the shaft is shown in fig. 3, whereby the element distribution is distinguished.

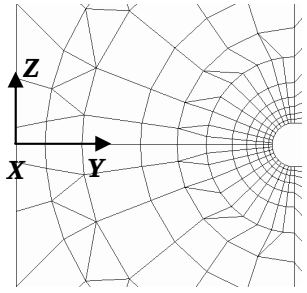

Fig. 3. Mesh configuration

The material law of the aluminum alloy Al5083 is considered. The experimentally determined values of the cyclic hardening coefficient K' and the cyclic hardening exponent n' amount to K' = 544 N/mm^2 and n' = 0.075, respectively. The elastic modulus E and Poisson's ratio ν amount to E = 68000 N/mm^2 and ν = 0.32, respectively.

5. Loading cases

Table 2 summarizes the non-proportional synchronous loading cases investigated here.

Table 2. Loading cases under investigation

Load case	C	S_m [N/mm^2]	T_a [N/mm^2]	S_{eq} [N/mm^2]
L1	0	0	225.630	390.8
L2	0.623	132.269	212.311	390.8
L3	1.000	195.402	195.402	390.8
L4	1.605	265.626	165.499	390.8
L5	5.000	369.275	73.855	390.8
L6	10.00	385.070	38.507	390.8
	D	T_m [N/mm^2]	S_a [N/mm^2]	S_{eq} [N/mm^2]
L7	0	0	390.804	390.8
L8	0.623	65.492	265.637	390.8
L9	1.000	195.402	195.402	390.8
L10	10.00	225.255	22.525	390.8

Two main loading categories are distinguished in Table 2: (a) cyclic fully reversed tension-compression combined with monotonic torsion, and (b) cyclic fully reversed torsion combined with monotonic tension. The mean value of the individual cyclic load component is kept zero in all cases.

For convenience, the ratio $c=S_m/T_a$ of the constant nominal normal stress S_m to the nominal shear stress amplitude T_a is used to describe the load situation. The ratio $d=T_m/S_a$ of the constant nominal shear stress T_m and the nominal normal stress amplitude S_a is also considered. The nominal equivalent stress S_{eq} is kept constant and larger than the value of the material flow stress σ_y in all loading cases.

Note that the monotonic loading component acts first on the notched shaft. When it reaches its pick value then the cyclic loading component is applied. Therefore, the attained phase difference between the two loading components is 90^o.

6. Results

Results derived from the finite element analyses and the analytical model are discussed in this section. For clarity, each result is specified with a code name; the first letter refers to the solution method (F for the

finite element procedure, A for the analytical procedure). The letter "L" follows, denoting loading. Next, a number (1 to 10) refers to each one of the ten loading cases presented herein.

The stabilized notch stress-strain curves will be considered in the following discussions of the results.

Figure 4 shows the τ_{yz}-γ_{yz} results for the loading case L2.

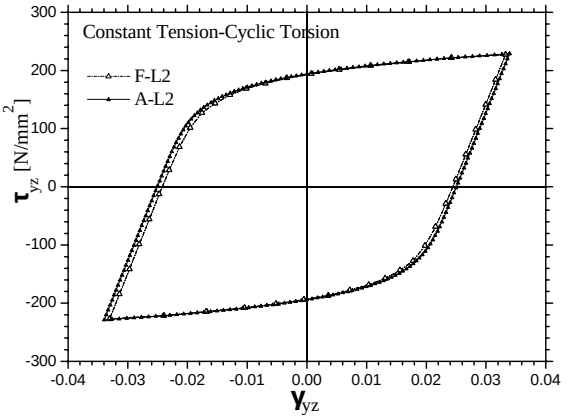

Fig. 4. Comparison of the τ_{yz}-γ_{yz} hystereses determined by FE analysis and the analytical model for the loading case L2

A very good agreement to both stress and strain results can be observed in that loading case as the two plotted stabilized τ_{yz}-γ_{yz} are almost identical.

Figure 5 shows the results for the loading cases L1 to L6, whereby the influence of the ***c***-value on the stress-strain behavior is explored.

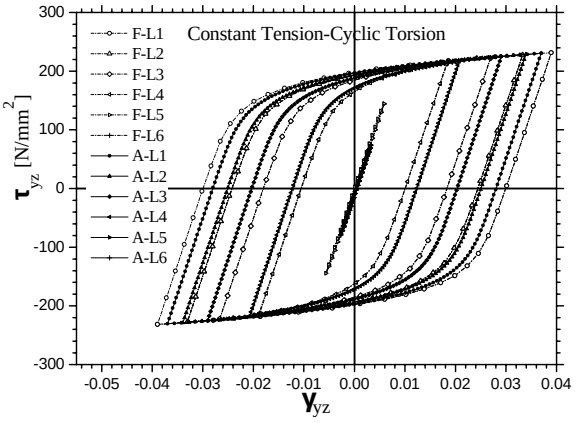

Fig. 5. Comparison of τ_{yz}-γ_{yz} hystereses determined by FE analysis and the analytical model for the loading cases L1 to L6

Thereby, the value of ***c*** increases from 0 (L1) to 10 (L6). In the cases of ***c***=5 (L5) and ***c***=10 (L6) with very low cyclic loads, the calculated plastic deformation is approximately zero. Therewith, the τ_{yz}-γ_{yz} response is nearly the same and it follows the Hooke's law. For ***c***<1.6, where the shear plastic deformation attains significant values, (small) discrepancies between the finite element and the analytical model's results occur.

It must be noticed that the finite element method calculates erroneously a radial stress component at the notch root. This error results from the stress extrapolation from the inner element Gaussian points to the corner element nodes. Therefore, according to the finite element solution the material shows a stiffer attitude because of the presence of the radial stress component. Theoretically, no radial stress should exist at the very notch root, as correctly assumed in the analytical procedure's formulation. The value of this erroneous radial stress component increases with increasing plastic deformations. Therewith, the observed disagreement between the numerical and the analytical results becomes more evident for greater ***c*** values.

Figure 6 shows the normal stress-normal strain response (σ_z-ε_z) at the notch root for loading case L10. Herein, the results of the analytical solution as well as the ones from two finite element analyses are compared. Each finite element solution corresponds to a different mesh configuration. The solution indicated with the letter "F" in fig. 6 was determined with the finite element mesh described in section 4. Another coarser mesh configuration has been created including only 1360 elements and 6077 nodes, in order to explore the effect of the radial stress on the finite element results and on the σ_z-ε_z path. The letter 'C' in fig. 6 stands for the finite element solution where the coarse mesh version is applied.

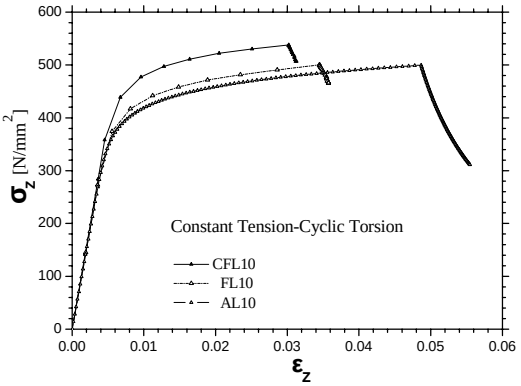

Fig. 6. Comparison of σ_z-ε_z hystereses determined by FE analyses and the analytical model for the loading case L10

A stiffer material response is regarded from the finite element solutions compared to the one derived from the analytical model. The finite element mesh refinement results in a subsequent increase in the number of integration points and therefore decreases the radial stress component value. That leads to a numerical solution where the material yields at lower normal stress values according to von Mises yield criterion. Nonetheless, the presence of a (erroneous)

radial stress component -even in the case of a finer mesh- yields results that differ from the ones derived from the analytical model.

The significant differences in the calculated normal strain are due to the assumption that the strain ratio $\varepsilon_2/\varepsilon_1$ should remain constant throughout the whole loading history according to the analytical model. This is valid for elastic stress-strain responses but not valid in cases where plastic strains are prevalent like in the loading cases under study.

The σ_z-ε_z diagram shown in fig. 7 incorporates results from the finite element and the analytical procedure implementation for several ***d***-values.

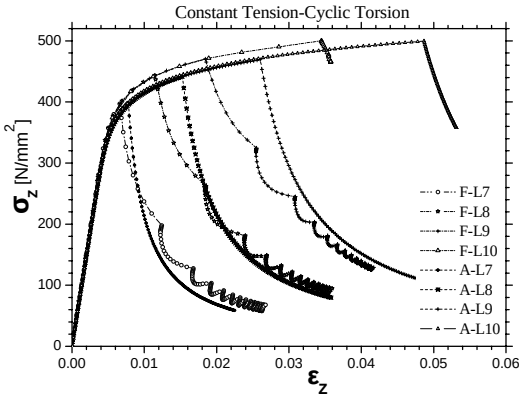

Fig. 7. Comparison of the σ_z-ε_z hystereses determined by FE analyses and the analytical model for the loading cases L7 to L10

As ***d*** increases successively from load case L7 up to L10, the observed differences to the calculated normal strain become more and more significant. This is due to the gradual increase of $\varepsilon_2/\varepsilon_1$ for increasing normal load values. This increase becomes prominent for the sharp notch investigated here because of the notch constraint.

7. Conclusions

An analytical procedure to evaluate the stress-strain response in notched components under synchronous nonproportional loading is assessed based on numerical results from finite element analyses for a circumferentially notched shaft subjected to synchronous non-proportional multiaxial fatigue loading consisting of cyclic and static load components. The following conclusions can be derived from the comparative analyses:

- A good agreement between the analytically and numerically determined shear stresses and shear strains has been observed even in loading cases with excessive plastic shear strain values.
- The application of a finite element mesh configuration that includes adequate number of nodes with high node density especially nearby the notch root is an indispensable prerequisite for a reliable finite element solution.
- The analytical model as far as the normal stress – normal strain path monitoring is concerned, achieves an acceptable description of the notch constraint.
- Deviations between the analytically and numerically calculated normal strains exist due to the assumption of a constant $\varepsilon_2/\varepsilon_1$-ratio within the framework of the analytical procedure, especially in loading cases causing pronounced plastic strains.

References

[1]. Amstutz H., Hoffmann M., Seeger T., 1988, ***Kerbbeanspruchungen II – Mehrachsige Kerbbeanspruchungen im nichtlinearen Bereich bei proportional und nichtproportional wechselnder Belastung***, Heft 139, Forschungshefte Forschungs-kuratorium Maschinenbau e.V., Frankfurt, Germany.

[2]. Barkey M.E., Socie D.F., Hsia K.J., 1993, ***A Yield Surface Approach to the Estimation of Notch Strains for Proportional and Nonproportional Cyclic Loading***, TAM Report No. 709-UILU ENG-93-6007, University of Illinois, Urbana-Champaign, USA.

[3]. Bathe K., 1996, ***Finite Element Procedures***, Prentice Hall, New Jersey.

[4]. Besseling, J.F., 1958, A Theory of Elastic, Plastic, and Creep Deformations of an Initially Isotropic Material Showing Anisotropic Strain-Hardening Creep Recovery and Secondary Creep, J. Appl. Mech., pp. 529-536.

[5]. Dietmann H., 1968, ***Berechnung der Fliesskurven von Bauelementen bei kleinen Verformungen***, readership thesis, University of Stuttgart, Germany.

[6]. Dowling N.E., Brose W.R., Wilson W.K., 1977, ***Notched Member Fatigue Life Predictions by the Local Strain Approach in Fatigue under Complex Loading***, Advances in Engineering, 6, SAE, Warrendale, pp. 55–84.

[7]. Esderts A., Amstutz H., 1994, ***Betriebsfestigkeit bei mehrachsiger Beanspruchung II***, Heft 188, Forschungshefte Forschungskuratorium Maschinenbau e.V., Frankfurt, Germany.

[8]. Filippini M., 2000, ***Stress Gradient Calculations at Notches***, Int. J. Fatigue, 22, pp. 397–409.

[9]. Glinka G., 1985, ***Energy Density Approach to Calculation of Inelastic Strain–Stress near Notches and Cracks***, Eng. Fract. Mech., 22, pp. 485–508.

[10]. Grubisic V., Sonsino C.M., 1982, ***Influence of Local Strain Distribution on Low-Cycle Fatigue Behavior of Thick-Walled Structures***, ASTM-STP 770, pp. 612–629.

[11]. Hardrath H.F., Ohman H., 1951, ***A Study of Elastic Plastic Stress Concentration Factors due to notches and fillets in plat plates***, Technical Note NACA TN 2566.

[12]. Hoffmann M., Seeger T., 1985, ***A Generalized Method for Estimating Multiaxial Elastic–Plastic Notch Stresses and Strains***. Part 1 - Theory, J. Eng. Mater. Technol., 107, pp. 250-254.

[13]. Hoffmann M., Seeger T., 1985, ***A Generalized Method for Estimating Multiaxial Elastic–Plastic Notch Stresses and Strains. Part 2 - Application and general discussion***, J. Eng. Mater. Technol., 107, pp. 255–260.

[14]. Hoffmann M., Seeger T., 1985, ***Kerbbeanspruchungen I – Ermittlung und Beschreibung mehrachsiger Kerbbeanspruchungen im nichtlinearen Bereich,*** Heft 115, Forschungshefte Forschungskuratorium Maschinenbau e.V., Frankfurt, Germany.

[15]. Hoffmann M., Seeger T., 1989, ***Stress–Strain Analysis and Life Predictions of a Notched Shaft under Multiaxial Loading, Multiaxial Fatigue – Analysis and Experiments***, SAE AE-14, Warrendale, pp. 81–101.

[16]. Knop M., Jones R., Molent L, Wang C., 1999, ***On the Glinka and Neuber methods for Calculating Notch Tip Strains under Cyclic Load Spectra***, Int. J. Fatigue, 22, pp. 743–755.

[17]. Kühnapfel K.F., 1976, ***Kerbdehnungen und Kerbspannungen bei elasto-plastischer Beanspruchung; rechnerische Ermittlung, Vergleich mit Versuchsergebnissen***, phD-thesis, TH Aachen, Germany.

[18]. Lemaitre J., Chaboche J.L., 1990, ***Mechanics of Solid Materials***, Cambridge University Press.

[19]. von Mises, R,. 1913, ***Mechanik der festen Körper im plastisch-deformablen Zustand***, Nachr. Konigl. Ges. Wiss. Göttingen, math. phys., pp. 582-593.

[20]. Mowbray D.F., McConnelee J.E., 1073, ***Applications of Finite Element Stress Analysis and Stress–Strain Properties in Determining Notch Fatigue Specimen Deformation and Life***, ASTM STP 519, pp. 151–169.

[21]. Mroz Z., 1967, ***On the Description of Anisotropic Work Hardening***, J. Mech. Phys. Solids., 17, pp. 163-175.

[22]. Neuber H., 2001, Kerbspannungslehre, 4th edition, Springer-Verlag.

[23]. Neuber H., 1961, ***Theory of Stress Concentration for Shear strained Prismatical Bodies with Arbitrary Nonlinear Stress–Strain Law,*** J. Appl. Mech., 28, pp. 544–550.

[24]. Noda N.A., Takase Y., 1999, ***Stress Concentration Formulae useful for any Shape of Notch in a Round Test Specimen under Tension and under Bending***, Fatigue Fract. Engng Mater. Struct., 22, pp.1071–1082.

[25]. Peterson R.E., 1974, The Stress Concentration Factors Handbook, John Wiley and Sons, New York.

[26]. Prager W., 1955, ***The Theory of Plasticity: A Survey of Recent Achievements.*** Proc. Inst. Mech. Engrs., 169, pp. 41-57.

[27]. Saal H., 1975, ***Näherungsformeln für die Dehnformzahl***, Materialprüfung, 17, pp. 395- 398.

[28]. Savaidis A., 1994, ***Finite-Element Untersuchungen und Entwicklung eines N€aherungsverfahrens zur Beschreibung mehrachsiger elastisch-plastischer Kerbbeanspruchungen bei synchroner nichtproportionaler zyklischer Belastung***, 52, Institut für Stahlbau und Werkstoffmechanik, TU Darmstadt, Germany.

[29]. Savaidis A., Savaidis G., Zhang Ch., 2001, ***FE Fatigue Analysis of Notched Elastic-Plastic Shaft Under Multiaxial Loading Consisting of Constant and Cyclic Components***, Int. J. Fatigue, 23, pp. 303-315.

[30]. Savaidis A., Savaidis G., Zhang Ch., 2001, ***Elastic-Plastic FE Analysis of a Notched Shaft Under Multiaxial Nonproportional Cyclic Loading,*** Theor. Appl. Fract. Mech., 32, pp. 87-97.

[31]. Savaidis A., Savaidis G., Zhang Ch., 2002, ***Numerical Analysis of Notched Elastic-Plastic Structures Under Multiaxial Variable Amplitude Loading***, Computers and Structures, 80, pp. 1907-1918.

[32]. Savaidis A., Savaidis G., Zhang Ch., 2003, ***Approximate Elastic-Plastic Analysis of a Notched Bar Under Tensile and Torsional Fatigue***, Theor. Appl. Fract. Mech., 40, pp. 85-96.

[33]. Seeger T., Beste A., 1977, ***Zur Weiterentwicklung von Näherungsformeln für die Berechnung von Kerbbeanspruchungen im elastisch-plastischen Bereich***, VDI Verlag, Reihe 18, No 2, pp. 1–56.

[34]. Seeger T., Heuler P., 1980, ***Generalized Application of Neuber's Rule***, J. Test. Eval., 8, pp. 199–204.

[35]. Sih G.C. (Ed.), 1978, ***Stress Analysis of Notch Problems, Mechanics of Fracture***, 5, Noordhoff International Publishing, Leyden.

[36]. Stowell E.Z., 1950, ***Stress and Strain Concentration at a Circular Hole in an Infinite Plate***, Technical Note NACA TN 2073.

[37]. Topper T.H., Wetzel R.M., Morrow J.D., 1969, ***Neuber's Rule Applied to Fatigue of Notched Specimens***, J. Mater., 1, pp. 200–209.

[38]. Walker E.K., 1977, ***Multiaxial Stress–Strain Approximations for Notch Fatigue***, J. Test. Eval., 5, pp. 106–113.

[39]. Ziegler H., 1959, A ***Modification of Prager's Hardening Rule.*** Quart. Appl. Math., 17, pp. 55-60.

[40]. Zheng M., Niemi E., 1997, ***Analysis of the Stress Concentration Factor for a Shallow Notch by the Slip-Line Field Method***, Int. J. Fatigue, 19, pp. 191–194.

THE ANNALS OF "DUNAREA DE JOS" UNIVERSITY OF GALATI.
FASCICLE IX. METALLURGY AND MATERIALS SCIENCE
N^0. 2 – 2008, ISSN 1453 – 083X

THERMAL ANALYSIS OF INOCULATED GREY CAST IRONS

Mihai CHISAMERA, Stelian STAN, Iulian RIPOSAN, Eduard STEFAN, George COSTACHE
Politehnica University of Bucharest
e-mail: riposan@foundry.pub.ro

ABSTRACT

A research was done to investigate the effect of 0.05…0.25wt.% addition rate of Ca, Zr ,Al – FeSi alloy, in ladle and in-mould inoculation of grey cast irons. In the present paper, the conclusions drawn are based on thermal analysis. For solidification pattern, some specific cooling curves characteristics, such as undercooling degree at the beginning of eutectic solidification and at the end of solidification, as well as recalescence level, were identified to be more influenced by the inoculation technique. In order to secure stable and controlled processes, representative thermal analysis parameters could be used, especially in thin wall grey iron casting production.

KEYWORDS: Thermal Analysis, Grey Cast Irons, Inoculation, In-mould Inoculation, Ladle Inoculation

1. Introduction

Inoculation has a vital role to play in the continuing progress of cast iron. The objectives of various additions to the iron melt are to control the graphite size and shape, to promote A-type flakes instead of fine under-cooled forms (D-type graphite), to obtain freedom from chill in thin sections, to promote uniformity throughout different sections sizes, to improve machinability and mechanical properties, etc.

The development of inoculants started by the control of calcium and aluminium in ferrosilicon and continued by addition of other active/inoculating elements, such as Sr, Ba, Zr, Ce, etc. Inoculation techniques were also continuously improved, in order to increase efficiency and to reduce the inoculant consumption, to avoid the fading, etc [1, 2].

The chemistry of the base iron and the treatment alloys are very important in controling the structure formation at lower eutectic undercooling conditions. It was found that Mn and S, strong deoxidizing elements (Al and Zr) and inoculating elements (Ca, Sr, Ba, RE etc.) have a key role in complex (Mn, X)S compounds formation, which act as the major nucleation sites for graphite in grey cast irons [3-7].

Recently, the thermal analysis became an important tool to reflect the solidification behavior of cast irons. The cooling curve itself, as well as its derivatives and related temperatures and calculated parameters are patterns that can be used to predict the characteristics of irons. On the other hand, the use of thermal analysis can help assess the inoculation requirements for the melt [7-13].

The current experimental investigation in this paper was designed to estimate the cooling curves parameters of low sulphur (0.025%S), low residual aluminium (0.003%Al), hypo-eutectic grey irons (3.5-3.6%CE), subjected to in-mould and in-ladle inoculation by the same type of inoculant (Zr, Ca, Al - FeSi) added at various rates (0…0.25wt.%).

2. Experimental Procedure

Table 1 shows the representative experimental procedure parameters. The charge was melted in a graphite crucible medium frequency induction furnace, mainly as a synthetic pig iron contribution, to ensure a low level of trace elements. It was obtained a relative low carbon equivalent, hypo-eutectic base cast iron (CE = 3.55%), at low content of sulphur (0.025%S) and residual aluminium (0.003%Al), too.

Thermal analysis was used to estimate and quantify nucleation characteristics of different inoculated irons. The thermal analysis was carried out using shell sand Quick-Cups, with a modulus of approximately 0.75cm (30 mm diameter bar

equivalent). The cooling curve and its first derivative were considered for un-inoculated and inoculated irons, at different inoculant addition rates.

Table 1. Experimental Procedure Parameters

Parameters	Values
I. MELTING **1.1. Melting Furnace** **1.2. Metallic Charge:** **-Synthetic Pig Iron (94%):** **-Steel Scrap (6%):** **1.3. Base Metal**	Graphite Crucible Induction Furnace, 10Kg, 8000Hz 3.48%C, 1.72%Si, 0.50%Mn, 0.12%P, 0.025%S, 4.03%CE 0.2%C, 0.3%Si, 0.50%Mn, 0.03%P, 0.03%S 3.02%C, 1.65%Si, 0.49%Mn, 0.11%P, 0.025%S, 0.0026%Al, 0.006%Ti, 0.042%Cr, 0.0078%Mo, 0.028%Ni, 0.044%Cu
II. INOCULATION **2.1. Inoculant** -System -Chemistry -Additional Rate **2.2. Inoculation Technique** -In-Mould -Ladle	 Ca, Zr, Al-FeSi, 0.2-0.7mm size 75%Si, 2.2%Ca, 1.5%Zr, 1.2%Al, Fe bal. 0.05, 0.10, 0.15, 0.20 and 0.25wt.% Quick-Cups [Thermal Analysis System] Ladle addition, after tapping
III. TEST **Cooling Curve Analysis**	 Shell Sand Cup, 0.75cm Cooling Modulus

A complex inoculant in Ca,Zr,Al – FeSi system was used, at various addition rates (0…0.25wt.%). Two inoculation techniques were applied, in – mould (M) and in – ladle (L) alloy addition, as representative for high performance grey cast iron production. In the first experimental program, Zr, Ca, Al - FeSi alloy was employed at 0.05%, 0.10%, 0.15, 0.20% and 0.25% levels, into the shell sand cup. In the second program, a ladle inoculation was applied with the same prescribed amount of alloy, which was added in the in-mould/cup tests.

3. Results and Discussion

Figure 1 shows the aspect of a typical cooling curve and its first derivative for a hypoeutectic grey iron (CE < 4.3%).

The signification of the most important events and parameters on these curves is included in Table 2 [7-13].

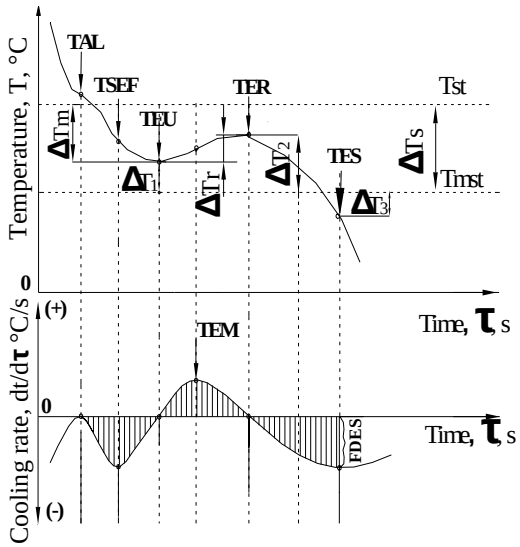

TAL - temperature of austenitic liquidus, °C**;**
TSEF - temperature of start of eutectic freezing (eutectic nucleation),°C**;**
TEU - temperature of eutectic undercooling, °C**;**
TER - temperature of graphitic recalescence, °C**;**
TES - temperature of the end of solidification (end of solidus), °C**;**
TEM - maximum recalescence rate, °C/s**;**
Tst - graphite eutectic equilibrium temperature, °C**;**
Tmst - carbide eutectic equilibrium temperature, °C**;**
ΔTm - maximum degree of undercooling (ΔTm = Tst-TEU), °C**;**
ΔTr - recalescence degree (ΔTr = TER-TEU), °C**;**
ΔTs - range of equilibrium eutectic temperature (ΔTs = Tst-Tmst), °C;
FDES - minimum value of the first derivative of cooling curve on the end of eutectic solidification, °C/s;
ΔT_1 = TEU – Tmst; ΔT_2 = TER – Tmst; ΔT_3 = TES – Tmst

Fig. 1 Typical cooling curve and its first derivative.

Table 2. Thermal Analysis Parameters of Hypo - Eutectic Grey Cast Irons

Param. (Fig.1)	Signification	Comments
Tst	Stable (graphite) eutectic equilibrium temperature	*Theoretical temperature for C to precipitate as graphite *It should be as high as possible [Tst = 1153 + 6.3 (%Si)]
Tmst	Metastable (white) eutectic equilibrium temperature	*Temperature when C is chemically combined with iron (Fe_3C) *It should be as low as possible [Tmst = 1147 - 12 (%Si)]
ΔTs	Range of equilibrium eutectic temperature [**Δ**Ts = Tst - Tmst]	*ΔTs should be as large as possible *Favourable elements: Si, Ni, Cu, Co, Al
TAL	Liquid temperature commences solid precipitation, as pro- eutectic austenite	*First arrest temperature (no recalescence has occurred) *The first derivative is zero *TAL should have a well-defined plateau, 2-10 sec *TAL can sometimes be reduced by inoculation
TSEF	Temperature of the start of eutectic freezing (nucleation)	*Derivative has a minimum, between TAL and TEU, grey iron. *It should not be too deep
TEU	Lowest eutectic temperature	*The minimal point from which the temperature is increasing *The first derivative is zero *Inoculation increases TEU [TEU, about 25^{o}C above Tmst]
TER	Highest eutectic temperature	*The maximum temperature after the increase in temperature *The first derivative is zero *High cooling rates may not achieve this temperature
ΔTm	Conventional eutectic undercooling degree [**Δ**Tm = Tst - TEU]	*Comparing to graphite eutectic temperature (Tst) *The maximum eutectic undercooling *A high undercooling means: -D-graphite might develop -More austenite, risk of macro-shrinkage and outer sunk -Free carbides (chill) if **Δ**Tm > **Δ**Ts *Higher the **ΔT**m of base iron, the higher the need for inoculation: base iron, **Δ**Tm = 20…35^{o}C, as normal value *Inoculation reduces eutectic undercooling
ΔT_1	Undercooling comparing to Tmst [ΔT_1 = TEU - Tmst]	*Beginning of eutectic reaction *Carbides (chill), if $\Delta T_1 < 0$ [TEU < Tmst] *Undercooled graphite (D-type) if $\Delta T_1 > 0$ [TEU close to Tmst] *Inoculation increases ΔT_1 parameter [ΔT_1 > + 20^{o}C normally]
ΔT_2	Undercooling comparing to Tmst [ΔT_2 = TER - Tmst]	*End of eutectic reaction, no white iron if $\Delta T_2 > 0$ *Higher ΔT_2, lower incidence of D-type graphite *Inoculation increases ΔT_2, at lower power comparing to ΔT_1
ΔT_r	Recalescence Degree [**Δ**Tr = TER - TEU]	*It reflects the amount of austenite and graphite that are precipitated during the first part of eutectic freezing *Too high recalescence might be harmful, in soft moulds *Ideal values depend on the type of mould and the casting modulus: **Δ**Tr = 2…5^{o}C, as a guideline *Inoculation normally reduces recalescence
TES	Temperature of the end of solidification (solidus)	*All metal has solidified *Lowest value of the negative peak on the first derivative *Lower (TES), higher sensitiveness to contraction defects
ΔT_3	Undercooling at the end of solidification [ΔT_3 = TES - Tmst]	*Usually at negative values, as TES < Tmst *Intercellular carbides, inverse chill and micro-shrinkage occurrence, especially if $\Delta T_3 > 20^oC$ (more negative) *Inoculation normally decreases ΔT_3 and the incidence of contraction defects
FDES	The depth of the first derivative at solidus	*The depth of the negative peak *It should be less than -3.5 (i.e. deeper) for grey irons (high amount of graphite at the end of solidification) *Inoculation normally has a positive influence
TEM	Maximum recalescence rate	*Maximum value of the first derivative between TEU and TER

There are many elements which individually have favourable or unfavourable influence on the equilibrium temperatures in stable (Tst) and metastable (Tmst) systems (Table 3).

Silicon appears to be the most important influencing element in un-alloyed irons especially at very low content of trace elements [Tst = 1153 + 6.7 (%Si); Tmst = 1147 – 12 (%Si)] [8,9].

Table 4 includes the most important experimental parameters, as thermal analysis data, while Figures 2 and 3 illustrate the effects of the two major influences, i.e. the inoculation technique (in-mould/cup and ladle inoculation) and the inoculant addition rate (0…0.25wt.% alloy), respectively.

Table 3. Favourable and Un-Favourable Elements as ΔTs = Tst - Tmst Influence

Equilibrium Temperature	Favourable Elements		Un-favourable Elements	
	Elements	Action	Elements	Action
Tst	Si, Ni, Cu, Co, Al, Pt	increase Tst	Cr, V, Ti, Mn, Mo, Sn, Sb, W, Mg, P	decrease Tst
Tmst	Si, Ni, Cu, Co, Mn, Sn, Sb, W, Mg, P	decrease Tmst	Cr, V, Ti, Al, Pt	increase Tmst

Table 4. Thermal Analysis-Representative Parameters

Inoculation		TEU (^{o}C)	TER (^{o}C)	TES (^{o}C)	**ΔTm** = Tst – TEU (^{o}C)	**ΔT$_1$** = TEU - Tmst (^{o}C)	**ΔT$_2$** = TER- Tmst (^{o}C)	**ΔT$_3$** = TES - Tmst (^{o}C)	**ΔTr**= TER- TEU (^{o}C)	FDES (^{o}C/s)
Addition (wt. %)	Type									
U.I.	M	1124.7	1125.1	1100.2	38.9	-3.3	-2.9	-27.8	-	-2.3
	L	1122.8	1125.2	1089.9	40.8	-5.2	-2.8	-38.1	2	-1.79
0.05	M	1132.5	1141.5	UD	31.3	4.9	13.9	UD	9	UD
	L	1123.6	1127.3	1093.9	40.2	-4.0	-0.3	-33.7	4	-2.12
0.10	M	1133.5	1142.3	1106.3	30.6	6.4	15.2	-20.8	9	-3.13
	L	1127.9	1134.9	1094.4	36.2	0.8	7.8	-32.7	7	-2.40
0.15	M	1135.4	1140.6	1107.2	28.9	8.7	13.0	-19.5	5	-3.13
	L	1130.1	1137.6	1097.4	34.2	3.4	10.9	-29.3	8	-2.88
0.20	M	1135.3	1140.1	1104.1	29.3	9.1	13.9	-22.1	5	-2.77
	L	1132.8	1139.1	1101.2	31.8	6.6	12.9	-25.0	6	-3.22
0.25	M	1136.4	1140.2	1105.1	28.4	10.6	14.4	-20.7	4	-3.23
	L	1133.2	1138.8	1100.8	31.6	7.4	13.0	-25.0	6	-3.45

*M-In-mould/cup inoculation; L-ladle inoculation.

The most pronounced effect of inoculation is that the temperatures of eutectic undercooling (TEU) and graphite recalescence (TER) are increased. When TEU is reached, the generated heat from released specific heat and latent heat (from the first austenite dendritic solidification and latent heat from the start of eutectic freezing) just balance the heat losses. The eutectic reaction then occurs and the released energy causes the temperature to rise until TER is reached. Un-inoculated irons are characterized by low TEU and TER temperatures.

Although inoculation increases both of these temperatures, the amount of the increase is dependent on the inoculant addition rate and inoculation technique. TER level is stabilized in a shorter time comparing to TEU level, as inoculant addition rate increases, especially for in-mould/cup treatment. Conventionally, undercooling is defined with reference to the graphitic equilibrium eutectic temperature (Tst), as **Δ**Tm = Tst - TEU. If TEU is closed to white eutectic temperature but above it (TEU > Tmst) then undercooled graphite might develop. Free carbides occurrence is typical for TEU < Tmst condition. The importance of the position of the start of eutectic reaction (TEU) comparing to metastable (white) eutectic temperature (Tmst) is revealed by **Δ**T$_1$ = TEU – Tmst. For the end of eutectic reaction temperature, **Δ**T$_2$ = TER - Tmst parameter was introduced.

The efficiency of inoculation is measured by its ability to decrease the **Δ**Tm level and to increase the **Δ**T$_1$ and **Δ**T$_2$ levels, respectively (Table 4, Figure 2).

In all cases, the in-mould/cup inoculation is clearly more effective compared to ladle inoculation, represented by variation of the **Δ**T$_1$ and **Δ**T$_2$ parameters. In both experimental programs, the un-inoculated irons start and end the eutectic reaction in the white iron field (**Δ**T$_1$ < 0, **Δ**T$_2$ < 0). Inoculation is known to move the solidification pattern to the grey iron feature. The increasing of the alloy addition rate led to the increasing of the distance of the both TEU and TER events, from the metastable (white) eutectic temperature. In mould/cup inoculation appears to be more efficient compared to ladle inoculation at low inoculant addition rates, such as 0.05-0.10wt.% level. No big difference in efficiency from the inoculation technique was found for more than 0.20wt.% alloy addition rate. Generally, the efficiency of 0.05-0.15wt.% alloy for in-mould/cup inoculation is comparable to or better than 0.15-0.25wt.% additions in ladle inoculation procedures.

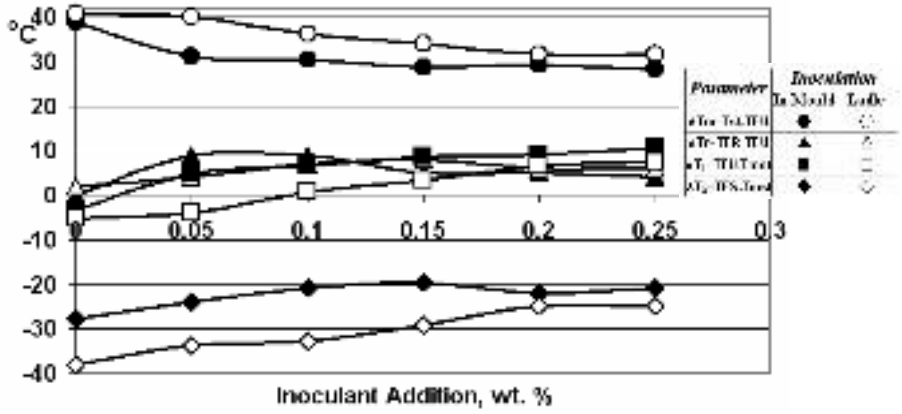

Fig. 2 Influence of the inoculant addition rate and inoculation technique on the representative thermal analysis parameters

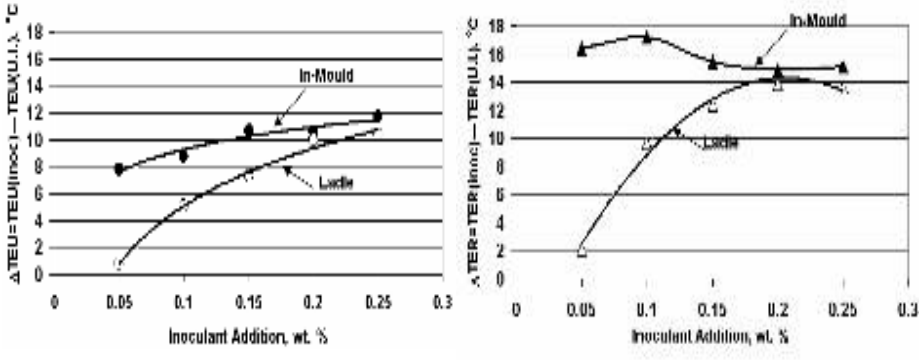

Fig. 3 Undercooling (a) and Recalescence (b) difference of un-inoculated and in-mould/ladle inoculated irons

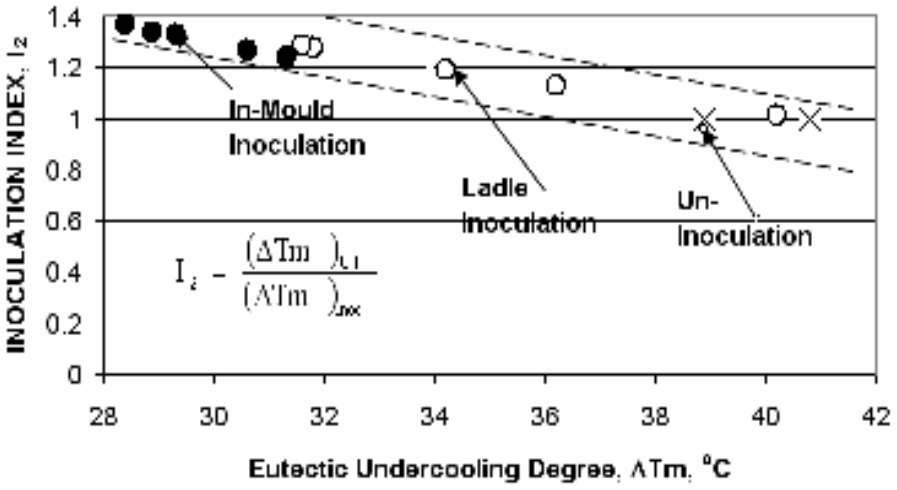

Fig. 4 Inoculation Index (I_2) of Treated Irons

The difference between un-inoculated and inoculated irons is strongly affected by the alloy addition rate, much more for ladle inoculation as the lowest eutectic temperature (TEU) shows (Fig. 3). Late inoculation technique is consistently at higher efficiency for the entire range of inoculant additions, but especially at lower levels (less than 0.20wt.%). Late inoculation technique is characterized by lower eutectic undercooling degree (**Δ**Tm) and higher inoculation index (I_2) level, respectively (Fig. 4).

In many cases, graphitic recalescence (**Δ**Tr = TER - TEU) is also an important parameter to evaluate the

behavior of inoculated irons. It is a function of the amount of austenite and graphite that are precipitated during the first part of eutectic freezing. The higher is recalescence, the higher is the probability for micro-shrinkage and porosity occurrence, especially in soft moulds media, such as green sand moulds (high metal volume expansion). Figure 2 shows the evolution of the level of recalescence (ΔTr), as inoculant addition rates increase. A peculiar difference appears in the behavior of in-mould/cup and ladle inoculated irons. At no more than 0.1wt.% alloy addition, high recalescence level characterizes the in-mould treated irons especially due to the higher TER temperature. An opposite result was obtained for these two inoculation techniques at more than 0.10wt.% alloy addition rate, when higher recalescence was typical for ladle inoculated irons. Lower differences were obtained between the two techniques for more than 0.20wt.% inoculant.

White iron solidification as intercellular carbides or/and inverse chill formation is also dependent on the position of the temperature of the end of solidification (TES), compared to the metastable (white) eutectic temperature (Tmst). Figure 2 illustrates the evolution of the TES, its position given Tmst (ΔT_3 = TES - Tmst), as the inoculant addition rate increases. Because this difference (ΔT_3 parameter) is generally more than 20^{o}C, these irons will be sensitive to chill tendency and micro-shrinkage formation.

Beneficial end of solidification means high solidus temperature and low level of the ΔT_3 parameter (usually at low negative value, as TES < Tmst in the most of cases). A low value of FDES (more negative level) is also favourable as it is correlated to a high amount of graphite at the end of freezing. Increasing of the alloy addition rate improves the behavior of irons at the end of solidification but in a different manner for in mould/cup and ladle inoculation methods. 0.10-0.20wt.% inoculant stabilizes the representative solidification parameters at a favourable level for in mould/cup inoculation comparing to 0.20-0.25wt.%, for ladle inoculation.

4. Conclusions

*The present study clearly indicates that thermal analysis methodology can be very successfully used to optimize and control the complicated cast iron solidification processes;
*Eutectic undercooling degree of the electrically melted base iron having 0.025%S, 0.003%Al and 3.5%CE is excessively high (39-40^{o}C), generating a relatively high need for inoculation;
*Under these conditions, the in-mould inoculation had a significant effect compared to ladle inoculation, inclusively at lower inoculant usage (less than 0.20wt.%);
*Lower levels of eutectic undercooling (ΔTm), recalescence (ΔTr) and the undercooling at the end of solidification (ΔT_3) are characteristic for in-mould treatment at lower inoculant addition rates;
*The difference between un-inoculated and inoculated irons is strongly affected by the alloy addition rate, much more so for ladle inoculation.
*Generally, the efficiency of 0.05-0.15wt.% alloy for in-mould inoculation is comparable to or better than 0.15-0.25wt.% addition in ladle inoculation procedures;
*The Ca,Zr,Al-FeSi alloy appears to be efficient in low S, low Al, low CE hypo-eutectic grey cast irons, especially for late inoculation.

References

[1]. **Loper Jr., C.R. and Gundlach, R.B.**, 1998., ***Inoculation What is it and How Does Inoculation Work,*** AFS International Inoculation Conference, Chicago
[2]. **Loper Jr., C.R.,** 1999, ***Inoculation of Cast Iron-Summary of Current Understanding***, AFS Transactions, Vol. 107, pp.523-528.
[3]. **Chisamera, M., Riposan, I. and Barstow, M**., ***The Importance of Sulphur to Control Graphite Nucleation in Cast Iron***, AFS International Inoculation Conference, Chicago, 1998.
[4]. **Riposan, I., Chisamera, M., Stan, St. and Skaland, T.**, 2003, ***Graphite Nucleant (Microinsclusions) Characterization in Ca/Sr Inoculated Irons***, International Journal of Cast Metal Research, Vol. 16, No.1-3, pp.105-111.
[5]. **Riposan, I., Chisamera, M., Stan, St., Skaland, T. and Onsoien, M.I**., 2001, ***Analyses of Possible Nucleation Sites in Ca/Sr Over Inoculated Gray Irons***, AFS Transactions, Vol. 109, pp.1151-1162.
[6]. **Riposan, I., Chisamera, M., Stan, St. and Skaland, T.,** 2005, ***A New Approach to Graphite Nucleation Mechanism in Gray Irons***, Proceedings of the AFS Cast Iron Inoculation Conference, Sept. 29-30, 2005, Schaumburg, USA, pp.31-41.
[7]. **Riposan, I., Chisamera, M., Stan, St., Ecob, C. and Wilkinson D.,** 2007, Role ***of Al, Ti, Zr in Grey Iron Preconditioning/Inoculation, World Foundry Organization (WFO)*** Technical Forum, Dusseldorf, Germany, 12-14.06.2007.
[8]. **Sillen, R.V**., 1998, ***Optimizing Inoculation Practice by means of Thermal Analysis,*** AFS International Inoculation Conference, Chicago.
[9]. **Sillen, R.V**, ***Novacast Technologies***, www.novacast.se, 2006.
[10]. **Sparkman, D.,** 1994, ***Understanding Thermal Analysis of Iron***, AFS Transactions, Vol. 102, pp.229.
[11]. **Sparkman, D. and Bhaskaram, C.A.,** 1996, ***Chill Measurement by Thermal Analysis***, AFS Transactions, Vol. 104, pp.969-976.
[12]. **Gunay, Y., Decirmenci, S., Metan, I. and Sirin, B.,** 2004, ***The Application of Adaptive Thermal Analysis System (ATAS) on Grey and Ductile Iron Production,*** 66th World Foundry Congress, 06-09.09. Istanbul, Turkey.
[13]. **Chisamera, M., Riposan, I., Stan, St., Albu, C.B., Brezeanu, C. and Naro, R.I.,** 2007, ***Comparison of Oxy-sulfide Alloy Tablets and Ca-bearing FeSi75 for Late Inoculation of Low Sulfur Grey Irons,*** AFS Transactions, Vol. 115, Paper 07-023.

THE ANNALS OF "DUNAREA DE JOS" UNIVERSITY OF GALATI.
FASCICLE IX. METALLURGY AND MATERIALS SCIENCE
N^0. 2 – 2008, ISSN 1453 – 083X

ON THE CONSTITUTIVE EQUATION OF A LOW CARBON STEEL

Nicolae CANANAU, Petrica ALEXANDRU,
Ionel PETREA, Gheorghe GURAU
"Dunărea de Jos" University of Galati
e-mail: nicolae.cananau@ugal.ro

ABSTRACT

The paper shows the results of the researches concerning the equation of deformation behavior of low carbon steel. The behavior law is established starting from the experimental torsion moment. The composed constitutive law had very good experimental verification.

KEYWORDS: constitutive equation, torsion test, stress intensity, strain intensity

1. Introduction

The establishing of the equation of plastic deformation behavior is a process of transformation of the torsion moment function in the stress intensity function, respectively, the equation between the stress intensity, strain, strain rate and temperature [1]:

$$\sigma = \sigma(\varepsilon, \dot{\varepsilon}, T) \qquad (1)$$

In this equation σ is the stress intensity in the real deformation conditions, ε - strain intensity, $\dot{\varepsilon}$ - strain rate intensity, T – temperature.

This paper it presents the results of researches effectuated for transformation of the torsion moment diagrams, in the aim of establishing the equation of plastic deformation behavior for low carbon steel.

The influence of the strain rate and temperature is defined by the equation [1]:

$$M_{max} = 0{,}081786\ \dot{\varepsilon}^{0{,}115973}\ \exp\frac{4949{,}259}{T} \qquad (2)$$

The function of the stress intensity is defined by the equation (3):

$$M(\varepsilon, \dot{\varepsilon}, T) = \begin{cases} A_1\ (1 - exp(-n\varepsilon))\ \left(\frac{\dot{\varepsilon}}{\dot{\varepsilon}}\right)^m\ exp\ \frac{mQ}{RT} & for\ \varepsilon \le \varepsilon_0 \\ A_2\ exp\ -p\ (\varepsilon - \varepsilon_0)\ \left(\frac{\dot{\varepsilon}}{\dot{\varepsilon}}\right)^m\ exp\ \frac{mQ}{RT} & for\ \varepsilon > \varepsilon_0 \end{cases} \qquad (3)$$

In this equation A_1 and A_2 are function of the strain rate and temperature, ε is the strain intensity, $\dot{\varepsilon}$ - strain rate intensity, T – temperature, m – exponent of the strain rate, Q – activation energy, R – perfect gas constant.

2. Experimental results

The first expression is valuable for the small values of the strain and the second for the great values of strain.

The calculus demonstrated that the good value of the factor n for the description is of 0.82.

Using this value for n and the experimental values from the torsion moment diagrams we obtained the values of A_1 factor which are rendered in figure 6.

The factor A_1 increases at the increasing of the temperature. The variation of this factor with the strain rate is a function with minimum.

Using the statistic calculation program and adopting a polynomial function we obtained the following expression:

$$A_1 = a + b\ \dot{\varepsilon} + c\ \dot{\varepsilon}^2 + d\ T + e\ T^2 \qquad (4)$$

The constants have the values:

a = -25.8439
b = - 0.67378
c = 0.323974
d = 0.064487
e = -3.33E-05

The coefficient of multiple determination (R^2) = 0.8933896392.

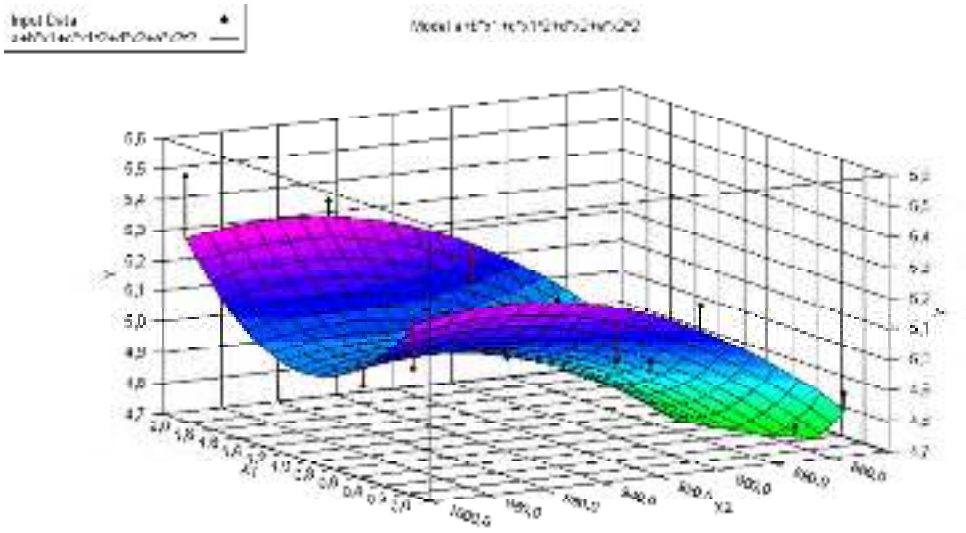

Fig. 6. The variation of the factor A_1 with the $\dot{\varepsilon}$ and T

At the great strains we must use the second expression for calculus of the stress intensity. This expression shows that the values of the stress decrease exponentially with the strain because of thermal deformation effect. The thermal effect is greater at the great values of the strain rate.

Taking the values for the maximum torsion moment and what corresponds to the strain equal to 1, we obtained the values of the factor ***p*** rendered in the graphic in figure 7.

This factor increases with the strain rate and temperature.

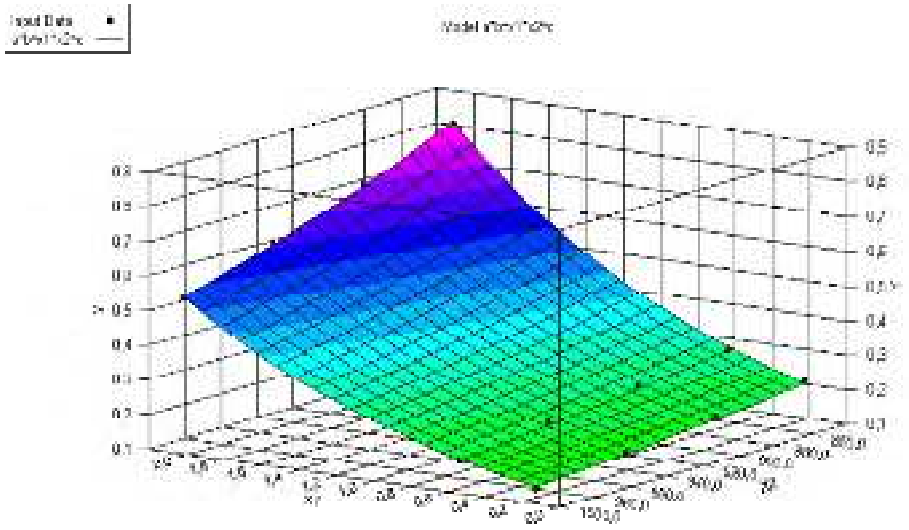

Fig. 7. The variation of the factor p with the strain rate and temperature

The function of the ***p*** has the expression:

$$p = a \quad b^{\dot{\varepsilon}} \quad T^{c} \qquad (5)$$

The constants from this equation have the values:

a = 5182737
b = 2.006384
c = -2.52708

The coefficient of Multiple Determination (R^2) = 0.9992338986

The factor A_2 is defined in function of the maximum values of the torsion moment. We obtained the values of this factor which are remade and rendered in figure 8.

The function of the factor A_2 has the expression:

$$A_2 = a + b\ \dot{\varepsilon} + c\ \dot{\varepsilon}^2 + d\ T + e\ T^2 + f\ \dot{\varepsilon}\ T \qquad (6)$$

The constants from this equation have the values:

a = -0.33971
b = -0.04087
c = 0.000952
d = 0.005274
e = -5.31E-07
f = 3.20E-05

The coefficient of multiple determination (R^2) = 0.9473061163

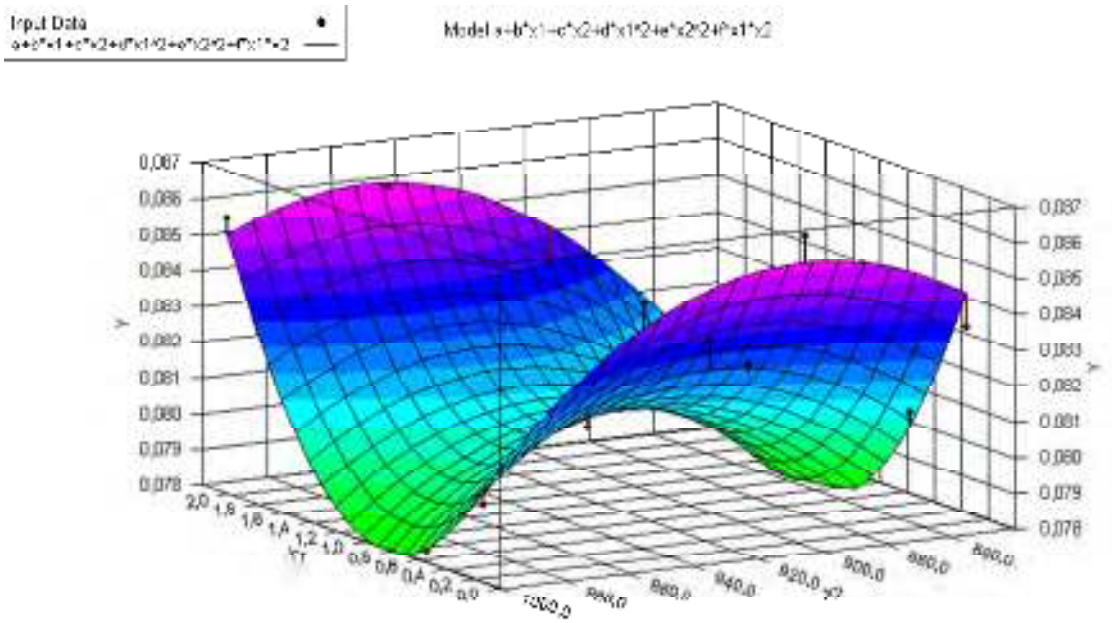

Fig. 7. The variation of the factor A_2 with the strain rate and temperature

It may be observed that the mathematical model defined based on experimental data has a good verification, the coefficients of multiple correlation have great values.

For the practical calculus is necessary the constitutive equation of the material defined as the function of the stress intensity in correlation with the plastic deformation factors: strain intensity, strain rate intensity and temperature.

Therefore the transforming of the equation of the torsion moment is necessary.

The stress intensity is defined in function of the torsion moment using the general transforming equation of:

$$\sigma = \frac{\sqrt{3}}{2\pi R^3}\left(3M + \dot{\varepsilon}\frac{\partial M}{\partial \dot{\varepsilon}} + \varepsilon\frac{\partial M}{\partial \varepsilon}\right) \qquad (7)$$

It is evident that the stress intensity is defined identically with the torsion moment.

Taking the expression of the dependence of the torsion moment in function of the strain rate, the second factor from parentheses has the value equal to ***m***.

Respectively, we have:

$$\dot{\varepsilon}\frac{\partial M}{\partial \dot{\varepsilon}} = m$$

Thus the expression for the calculus of stress intensity, starting of the equation (3) becomes:

$$\sigma(\varepsilon,\dot{\varepsilon},T) = \begin{cases} \frac{\sqrt{3}}{2\pi R^3}(1+m)\,A_1\,(1-exp(-n\varepsilon))\left(\frac{\dot{\varepsilon}}{\dot{\varepsilon}}\right)^m exp\,\frac{mQ}{RT} & for\ \varepsilon \le \varepsilon_0 \\ \frac{\sqrt{3}}{2\pi R^3}(1+m)\,A_2\,exp\,-p\,(\varepsilon-\varepsilon_0)\left(\frac{\dot{\varepsilon}}{\dot{\varepsilon}}\right)^m exp\,\frac{mQ}{RT} & for\ \varepsilon > \varepsilon_0 \end{cases} \qquad (8)$$

In this relation ***R*** is the radius of the sample used at the experimental researches, the torsion testing.

Finally, the expression (8) will be used at the modeling of the deformation process.

4. Conclusions

The knowledge of the constitutive equation of the material is necessary for the modeling, simulation and optimization of the plastic deformation process. The best method for establishing the constitutive equation is the torsion testing.

Applying a research program at the torsion testing machine in the Plastic deformation laboratory at the Faculty of Metallurgy and Materials Science from ***Dunarea de Jos*** University of Galati was it established the constitutive equation of a low carbon steel with great mechanical characteristics. The constitutive equation shows that the influence of strain rate is described by the power mathematical relation, the influence of the temperature is described by an exponential function.

The strain has a complex influence described by a compose function.

References

[1]. Cănănău N., 1994, ***Teoria deformării plastice,*** Universitatea Dunarea de Jos din Galati

[2]. Dumitrescu A.T., 1986, ***Contribuţii la modelarea laminarii in calibre***. Teza de doctorat, Institutul Politehnic Bucureşti

[3]. Corobete, G. 2006, ***Contribuţii la cercetarea procesului de laminare a sârmelor din otel cu caracteristici mecanice superioare. Teza de doctorat,*** Universitatea Dunărea de Jos din Galaţi

[4]. Moussy F., Franciosi P., 1990, ***Physique et mecanique de la mise en forme des meteaux.*** Presses du CNRS, Paris, ISBN 2-87682-023-4

[5]. Cananau N., Petrea I, Corobete G., 2005, ***Modelling of the flow and deformation fields at the profiles rolling by field lines method*** , The Annals of "Dunarea de Jos" University of Galati, Fascicle IX.

THE ANNALS OF "DUNAREA DE JOS" UNIVERSITY OF GALATI.
FASCICLE IX. METALLURGY AND MATERIALS SCIENCE
N^0. 2 – 2008, ISSN 1453 – 083X

CONTRIBUTIONS IN THE DOMAIN OF THE CONTACT STRESSES BETWEEN CYLINDERS OF COLD ROLLING

A.D. MAIMON[1], D. BOAZU[2], L. STOICESCU[2]
[1]ARCELOR – Mittal Steel Galati
[2]"Dunărea de Jos" University of Galaţi
email: dboazu@ugal.ro

ABSTRACT

Elasto-plastic contact stresses between working cylinder and support cylinder of cold rolling using FEM are presented in this paper. Pressure and tractions resulted from the rolling process were obtained by using a calculus program and they were used as loads on a working cylinder.

KEYWORDS: cold rolling, elasto-plastic contact stresses, rolling process

1. FEM model of contact between working cylinder (585mm) and support cylinder(1525mm) of cold rolling

For the modelling process COSMOS/M version 2.5 was used. The two cylinders were modelled using PLANE2D (plane strain) elements with 4 nodes and two degrees of freedom per node. 2D model is represented in Fig. 1. A zoom of fin mesh in the vicinity of contact between the two cylinders is presented in Fig. 3 and the mesh in loading zone (load is given by normal and tangential pressure from rolling process) is represented in Fig. 2. The whole model has 14517 nodes and 17101 elements.

One node GAP elements (in 2D node-line contact elements) were used for transmission of stresses and deformations through contact zone.

The two cylinders were considered supported by elastic elements whose rigidity is given by that of the rolling system. Working with GAP elements imposed an incremental loading and so the analysis is static but nonlinear.

The contact between cylinders is a non-conforming contact problem because the extension of contact zone is not known from the beginning.

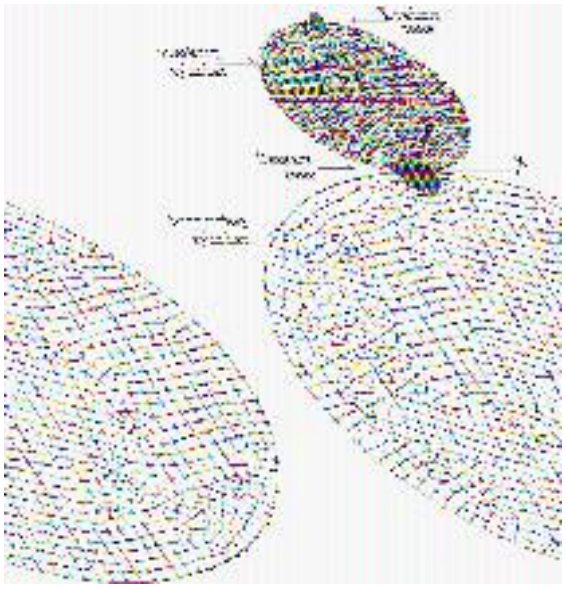

Fig. 1. FEM model between working cylinder and support cylinder of cold rolling.

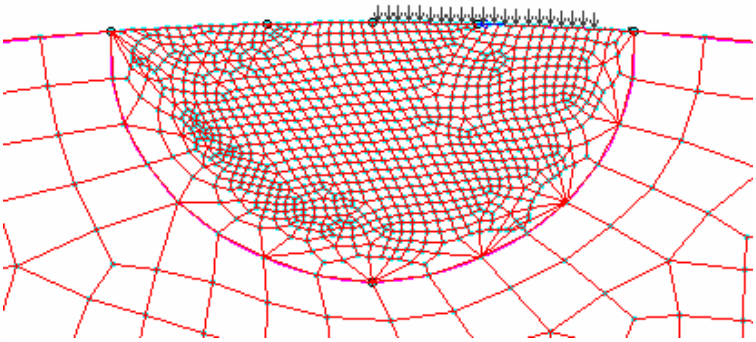

Fig. 2. Mesh in loading zone of working cylinder

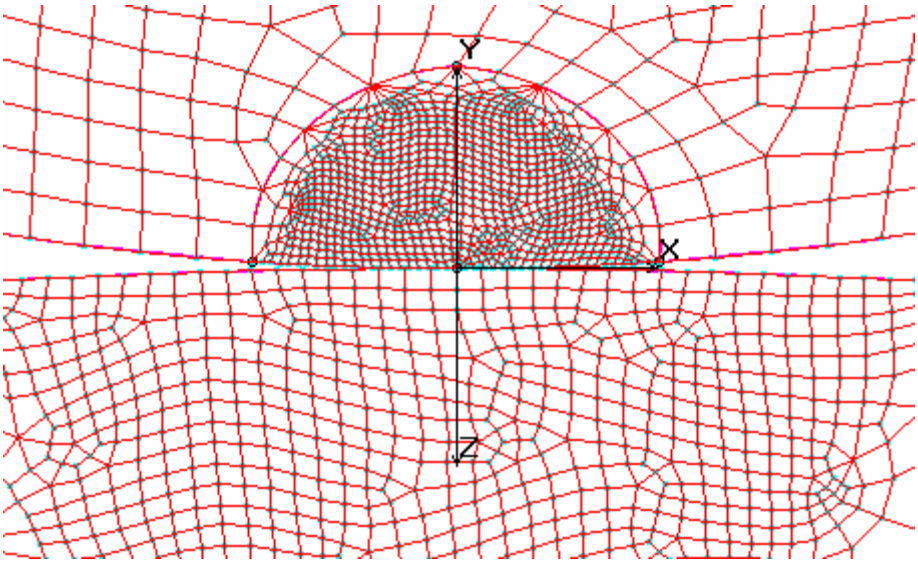

Fig. 3. Mesh in contact zone between the two cylinders

2. Material model

The elasto plastic behaviour of material (special steel) of the two cylinders was considered von Mises with isotropic hardening. Principal parameters of material model are: Young modulus E=2.1 10^4 daN/mm^2, Poisson ratio 0.3, yield stress 73 daN/mm^2, and tangent modulus 20daN/mm^2).

3. Studied cases

It was analyzed two cases with the 5 phases of sheet thickness reduction. (17.7%, 20.6%, 24.2%, 20.8, 17.5%). In the first case the friction coefficient was considered μ=0.1 and in the second case friction coefficient was considered μ=0.075. The width of the sheet was considered 1250mm.

The loading conditions for cold rolling were established according to reference [3].

For these analyzed cases the equivalent von Mises stress distribution and principal stresses are represented in Fig. 4-8 (μ=0.1) and Fig. 9-13 (μ=0.075). The extension of contact zone is of 40mm. The contact stain extends to about 40 mm.

The results of nonlinear analysis are given in Table 1 (Case 1 (μ=0.1)) and Table 2 (Case 1 (μ=0.1))-von Mises stresses from contact zone (σech - for working cylinder) and (σech - for supporting cylinder) and principal stresses in the contact zone $\sigma_1, \sigma_2, \sigma_3$. The stress state in the vicinity of contact is 3D. In Tables 1 and 2 principal stresses $\sigma_1 < \sigma_2 < \sigma_3$ are negative values and the biggest one σ_3 is considered the contact stress (Hertzian pressure). The equivalent von Mises stress was evaluated at a distance of 2 mm from contact effective zone, because in the contact zone the components of deviator tensor are unmeaningful.

The influence of friction on loading and contact behaviour was considered by modifying friction coefficient (μ=0.1 for dry friction) and (μ=0.075 for lubrification).

The equivalent von Mises stress is calculated using the formula:

VON = $\{(1/2)[(\sigma_X - \sigma_Y)^2 + (\sigma_X - \sigma_Z)^2 + (\sigma_Y - \sigma_Z)^2] + 3(\tau^2_{XY} + \tau^2_{XZ} + \tau^2_{YZ})\}^{(1/2)}$

Or by means of principal stresses:

VON = $\{(1/2)[(\sigma_1 - \sigma_2)^2 + (\sigma_1 - \sigma_3)^2 + (\sigma_2 - \sigma_3)^2]\}^{(1/2)}$

Table 1

Case 1 (μ=0.1)	σech [daN/mm^2]	σech [daN/mm^2]	$\sigma_{1,max}$ [daN/mm^2]	$\sigma_{2,max}$ [daN/mm^2]	$\sigma_{3,max}$ [daN/mm^2]
Phase A1	72.95	72.95	79.95	117.97	150.91
Phase A2	73	73	150.4	178.9	215.5
Phase A3	73	73	156.068	184.79	230.258
Phase A4	72.99	72.99	130.989	146.134	200.24
Phase A5	73.563	73.563	253.754	289.142	330.84

Table 2

Case 1 (μ=0.075)	σech [daN/mm^2]	σech [daN/mm^2]	$\sigma_{1,max}$ [daN/mm^2]	$\sigma_{2,max}$ [daN/mm^2]	$\sigma_{3,max}$ [daN/mm^2]
Phase F_A1	72.953	72.953	73.389	108.123	136.507
Phase F_A2	72.890	72.890	81.960	118.186	153.887
Phase F_A3	73.044	73.044	141.576	172.475	217.362
Phase F_A4	72.937	72.937	105.476	129.328	169.797
Phase F_A5	73.036	73.036	167.813	197.075	241.869

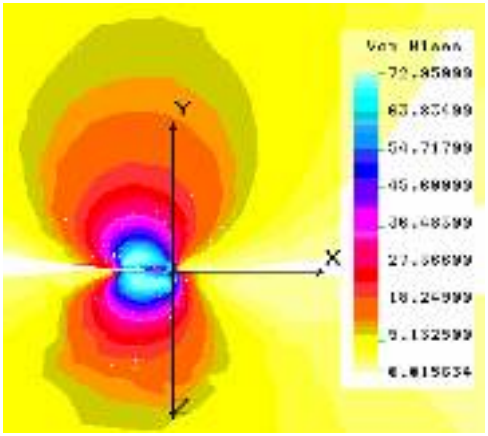

Fig. 4a. Case 1 (μ=0.1) Phase A1 von Mises stress

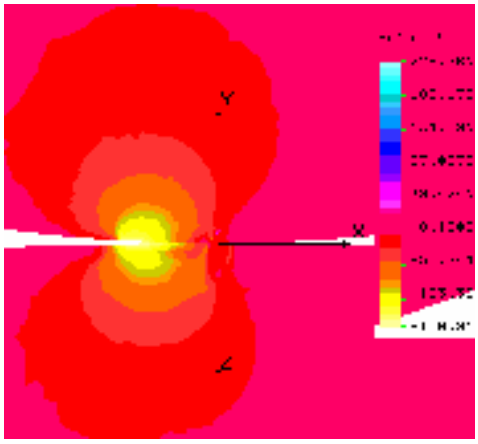

Fig.4b. Case 1 (μ=0.1) Phase A1 principal stress σ3

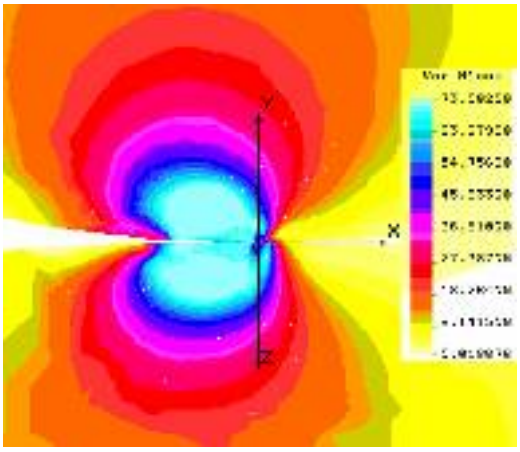

Fig. 5a. Case 1 (μ=0.1) Phase A2 von Mises stress

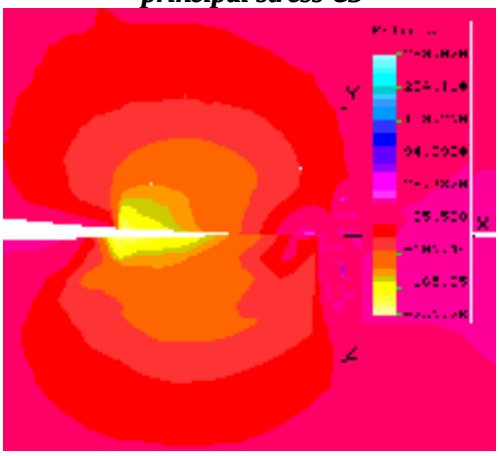

Fig. 5b. Case 1 (μ=0.1) Phase A2 principal stress σ3

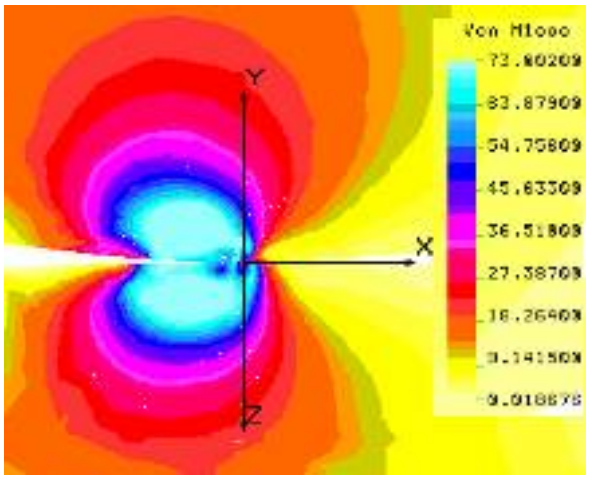

Fig. 6a. Case 1 (μ=0.1) Phase A3 von Mises stress

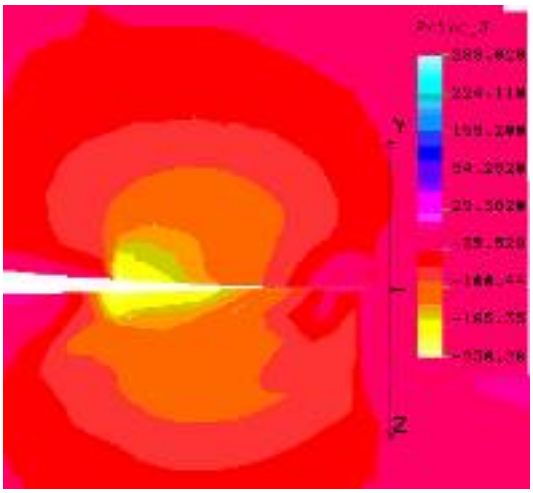

Fig. 6b. Case 1 (μ=0.1) Phase A3 principal stress σ3

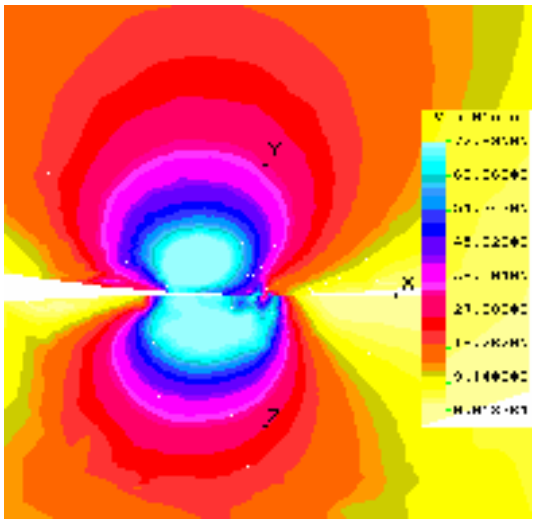

Fig. 7a. Case 1 (μ=0.1) Phase A4 principal stress σ3

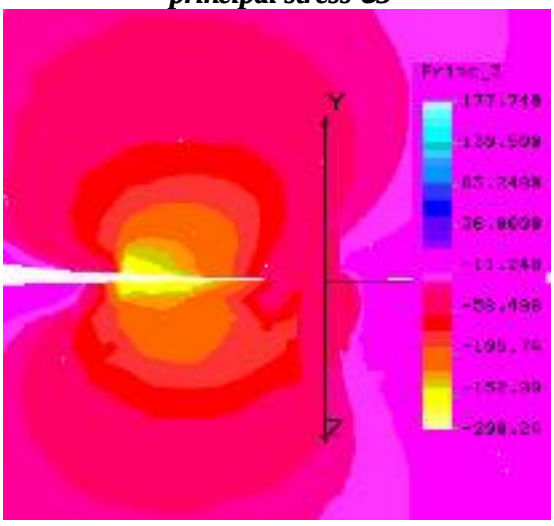

Fig. 7b. Case 1 (μ=0.1) Phase A4 principal stress σ3

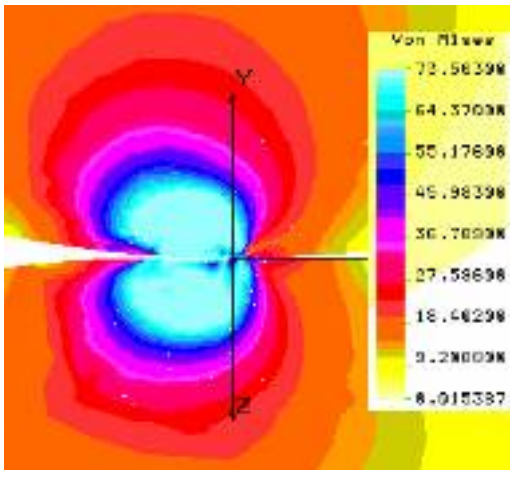

Fig. 8a. Case 1 (μ=0.1) Phase A5 principal stress σ3

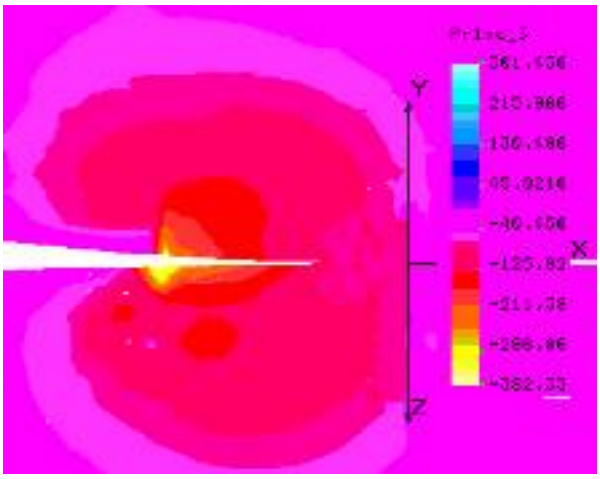

Fig. 8b. Case 1 (μ=0.1) Phase A5 principal stress σ3

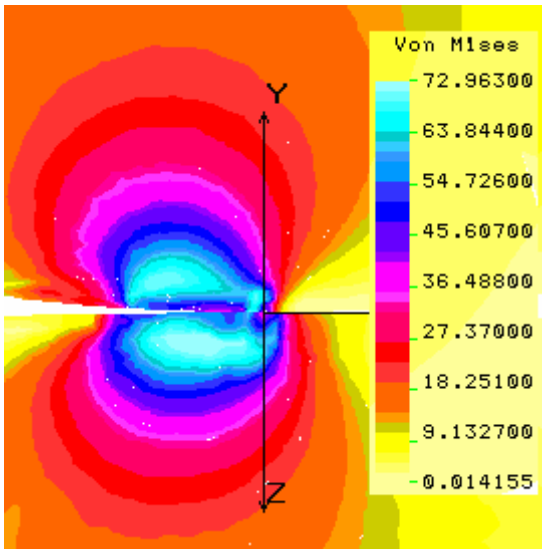

Fig. 9a. Case 2 (μ=0.075) Phase F_A1 principal stress σ3

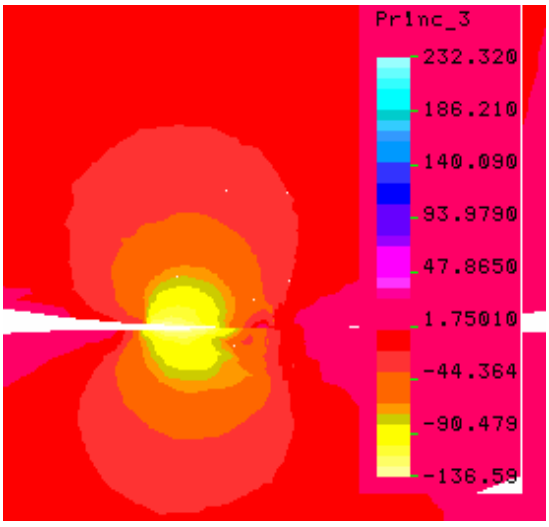

Fig. 9b. Case 2 (μ=0.075) Phase F_A1 principal stress σ3

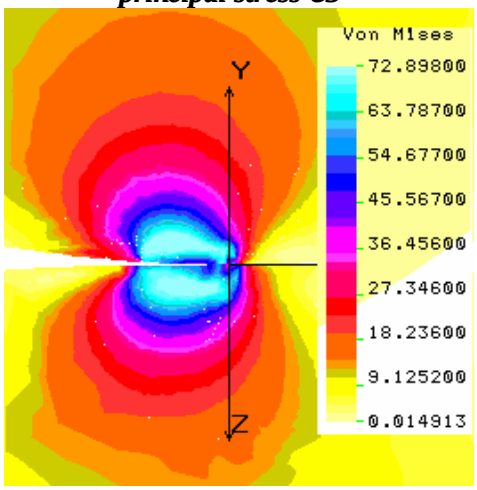

Fig. 10a. Case 2 (μ=0.075) Phase F_A2 principal stress σ3

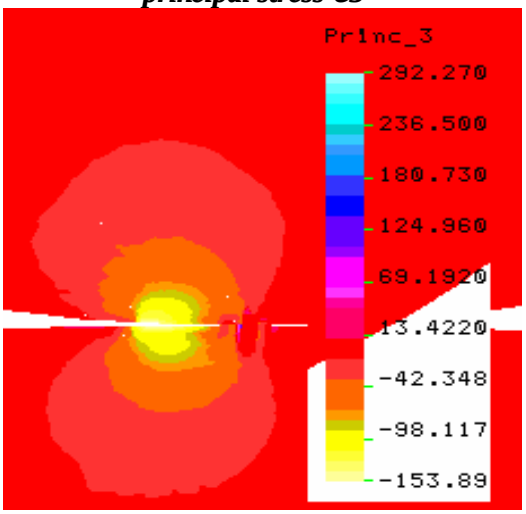

Fig. 10b. Case 2 (μ=0.075) Phase F_A2 principal stress σ3

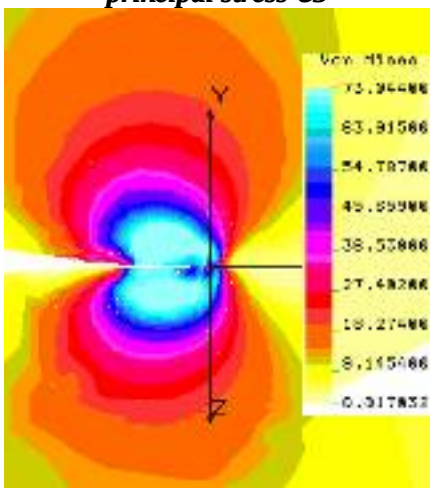

Fig. 11a. Case 2 (μ=0.075) Phase F_A3 principal stress σ3

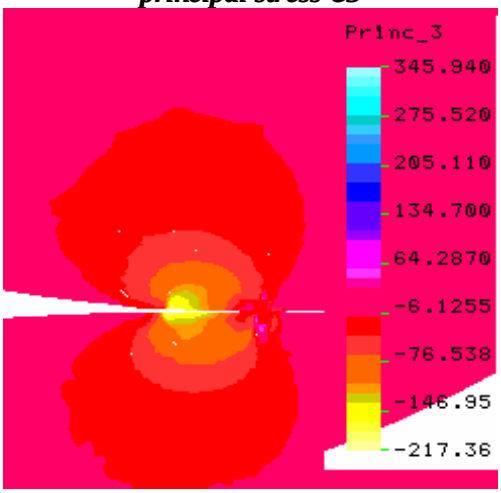

Fig. 11b. Case 2 (μ=0.075) Phase F_A3 principal stress σ3

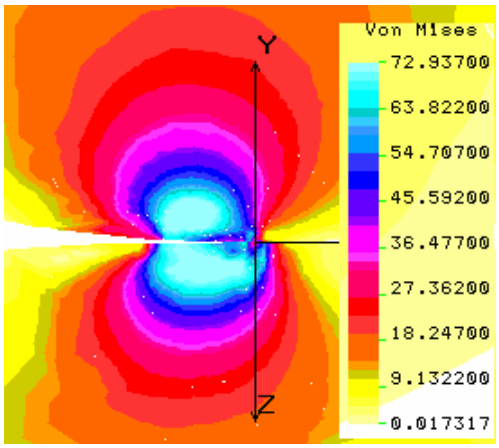

Fig. 12a. Case 2 (μ=0.075) Phase F_A4 principal stress σ3

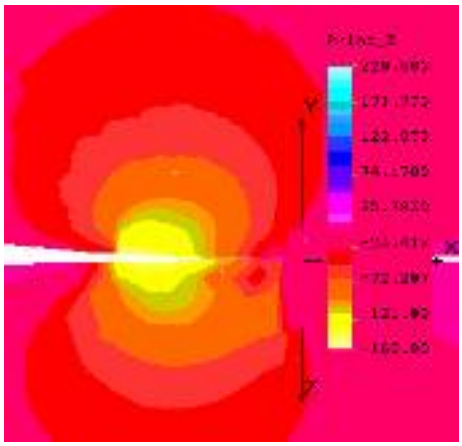

Fig. 12b.Case 2 (μ=0.075) Phase F_A4 principal stress σ3

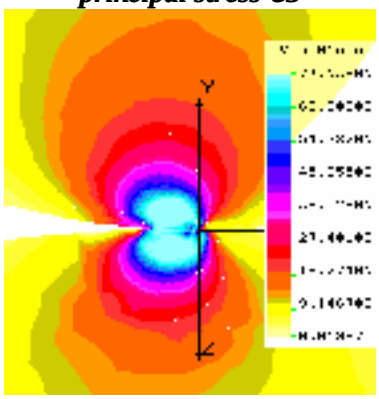

Fig. 13a. Case 2 (μ=0.075) Phase F_A4 principal stress σ3

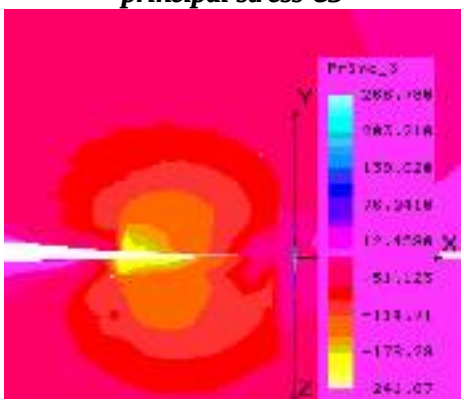

Fig. 13b. Case 2 (μ=0.075) Phase F_A4 principal stress σ3

4. Conclusions

From Fig. 14 one can observe that contact stresses are bigger when the rolling process is not lubrificated.

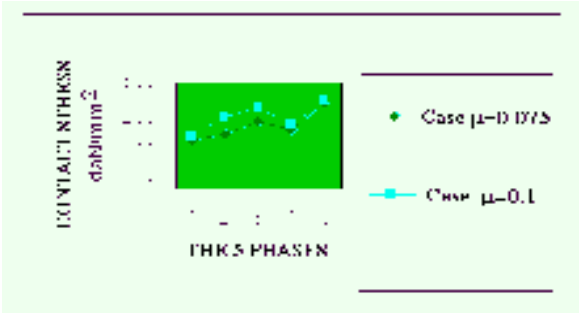

Fig. 14.

For all loading cases there are important plastic zones of elliptic shape. In the worst loading case (Case 1 (μ=0.1) Phase A5 - see table 1) this elliptic region is determined by the two semiaxes of 30mm and 25mm; the eccentricity of this plastic zone in respect to vertical axis of the two cylinders is about 40mm.

References

[1]. Bern A., 1990, ***Le laminage a froid***, Symposium franco-roumain, Galati.

[2]. Poloukhine V., 1977, ***Simulation mathematique et calcul sur ordinateur des laminoirs a toles***, Edition MIR, Moscou,.

[3]. Stoicescu L., Gavrilescu I., Boazu D., 1995, ***Algoritm şi program pentru modelarea laminării la rece***, Asociaţia oamenilor de ştiinţă, filiala Galaţi, Departamentul de Inginerie Tehnologică şi Deformare Plastică, tom 21, octombrie 1995, pg. 123-128.

THE ANNALS OF "DUNAREA DE JOS" UNIVERSITY OF GALATI.
FASCICLE IX. METALLURGY AND MATERIALS SCIENCE
N^0. 2 – 2008, ISSN 1453 – 083X

STRUCTURAL CHARACTERISTICS IN COBALT BASED ALLOYS

Brânduşa GHIBAN[1], Cristina BORȚUN[2], Sorin CIUCA[1]
[1]University Politehnica of Bucharest
[2]"V. Babeş" University of Medicine and Pharmacy Timişoara
e-mail: brandusa@sim.pub.ro

ABSTRACT

In the present paper there are presented results of investigations on samples of partially removable denture made of cobalt base alloys (Co-Cr-Mo) regarding specific structural analysis: determination of structural phases by quantitative and qualitative microstructural analysis, microhardness determinations versus different casting parameters [1,2,3,4]. By metallographic analysis some important structural aspects may be pointed: the presence of lace eutectic and carbides with discontinuous precipitation in metallic matrix, non-uniform dendritic structure with interdendritic micro-porosities, interdendritic cracks in a structure with fine lace eutectic. Different types of welding were tested, which gave both structural modification and morphology of constituents. Structural modifications which can be made for repairing of prosthesis may diminish mechanical properties of prosthesis, microhardness values of two cobalt base alloys welded by laser technology being high, which may confer a brittle behaviour.

KEYWORDS: denture prosthesis, cobalt base alloy, structural analysis, microhardness

1. Introduction

Cobalt based superalloys continue to be used with great interest in dentistry due to simultaneous properties, such as: high mechanical characteristics (yielding strength, ultimate strength, hardness), biocompatibility, or wear resistance [1,2,3,4,5]. In dentistry cobalt is still used for realizing partial or total prosthesis. The most used cobalt base alloy for dentistry is Co-Cr-Mo with a carbon content of about 0,03%. The problems which are met during casting of prosthesis are connected to crack susceptibility and brittle behaviour after a rather short time of prosthesis working. Present paper is focused on structural modification analysis of different cobalt alloys used for denture prosthesis.

2. Experimental Methods

In the present paper there are presented results of investigations on samples of partiallz removable denture made of cobalt base alloys (Co-Cr-Mo) regarding specific structural analysis: structural phases (by X-Rays diffraction), quantitative and qualitative microstructural analysis, microhardness determinations versus different casting parameters [1,2,3,4]. Since the interdendritic phases are associated t reduced ductility and reduced corrosion resistance, cast Co-Cr-Mo is the typically solution annealed at approximately 1225°C. Such a thermal treatment results in the transformation of **σ** phase to $M_{23}C_6$ and the partial dissolution of the $M_{23}C_6$ phase. It was determined that 1225°C is the optimal temperature for annealing since, at this temperature, a complete and rapid transformation of the carbides $M_{23}C_6$ to M_6C or **σ** occurs. Solution annealing for extended times (24-48h) leads to a homogeneous microstructure. The CoCrMo alloy used in dentistry is particularly susceptible to work-hardening so that the normal fabrication procedure used with other metals cannot be employed.

The experimental alloys were cast by a investment casting method, following the steps:
1. A wax pattern of the desired component was made.
2. The pattern was coated with a refractory material, first by a thin coating with a slurry followed by complete investing after drying.
3. The wax was melted out in a furnace (100-150°C).
4. The mold was heated to a high temperature burning out any traces of wax or gas-forming materials.

Fig. 1- Caloris CD 1016 Heating Furnace

5. Molten alloys were poured with gravitational or centrifugal force. The mold temperature was about 800-1000°C and the alloy was at 1350-1400°C, in figure 1 being shown the experimental furnace.

Controlling the mold temperature will have an effect on the grain size of the final cast; coarse ones are formed at higher temperatures, which will decrease the strength. However, high processing temperature will result in larger carbides precipitates with greater distances between them resulting in a less brittle material.

X-Rays diffraction was made on DRON 3 device, qualitative and quantitative microstructural analysis was made on REICHERT microscope equipped with IMAGE –Pro software for analysis. Different types of welding were tested, which gave both structural modification and morphology of constituents.

3. Results and Interpretations

Results concerning the chemical composition of the experimental alloys are given in table 1.
Macroscopic analysis of the experimental alloys is shown in figure 2.

Table 1. Chemical composition of the experimental cobalt base alloys

Experimental alloys	Chemical Composition, %							
	C	Cr	Mo	Ni	Fe	Mn	Si	Co
A	0.29	26.5	5.35	0.60	0. 64	0.67	0.97	Rest
B	0.35	26.4	5.38	0.85	0.74	0.63	0.89	Rest
Welded prosthesis	0.05	28.9	5.6	0.21	0.17	0.79	0.49	Rest
IS0 5832 /4/	Max 0.35	26.5-30	4.5-7	Max 1.0	Max 1.0	Max 1.0	Max 1.0	Rest

alloy A

alloy B

Welded prosthesis

Fig. 2. Macroscopic aspects of experimental cobalt samples for dentistry applications.

The microstructure results of the as - cast alloys are shown in **Figures 3 (a)**, consisted of cobalt-rich FCC matrix dendrites and a very fine interdendritic eutectic. In the high carbon alloy, slow cooling from below the eutectic temperature gave rise to relatively coarse grains, continuous grain boundary carbide films, and interdendritic blocky carbides. In alloy B it was observed non-uniform dendritic structure with interdendritic microporosities (figure 3 b, c). By welding of the samples of Co-Cr-Mo it can be studied the structural modifications which can be made for repairing prosthesis, it is given in **figure 3d** and **3e** interdendritic cracks in a structure with fine lace eutectic.

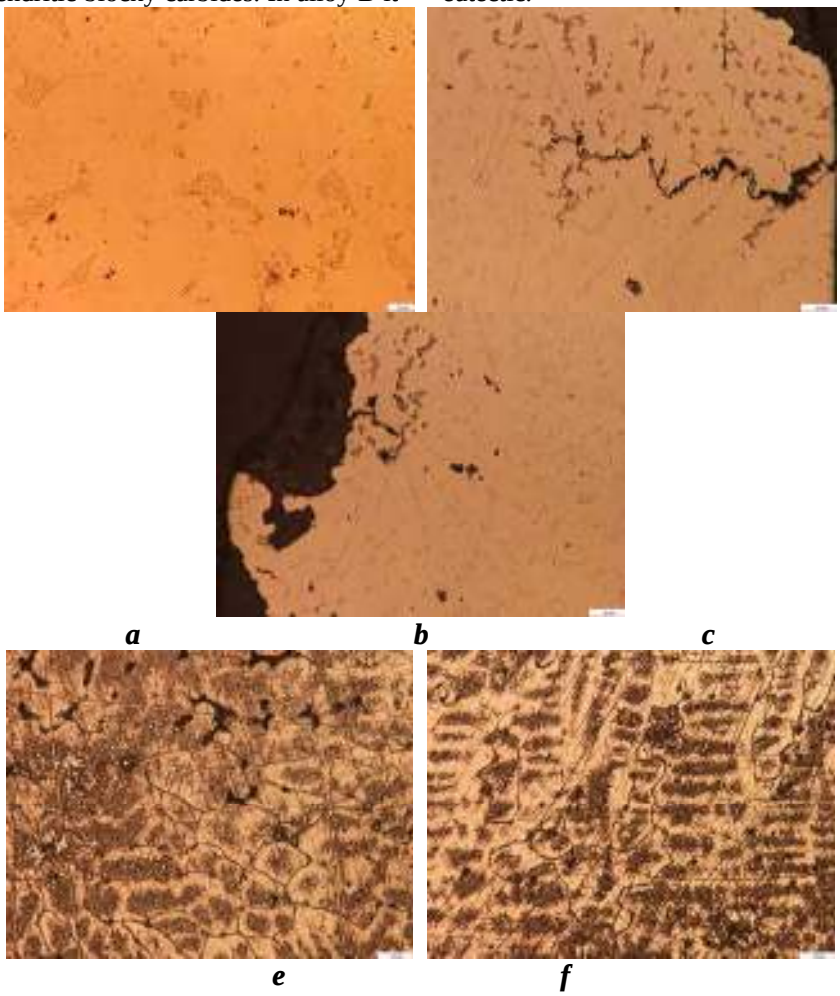

Fig. 3. Microstructural aspects of different samples of Co-Cr-Mo alloys used for dental applications

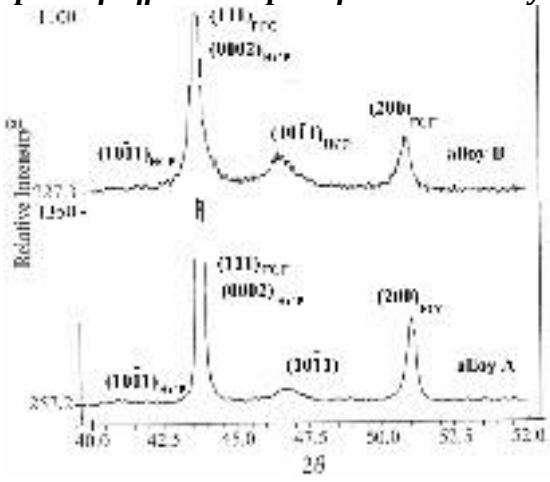

Fig. 4. X-Ray Diffractions of experimental alloys.

The eutectic presented in experimental alloys was identified as a mixture of $M_{23}C_6$, ***σ*** phase and FCC Co-rich phase, it is illustrated in **figure 4**. By heating the cobalt sample at different temperatures, respectively 825°C, 950°C and 1100°C two structural parameters were studied. Results concerning the influence of heat treatments on grain size are given in **figure 5** and results concerning the influence of heat treatments on precipitation size are shown in **figure 7**. Results concerning microhardness values of two cobalt base alloys welded by laser technology are illustrated in **figure 7**.

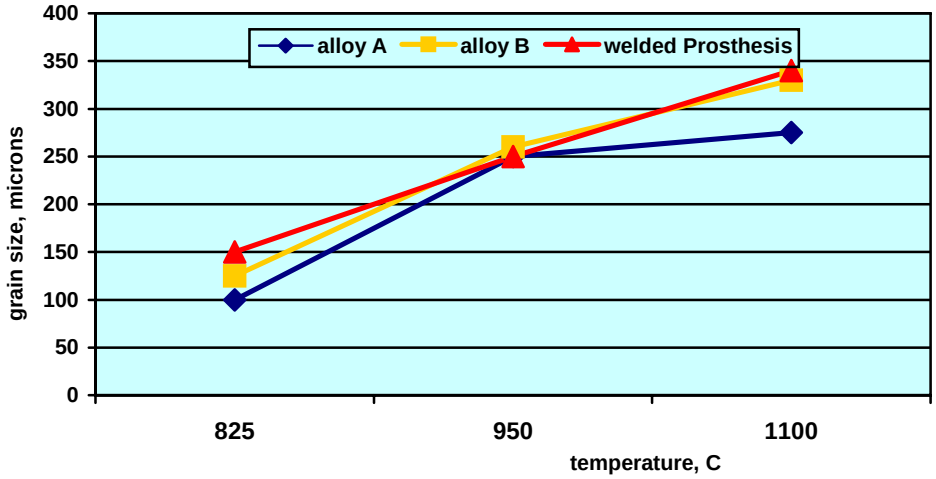

Fig. 5. Influence of heating temperature on grain size of experimental cobalt alloys

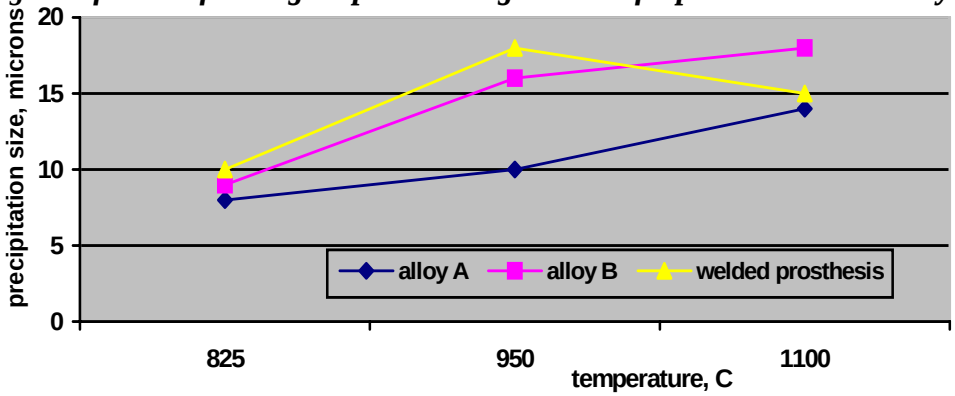

Fig. 6. Influence of heating temperature on precipitation size of experimental cobalt alloys

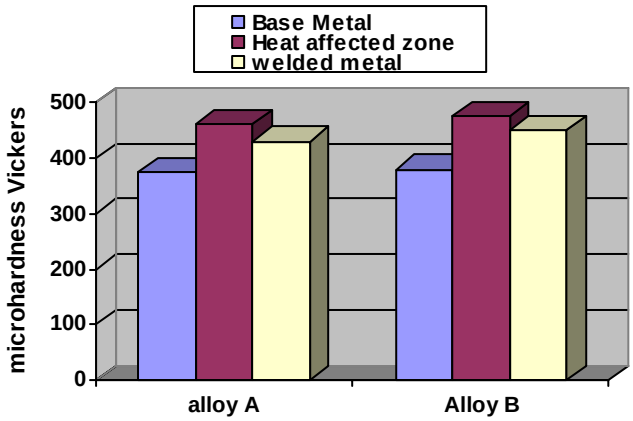

Fig. 7. Microhardness Vickers values of the investigated cobalt samples

4. Discussions

For both carbon contents, alloy heating at 815ÛC produced a fine carbide precipitate and fine –grained structure with a relatively large volume fraction of precipitates confined to the grain boundaries. The obtained microstructures were in agreement with those reported in a previous work. Furthermore, heating at 815ÛC led to relatively large stacking fault densities coupled with intragranular striations. These striations became apparent after preferential precipitation of carbides on the stacking faults. The precipitation reactions can be attributed to preferential solute diffusion to the stacking faulted regions due to the local hexagonal crystal structure. Also, carbide precipitation in favoured at hcp Co{0001} planes, which are nearly identical to $M_{23}C_6${111} planes. Alloy heating at 950 ºC induced a transition in the precipitate morphology, nucleation seems to occur at undissociated dislocations, whereas growth takes place along distinct crystallographic planes, predominantly of the {111}type. During heating at 1100ºC, precipitate spheroidization is dominant in both alloys.

The different precipitate morphologies associated with the implemented heats are responsible for the final microstructure obtained after solutioning at 1225ºC. Apparently, heating at 815ºC prior to solutioning inhibited, up to a certain extent, grain growth in both alloys. It is well known that a fine distribution of precipitates can effectively pin grain boundaries during grain growth, in so far the particles do not dissolve nor coarsen at the temperatures of interest. Assuming that appreciable carbide dissolution occurs at 1225ºC the interaction between moving boundaries and solute also contributes to limiting grain growth. Grain growth was effective in the alloys previously heated at 950ºC or 1100ºC. Apparently, in these heats, the intrinsic differences in carbide morphology (type) and distribution were responsible for the lack of substantial grain boundary pinning. Furthermore, at 1225ºC, grain boundaries become preferred sites for carbide coarsening, promoting the development of continuous films in the 950ºC and 1100ºC annealing.

These structural changes may explain the grain size and precipitation size modifications at different temperatures heating.

That is why by increasing the temperature, both grain size and precipitation size may increase, due to fill forming and grain growth.

5. Conclusions

- Optical microscopy observations indicated that Co-Cr-Mo-C alloys fabricated by investment castings exhibited large microstructural defects, which included interdendritic carbides, solute segregation, relatively large grains, and porosity. These microstructural defects tend to promote crack initiation and growth and explain the poor ductility and strength exhibited by as-cast alloys.
- The tensile properties of the heat-treated alloys exhibited significant improvements in ductility and strength when compared with the as-cast counterparts. The main effect of alloy preheating was manifested as a removal of the extensive interdendritic carbide precipitation and appreciable break-up of the dendritic grain structure. This leads to the development of a homogenous equiaxial grained structure and the consequent improvement in mechanical behaviour (by microhardness measurements).
- By welding with different laser technology, the materials for dental applications may be repaired. Cracks may appear either due to casting technology, or to welding by laser.

References

[1]. B. Ghiban, G. Cosmeleaţă, G. Dinescu, A. Faur, 2004, ***Structural Analysis of Some Total Hip Joint replacement after Revision***, International Conference on Advanced Materials and Technologies, 21-22 oct. 2004, ROMAT, pp. 56-63.

[2]. C. Borţun, I.Mitelea, L.Miloş, V.Bîrdeanu, L. Sandu 2005, ***Analysis of laser welded joints on „C" alloy used in removable partial dentures technology***, European Cells and Materials vol.10 Suppl. I pg 31.

[3]. L. Sandu, C. Borţun, L. Ardelean, N. Faur, 2005, ***Finite element analysis of stress distribution induced by thermal variations on cast clasps,*** European Cells and Materials, vol.9 Suppl.1 pg 3-4.

THE ANNALS OF "DUNAREA DE JOS" UNIVERSITY OF GALATI.
FASCICLE IX. METALLURGY AND MATERIALS SCIENCE
N^0. 2 – 2008, ISSN 1453 – 083X

STEEL AND REFRACTORY CHEMICAL INTERACTIONS AND MECHANICAL BEHAVIOR OF PLATES FOR SLIDING GATE DURING STEEL CONTINUOUS CASTING

Viorel MUNTEANU
"Dunarea de Jos" University from Galati
e-mal: Viorel.Munteanu@ugal.ro

ABSTRACT

The main objective to increase CC productivity as well as steel quality by using optimized refractory from ladle-tundish-to-mold lead to techniques that allow the prediction of steel and refractory chemical interactions as well as mechanical behavior of refractory component. Specific models (CFD) have also been developed to better take into account the physical parameters at the steel/refractory interface and to optimize steel flow control. They are completed by dedicated thermal stress analysis in order to improve thermal shock resistance. The mechanical Finite Element Analysis evaluations take into account specific mechanical behavior of refractory components as well as high temperature evolution of their properties.

KEYWORDS: continuous casting, refractory materials, chemical and mechanical behavior

1. Introduction

To improve the performances of steel flow control, new approaches have been developed in order to better understand the high temperature behavior of refractory components.

One of the main objectives was to precisely evaluate steel refractory interaction to determine corrosion mechanisms. This has been achieved by coupling specific experimentation and thermodynamic evaluation. A second objective has been to determine high temperature mechanical behavior of refractory components, which are composite products. The implementation of specific properties in Finite Element Analysis codes allows improved design of components and evaluation of material characteristic influences.

Finally the development of dedicated fluido-dynamic codes allows the prediction of physical and chemical phenomena occurring during steel continuous casting.[1]

2. Optimization of the sliding gate refractory plates

The plates are the core of a ladle slide gate, and the investigations concentrated initially on establishing the optimum plate design.

Existing plate design weaknesses:

The historical rectangular-rounded plate shape has been applied in many variants such as asymmetric or symmetric versus the bore position, canned or banded, with or without spigots. Their dimensions were generally oversized. Their wear pattern showed some weaknesses such as the formation of cracks in critical zones and particularly in the throttling and tracking areas.

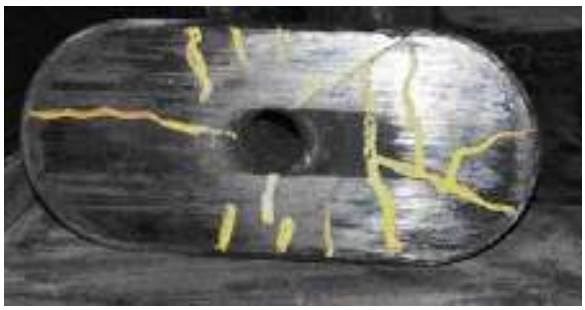

Fig.1. Rectangular-rounded plate with cracks

Modern analysis method:

Empirical research had already resulted in the development of more sophisticated plate shapes but the team decided to investigate using modern analysis methods such as Finite Element Analysis (FEA),

mathematic modelling, other laboratory constraint measurements and field trials to identify an optimized pattern. [4]

The material model considered the Young's modulus, the yield stress (plastic), the thermal conductivity, the heat capacity and the thermal expansion. The thermal boundary conditions were established based on field temperature measurements.

The mechanical boundary conditions were imposed by the mechanism design.

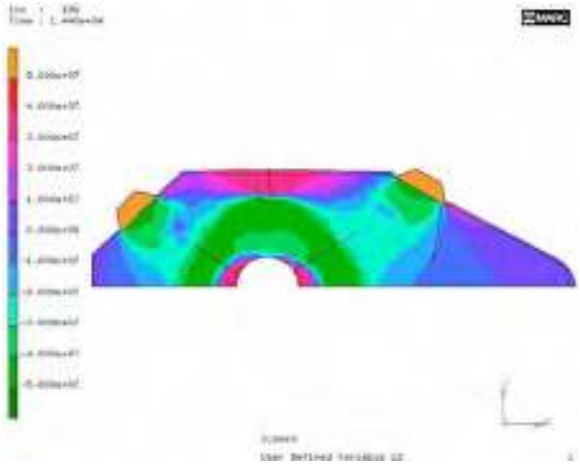

Fig.2. Finite element analysis of an optimized plate

Crack definition:

The observation of used plates allowed us to define three crack modes such as: outside cracks, longitudinal cracks and transversal cracks.

The outside cracks are related to the free expansion whilst the longitudinal cracks are related to the "clamping angle", the plate length/width ratio and the bore size. The transversal cracks are linked to the plate support load.

Sensitivity analysis carried out using elastic and elasto-plastic material models.

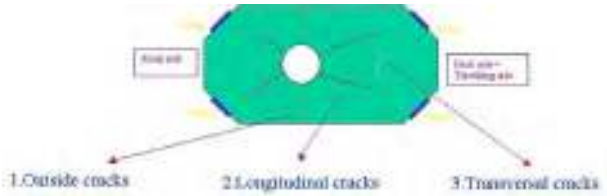

Fig.3. Crack definition

Theoretical conclusions:

The conclusions of this analysis can be gathered as follows:

-Critical influence of material plasticity

-Front and back-side stress pattern quite independent

-Clear influence of clamping angle on the stress pattern

-Minor influence of bore size on the stress pattern

-Clamping closest to the bore

-Limit the force applied on the plate through the clamp

"The crack cannot be avoided but the pattern can be influenced by the plate shape and clamping design" is the basis of the plate concept. Therefore, the cracks have been orientated to non-critical zones by the application of optimized clamping angle and clamping force.

Theoretical plate shape:

The so called "Coffin shape" plates are roughly fitting some of those conditions. This is the "basic design", however, this is not enough to comply with all production and operation requirements.

It is crucial to note that due to the optimised shape, smaller plates are performing better life with equivalent bore size. It strongly improves the recycling rate when using the plate on both faces (FLIP process). This significantly reduces the operation cost of the plates and the system.

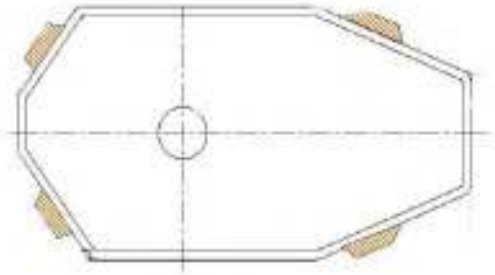

Fig.4. "Coffin shape" plate

Tuning this shape required more sophisticated considerations that generated a practical "optimized shape" that can be manufactured and efficiently applied in the mechanism.

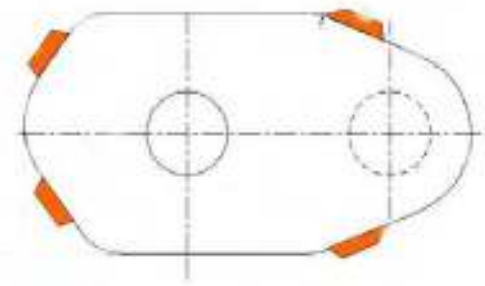

Fig.5. "Optimized" plate shape

A mathematical relationship has been identified between the different parameters.

The actual plate wear pattern recorded during many tests and industrial application confirmed the validity of the design.

3. Chemical behavior of refractory component during steel casting

The classical experimental evaluation of steel corrosion is not enough to determine refractory components. Standard experimentation is conducted with limited amount of steel, while in reality steel is continuously renewed at the refractory interface.

The second limitation faced with today is that refractory interface is, in reality, controlled by variables like steel dissolved elements and steel inclusions. For instance, the volume of inclusion during continuous casting is comparable to the volume of refractory components used so they have a strong influence on steel/refractory reactivity. So the only possible approach to corrosion is to determine experimentally mass transfer from refractory to steel and to extrapolate for continuous casting conditions.

3.1 Steel and refractory interaction model

To define the nature of chemical reactions, specific experiments have been conducted. For the first type of experiment, pure iron is melted in an induction furnace with tailored alloy additions.

A rotating refractory sample is placed in the melt and steel chemical composition changes are determined by steel sampling during the experiment. A second set of experiments consists of degassing evaluation on refractory samples using a mass spectrometer at increasing temperatures.[2]

For the different types of refractory composition used in steel casting the following major reactions have been determined and quantified:

- Charbon dissolution $C \rightarrow \underline{C}$ (1a)

- Silica reduction $SiO_2 + C \rightarrow SiO(g) + CO(g)$ (1b)

- Magnesia reduction $MgO+C \rightarrow Mg(g) + CO(g)$ (1c)

- Zirconium reduction $ZrO_2 + 3C \rightarrow ZrC + 2CO(g)$ (1d)

- Oxydes dissolution $M_xO_y \rightarrow x\underline{M} + y\underline{O}$ (1e)

The different reaction kinetics have been determined depending on steel grade, refractory composition, microstructure and physical parameters at the refractory interface (i.e. pressure and temperature). For example the model for carbon dissolution is shown in Figure 6.

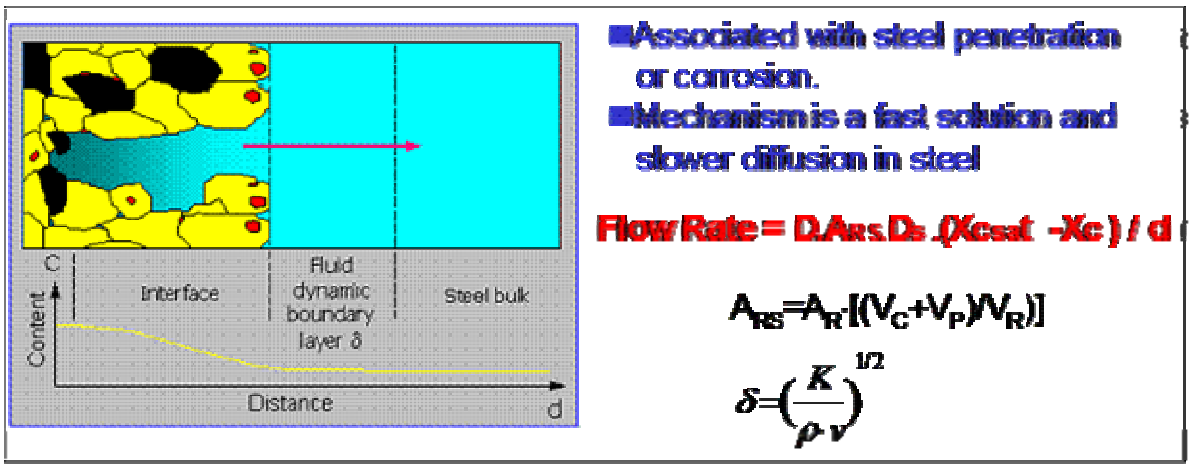

Fig. 6.. Carbon dissolution: carbon flow rate as a function of reactive surface (A_{RS}), carbon content (X) and steel flow.

The global result is a mathematical program, which calculates the flow rate of species passing from the refractory interface to the steel.

4. Mechanical behavior of steel casting refractory components

The mechanical behavior of refractory components is by far more complex than generally admitted.

This is mainly caused by the composite nature of the component and the large temperature range in use.

Refractory materials behave like composite structures with specific features coming from the phase transformations occurring at high temperatures.

The standard mechanical evaluations like 3 point bending or sonic measurement of elasticity induce important approximations in thermal shock evaluation. Unfortunately the consequences are inappropriate choices for product design.

4.1 Example of mechanical properties

Cold mechanical properties of standard alumina graphite composites have been evaluated in tension and compression mode. The results presented in Figure 7 and detailed in Figure 8, are typical for graphite containing materials used in continuous casting.

The important difference between tension and compression are classical for ceramic material but the relative important plasticity observed is characteristic of a bi-phasic composite. One major consequence is that strength determined by 3 point bending is overestimated when compared to tension that is the main failure mode.[5]

The sonic determination of elasticity is only valid for limited strain while the real pseudo-elasticity is much lower. This leads to overestimated stress levels caused by a thermal gradient. Finally the permanent strain occurring during thermal loading needs to be taken into account for thermal cycling.

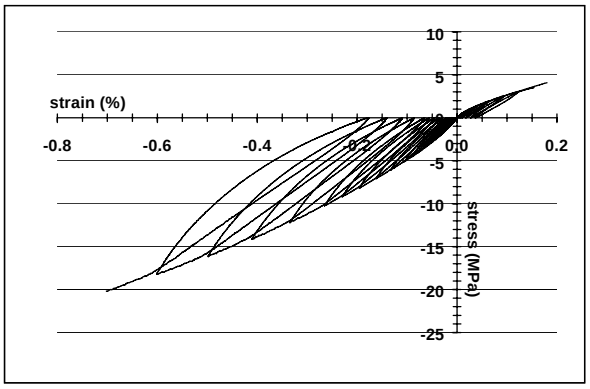

Fig.7. Stress strain behavior of alumina graphite in tension and compression.

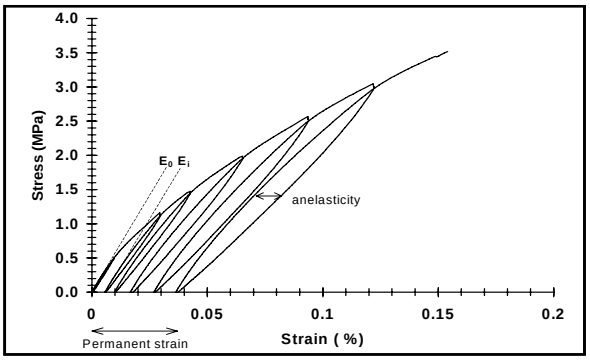

Fig.8. Tension behavior of alumina graphite.

4.2 Thermo-mechanical stress models

Standard Finite Element Analysis (FEA) codes don't take into account specific refractory properties. In order to overcome this problem, dedicated Finite Element Analysis models take into account refractory material specificity.[3]

The commercially available basic code (Abaqus) is implemented with subroutines, which incrementally give a more precise model of refractory thermal loading. The subroutines take into account phenomena such as inelasticity, creep deformation, and/or phase change. Model results are compared with sensitivity analysis and validation experimentation in order to ensure the validity of the results.

4.3 Material and design development

The thermal cycling of continuous casting refractory materials generates very different stress levels during operating time. The different stress evolution between transient heating and stationary working conditions needs to be carefully analyzed with appropriate product property determination. The effects on refractory material and design are highly dependent on operating conditions. In other words, a refractory product can not be ranked in terms of global thermal shock resistance but for only one given thermal shock situation in a given application.

Thermal stress situations have to be carefully analyzed in order to determine the major cause of failure: material properties or design. The optimization of refractory component consistency, as a function of steel casting efficiency, is depending on the model accuracy. An example of nozzle design for a thin slab caster is shown in Figure 9. The view represents a quarter of the total pieces cut by the 2 symmetric planes.

The maximum stress is localized on the narrow face of the nozzle where the thermal shock cracking is usually observed. The analysis of the stress during the transient start up of the cast show that the maximum stress is developed minutes after steel casting starts and that the stress developed during preheating is much lower. As a consequence the increase of thickness of the insulation layer (Thermacoat) has reduced significantly the stress level and reduce the cracking tendency.

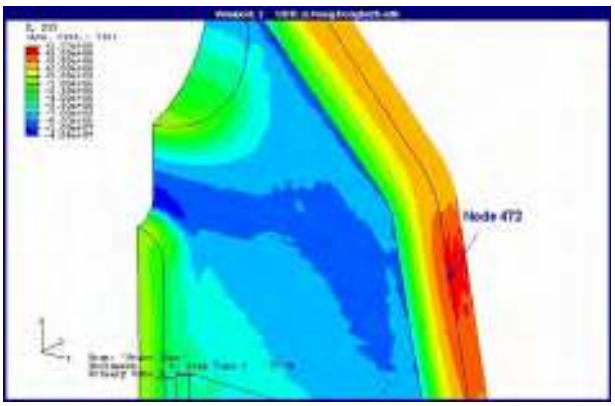

Fig. 9. Stress evaluation of thin slab nozzle.

4. Conclusion

Increasing demands for steel quality and continuous casting productivity require new approaches in terms of refractory component development. Advanced refractory design is achieved by coupling dedicated thermochemical and thermomechanical models with fluido-dynamic simulations. When appropriate material behavior at operating temperatures is experimentally demonstrated and validated, model results provide innovative solutions for refractory component optimization. These new approaches, combined with empirical field experience, are necessary to improve current and future steel continuous casting processes. The new scientific investigation methods applied to the sliding gate refractory and mechanism designs, cross checked with actual operating results allowed us to better understand the phenomena of crack formation and crack control leading to the implementation of optimized refractory patterns and flow control systems.

References

[1]. Munteanu, V., 1984, ***Contributii la dinamica mecanismelor de inchidere a recipientilor pentru turnarea otelului*** – Teza de doctorat, Universitatea "Dunarea de Jos´´.Galati

[2]. Munteanu,V., 2007, ***Steel flow control of continuous casted slabs using submerged entry nozzle exchange system for tundish***- The Annals of ''Dunarea de Jos''University of Galati, Fascicola IX, Metallurgy and Materials Science, Nr.1-2007, ISSN 1453-083x

[3]. Vincent Boisdequin, Philippe Mutsaarts, 2006, VESUVIUS SYSTEMS Belgium - Scientific optimisation of ladle sliding gate mechanism and refractory-Report 2006

[4]. Duderstadt, G.C., Iyengar, R.K., Matesa, J.M., 1968, "Tundish Nozzle Blockage in Continuous Casting", Journal Of Metals, Vol. 20, No. 4, 89-94.

THE ANNALS OF "DUNAREA DE JOS" UNIVERSITY OF GALATI.
FASCICLE IX. METALLURGY AND MATERIALS SCIENCE
N^0. 2 – 2008, ISSN 1453 – 083X

X-RAY DIFFRACTION STUDY OF THE REVERSE MARTENSITIC TRANSFORMATION IN Cu-Al-Ni SHAPE MEMORY ALLOY

Carmela GURAU[1], Gheorghe GURAU[1], F. M. Braz FERNANDES[2]

[1]"Dunarea de Jos" University of Galati
[2]CENIMAT Department of Material Science, FCT/UNL, Campus da Caparica, 2829-516 Caparica, Portugal
email: carmela.gurau@ugal.ro, gheorghe.gura@ugal.ro

ABSTARCT

The paper presents an X ray diffraction study for a cooper based shape memory alloy. The behavior of CuAl13Ni4 alloy, which exhibits a peculiar property, is evaluated by structural changes. On cooling, the martensitic transformation takes place from the ordered structures to the long period two layered structure. The crystalline phase transformations of those alloys are very sensitive to the heat treatments, deformation degrees and also to the undesired aging effects. In particular, the study has been made on the CuAl13Ni4 shape memory alloy samples after being hot extruded, quenched and aged in martensitic state.

KEYWORDS: Shape memory alloy, Shape memory effect; Martensitic transformation, XRD

1. Introduction

The shape memory alloys (SMA) are in a so called class of smart materials whose properties have high performances especially their ability to recover the desired shape only by changing temperatures. SMAs are a typical smart material fully reversible. Martensitic transformation is a first-order diffusionless structural phase transformation between a high temperature austenite phase and low temperature martensite phase [1].

The shape memory effect is related essential by to a thermoelastic martensitic transformation [2]. A shape memory alloy plastic deformed at temperature below the martensite finish temperature, M_f, by heating over the austenite start temperature, A_s, recovers the undeformed original shape. The characteristic is called shape memory effect (SME). After thermomechanical treatments the change reoccurs during heating and cooling processes, the characteristic is called two way memory effect (TWSME). Due to the shape recoverable properties these alloys can be used as devices like sensors and actuators. Cooper based alloys exhibit shape memory within a certain range of composition. It is known that for the particular composition CuAl13Ni4 from the metastable beta phase whit DO_3 structures, after quenching, takes place a martensitic transformation with two long period layered structures (18R and 2H) [3-5].

2. Experiment

The CuAl13Ni4 shape memory alloy was obtained by a classic direct melting method using high purity for components and precised chemical composition. The cast ingots were turned in cylindrical shapes **Φ**35X35 mm. The samples were plastic deformed by extrusion in three steps until **Φ**4mm wires. After last extrusion the samples were cooled in air. The samples were 9 months hot extruded wires 4mm diameter and 145 mm length. The samples were machined for following tests. For X ray diffraction tests we studied the same sample: in extrusion state after nine months aged; a subsequent quenched; in quenched state after fourteen months aged. The experiments for quenched samples comprised heat treatment using a vertical furnace, air environment, holding at 850^{0}C during 30 minutes. After solubilization, the specimens were immediately quenched in ice water. Few samples were deliberately kept in martensitic state at room temperature.

Prior to experiments all samples were submitted to the chemical etching in order to remove the layer deformed by cutting operation as well as the oxide.

The XRD analysis was run in a RIGAKU (Cu sealed tube) at room temperature using 20mmX2mmX1mm dimension samples. The $2\Theta_{hkl}$ was between 10^0 and 90^0. The acquisition time was 1s per point.

The goniometer radius is 180 mm. The radiation used was Cu-K_a. The widths of divergence, dispersion and transmission slots were 1^0, 1^0 and 0.15mm. The XRD analyses were made at 50kW/30mA. The (h k l) planes related to diffraction lines were identified using ICDD data base built in computer in EVA program 7.0 version.

3. Results and discussion

The CuAl13Ni4 shape memory alloy was studied in different stage of deformation respectively extruded and quenched samples.

The hot extruded sample had in structure: solid solution a; a mechanical mixture a and g_2 an intermetallic compound NiAl and premartensitic structure.

The subsequent quenched samples and after fourteen months aging were entirely martensitic structure at room temperature.

Two morphological types of martensite structure coexist in CuAl13Ni4. In table 1 are shown the crystalline parameter and the diffraction line specific to martensitic structures.

Table 1

Martensite type	Parameters of crystal lattice	Angles of crystal lattice	Diffraction planes
Monoclinic $Al_7Cu_{23}Ni$	a= 4.44 b = 5.31 c = 37.86	a=90^0 b=89.36^0 g=90^0	(-1 2 5) (0 0 18) (-1 1 15) (3 2 4) (-2 1 4)
Orthorhombic $AlCu_3$	a= 4.494 b = 5.189 c = 46.61	a=90^0 b=90^0 g=90^0	(1 1 1) (0 1 11) (0 2 1) (2 0 2) (2 0 12) (3 2 13)

The memory properties like SME and TWSME, transformation characteristic temperatures, thermal hysteresis, recovery deformation, generating mechanical work are influenced by heat treatments history and aging phenomena in initial state but also in martensitic state. The main objective of this work was to study the changes in fine internal structure for extruded and quenched samples the aging process accompanied by martensite stabilization. The XRD analyses taken three times, reveal important modification in crystallographic lattice. In figure 1 are shown the XRD diffractograms taken from alloy in extrusion state.

In figure 2 are shown the XRD diffractograms taken from alloy in quenched state.

In figure 3 are shown the XRD diffractograms taken from alloy in quenched state aged fourteen months at room temperature. The electron diffraction patterns of extruded alloy have a disordered structure. In this case it can be observed that the characteristic lines have large widths. The maximum line intensity is corresponding to the monoclinic martensite (-1 1 15) hkl plane. As seen from diffraction patterns from figure 2, CuAlNi martensite have the ordered structure and exhibit superlattice reflection. After the heat treatment they have the ordered structures. It can be observed that the maximum intensity of monoclinic (-1 1 15) hkl plane was kept. The aspect of diffraction lines were really narrow because the long period order and the coarse martensite specific this alloy.

The diffraction patterns from figure 3, reveal the same ordered structure and exhibit superlattice even after martensitic aging.

Anyway the maximum intensity was kept for the same monoclinic (-1 1 15) hkl plane and near that it can be observed the pick for the pair plan (-2 1 4) and both structures are monoclinic. It can be observed a flattening of diffraction picks corresponding to plan (2 0 2) and (0 0 18). The (2 0 2) habitus plan is an attribute of orthorhombic martensite.

The (0 0 18) habitus plan is an attribute of monoclinic martensite.

It turns out that the pick accordingly to diffraction plan (-1 2 5) was missing. The pick accordingly to diffraction plan (2 0 12) was reduced until flattening. The structure was partially ordered after martensitic aging time.

In cooper based SMAs as in Ti Ni, Ni Al or Fe Al alloy systems there can be observed a lot of aging process. Cooper based especially brasses are in general predisposition for aging even at room temperature [1].

The aging at high temperatures is determined for the precipitation from austenite phase in Cu_9Al_4 (γ_2) and NiAl (B_2) phases. In ternary Cu Al Ni alloy system the precipitation for γ_2 phase is inhibited by nickel addition.

It is considered that the precipitation brakes MT throw two mechanisms:

- Coherence of the fields around precipitations and/or destroyed potential germination centers in martensite state;
- Introducing vacations at quenching and precipitation process.

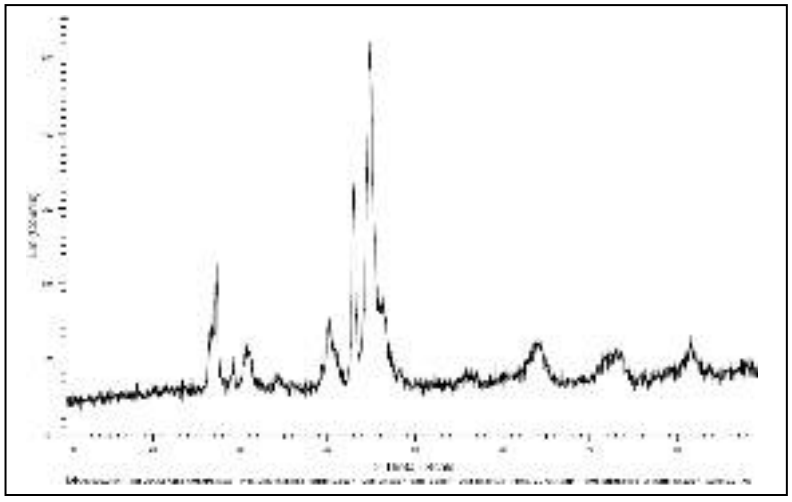

Fig. 1. X ray diffractogram of hot extruded sample

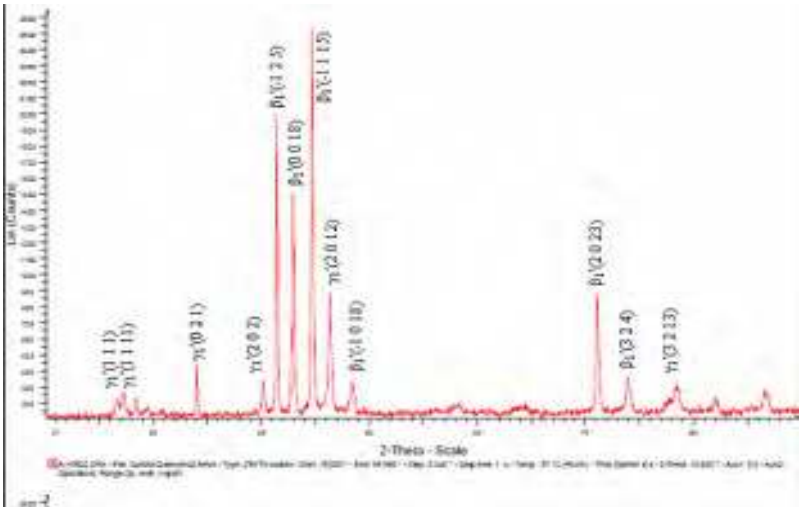

Fig. 2. X ray diffractogram of quenched sample

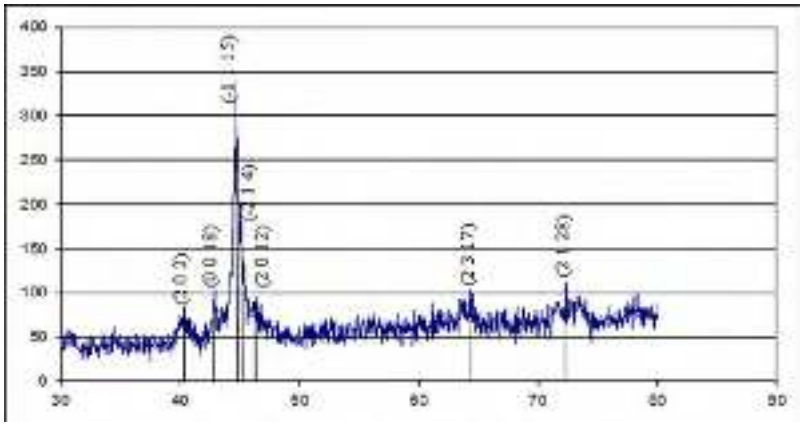

Fig. 3. X ray diffractogram of quenched and 14 months aged sample

The increasing precipitates manage to changes in chemical composition of initial phase that modify transformation temperatures. In these conditions the shapes recovery becomes more difficult. Aging effect changes the memory characteristics for SMAs. The martensitic aging effect is accompanied by martensite stabilization process. The aging time in martensitic phase influences direct critical temperatures and sometimes the reverse martensitic transformation is canceled. The origin of the martensitic stabilization lies in two different mechanisms. One of them consists in internal crystalline structure changes. An atomic reorder takes place in martensite and that determined a relative stabilization between initial phase and martensite. It has been reported that the base plane of monoclinic martensite originates from one of $(0\ 0\ 1)_b$ planes of the matrix [3].

The reversible transformation occurs as:

$$\beta(DO_3) \underset{T\uparrow,\sigma=ct}{\overset{T\downarrow,\sigma=ct}{\Leftrightarrow}} \beta_1'(18R) \underset{T\uparrow,\sigma=ct}{\overset{T\downarrow,\sigma=ct}{\Leftrightarrow}} \gamma_1'(2H)$$

The mechanism is crystallographically describable by two steps. The transformation involves lattice deformation called Bain distortion and the second step called lattice invariant deformation when one of the close packed $(0\ 0\ 1)_b$ planes of matrix becomes martensite basal plan[8]. The martensite basal plan is distorted in case atom sizes are different and become sregular in case atom sizes are equal. Because of this deviation, the spacing differences Δd between the adjacent diffraction planes became different from null and it can be a measure of martensite order. It was observed that alloys from Cu Al Ni system undergo a partial order disorder transformation in primary aging stages so as in long term aging.

The second mechanism doesn't explain aging in single crystals but is valid for polycrystalline SMAs. One of SMAs properties behavior like rubber is determined by martensite stabilization. After quenching the alloy has the ordered structure and exhibits superlattice reflection.

4. Conclusions

The behavior of CuAl13Ni4 alloy, which exhibits shape memory properties, was evaluated by structural changes.

The alloy was studied, in different stages of deformation respectively extruded and quenched samples, using XRD analysis:

1. The memory characteristics are influenced by heat treatments history and aging phenomena in initial state but also in martensitic state.

2. The electron diffraction patterns of extruded alloy have a disordered structure with large widths of the characteristic lines. The structure was only partially premartensitic.

3. After quenching the alloy has the ordered structure and exhibit superlattice reflection. The aspect of diffraction lines were narrow because the long period order and the coarse martensite specific this alloy. In Cu Al13Ni4 SMA coexists two martensite types (monoclinic and orthorhombic).

4. The structure was partiallz ordered after martensitic aging time but it can be observed modification in accommodation of different habitus plans. Near the (-1 1 15) hkl plane it can be observed increasing the pick for the pair plan (-2 1 4) the both structures are monoclinic.

References

[1]. K.Otsuka and C.M. Wayman - "***Shape memory materials***" 1999

[2]. R. Zengin, S. Ozgen, M. Ceylan, 2004, ***Oxidation behaviour and kinetic properties of shape memory $CuAl_xNi_4$ alloys***, Thermochimica Acta 414

[3]. G Gurau, C Gurau, D Tanase, 2006, ***Processing Smart Wires Cu Al Ni System authors,*** Metal, 15th International Metallurgical & Material Conference, TANGER Ltd., Ostrava, Czech Society for New Materials and Technologies, ASM International, Czech Chapter, Czech Metallurgical Society, VSB-Technical University, Ostrava

[4]. H. Morawiec, J. Lelatko, D, Stroz, Gila, 1999, ***Structure and properties of melt-spun Cu-Al-Ni shape memory alloys,*** Met Sci Eng, A273- 275

[5]. V. Recarte, J.I. Perez-Landazabal, A. Ibarra, M.L. No, J. San Juan, 2004, ***High temperature β phase decomposition process in a Cu-Al-Ni shape memory alloy,*** Mat.Sci.Eng. A378

[6]. R.Gastien, C.E.Corbellani, M.Sade Thermomechanical aspects of martensitic transformations in CuAlNi single crystals"

[7]. Paula, J.P.H.G. Canejo, R.M.S. Martins, F.M. Braz Fernandes, 2004, "***Effect of thermal cycling on the transformation temperature ranges of Ni-Ti shape memory alloy***"- A.S., Mat.Sci. Eng., A378

[8]. A. Aydgdu, Y. Aygdogdu, O. Adiguzel, 2004, ***Long-term ageing behaviour of martensite in shape memory Cu-Al-Ni alloys***, Journal of materials Processing Technology 153/154.

THE ANNALS OF "DUNAREA DE JOS" UNIVERSITY OF GALATI.
FASCICLE IX. METALLURGY AND MATERIALS SCIENCE
N^0. 2 – 2008, ISSN 1453 – 083X

BEHAVIOUR OF SOME IMPORTANT COMPONENTS IN A COLD ROLLING MILL

Stefan DRAGOMIR, Georgeta DRAGOMIR, Marian BORDEI
"Dunărea de Jos" University of Galati
e-mail: doromir@yahoo.com

ABSTRACT

For a good behaviour of mill parts and accurate functioning it is necessary to have an integrated system for all mill tandem. It is important to know the speed controls and strip tension in correlation with torque, laminated force and rotation angle. The management system incorporates all gap control existing inside the rolling mill machine.

KEYWORDS: system management, behaviour, rolling mill, gap control

1. Introduction

The simulation of the dynamic behavior of components or parts of a rolling mill has contributed at the decrease of hardness of these movement parts, a new and functional design, the diminishment of energetically consumption. During the workshop are tested and optimized the basic functions and the dynamic behavior. Taking into account the complexity of the geometric shape and loading it was studied the Stress State using the Finite Element Method.

The model accepted for simulation is composed of resorts which substitute the actual masses in work. The hardware and the software for function control in work are connected to the simulated model. The model must be simulated in real time function work.

The advantage of this system simulation is that both the hardware and software may be tested, regulated and optimized without any risk of comparison with the existent system.

During the works are tested and optimized the basic functions and the dynamic behavior.

To investigate the behavior of rolling mills we always first the model behavior. The dynamic simulations on the created stand show the influence of diverse causes during work such as:

- High – frequency torsion vibration in the drive system;
- Eccentricity and state surface of work roll shape;
- Mill speed;
- Reduction;
- Strip tension;
- Roll lubrication.

The model stands satisfy the most stringent requirements on control dynamics and shock capacity and are largely free of maintenance.

The equipment used has the following advantages:

- No limit in drive rating;
- Better control performance;
- Rotor of engine (machine) has lower moments of inertia;
- Less spare parts;
- Greater flexibility of parts;
- Simple start-up procedure;
- High reliability and availability;
- Output frequencies from 0 to 600 Hz;
- Frequency control with senseless vector control;
- Highly accurate speed and torque control;
- Fast serial interface communication between line speed and slave units;
- Positioning controls
- Parameter indicator, text display, graphic display.

2. Experiments and results

Now modern tandem mills have hydraulic gap controls on all stands. The control loops employed are position control; tilt control. The roll forces are measured either indirectly by pressure transducers attached to the hydraulic cylinders or, directly by roll force transducers located in the line of force of the hydraulic cylinders.

It is in action when the gap is open, during threading operation and as a subsystem of the gouge control. The signals from the position transducers on each side of the stand are subtracted to produce the actual value for the tilt controller, which alters the tilt

about the centerline of the stand. This control loop is effective during rolling and is only switched off during calibration after the calibration force has been reached. A typical response time is approx. 30ms.

Roll force control is measured for each roll work. The total tension reference value is calculated in the control system in accordance with the rolling program and the strip dimensions and is sent to the tension controller.

The tension is measured by tensiometers mounted under the bearing blocks of the deflector rolls. As the control system depends very heavily on the speed with respect to the gain and time response, the gain of the tension controller is matched out adaptively to the properties of the controlled system.

The work rolls and the intermediate rolls are equipped with separate cylinders for positive as well as negative bending. The cylinders on the drive and the operator sides are complied in parallel for each bending direction.

The strip tension is kept constant. During work if it is necessary, we must apply a speed correction. The exit thickness of strip must be adjusted like: thickness error measured by the gauge before the stand and compared with the measured exit thickness error. The difference is added to the exit thickness set point and the sum forms the set point for the thickness gauge before sand (experimental mill) fig.1. Also a processor is used to detect if milling process is driven in fixed parameters.

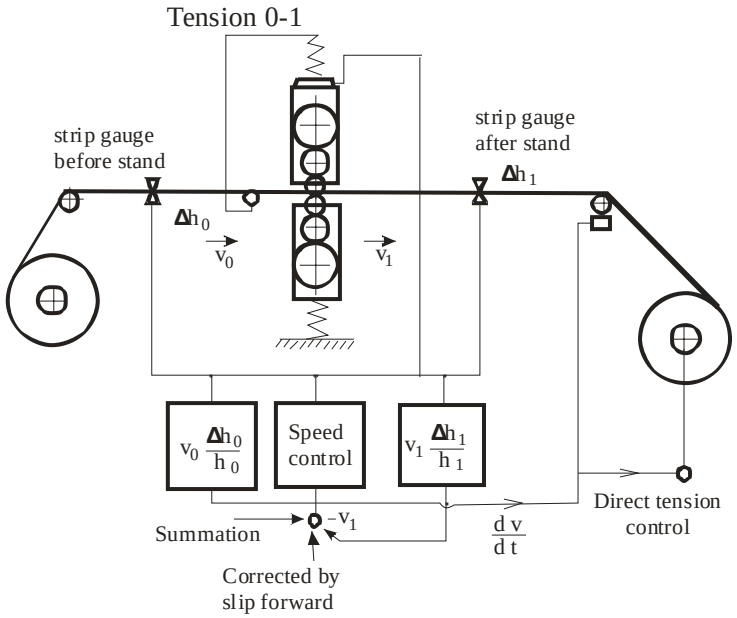

Gauge control modes

Fig.1. Management of rolling mill system.

3. Mill mathematical model

The audible noise is often the only indication to the mill operator that the mill is vibrating. As stated earlier, this type of vibration is self-exciting. There is a feedback mechanism that provides a sustaining force to increase the mill vibration amplitude which is a consequence of the vibration motion itself. This mechanism has its origins in the roll bite and is a consequence of the continuity of mass flow through the stand.

$$H_1 v_1 = H_2 v_2 \qquad (1)$$

where:

H_1 and H_2 are the entry and exit gauges and v_1 and v_2 are the entry and exit strip speeds.

On the basis of continuity of mass flow through the mill stand during rolling, it can be shown that a change of exit gauge will produce a change in entry strip speed, assuming the entry gauge and exit speed remain constant.

$$H\delta v_1 = H_2 \delta v_2 \qquad (2)$$

The change in strip speed at one end of the entry strip compared to the other, v_c, will produce a change in entry strip tension, T_1, as follows

$$\delta T_1 = K_1 \int (\delta v_1 - \delta v_c) dt \qquad (3)$$

where: K_1 is the stiffness of the entry strip given by the following equation

$$K_1 = H_1 l \; E / L \qquad (4)$$

where: E Is the elastic modulus of the material being rolled, l is the strip width and L is the length of the entry strip over which the speed difference was applied.

A change in entry tension will produce a change exit gauge thus completing the loop as follows

$$\delta H_2 = \frac{\partial H_1}{\partial Rl} \; \frac{\partial Rl}{\partial T_1} \; \partial T_1 \qquad (5)$$

where: Rl is the rolling load.

The ratios in equation (5) are roll gap sensitivities that will depend on rolling variables such as the roll gap friction. There is a 180 degree phase change around the feedback loop in figure 3, 90 degrees coming from the mill vibration mode and 90 degrees from the integration required to convert strip velocity to tension in equation (3).

Analogous to electrical control system instabilities, if there is a 180 degree phase change around the loop then the loop will go unstable as the gain is increased above a certain threshold value. From the above equations coupling each term in the loop it can be seen that gain is proportional to the exit speed of the strip (equation (2). This explains why rolling mills prone to gauge chatter vibration exhibit the problem suddenly as the speed is increased above a threshold value. Other factors such as the material being rolled, the rolling conditions and the natural damping of the mill stand resonance will all affect the threshold rolling speed for vibration. However, these are difficult to change and none vary as significantly as the speed during a particular rolling pass.

The mode involves the two work rolls moving in-phase and vibrating between the two backup rolls. The backup rolls move in anti-phase to the work rolls but their amplitude is significantly less than the work roll amplitude. The evidence linking this mode to roll and strip marking is presented elsewhere [1, 4]. The relative motion between the work roll and the backup roll damages the backup roll surface during the period that the backup roll is in the mill.

The predicted mode involves significant bending of the work roll necks. It should be noted that this type of mode belongs to a family of fifth octave modes, all capable of damaging the backup roll through relative motion between the work roll and backup roll.

Some solutions to this problem may require an on-line monitoring strategy on the grinder and/or the mill to identify the source and then minimize its impact.

This is an effective operational strategy to maximize productivity while maintaining high quality of the strip surface.

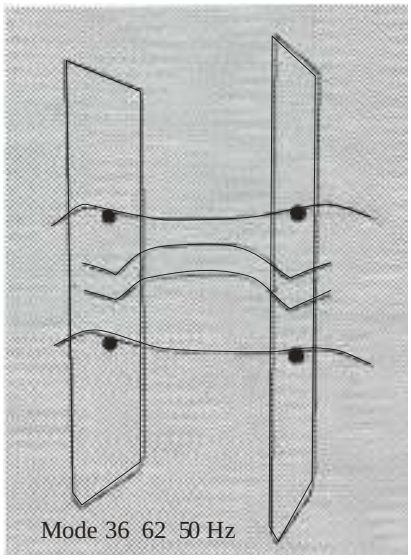

Fig.2. Typical mode shape of rolling mill resonance. The lines represent the central axes of the rolls and housing frames.

Roll eccentricities caused by temperature effects, grinding inaccuracies, wear, cause periodic fluctuation whitch cannot be compensated by the gauge control. The gauge error based eccentricity compensation system analyses the measured strip thickness instead of the roll force. The system works on the principle whereby the roll eccentricities are simulated by means of an error model composed of discrete oscillations whose frequency phase and amplitude can be controlled. The measured thickness error is converted by means of a roll gap model into a corresponding gap position. The value is compared with the asseverated measured gap position, whereby the time delay is taken. The system also has effect of compensating for thermal growth since the amplitudes of the respective frequencies are tracked and compensated automatically.

Chatter is severely influenced by the rolling mill process. For predict the real roll force is necessary to introduce all variables into a corrective neural network. A corrective neural network can eliminate the error in roll force prediction. This network can reduce the prediction errors at 25%. Additional variables, which were not used in the mathematical model, were necessary for the substitutive model only.

The chemical composition of coil and temperature variable were fed to the network.

4. Conclusion

The use of proposed system milling (stand) improves the accuracy of work parameters (in particular rolling force).

Some parameters not considered in the mathematical model can be easily introduced in a mill system.

The management system works on the principle whereby the roll eccentricities are simulated by means of an error model composed of discrete oscillations whose frequency phase and amplitude can be controlled.

A method of preventing roll chatter in a rolling mill stand during the process of directing a strip of material through the stand, the stand having a natural frequency of vibration, the method comprising:

The stand has a rolling gap and hydraulic systems for respectively adjusting the rolling gap and for controlling the force at which backup rolls press against work rolls of the stand, the method including: vibrating one or both of the hydraulic systems at a variable frequency. The method in which the vibrating component is provided with a varying frequency and varying amplitude.

The method of claim 1 wherein the octaval frequency of roll chatter is at third and fifth octaves, whose the frequency ranges from100 to 200 and 500 respectively to 700 Hertz.

A method of controlling the vertical motions of a plurality of vertically disposed rolls in a rolling mill during the process of directing a strip of material through the mill, said vertical motions occurring at a natural frequency of the rolls, the method comprising: introducing into the mill a vibration component having a frequency different from the natural frequency of the vertical motions of the rolls such that said vertical motions become no synchronous with each other.

References

[1] N.Portmann, 1995, ***Application of neural networks in rolling mill automation***. Iron and Steel Eng. Vol.72 no.2 pp.33-36.

[2].Kong, T, Yang. D., 1993, Journal of Process Mechanical Engineering.Vol.207.pp143-150.

[3] Benhafsi, Y., Farley, T.W.D., and Wright, D.S., 1999, ***An Approach to On-Line Monitoring of fifth Octave Mode Mill Chatter to Prolong Back-up Roll Life***, Conference: Measuring Up to Customers Needs: Advances in On-Line Instrumentation for Finishing Processes in Strip Production, Institute of Materials, London, UK, 27-28 April1999.

THE ANNALS OF "DUNAREA DE JOS" UNIVERSITY OF GALATI.
FASCICLE IX. METALLURGY AND MATERIALS SCIENCE
N^0. 2 – 2008, ISSN 1453 – 083X

POLLUTANT EMISSIONS, CONTROL AND PREVENTION IN THE SECONDARY COPPER INDUSTRY

Anisoara CIOCAN, Stefan BALTA
"Dunărea de Jos" University of Galati
e-mail: aciocan@ugal.ro

ABSTRACT

This paper presents an analysis of pollutant emissions specifics to copper waste valorization. There are made appreciations of the role and importance which have the characteristics of mixed charge with waste having a variable content of copper (copper and copper alloy waste, residues, sludges, slimes, dusts etc.) having impurities or contaminants (especially organic pollutants) as well as fluxes and fondants (NaCl, KCl etc) used as first important source of pollutant emissions for secondary copper metallurgy.

KEYWORDS: secondary copper metallurgy, pollutant emissions

1. Introduction

The diversity of aspects and factors involved in secondary copper obtaining processes make the pollutant emissions have big variations from qualitative and quantitative point of view.

In the secondary copper metallurgy are used the flow sheets with multiple configurations of processes; it is possible to use a big variety of smelting aggregate types with possibility to operate in different mode, with different capabilities to monitor and control the pollutant emissions.

At the same time, the input materials are proceeded from different sources, so they have different characteristics and are prepared by different methods, before introduction in the processing steps.

2. Emissions at the secondary copper obtaining

At the secondary copper metallurgy, emissions which contain microelements reported to the total amount evacuated in the atmosphere, to the global level, at the beginning of 1980 for Europe, were appreciated as non significant: less then 1% from the total emissions of copper, arsenic, selenium, and zinc [1-3]. At the local level, the secondary copper smelting or copper refining process can be considerated important source of contamination with microelements. According to CORINAIR90 Report (made for 28 countries), the rate of participation of emissions generated by secondary copper production to the total emissions, microelements, respectively emissions generated at the fuel burning, specific to the secondary copper production sectors from this countries, are presented in tables 1, 2 and 3 [4].

Table 1. Emissions generated from secondary copper production to the total emissions according to the CORINAIR90 Report

Source	Cod SNAP	Contribution to the total emissions, %							
		SO_2	NO_x	NMVOC	CH_4	CO	CO_2	N_2O	NH_3
Secondary copper production	030309	●	-	●	-	●	-	-	-

● emissions are reported by the countries in the limit of 0,1%, but without the exact value;
- emissions are not reported.

Table 2. Element emissions in the secondary copper metallurgy, g/t copper made

Element	Estimate Pacyma (1986)	Estimate in Canada (Jacques 1987)	Program PARCOM (1992)	Estimate in England (Leech 1993)	Estimate in Austria (Schneider 1994)	Interval or resulted values
As					2	2
Sb	3					3
Cd	4		5	5	2	2-4
Cu	150	200-400				
Pb	50-200	230	130	130	50	50-130
Ni		1				1
Zn	500-1600		500	500	250	250-500

Table 3. Emissions of gaseous compounds in the secondary copper metallurgy, on the different type of fuel [CORINAIR90] [1)]

Fuel type	Cod	Emission factors						
		SO_2 [2)]	NO_x [3)]	NMCOV [4)]	CH_4	CO	N_2O	CO_2, kg/GJ
		g/GJ						
Liquid	203	495-1.470[1)]	150[1)]	30[1)]	30[1)]	15[1)]	2[2)]	76-78[1)]
Liquid	204	94-1.410[1)]	100[1)]	1,5[1)]	1.5[1)]	12[1)]	2[1)]	73-74[1)]
Natural gas	301	0.8[1)]	100[1)]	4[1)]	4[1)]	13[1)]	1[1)]	57[1)], 60[5)], 59[6)]
Liquid gas	303	0.04[1)]	100[1)]	2.1[1)]	0,9[1)]	13[1)]	1[1)]	65[1)]

[1)] The adnnotation under the table can make references at the emission factors which include the burning fuels and other processes from secondary copper metallurgy

[2)] SO_x: (EPA, 1990)

750g/t charge – dry waste (rotary furnace)

6400g/t charge – burning cable, incinerator

250g/t charge – crucible furnace, input brass and bronze wastes

15g/t charge – electric arc furnace, input brass and bronze wastes

15g/t charge - induction furnace, input brass and bronze wastes

2182g/t charge – refining process

17209 S g/m^3 fuels – secondary copper production (fuel with sulfur content)

19006 S g/m^3 fuels - secondary copper production (fuel with sulfur content)

[3)] NO_x: (EPA, 1990)

6400g/t charge - burning cable, incinerator

40g/t charge – reverberation furnace, input brass and bronze wastes

300g/t charge - rotary furnace, input brass and bronze wastes

2397g/m^3 fuel - secondary copper production

6591g/m^3 fuel - secondary copper production

[4)] COV (volatile organic compound): (EPA, 1990)

2g/t charge – dry waste (rotary furnace)

300g/t charge – burning cable, incinerator

300g/t charge - rotary furnace, input brass and bronze wastes

60g/t charge – furnace with selective smelting

223500g/t coke charge – cupola furnace, input copper wires waste or copper and brass wastes

90g/t charge – cupola furnace, input copper and brass waste or copper waste

2600g/t charge - reverberatory furnace, input copper or brass and bronze

1200g/t charge - rotary furnace, input brass and bronze wastes

3350g/t charge – crucible furnace, input brass and bronze waste

1950g/t charge – electrical arc furnace, input copper

0g/t charge – electrical arc furnace, input brass and bronze

0g/t charge – induction furnace, input copper or brass and bronze

24g/m^3 fuel - secondary copper smelting

34g/m^3 fuel - secondary copper smelting

44851g/Mm^3 fuel - secondary copper smelting

[5)] CO_2: input local contaminated waste, brass production (Bremmer 1995)

[6)] CO_2: input highly contaminated waste, brass production (Bremmer 1995).

The analysis of presented data can appreciate that, in general, the secondary copper metallurgy

represents a minor source of pollutant emissions in comparison with primary copper metallurgy.

However recently, the thermal processes from secondary copper metallurgy, together with the specific processes of the primary copper metallurgy (and other thermal processes from metallurgical industry and sintering preparation of ores in steelmaking industry, aluminum and zinc production from non-ferrous metallurgy), has been defined as an important source of dioxins generation. UNEP (United Nations Environment Programme) convention respecting the persistence organic pollutants, adopted at Stockholm in May 2001, placed the thermal processes from copper industry in the second category of dioxin source (after the waste incineration placed in the first category 1, the most important generator of dioxins), table 4 [5].

3. Generating sources of pollutant emissions in the secondary copper industry

3.1. Raw materials

Raw materials used for copper smelting, the mixed charged compounds of wastes with variable contents of copper (copper waste, alloys with copper content, together with dross, slag, slime and dust, etc.) with an impurity and contaminate content (especially the organic pollutants), and salts used as flux (NaCl, KCl etc.) represent the main source for the pollutant emissions in the secondary copper metallurgy.

Therefore, the chemical composition of the input materials is considered the determinant factor in the quantity and chemical composition of generated emissions at the secondary copper production.

Table 4. UNEP matrix for the dioxin sources placed in the second category and emissions factors for the modern technologies from the ferrous and non-ferrous metallurgy, µg I-TEQ/t product

Category. UNEP	Cod SNAP	Sector	Dioxins in:				
			Air	Water	Soil	Product	Waste
2a	30301/40209	Sinter plant	0.3				0.003
2b	-	Coke production	0.3	0.06	X	X	X
2c	40200/30303	Iron and steelmaking industry, Foundry	0.01-0.03				0.2-15
2d	**30306/30309**	**Copper production**	**0.01**				**0-630**
2e	40301/303010	Aluminium production	0.5-150 (wastes)				100-400
2f	30304/30307	Lead production	0.5				X
2g	30305/30308	Zinc production	0.3				X
2h	-	Brass production	0.1				
2i	40304/30323	Magnesium production	50	24			9000
2j	-	Other non-ferrous metals production	2	X			X
2l	-	Mechanical preparation by shredder	0.2				X
2m	-	Wires recuperation	3.3	(X)	X		X

The burning impurities present to the input metallic materials and the participation of the fluxes with chlorine content in different process steps can lead to dioxine formation. Undesired elements (sulfur, arsenic, lead, zinc, cadmium, mercury etc.) and their combination, presented in small quantities in waste used to obtain secondary copper (unlike the copper ores utilized to obtain primary copper), are emission generators. The zinc, characterized by a high vapor pressure and a big oxidation tendency (it forms a important quantities of zinc oxide particles with micrometric dimensions) is the most important element which needs to be taken into consideration [6]. Without pre-treatment operations, the input materials with a cable waste content carry in furnaces and in other installations or process equipment, impurities like organic substances (from plastic materials, paints, solvents, oils), and lead compounds (from stabilizer present in old cable isolation). These impurities lead to the formation of pollutant substances with the other types of gaseous compounds or solid waste materials, corporate like waste and emissions resulted from secondary copper obtaining fluxes steps.

3.2. Processes and aggregates generating pollutant emissions

Starting with input materials preparation and finishing with the secondary copper or its alloy casting, results dust and volatile compounds distributed in effluents or solid waste from secondary copper processes, with allocation in air, soil, water (fig.1).

Thermal processes, from the waste pre-treatment and from elaboration steps (smelting, refining and alloying) are responsible for generating the pollutant emissions.

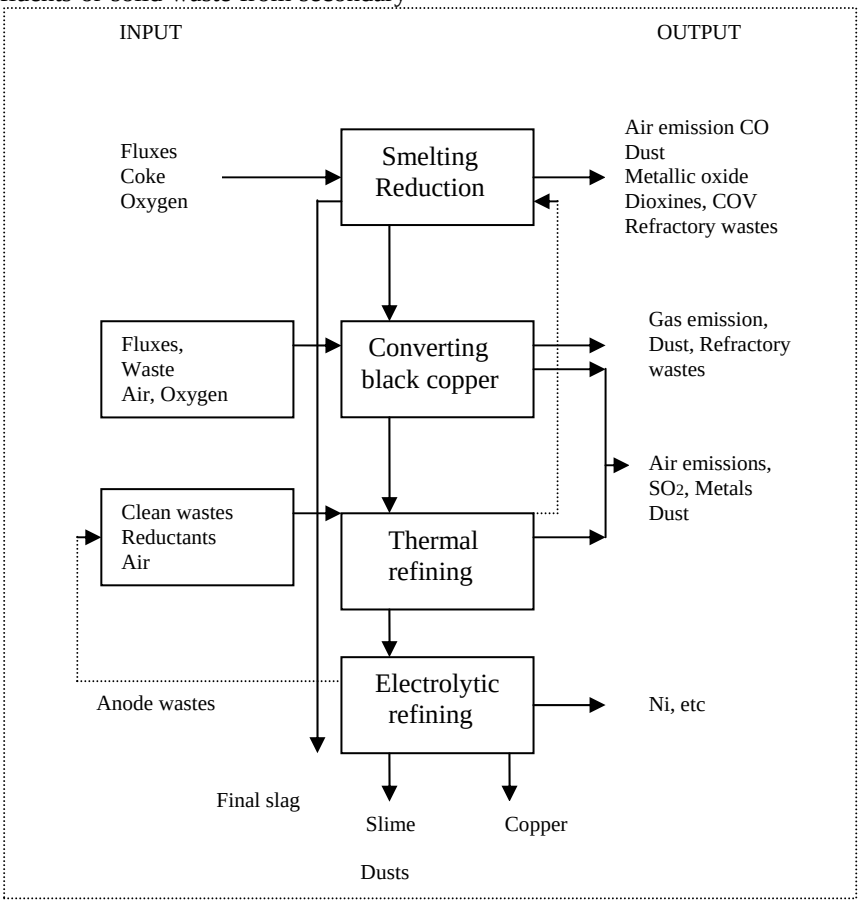

Fig.1. Emissions from different secondary copper metallurgy [7]

a. Raw materials preparation. In the preparation operations, thermal processes are utilized to remove the cables isolations, oil excess and other technological fluids from cuttings, turning, etc.

These processes are generating the volatile organic compounds and products from the incomplete burning and because of these off gas needs to have a cleaning treatment.

The gas post-combustion in the special rooms, at temperatures more than 1000^0C, can determine purification efficiency bigger than 90%. The combustion is not sufficient if the isolations contain PVC, the chloride acid in gaseous stage is produced and because it cannot be controlled in the post-combustion stage, it is necessary its capture before the off gas evacuation. In this case, the cable waste preparation is recommended to remove the isolations by mechanical methods, even if the burning can be the most used method for its easiness.

For minimisation of pollutant emissions it is imposing a mechanical preparation of raw material (metallic materials) for compacting and bringing to the necessary dimensions to charge them in the furnaces by single step. In the case of insufficient compacted materials, charging the materials through on the surface of metallic bath, can produce important quantities of gases which can exceed the capacity of installations capture. In this situations we need to locate a supplementary gas capturing system to take the exceed gases from accidental production.

b. Processes and furnaces. From qualitative and quantitative point of view, the pollutant emissions are determined by the furnace type and the technologies applied. For pollutant emissions minimisation, it is recommended as the best technological solutions those in which the processes are made in aggregates which work in isolated or hermetic spaces with

possibility to install systems for collecting and capturing gases.

c. Copper and copper alloys casting. Gases and pulverous emissions are made during the casting operations time. Those results from the interaction of alloy with the forming materials, refractory paints etc. Important quantities of gases are made in the graphite dust burning used for casting metals interface protection.

4 Pollutant emissions, measured and admissible levels

For secondary copper metallurgy, the most significant and important are air emissions. Emissions level can be found from measurements and results of different monitoring published in branch literature. For water emissions, this type of data issn't published, since these emissions are less important. This is due on the one hand to their reduced solubility of dioxins in water (these is an accumulation of dioxins in water sediments) and on the other hand, the lightness that the admissible pollutant substances concentrations may have in water by treatment before the evacuation in environment. The air emissions consist in nitrogen oxides (NO_x), carbon monoxide (CO), dust, organic compounds, dioxins (PCDD/PCDF). Normally, the evacuated gases don't have sulphur dioxide (SO_2), small quantities can be presented at utilisations of the same materials with sulphur content [7]. The most important are the solid particles. The powders are situated in the hazardous pollutants category (especially the PCDD/PCDF type) because these are harmful compounds deposed on the dust surface (by condensation and absorption) [8, 9]. For the secondary copper metallurgy, the typical emission factor for Europe is 50µg-TEQ/ton of copper refined (with variation between minimal and maximal limits, by 5 and 500µg-TEQ/ton). The reported emission factor by Germany for the shaft furnace or converter and reverberatory furnaces is variable 5.6 and 110µg-TEQ/ton and between 0.005 and 1.56µg-TEQ/ton. The reported emission factors for two furnace from Sweden (for charging was used clean wastes) was 0.024 and 0.04µg-TEQ/ton.

At the secondary copper production in Austria was reported an emission factor of 4µg-TEQ/ton. In Portugal, at utilisation of a gas cleaning system (cyclone and filter bag, including a cooling step to prevent the novo-synthesis process of the dioxins) for electrical furnace utilised for zinc and copper, respectively for brass elaboration, the emission factors were variable between 0.09 and 0.4µg-TEQ/ton.

For Holland, with three companies for the brass (48kt/year) and copper with bronze (1kt/year) (gifted later with filtering systems), the undertake emission factors are 5µgI-TEQ/ton for brass elaboration from charges lightly polluted, respectively 35µgI-TEQ/ton for secondary copper and bronze elaboration from charges with more impurities [10]. For SUA, according to EPA Dioxin Inventory (US EPA, 2000) which takes into consideration the recent data related to the elaboration in shaft furnaces provided with burner for post-combustion of evacuated gases and dry cleaning systems, when was used the mixed charges from copper contaminated with plastic materials, the emission factor was 779µg-TEQ/t waste (810µg-WHO-TEQ/ton). The measurements made for other furnaces of the same type, used to obtain the blister copper and gifted with post-combustion systems, cooling towers and filter bags get the value of 16.618µg-TEQ/t waste or 16.917µg-WHO-TEQ/t (diminution, of the work condition). For the third company where were made measurements and which worked in oxidation conditions with charges from relatively clean wastes and rotary furnace with a primary cooling system and Venturi scrubber, was obtained an emission factor of 3.6µg-TEQ/t waste or 3.66µg-WHO-TEQ/t [11]. For cooper metallurgy the air and water emission levels, accepted by World Bank Group (related to the legislation of the most important countries copper producers and Pollution Prevention and Abatement Handbook, adapted to the local conditions of this producers), are presented in next tables 5 and 6 [12]. The most dangerous substances which need to taken into consideration to the secondary copper elaboration from wastes are dioxins (PCDD/PCDF), the identified pollutants in the big family known under the name of "dioxin" and classified as belonging to the dangerous substances category.

Table 5. Maximal admissible level of air emissions from copper production, mg/Nm^3

Parameter	Maximal value
SO_2	1000
Arsenic	0.5
Cadmium	0.05
Copper	1
Lead	0.2
Mercury	0.05
Powdery emissions from elaboration	20
Powdery emissions from other sources	50

Table 6. Maximal admissible level of effluents at the copper elaboration, mg/Nm^3

Parameter	Maximal value *)
pH	6-9
Total of solid particles in suspension	50
Arsenic	0.1
Cadmium	0.1
Copper	0.5
Iron	3.5
Lead	0.1
Mercury (total)	0.01
Zinc	1.0
Total metals	10
Advance temperatures	≤3^{0}C **)

*) the value is referred to the direct discharge to the surface water;
**) the effluent can determine the advance temperature but not with more than 3^{0}C in the initial blend zone. If this zone is not definite, than there can be considered 100 m from the discharge point.

The most important part of them is in air emissions, his presents in emissions from the gases current have at origins the chlorine of plastic materials from wire isolation or the remain of other organic contaminants presents at the surface of waste used at the secondary copper elaboration. The PCB existence in the wire insulations, included in the dangerous substance category (according to Council Directive 91/689/EEC regarding the dangerous wastes), creates supplementary problems for the treatment of cable waste by thermal methods.

The dioxins are chemical compounds very stable in generally at temperatures higher than 750^{0}C. PCDD/PCDF is formed in thermal processes when the organic compounds and chlorine are presented in wastes which compose the charging materials (because of the incomplete burning or as a result of novo-synthesis specific processes). The presence of precursors as well as PCB from some insulation accelerates the dioxins forming. The PCDD/PCDF are easily adsorbed and condensed on the bigger surface of the solid fine particle, being especially in suspension in gases and in a less quantity in other outlet processes (waste water, soil etc.).

The presences of organic materials and oils in waste or the presence of other carbon sources (incomplete fuel burning or reducer like coke) can do that the carbon fine particles go into reaction with chlorine compounds, and determine at temperatures less than 500^{0}C the forming of PCDD/PCDF. For dioxins generations are necessary the combustion conditions, but are also important the cooling conditions of gases formed in the capture installations. With the oxygen presence, the optimal interval of temperatures for dioxins formations is 250–500^{0}C.

The specific synthesis processes are accelerated by the presence of same metals like copper or iron which have a catalyst role. Because of this the thermal processes from the copper obtaining play an important role in the dioxin formation, copper being the most efficient catalyst of the forming process for PCDD/PCDF.

5. Measurements for prevention and control of processes generating of pollutant emissions

- ***charges preparation*** need to have a pre-sorting of the wastes used in the charges, in correlation between dimensions and contamination degree in that way to easily eliminate the insulations, followed by the gases post-combustion to destroying any organic compound. Is necessary to use mechanical preparation techniques for charging materials treatment with possibility of collecting and capturing the generated dust. The resulted particles can be treated for metallical fractions recuperation by gravimetric and pneumatic separation methods. The modern methods are necessary in order to remove the cable insulations (for example by cryogenic treatment, when these are crumbly and can be easily separated). It is also necessary to adequately mix the materials in order to realize homogenous charges, capable to ensure the processes deployment in constant parameters, easily controllable.

- ***effective control of process*** which need to develop in constant and stable parameters, at certain values, can lead to minimisation of the PCDD/PCDF generated quantities. It is ideal to have the continuous monitoring of PCDD/PCDF emissions level. If this is not possible, the other variables like temperatures and gases compositions, maintaining–stationary time, smoke parameters at the basket register, need to have a continuous monitoring and to be maintained at the optimal values in order to have a minimal PCDD/PCDF formation.

Other measures, which do not eliminated the pollutant substance generation, but can offer prevention tools are:

- ***smoke and gas collection*** by furnace isolation or work space (the manipulation and transport installations) and correct selection of the cleaning systems to eliminate the non-controlled emissions.

- ***separation with maximal efficiency of dust them the gases collected***. The elaboration processes generate important quantities of pulverous particles with small adsorption surface for PCDD/PCDF. By reducing the quantities of dust and metallic compounds the PCDD/PCDF emissions are indirectly reduced.

The particles can be collected in the filtering and dust collection systems which need to be chosen in function of physical and chemical characteristics. The maximal retention efficiency of the pulverous materials from gases is given be the filter with texture. For copper or copper alloys making process, the filters with texture (so called filter with bags or dust bags) are considered the most efficient cleaning gas treatment in the secondary copper metallurgy. The electrostatic precipitator is not recommended because it has diminished efficiency and oxides, lead or zinc dense particles retention. The installations with scrubbers are inefficient because they are recommended for particles with dimensions bigger than 1μm and solid particles presented in gases from copper elaboration having submicrometer dimensions. For emissions generated in dry processes (which take place at temperatures more than 150^{0}C) these can be used filter bags situated after electro-filter.

Separately, the collected dust can be treated at bigger temperatures for absorbed PCDD/PCDF destruction. The modern capture equipments have included "on-line" systems for purification and use the catalytic principles for PCDD/PCDF destruction.

- ***post-combustion and rapid cooling.*** Because the PCDD/PCDF dioxins are formed in the 250–500^{0}C temperatures interval and are destroyed up to 850^{0}C in oxygen presence, to reduce the dioxin content, gases are conducted into a supplementary burning (post-combustion) chamber, where PCDD/PCDF are destroyed at temperatures up than 950^{0}C. To prevent the dioxin formation process after the combustion chamber, gases are rapidly cooled into "reforming windows". This processing loop can be placed on the evacuated gasses flow in the capture systems and in some cold places of furnace, such as the superior one in which takes place the feeding with charges and is necessary to oxygen injection. In the same time, to limit this phenomena it is necessary to reducte to the minimum the stationary time of the gases in these windows. The active carbon can be utilized to remove the PCDD/PCDF from evacuated gases. For this treatment can be used reactors with fixed or mobile bad or can inject carbon particles in gases, after this operation taking place the dust separation in filters and its treatment.

Recent researches in this domain to reduce and eliminate emissions of PCDD/PCDF are concentrated on the catalytic oxidation. In looking to oxidation process course of components from evacuated gases until H_2O, CO_2 and HCl, in the temperature interval of 370–450^{0}C (comparative with typical temperatures necessary to destroy the PCDD/PCDF which need to be more than 950^{0}C) by utilisations of some metals as catalyst. Catalytic oxidation need to take place in a short time, with small energetic consumption and maximal efficiency (over 99%). A big efficiency can be obtained if the evacuated gases are before dust separated. This method can be applied for contaminants which are in vaporous stage.

The level of PCDD/PCDF emissions at the secondary copper elaboration, obtained by application of the enumerated methods is <0.1ng/Rm^3 TEQ (in standard conditions at 298K and 101.3kPa for dry gas) or for air 0.01μg I-TEQ/t product and for waste in 0 - 630μgI-TEQ/t copper interval, for copper production [7, 11]. The given factor by UNEP for non-modern sectors of secondary copper elaboration is 800μgI-TEQ/t copper product, to the non-controlled burning of cable waste is 5.000μgI-TEQ/t waste [11].

References

[1]. Pacyna, J.M., 1982, „***Trace element emission from anthropogenic sources in Europe***" Norvegian Institute for Air Research, NILU rept.TR 10/82, Lillestrom, Norway

[2]. Pacyna, J.M., Ottar, B., „***Control and fate of atmospheric trace metals***", Kluwer Academic publ., Dordrecht, Olanda

[3]. Pacyna, J.M., 1994, „***Emissions of heavy metals in Europe", background Document for the EMEP Workshop on European Monitoring, Modeling and Assessment of heavy metals and Persistent Organic Pollutants***, Beekbergen, Olanda, 3 – 6 may, 1994

[4].***http://ec.europa.eu/environment/enveco/climatechange/nitrous_oxide_emissions.pdf

[5]. *** OSPAR Background document on dioxins: Hazardous substances series - Dioxins, ISBN 0 946956 92 8, Publication number: 2005/152

[6]. Jolly, J., 2003, ***The U.S. Copper-base scrap Industry and its by-products***", Copper development Association Inc. Dayton Maryland USA

[7]. *** 2004, „***Draft Guidelines on Best Available Techniques (BAT) for secondary copper production***", Section V.D. 1, DRAFT 22.04 2004, coordinated by Mr. Patrick Finlay, Canada

[8]. Ayres, R.U., Ayres, L.W., Rade, I., 2002, „***The Life Cycle of Copper Production, its Co-Products and By-Products***", Mining, Minerals and Sustainable Development, January, No.24

[9]. Jolly, J., 2000, „***The US copper-base scrap industry and its by products: An overview***", Technical report (A1309-00/00), Copper Development Association Inc., New York, July 31

[10]. *** „***Secondary copper production***", http://europe.eu.int/comm/environment/dioxin.pdf

[11]. *** 1998, „***UNEP Standardized Toolkit for identification and quantification of dioxin and furan releases***", Geneva, UNEP Chemical DRAFT, January

[12]. *** 1998, „Copper smelting", World Bank Group, Pollution Prevention and Abatement Handbook.

THE ANNALS OF "DUNAREA DE JOS" UNIVERSITY OF GALATI.
FASCICLE IX. METALLURGY AND MATERIALS SCIENCE
N^0. 2 – 2008, ISSN 1453 – 083X

QUALITY OF MICROHARDNESS MEASUREMENT PROCESS

Pavol PALFY, Jozef PETRÍK
Technical University of Kosice, Kosice, Slovakia
e-mail: pavol.palfy@tuke.sk

ABSTRACT

The capability of microhardness measurement process was assessed by MSA - Gear Repeatability and Reproducibility method. Experimental sample materials were: annealed ferrite, semiconductor-grade copper and aluminium. The measurement system consisted of microhardness tester Hanemann, type Mod D32 coupled with Neophot 32 optical microscope. Measurements were conducted by two appraisers. Obtained experimental data was evaluated by standard MSA process, using software Palstat CAQ, modul MSA. The assessment of the GRR capability indexes led to the conclusion that measurement process non-capability is typical for microhardness testing and it is also influenced by the type of tested material.

KEYWORDS: measurement capability, repeatability, reproducibility, microhardness, MSA, GRR

1. Introduction

The microhardness measurement method is frequently used for determination of hardness of small objects, thin layers, and phase identification in metallography. Its principle is identical to Vickers method, except for considerably smaller loads used. The determined value of microhardness depends on the load, accuracy of scale reading, and the indentation size. As for every test of mechanical properties, there is a natural requirement for reliability of measurement results, which is unthinkable without sufficient capability of measurement process. There are two ways of measurement process capability assessment. The first one is based on analysis of control processes according to uncertainty of measurement. The second is based on the measurement system analysis (MSA). In this case it is possible to use repeatability and reproducibility (GRR) or the variability (ANOVA). Due to simpler realization, the GRR method was used. In the Gear Repeatability and Reproducibility method, individual components of the measurement system (measuring device, operator, measured material...) are analyzed, and subsequently the capability of the whole system is numerically evaluated by indices.

Thus it is probable that the process of measurement taking place in capable system is also capable.

2. Experimental materials

Experiments were realized with three materials: iron, copper, and aluminium.

1. Pure iron - annealed ferrite was divided into 10 samples with size of 5×10×2 mm. Those were cast into epoxide resin Dentacryl. The grinding was done on SiC papers with water cooling on gradually decreasing grain size (according to ANSI/CAMI) 220 - 3000. Water suspension of Al_2O_3 was used for mechanical polishing. The sample was etched with 5% nital (5% HNO_3 in CH_3OH) for 10 seconds. The microstructure was uniform throughout the whole sample surface, consisting of isoaxial grains. The grain size was determined according to standard STN 42 0462 by grain counting method. Mean grain size 36.3 μm (standard deviation 2.58 μm) was determined from 30 analyses. Before microhardness measurement samples were grinded on No. 3000 paper and polished as stated above.

2. The semiconductor copper Cu - K3A - 534 EG, manufacturer VUK Panenské Břežany, Czech republic was used as experimental material. The copper was delivered as a cylinder φ 40 mm. The surface for metallographic analysis was prepared in standard way by grinding through a series of finer and finer silicon carbide water cooled papers.

The sequence was 220, 240… and 3000 grit (ANSI/CAMI grit size scale).

Finally, it was mechanically polished with Al_2O_3, moistened with water and cleaned with ultrasonic cleaning equipmnent. Polished surface was etched with 4 g $FeCl_3$ - 30 cm^3 HCl - 1000 cm^3 CH_3OH.

The material had coarse - grained microstructure with grain diameter of 8 - 15 mm. The samples for microhardness analysis No. 1 - 4 were taken from the grain No. 1, the samples No. 5 - 9 from the grain No. 2 and sample 10 was part of the grain No. 3. The dimensions of samples were 3×5 mm with thickness of 6 mm. Before microhardness measurement the samples were mechanically polished as well as before etching.

3. Electroconducting aluminium STN 42 4004 cast at 760 °C with cooling rate 2 $°Cs^{-1}$ was used as experimental material. Ten samples with size of 10×10×5 mm were taken from the casting. The sample surface was processed the same way as for iron samples. For microstructure development etching solution of 0.7 % HF in water was used. The semiproduct had a coarse microstructure with grain diameter gradually decreasing from 170 μm in sample No. 1 to 90 μm in sample No. 10.

3. Measurement equipment and method

The optic microscope NEOPHOT 32 with microhardness tester Hanemann, type Mod D32 were used as measurement equipment. The microhardness was measured according to standard STN EN ISO 6507 - 1 with load of 20 g and loading time of 10 s. The load was chosen so that the size of the imprint diagonal would not exceed 50 % of the grain size. The tester was up to standard of linearity between loads 10 - 50 g. Discrimination (readability or resolution) is the amount of change from a reference value that an instrument can detect and faithfully indicate.

The measure of this ability is typically the value of the smallest graduation on the scale of the equipment's measurement system. A general rule of thumb is that the measuring instrument discrimination ought to be at least one - tenth the process variation.

Table. 1. Discrimination and standard deviation

Material	Fe			Cu			Al		
Measurement	1	2	3	1	2	3	1	2	3
Discrimination	5.3	5.0	6.5	3.18	3.33	2.45	0,69	1.6	0.67
SD (HV0.02)	9.29	9.54	11.56	9.49	8.84	7.84	2.09	1.17	1.68

The measurement system is said to have sufficient sensitivity threshold if its resolution is small compared to the process variability. The discrimination and corresponding SD are listed in the Tab. 1. The discriminations for all measurements and materials were not sufficient.

The measurement was carried out by two (A and B) same skilled appraisers. Each of them carried out 3 trials (indentations) on each sample The measurements were made in a random order to ensure that any drift or changes that could occur would be spread randomly throughout the measurement.

For evaluating a term variability of capability indices, the microhardness tests were repeated 3 times on each material.

The results are in Tab. 2 and Fig. 1.

Table 2. The hardness and standard deviations

Microhardness HV0.02									
Material	Fe			Cu			Al		
Measurement	1	2	3	1	2	3	1	2	3
Appraiser A	135.3	135.8	140.3	99.9	97.0	95.6	34.9	34.8	32.7
Appraiser B	143.0	139.5	147.7	100.9	97.7	94.9	34.9	34.6	32.3
A and B	139.2	137.6	144.0	100.4	97.4	95.2	34.9	34.7	32.5
Standard deviation SD (HV 0.02)									
Material	Fe			Cu			Al		
Measurement	1	2	3	1	2	3	1	2	3
Appraiser A	8.13	9.59	8.43	9.62	8.77	8.06	2.39	1.36	1.8
Appriaser B	8.89	9.29	13.1	9.49	9.06	7.74	1.8	0.96	1.55
A and B	9.29	9.54	11.56	9.49	8.84	7.84	2.09	1.17	1.68

Grubbs' test (with significant level α = 0,05 %) detected no outliers. The statistical outliers indicate that the process is out of statistical control. Again ideally, the causes of outiers are eliminated and new data is obtained. Normal probability distribution is an assumption of the standard methods of MSA. In fact, there are measurement systems that are not normally distributed. When this happens and normality is assumed, the MSA method may overestimate the measurement system error.

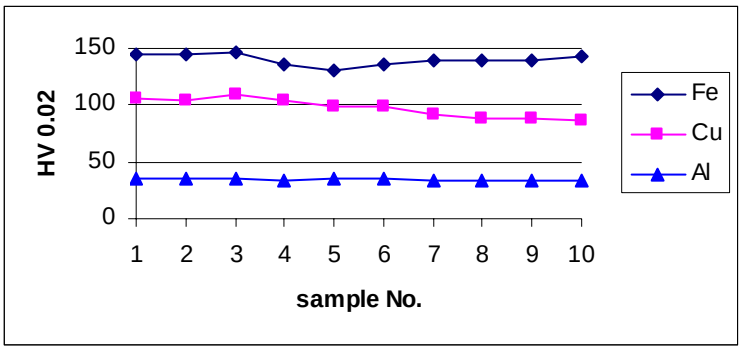

Fig. 1. The hardness of individual samples.

Therefore, before use, the data should be checked to confirm that its distribution is approximately normal.

The most simple check is probability plotting, which gives indications of unusual and non-normal distributions [1]. The normality was evaluated by normal probability plot, using software Freeware Process Capability Calculator by Symphony technologies. The normality of all samples, measured by particular appraisers was confirmed.

The GRR method - combined estimation of measurement system repeatability and reproducibility, described in [2] with confidence 99 % and coverageve 99 % (5,15 σ) was used for capability evaluation. A GRR study can quickly establish the short - time performance of a tester, including appraiser influence. The method will allow the measurement system's variation to be decomposed into two separate components, reproducibility and repeatability, but does not describe their interaction [4]

As well as %GRR value, determining the process capability, partial indices %EV, %AV and %PV were evaluated. Software Palstat CAQ, module MSA, was used for calculation.

4. Results

The measurement system ought to be under statistical control before capability is assessed. This means that under repeatable conditions, the variation in the measurement system is due to common causes only. The range control chart is used to determine whether the process is under statistical control. If all ranges are in control, all appraisers are doing the same job. If one appraiser is out of control, his/her method differs from the others. If all appraisers have some out of control ranges, the measurement system is sensitive to appraiser technique and needs improvement to obtain useful data.

As shown in the Tab. 3, the condition of system statistical control was not satisfied, except for the second and the third measurement on the aluminium. All values outside control lines were measured equally by both appraisers.

Table 3. Statistical control of measuremet system

Range control chart (% $\overline{R}$ - % values outside control lines)									
Material	Fe			Cu			Al		
Measurement	1	2	3	1	2	3	1	2	3
Appraiser A	0	0	0	10	10	10	10	0	0
Appraiser B	10	10	10	0	0	10	10	0	0
A and B	5	5	5	5	5	10	10	0	0
Average control chart (% $\overline{X}$ - % values outside control lines)									
Material	Fe			Cu			Al		
Measurement	1	2	3	1	2	3	1	2	3
Appraiser A	10	30	10	60	70	80	20	10	10
Appriaser B	0	30	30	70	80	70	0	0	0
A and B	5	30	20	65	75	75	10	5	5

The resulting chart for average shows "usability" of the measurement system. The area within the control limits represents the measurement sensitivity ("noise"). Since the group of samples used in the study represents the process variation, approximately one half or more of the averages should fall outside

the control limits. If the data shows this pattern, then the measurement system should be adequate to detect part - to - part variation and the measurement system can provide useful information for analyzing and controlling the process. If less than half falls outside the control limits then either the measurement system lacks adequate effective resolution or the sample does not represent the expected process variation. With respect to the Table 2, this condition was satisfied only for Cu measurements.

The number of distinct categories ("ndc" - number, based on Wheeler's discrimination ratio) should be more than, or equal to 5, but values between 2-5 may be conditionaly used for rough calculations.

As it can be seen from Fig. 2, low values of "ndc" bear witness of the low capability of evaluated process. The criteria as to whether a measurement system's capability is satisfactory depend on the rate of the manufacturing production process variability that is "consumed" by measurement system variation. This consumption is characterized by index %GRR.

The value of %GRR < 10 % is generally considered to be an acceptable measurement system, the value between 10 % and 30 % may be acceptable according to the importance of application and value > 30 % is considered to be not acceptable - every effort should be made to improve the measurement system.

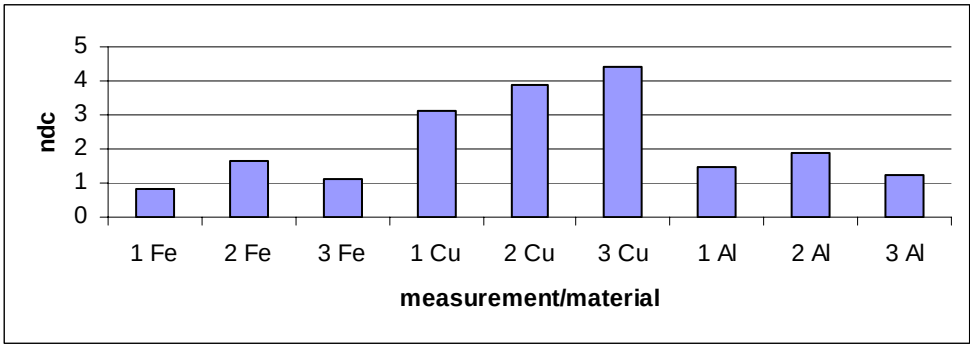

Fig. 2. The values of "ndc".

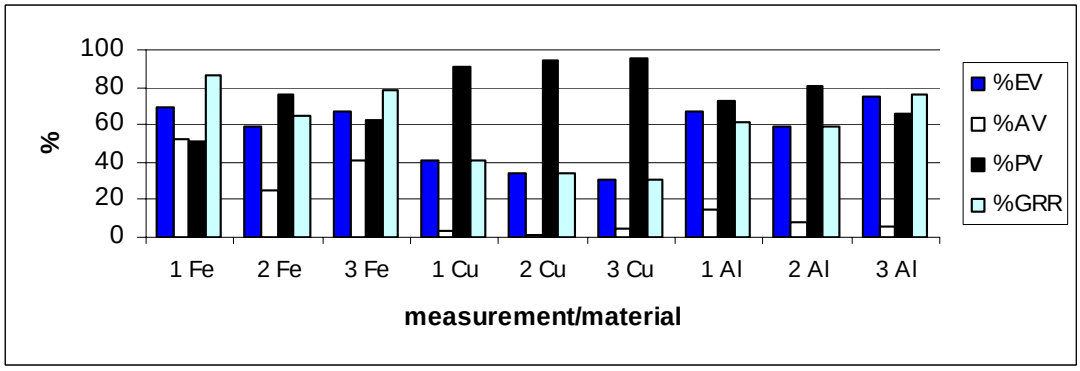

Fig. 3. The capability indices.

Repeatability is the inherent variation or capability of the equipment itself. Repeatability is commonly referred to as equipment variation (EV), although this is misleading. In fact, repeatability is common cause (random error) variation from successive trials under defined conditions of measurement. Possible causes for non - acceptable repeatability are equipment, standard, method, appraisers lack of experience, environment, wrong gage for the application.

Considering the same micrometer and standard measurement environment, %EV value depends on the relation between load and measured materials eventually getting the method under control by appraisers. The load is related to the imprint diagonal size, which should be comparable to the grain size. %AV index represents the influence of appraisers on variability, for example their competence, perceptions, skills discipline and vigilance. It is a function of average values of individual appraisers.

%PV index is function of range of average microhardnes of individual samples. It is sensitive to the variability influence among measured samples.

Its value indirectly defines propriety of used equipment for measurement.

The value of %PV above 99 % is for very accurate equipment, above 90 % for suitable, above 70 % for

satisfactory and above 50% for inaccurate one. The equipment with value up to 50 % is unsuitable [3].

Analyzed process was non - capable for all materials and measurements. It is possible, that non - capability is typical for microhardness, but also hardness measurement [4,5].

However, it is difficult to achieve only 10 % variation in hardness testers. The dead - weight testers typically achieve results of 15 to 20 %. The older testers in poor condition give much worse results [6].

Fig. 3 shows that the value of capability indices depends more on material type than repeated measurements; considerably lower values of %GRR were obtained for copper (average 42,1 %) than for iron (average 76.5 %) and aluminium (average 77.9 %). Two-factor analysis of variance between groups (ANOVA) without repeating confirms this conclusion for indices %GRR, %EV and %EV.

The lower values for copper may have been positively influenced by lower ratio of imprint diagonal to grain size, i.e. lower uneven influence of the results by grain interfaces.

5. Conclusions

1. The microhardness measurement process is non-capable for all three materials.
2. Non-capability is typical for microhardness (and hardness) measurement.
3. Capability is influenced by the measured material.

References

[1] Betteley, G. et al., 1994, ***Using statistics in industry***. Prentice Hall International. Hemel Hampstead, ISBN 0-13-457862-7, pp. 186.

[2] Measurement system s analysis (MSA). Reference manual. Third edition. 2003, pp. 102-120.

[3] Meloun, M. - Militký, J., 2002, ***Kompendium statistického zpracování dat. 1. vydanie.*** Praha: Academia, ISBN 80-200-1008-4, pp. 29.

[**4] Petrík, J. - Palfy,P.,** 2006, ***Kvalita procesu merania mikrotvrdosti***, Sborník 15. mezinárodní konference Jakost - Quality Ostrava, 23.-24.5.2006, Ostrava ČR. ISBN 80-02-01829-X, pp. 14.

[5] Petrík, J. - Špeťuch, V., 2005, ***The Dependence of Hardness Measurement System Capability on the Time***. Transactions of the Universities of Košice. 3/2005, ISSN 1335-2334, pp. 27-33.

[6] Tobolski, E., 2003, Uncertainty in Hardness testing. (part 2). Advanced materials & processes. May 2003, pp. 25.

Acknowledgement
This work was supported by the Slovak Grant Agency for Science VEGA 1/4141/07.

THE ANNALS OF "DUNAREA DE JOS" UNIVERSITY OF GALATI.
FASCICLE IX. METALLURGY AND MATERIALS SCIENCE
N^0. 2 – 2008, ISSN 1453 – 083X

HALF-FINISHED TECHNOLOGY OF STEELS AND FATIGUE STRENGTH

L. PALAGHIAN, S.CIORTAN, S. BAICEAN
"Dunărea de Jos" of University Galaţi
e-mail: liviu.palaghian@ugal.ro

ABSTRACT

The paper presents the bending fatigue testing for four steel brands. The test showed that the fatigue strength is decreasing with the increasing of both ingot size and the rolled sheet thickness. The fatigue strength is varying following the ingot area and the orientation of cutting direction versus rolling direction.

KEYWORDS: fatigue strength, ingot cast steel, continuously cast steel, rolled sheet thickness.

1. General considerations

It is well known that the behaviour of elements in metal constructions (shapes, sheets) and certain machine elements (shafts, axes, crankshafts etc.) depends on the semi-finished products, casting and rolling technology, among others factors, [1]. As the result of initial solidification from the molten state, before any of the operations to forge or roll it into useful sizes and shapes have begun, inherent flaws are present in metal.

Primary pipe is shrinkage cavity that is formed at the top of an ingot during metal solidification, which can extend deep into the ingot. Blowholes are secondary pipe holes in metal that can occur when gas bubbles are trapped as the molten metal in an ingot mold solidifies. Many of these blowholes are clean on the interior and are welded sheet into sound metal during the first rolling or forging of the ingot. However, some do not weld and can appear as seams of laminations in finished products.

Segregation is a non-uniform distribution of various chemical constituents that can occur in a metal when an ingot or casting solidifies. Segregation can occur anywhere in the metal and is normally irregular in shape. However, there is a tendency for some constituents in the metal to concentrate in the liquid that solidifies last.

The conventionally ingot cast steels have strongly segregated non-uniform distributions of carbides oriented in the direction of rolling, [1]. The obtaining by ingot casting of pure metal, without segregations and blowholes has as consequence the removal of the center which forms primers of the breaking fissure, especially at variable strains. Practice shows that as the ingot dimensions increase, their crystallization coarsens and segregation accompany it.

In case of continuous casting the quite rapid solidification does not allow a good elimination of inclusions and blowhole through flotation. Continuous castings are the most efficient way to solidify large volumes of metal into simple shapes with consistent quality, [2].

The ensuring through rolling and thermal treatment of the semi-finished products uniform structure leads to splitting or welding workings, to the burns avoidance, zones with a higher hardness but which can be primers of breaking. In the case of rolling of steels obtained appears the impossibility of casting structure modification because the reduction rate by thermal plastic strain is too small. Though casting and rolling technology greatly influences fatigue strength, the existing literature contains generally qualitative information.

Statistical scatter [3] of fatigue strength is not only a very important factor for the high strength steels but also for the low strength steels containing various types of defects. Especially in ingot cast steels the fatigue strength is controlled by the non-metallic inclusions which become the fatigue fracture origin. In a volume of material subjected to the cyclic stress, the fatigue failure occurs at the largest defect that is present in the volume; fatigue fracture is the so-called weakest link phenomenon, [4, 5]. Thus the mechanical properties of steel are controlled to a large degree by the volume fraction, size, distribution, composition and morphology or inclusions and precipitates, which act as stress raisers, [6, 7, 8].

2. Tested materials and applied method

There have been studied four steel brands (Table 1) with: R_c = (353÷380) MPa; R_m = (520÷580) MPa.; A_5 = (22÷23)%.

Table 1

Brand		B_1	B_2	B_3	B_4
% C (ingot)	Max.	0.22	0.13	0.14	0.12
	Min.	0.12	0.09	0.13	0.10
% C (cont. casting)	Max.	0.21	0.10	0.15	0.16
	Min.	0.19	0.09	0.13	0.14

The samples have been alternately symmetrically bended by rotating them with a frequency of 1500 rot/min. Wöhler curves have been drawn based on the obtained results.

3. Experimental results

Figures 1, 2, 3, 4 contain the experimental results for steels B_1, B_2, B_3, B_4 respectively, [9, 10].

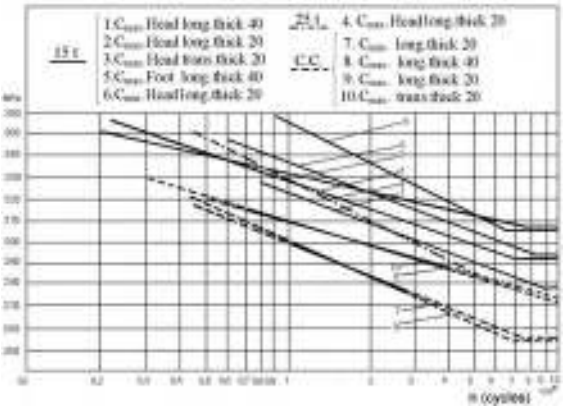

Fig.1. Steel brand B_1

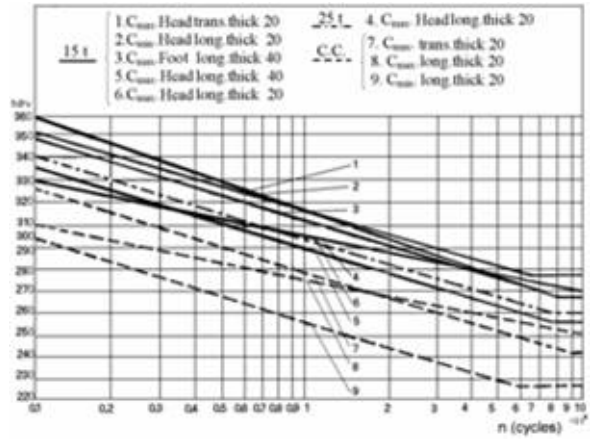

Fig.2. Steel brand B_2

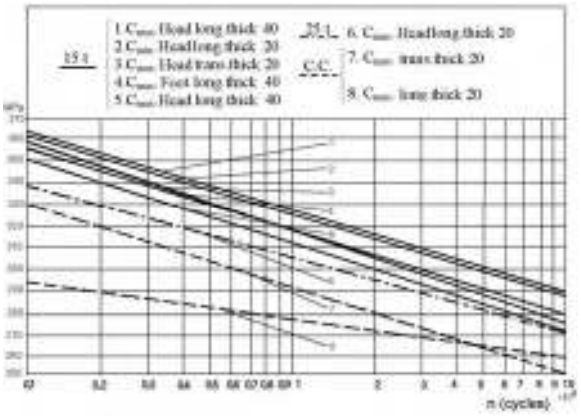

Fig.3 Steel brand B_3

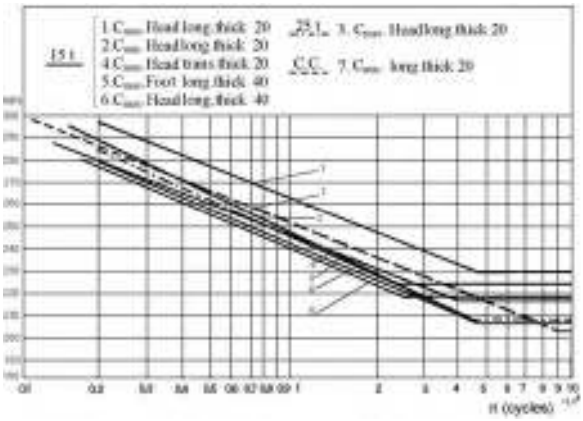

Fig.4. Steel brand B_4

The following abbreviations have been used:

C_{max}, C_{min} – maximum, respectively minimum percentage of carbon;

-head – samples from ingot's head;

-foot – samples from ingot's foot;

-long – samples cut on the rolling direction;

-trans – samples cut perpendicular on the rolling direction;

-15 t – ingot of 15 tons;

-25 t – ingot of 25 tons;

-thick.20 – samples made of 20 mm thickness sheets;

-thick.40 - samples made of 20 mm thickness sheets;

-c.c. - samples made of continuously casted sheets.

Tests prove that fatigue strength of samples made from ingots of 15 t is higher with around 10% than the fatigue strength of samples made from ingot of 25 t (figure 1, curves 2 and 4; figure 2, curves 6 and 4; figure 3 curves 1 and 9; figure 4 curves 1 and 9).

Samples of sheets from ingot's foot have a fatigue strength higher with around 5% than of samples drawn from ingot's head (figure 1, curves 5 and 1;

figure 2 curves 6 and 4; figure 3 curves 6 and 2; figure 4 curves 4 and 6).

Samples made of 20 mm sheets have a fatigue strength of about 10% higher than those of 40 mm (figure 1, curves 2 and 1; figure 2, curves 3 and 5; figure 3, curves 1 and 2; figure 4, curves 3 and 1).

Fatigue strength generally diminishes at samples transversally drawn in comparison with those longitudinally drawn (figure 1, curves 3 and 1; figure 2, curves 6 and 1; figure 3, curves 3 and 1; figure 4, curves 4 and 1). For samples drawn of sheets obtained from ingots the influence of carbon content on fatigue strength within the same steel brand is negligible (figure 1, curves 5 and 1; figure 2, curves 1 and 2; figure 3, curves 1 and 2; figure 4, curves 4 and 1). For samples drawn of continuously casted steel sheets the fatigue strength is not influenced by the rolling direction (figure 1, curves 9 ad 10; figure 3, curves 7 and 8; figure 4, curves 7 and 8).

The diminishing of continuously casted sheet thickness has as effect the increase of fatigue strength. Thus, the diminishing of sheet thickness from 40 to 20 mm leads to a fatigue strength increase around 5% (figure 1, curves 8 and 9; curves 9 and 8).

Unlike sheets obtained of ingot in case of continuously casting, within the same steel brand, the influence of carbon content on the fatigue strength is most obvious.

Thus, by increasing the carbon content the fatigue strength increases as well (figure 1, curves 9 and 7; figure 4, curves 8 and 9).

The fatigue limit of steel obtained by continuous casting is smaller than that of ingot cast steel (figure 1, curves 2 and 7; figure 2, curves 1 and 7; figure 3, curves 1 and 8; figure 4, curves 1 and 7).

The values of fatigue strength obtained for tested materials are presented in Table 2.

Table 2

Steel brand	Ingot type		σ_{-1} [MPa]			
			20 mm thick.		40 mm tick.	
			long.	trans.	long.	trans.
B_1	15 t	head	305 (305)	290	275	-
		foot	-	-	295	-
	25 t	head	280	-	-	-
		foot	-	-	-	
	cont. cast.		275 (255)	-	255	-
B_2	15 t	head	270 (280)	265	255	-
		foot	-	-	270	-
	25 t	head	260	-	-	-
		foot	-	-	-	-
	cont. cast.		250 (225)	240	-	-
B_3	15 t	head	290 (290)	275	270	-
		foot	-	-	-	-
	25 t	head	270	-	-	-
		foot	-	-	-	-
	cont. cast.		250	260	-	-
B_4	15 t	head	230 (205)	220	205	-
		foot	-	-	220	-
	25 t	head	205	-	-	-
		foot	-	-	-	-
	cont. cast.		(205)	-	-	-

Note: the values in the brackets are obtained for a minimum carbon percentage.

The analysis of fatigue tests on samples made by ingot steel brands (figures 5, 6, 7, 8) show a narrow scatter of experimental results.

Results obtained at testing the samples obtained by continuously casting technology shows a wider scatter of results (figure 9).

The two behaviour types in case of fatigue subjected samples can be considered as a result of a higher reduction ratio, due to rolling technology, in case of samples obtained from ingot comparing with those obtained by continuously casting method.

The same aspects can be praised in the results' scattering area analysis in fatigue life case, table 3.

The slopes of fatigue curves of steel brands (Eq.1) result from linear regression analysis.

$$k = \frac{\sigma_2 - \sigma_1}{\lg N_1 - \lg N_2} \qquad (1)$$

Following the concept of normalized Wöhler curves [11] was analyzed the scatter band of experimental results (table 3).

The experimental results are included between a inferior and superior curves resulted from regression analysis.

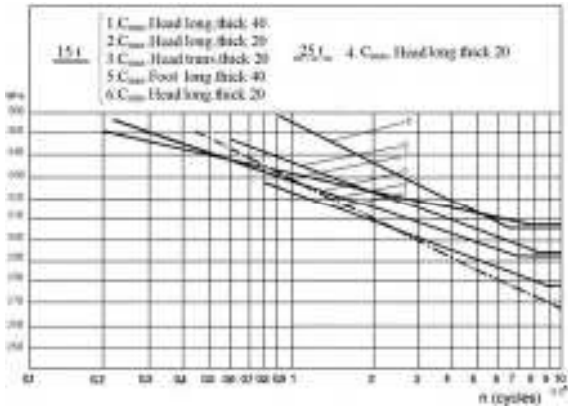

Fig.5. Steel brand B_1 – ingot cast

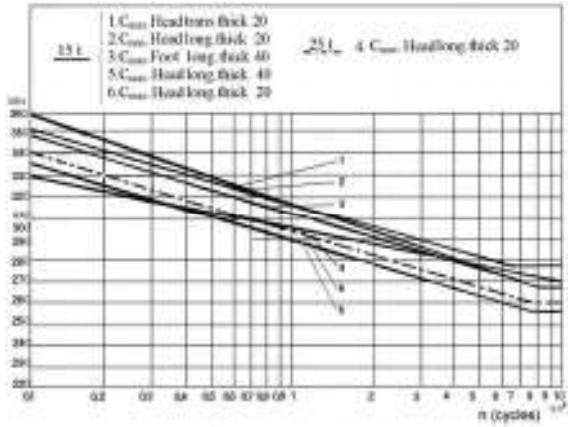

Fig.6. Steel brand B_2 – ingot cast

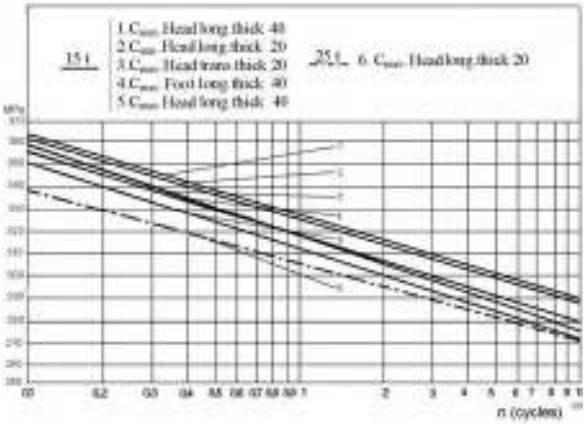

Fig.7. Steel brand B3 – ingot cast

Table 3

Steel brand	Slopes of fatigue curves **k**		
	inferior	superior	difference
B_1 – ingot cast	52,17	62,31	10,14
B_2 – ingot cast	43,7	50,72	7,02
B_3 – ingot cast	36,23	36,23	0
B_4 – ingot cast	46,15	48,83	2,68
cont. cast	36,23	50,79	14,56

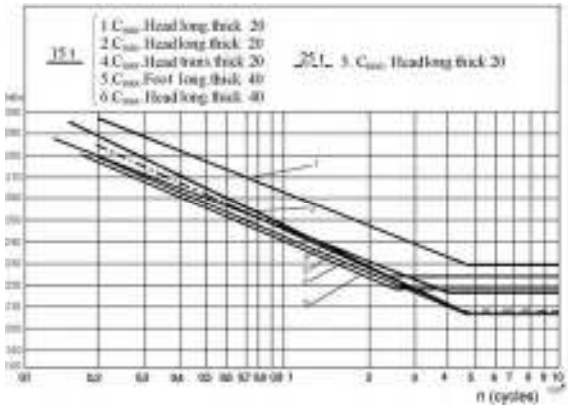

Fig.8. Steel brand B4 – ingot cast

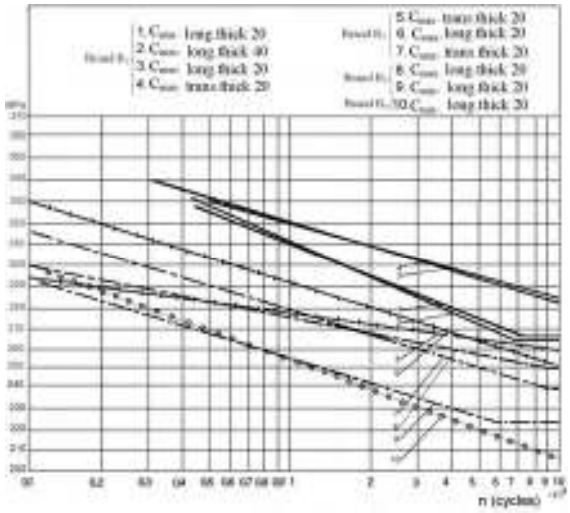

Fig.9. Continuously casting steel

4. Conclusions

The experimental tests worked on the four steel brands indicate that:

- Fatigue strength increases with the diminishing of both ingots dimensions and rolled sheets thickness, in case of either ingot cast steel and continuously cast steel. Rolled sheets of ingot's foot have higher fatigue strength than those rolled from ingot's head. Fatigue strength is higher for samples cut on longitudinal direction than those cut on transversal direction in case of ingot rolled sheets. This phenomenon is not

manifest in the case of continuously steel rolled sheets.

- Fatigue strength increases with the increase of carbon content. Within the same steel brand, for the ingot rolled sheets the variation of carbon percentage is negligible. For the sheets rolled of continuously cast steel, the fatigue strength increases the carbon content
- The fatigue strength of continuously cast steel is about 15% smaller than that of ingot cast steel.
- Experimental results indicate a wider scattering area for fatigue resistance values obtained in continuously casting case samples, comparing to the ingot cast ones.

References

[1]. Zhang, L., Rietow, B., Thomas, B.G., Eakin, K., 2006, ***Large Inclusions in Plain-Carbon Steel Ingots Cast by Bottm Teeming***, ISIJ International, vol.46, No.5 pp 670-679.

[2]. Thomas, B.G.,. 2004, ***Continuous Casting***, Yearbook of Science and Technology, McGraw-Hill**.**

[3]. Maluf, O., Milan, T.M., Spineli, D., Martinez, M.E., 2005, ***Residual Analysis Applied to S-N Dataof a Surface Rolled Cast Iron***, Materials Research, vol.8, No.3, pp. 251-255.

[4]. Anderson, C.W., Shi, G., Atkinson, H.V.., Sellars, C.M., 2000, ***The precision of methods using the statistics of extremes for the estimation of the maximum size of inclusions in clean steels***. Acta Materialia, 48(17), pp. 4235-4246.

[5]. Berreta, S.., Murakami, Y., 1998, ***Statistical analysis of defects for fatigue strength prediction and quality control of materials***. Fatigue & Fracture of Engineering Materials & Structures, 21(9), pp. 1049-1065.

[6]. *,** 2002, Steel Statistical Yearbook, ed. International Iron and Steel Institute, Brussels.

[7]. *,** 1958, Special Report No.63: Ingot Surface Defects, Sub-Committee (Steelmaking Division) of the British Iron and Steel Research Association.

[8]. Heuler, P., Berger, C., Motz, J., 1993, ***Fatigue behaviour of steel castings containing near-surface defects***, vol. 16(1), pp. 115.

[9]. Palaghian L., 1995, ***Five papers about the fatigue of naval steel D32***, Helsinki University of Technology, Otaniemi M-203.

[10]. Palaghian L., Barsan I, Ciortan S., 1999, ***Researches on the influence of making technology of steels used for naval structures constructions in corrosive environment fatigue strength***. Proc. of. The 15th International Conference on Port and Ocean Engineering in Arctic Conditions, Helsinki, pp 644-651

[11]. **Haibach, E.,** 2002, Betriebsfestigkeit [Structural durability], 2nd ed. Düsseldorf, VDI-Verlag.

THE ANNALS OF "DUNAREA DE JOS" UNIVERSITY OF GALATI.
FASCICLE IX. METALLURGY AND MATERIALS SCIENCE
N^0. 2 – 2008, ISSN 1453 – 083X

MODELLING BY FINITE ELEMENT ANALYSIS METHOD OF STRESS STATE ESTABLISHING FOR AN ALLOY STEEL

Silviu MACUTA, Marian BORDEI
"Dunarea de Jos" University of Galati
email: Silviu.Macuta@ugal.ro

ABSTRACT

The paper presents some results about the tension state in samples subject to pure bending fatigue process. Numerical simulation based on finite element method was used. The tension field induced by a vertical deformation imposed at the sample ends was generated on an original patented machine. The studies were carried out on two steels currently used in pressure vessel industry. Experimental data are in good agreement with the simulated ones.

KEYWORDS: steel, fatigue, low frequency, lattice parameter, texture, X-ray diffraction

1. Introduction

Developing mechanical constructions for the pressure vessel industry, aircrafts, construction equipment or shipbuilding calls for the investigation of the characteristics of the materials subject to a small number of tension load cycles close to the material elasticity limit [1].

To get a deeper insight into some aspects related to damage process of the materials used in the machine manufacturing variably subject to pure bending, a universal testing machine was designed and patented [2]. The steels considered for the investigations were: OL50,10TiNiCr180 basically used for the construction of pressure boiler and vessels.

To analyze the pressure states at the given moment, under forced deformations subject to pure bending on the above universal machine, the FEM method was applied.

2. Real structure discretization. Description of fem and the model used

The real structure discretization process consists in replacing the given structure, which is continuous, by a discrete one which is discontinuous and idealized.

The study of to the given structure is substituted by an approach to the entire assembly of the finite elements as obtained from discretization. [3]. Thus, the elastic element in Fig. 1, which represents the type of sample to be used for fatigue tests at high tensions and small number of cycles, has the shape of a plate.

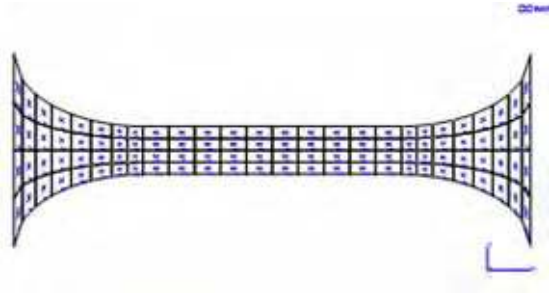

Figure 1.

The finite element used is an iso-parametric rectangular thick shell of six degrees of freedom across each node, and 24 degrees of freedom across an element which simulates the membrane and bending plate effects.

The sides of the quad element are straight, a disadvantage eliminated by a fine discretization in the curvature radius area.

Across the thickness five surface layers (Fig. 2) were considered by a suitable modeling of the tension field and the surface layer in the Z direction.

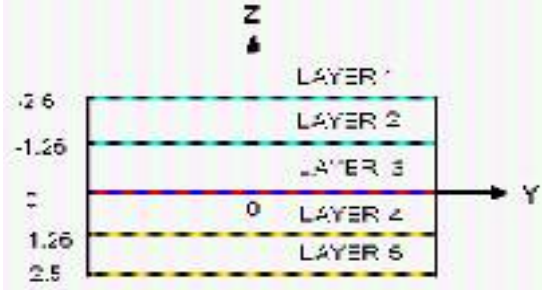

Figure 2.

The finite element model considers the displacement field as the main unknown parameter and assembling the structure finite elements results in a lineal algebraic problem of generalized nodal displacement unknown parameters.

The model used is the one illustrated in Fig. 3 with the following boundary conditions; free displacement and rotations blocked $d_y=0$, $r_x=0$, $r_z=0$ and forced/imposed displacement d_z (implicity angle **α**) at the fixing ends. The materials used for the samples have the features given in Table 1. [4, 5]

To make the appropriate calculations by the FEM method the program MARC version 6.2 was used.

Data pre – and post processing was carried out by MENTAT II 1995 program. The operating system is HP UNIX 10.10 installed on a work station HP 712 of processor PA RISC 9000.

The program is provided by the company MARC Analysis Research Corporation, California, USA, tested and recommed by Germanischer Lloyd and Technical University from Germany and Holland [6].

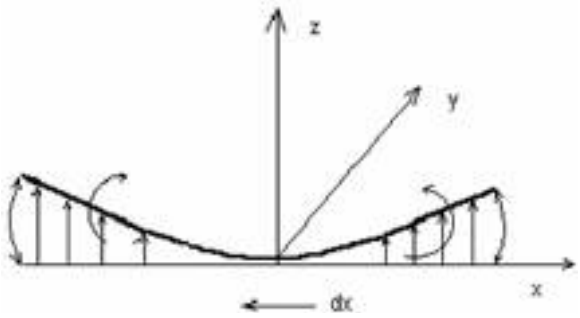

Figure 3.

Table 1.

Steel	**σ_c** [MPa]	**ν**	**E** [MPa]
OL 50	210	0.30	$2.10\ 10^5$
10TiNiCr180	205	0.26	$1.93\ 10^5$

After running the program for the two types of materials, for the imposed deformations the max sample tensions were obtained under the yieding limit at pure bending static load. The results are given in Table 2.

Table 2.

No	**Steel A [OL50]** E=2,1 10^5 [MPa]			**Steel B [10TiNiCr 180]** E=1,93 10^5 [MPa]		
	σ_{max} [MPa]	z [mm]	**α** [grad]	σ_{max} [MPa]	z [mm]	**α** [grad]
1	230	0.84	1.84	150	0.6	1.31
2	250	0.91	2	170	0.68	1.48
3	**270**	**0.99**	**2.16**	**190**	**0.76**	**1.66**

The paper presents the tension states at pure bending load for one sample only, at an imposed deformation, of alloyed steel currently used for the pressure vessels manufacture. Figures 4-6 illustrate the results of the FEM analysis for the alloyed steel OL50 (for 3 layers) as follows: fig. 4 shows the displacements over direction z, fig. 4.1 shows the axial tensions at the surfaces compression (layer 1), fig. 4.2 – detail from 4.1 for the area concerned, fig. 4.3 – the values of the network nodes for tensions $\sigma_X=\sigma_{11}$, fig.5.1 and 5.2 present elongation values $\sigma_X=\sigma_{11}$ at z=2.16 mm(layer2) and finally fig. 6.1 and 6.2 the elongation tension on the inner face (layer 3).

For all the other cases of imposed deformations of the two types of steels given in Table 2 the same variation laws of the normal tensions $\sigma_X=\sigma_{11}$ in the element layers.

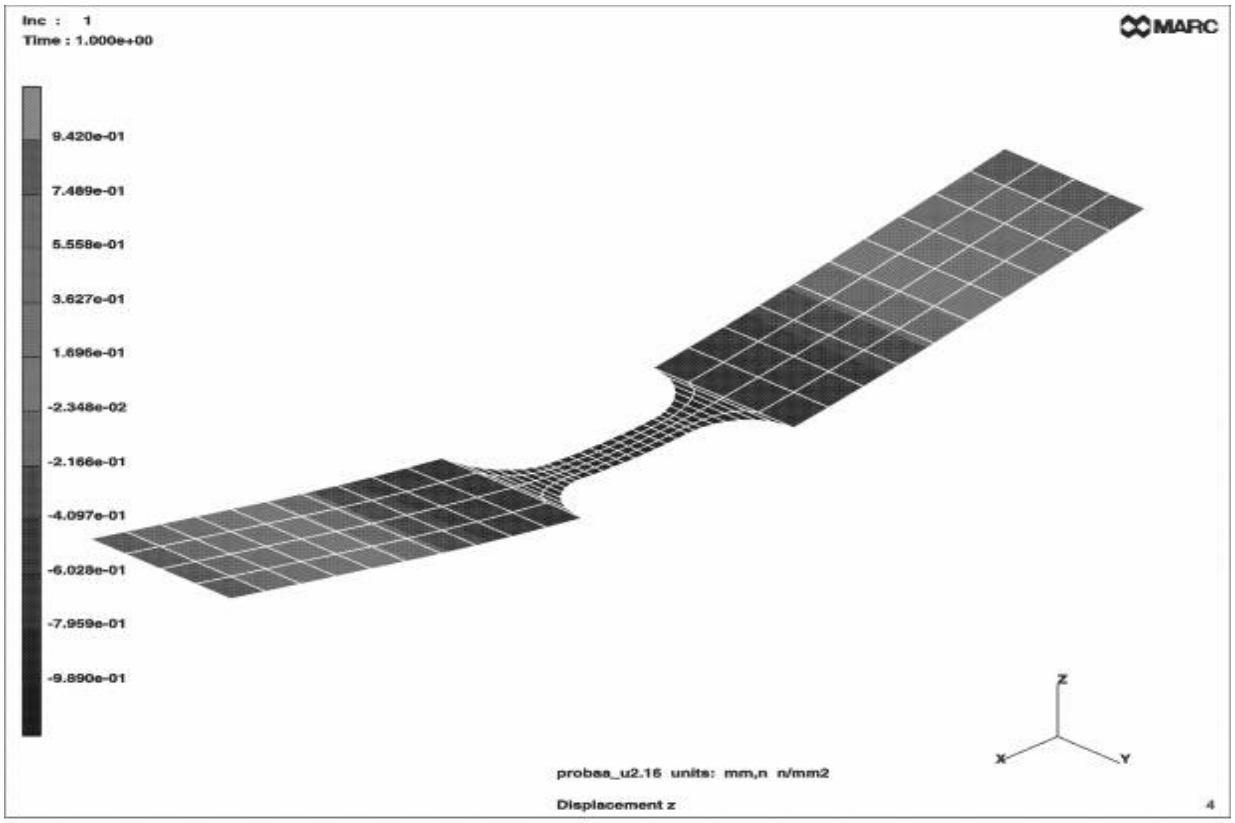

Figure 4.

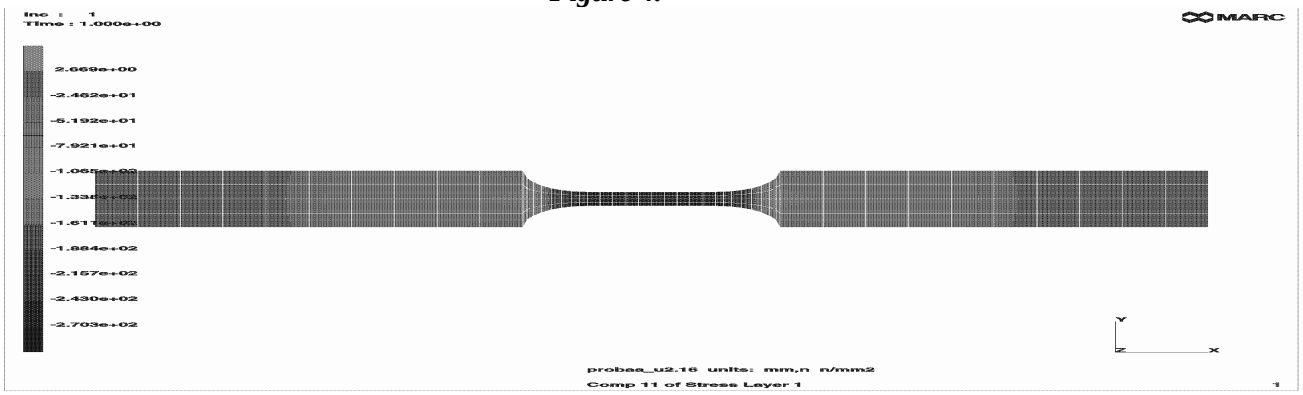

Figure 4a.

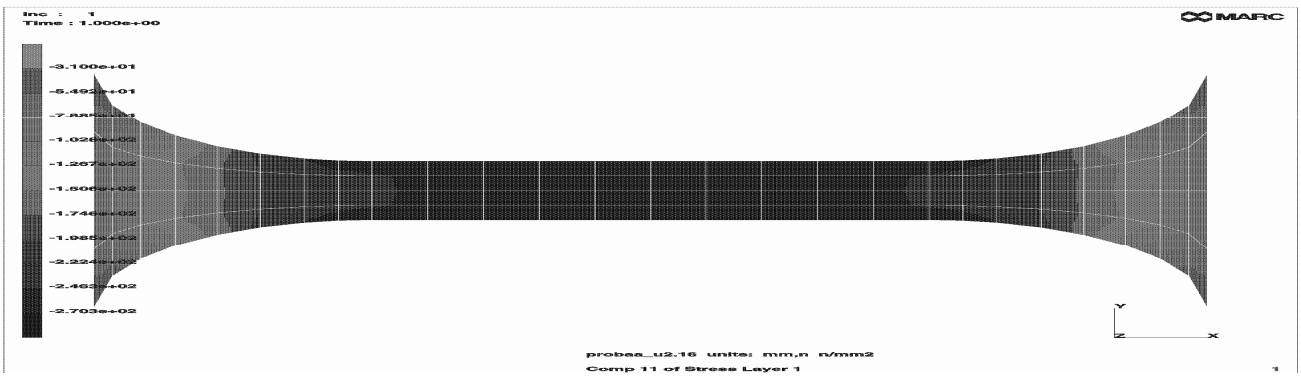

Figure 4b.

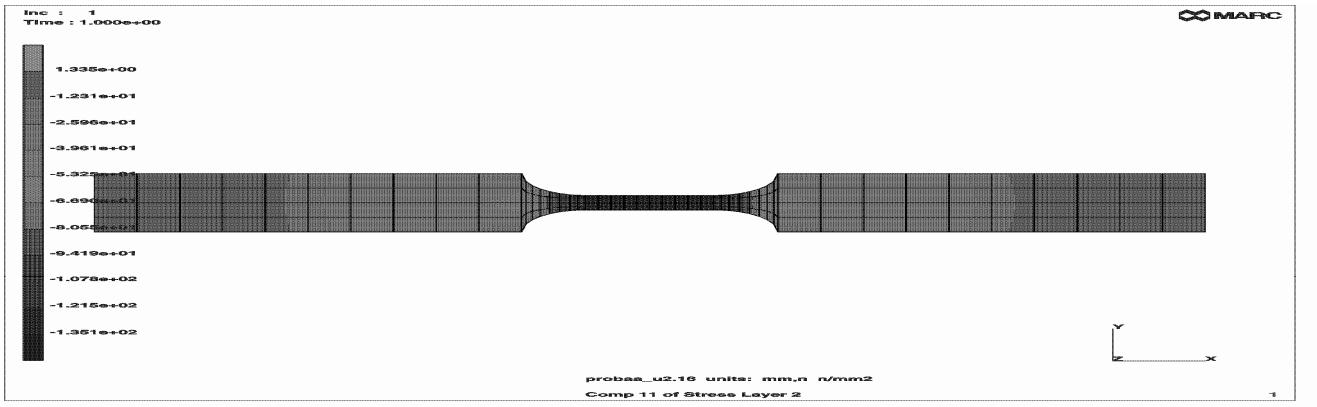

Figure 5a.

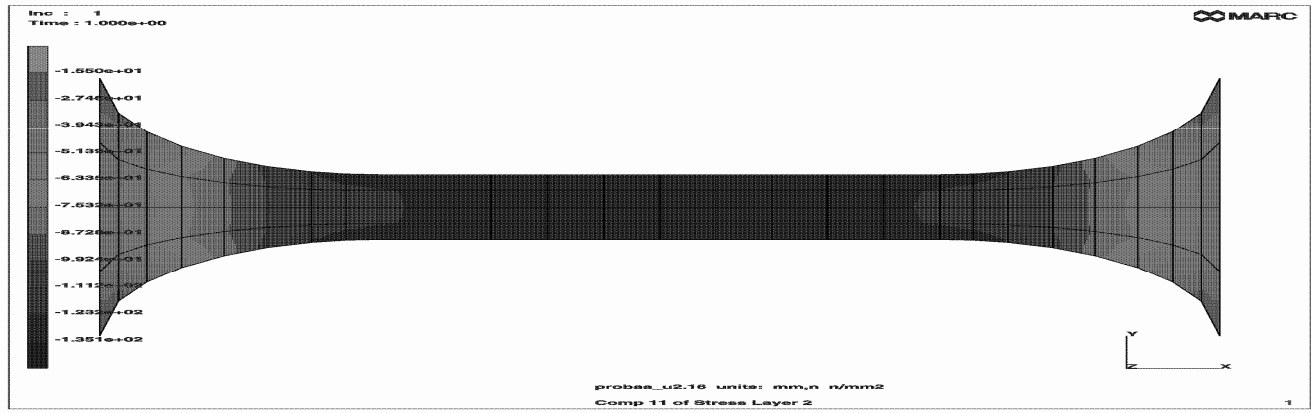

Figure 5b.

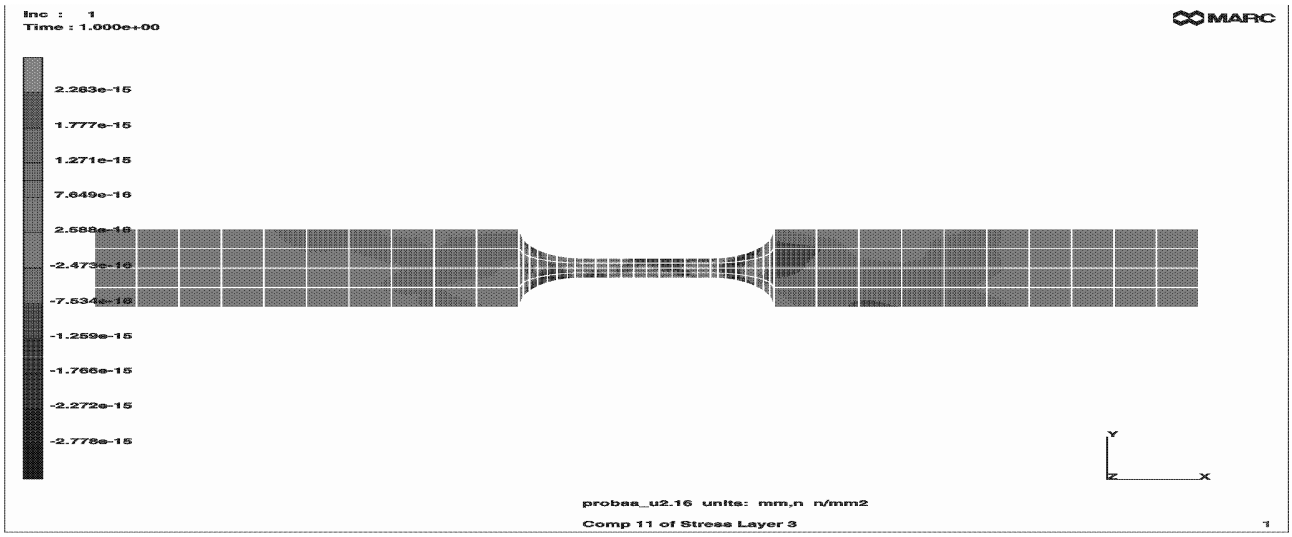

Figure 6a.

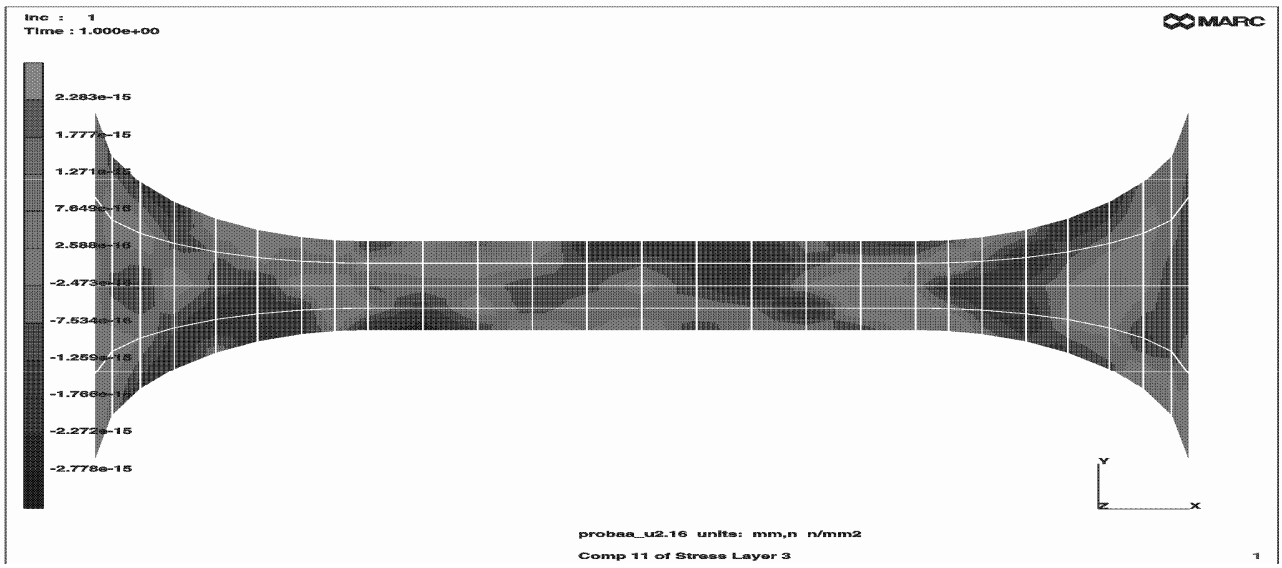

Figure 6b

Conclusions

From the analysis of figures 4-6 it can be seen in the area concerned that tensions are uniform over a stress layer while linearly varying across the layer thickness (the Navier model of tension distribution is complied with).

References

[1]. Karpenko, G.W, 1977, ***Maloţiklovaia ustalost' stali v rabocih sredah***, Izd. Naukova Dumka, Kiev, p. 5-105.

[2]. Crudu, I., Măcuţă, S., 1991, ***Maşina universală de încercat materiale***, Patent Machine 102714 / 1991.

[3]. Macuta, S., *Thesis Ph.d*., Univesity"Dunarea de Jos"of Galati, Galati, 1999.

[4]. Chesa, I., ***Alegerea şi utilizarea oţelurilor***, Ed. Tehnică, Bucureşti, 1977, p. 25-35.

[5]. Ştefănescu, I., Măcuţă, S., 1996, ***Materiale utilizate în construcţia instalaţiilor şi utilajelor specifice industriei alimentare şi frigorifice***. Tome I, University "Dunarea de Jos"of Galaţi, Galati, p. 40-65

[6]. C. Gheorghies, 1990, ***Control of fine structure of metal by X-rays***, Ed. Tehnica, Bucuresti p.128.

[7] *** ***User Manual for Marc-Mentat Analysis Research Corporation,*** California, USA, 1999.

THE ANNALS OF "DUNAREA DE JOS" UNIVERSITY OF GALATI.
FASCICLE IX. METALLURGY AND MATERIALS SCIENCE
N^0. 2 – 2008, ISSN 1453 – 083X

GLOW DISCHARGE OPTICAL EMISSION SPECTROMETRY (GDOES), AN EFFECTIVENESS METHOD FOR CHARACTERIZING COMPOSITION OF SURFACES AND COATINGS

Daniel MUNTEANU[1], Alexander SCHREINER[2]
[1]Transilvania University of Brasov, Romania
[2]Münchner Werkstofftechnik - Seminare, München, Germany
e-mail: muntean.d@unitbv.ro

ABSTRACT

Within the frame of this work, the technical procedures and real advantages of using Glow Discharge Optical Emission Spectroscopy (GDOES) for establishing depth concentration profiles of surfaces are presented. GDOES can detect low concentrations with high accuracy. It can be used for either quantitative bulk analysis (QBA) or quantitative depth profiling (QDP) in the nanometer to micron range. Non-conductive and conductive samples can be analysed.

The main applications of this spectral method are related to different technology fields such as: heat treatment processes, casting, heat and cold forming processes, thermochemical treatments, electro-chemical processes (galvanic coatings), chemical and physical vapour depositions (CVD, PVD), thermal oxidation processes and anodizing, thin-films and others.

KEYWORDS: ***glow-discharge, deep-profile composition, spectrometry***

1. Introduction

The increase of requirements for process control, quality assurance and documentation of product quality has led to an increased interest in the Glow Discharge Optical Emission Spectroscopy. Major organisations linked to the steel manufacturing industry, work for the establishment of an international standard for Zinc coating analysis by GDOES, where the technique is well established. The standard is currently being discussed in ISO TC 201, and in various European committees.

GDOES has various acronyms: GD-AES, GDOS, SDL, GDA, GDS. The GD source (or GD lamp) used in most commercially available GDOES instruments is based on the original design of the Grimm source. GDOES is an analysis technique used to determine the elemental composition of solids. A plasma is created by applying high voltage over an anode and cathode (the sample), thus igniting the argon gas in the analysis chamber. The argon gas is ionized and the ions are accelerated towards the sample, sputtering the sample surface. The sputters atoms from the sample are excited within the plasma to give optical radiation. Since each element has a unique radiation pattern and the intensity can be measured using photon detectors, the concentration of the elements can be determined by comparison to known standards.

Glow Discharge Analysis (GDA) made its first appearance in 1968 and was designed primarily for bulk spectrochemical analysis of various metals and their alloys. Since its introduction, this method has been steadily developed and has excelled in the areas of surface and coating analysis as well. Compared with conventional excitation techniques, the striking feature of Glow Discharge technology is the ability to discern defined surface layers in the material being examined. In the field of metal analysis the GDA is ideal for concentration profile analysis and surface analysis. All kinds of surface treatment processes as well as surface coating processes can be monitored by analyzing the surface and near-surface areas of the treated material. Coating thickness and chemical composition can be accurately measured using the technique of depth profile analysis. Glow Discharge Spectroscopy is the preferred method of analysis for materials that were previously impossible to analyze by traditional methods. Non-conductive materials and coatings such as glass, ceramics, varnish and paint layers can be analyzed using the optional Radio Frequency source.

Generally, the fields of application are: Heat treatment processes – in particular treatment of

ferrous and non-ferrous alloys, casting, heat and cold forming (forging, milling, drawing, deep-drawing) steel and non-ferrous alloys, electro-chemical (galvanic coatings), chemical and physical vapour-phase deposition (CVD, PVD), thermal oxidation processes and anodizing (anodizing process), thin-film technologies (ion implanting), thick-film technologies (plasma-powder polymer coatings).

- GD-OES is capable to analyse solid material with only little sample preparation;
- Due to the multi-matrix calibration GD-OES is a versatile tool for depth profiling on such materials;
- The analysis time is short compared to other depth profiling techniques;
- Low consumption of resources (Ar < 0.5 l/min);
- Easy operation of the equipment. The majority of the instruments are working in industrial labs or close to the production line.

2. Theoretical Background

In terms of GD-OES basic design, a hollow anode glow discharge chamber serves as the light source for the spectrometer. The two electrodes of the discharge cavity are designed as a tubular grounded copper tube and the flat sample to be analysed. In fact, the sample closes the discharge cavity: sample introduction is therefore extremely simple. The electrical power is supplied directly to sample. The spectrometer displayed here uses a concave grating in the Rowland circle or Paschen-Runge configuration and photo-multiplier tubes (PMT) for the light detection. The use of solid state detetectors, CCD's and photo diode array's have become a common alternative for PM Tubes. These detectors allow the acquisition of the entire spectrum, or at least a large portion of it, but are usually slower then PM Tubes and therefore not suitable for very short acquisition times used in thin film analysis. A schematic layout is given in figure 1.

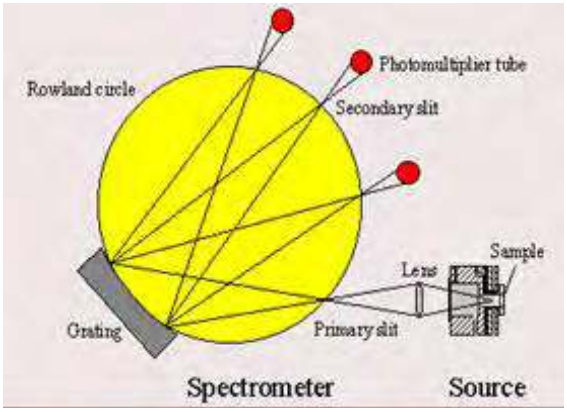

Fig. 1. The schematic layout of GD-OES design

After calibration, glow discharge optical emission spectroscopy can provide a quantitative depth profile (QDP) or compositional depth profile (CDP) of materials.

The glow discharge source (figure 2) is constructed by the so called Grimm type design with the sample acting as electrode and simultaneous sealing the source. The instrument can be equipped with anodes of 2.5 mm, 4 mm, and 8 mm inner diameter defining the size of sputter crater and the required sample surface.

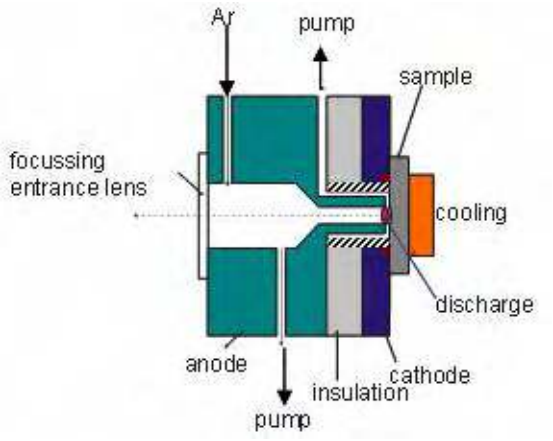

Fig. 2. The schematic layout of Glow Discharge Source (Grimm type)

Thus, the detector systems used in GD-OES could be: GD – PMT (High sensitivity / High speed), GD - CCD (High sensitivity / Channel flexibility), GD - PMT/CCD (High sensitivity, speed and flexibility).

3. Experiment

The paper presents some experimental data of GD-OES analytical possibilities. For the experimental program, a performing **GDA-750 Spectruma – Analytik Spectrometer** (manufactured by Spectruma – Analytik GmbH, Germany) was used.

With over 60 analytical element channels available, the GDA-750 Glow Discharge spectrometer is perfect for demanding applications requiring high resolution and analytical precision. Coatings can be analyzed down to a depth of 200µm, with a resolution of one atomic layer on the surface and 10% relative in deeper regions. The analytical software is powerful and flexible; chemical composition can be determined along with other characteristics such as density or mass distribution in the area of the layer being examined. Comparison of the surface characteristics before and after the technical coating process (CVD, PVD) ensures that the production process is being optimized and that

costly mistakes are avoided. The GDA 750 is also capable of bulk analysis (chemical composition of materials) providing superior linearity of calibration for complex matrices. Using the optional Radio Frequency Glow Discharge Lamp, the GDA 750 is proficient in analyzing non-conductive materials such as ceramics, glass and paint layers. GDA automation: automation of sample handling tuned to customer requirements (to/from conveyor belt-magazine-tipping pallet) by means of robotics is also possible. GDA 750 is used for the direct analysis of solids; two modes of operation are possible: Bulk mode (integrated intensities/conc), and DPA mode (time resolved intensities/conc). All elements of the periodic system detectable from 0,1ppm - 100% in a depth range: <10nm - >100µm.

In terms of GDA-750 RF excitation equipment, formerly, an impedance matching device ("matchbox") was used to adapt the plasma impedance to the output of the RF generator. At present, it will be replaced by the newly developed.

Spectruma RF generator. With this, instability of the RF power after switching on is reduced to a minimum. This makes possible the analysis of thin layers. Capacitors, which have to be adjusted according to the plasma impedance and which often have caused a second analysis, are no longer present.

The optical detection system is designed as a polychromator based on the Paschen-Runge mount.

The polychromator is equipped with a 2400 grooves/mm master grating with a focal length of 750 mm offering a resolution of 20 pm. Up to 64 emission lines can be detected with selected PM Tubes (PMT). The polychromator vessel is evacuated to extent the spectral range into the deep VUV region allowing the observation of wavelength down to 120 nm. Elements of interest like Nitrogen, Carbon, Sulphur and Phosphorous are easily detected using their most sensitive first order spectral lines. A set of CCD detectors can be added covering the spectral range from 200 nm to 800 nm. Another option is a monochromator with a spectral range of 200 nm to 730 nm. This adds flexibility in the choice of elements to be analyzed and spectral lines to be used without technical changes.

4. Results

For the beginning is given an example of an Aluminum clad material.

Usually this material is used in the automotive industry for radiator tubes, condenser tubes etc.

The defining characteristic of this type of product is that the material is actually two different aluminum alloys bonded together in the manufacturing process by heat and pressure.

This creates a multi-layer system, which at first glance may seem to be one solid piece.

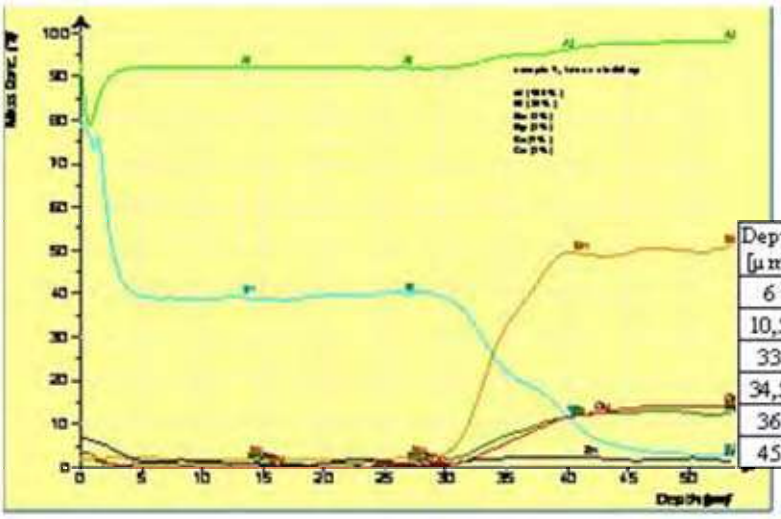

Depth [µm]	Al [%]	Si [%]	Mg [%]	Mn [%]	Zn [%]	Cu [%]
6	92,1	7,846	0,016	0,042	0,014	0,002
10,5	92,16	7,736	0,014	0,041	0,015	0,001
33	93,97	6,677	0,072	0,253	0,016	0,043
34,5	94,72	5,336	0,115	0,487	0,019	0,08
36	95,02	4,331	0,15	0,666	0,021	0,116
45	97,51	0,968	0,248	0,976	0,017	0,265

***Fig. 3.** Aluminum cladding GD-OES analysis results*

Producers of this material must control not only the thickness of the clad, but also the possibility for surface or clad contamination coming from elements migrating from the core to the outer layers. The clad material analysed in Figure 3 consists of a 4043 aluminum alloy bonded to the core material, which is a 3005 alloy type. The thickness of the clad material is 30 microns as seen by the graph and the following data table (figure 3). Secondly, it is presented an example of analysis of zinc coatings. This analysis gives the possibility to know integration of the Zn-concentration or total concentrations versus depth

delivers the coating weight and to control the important elements in the coating like Al, Pb (figure 4). Figure 5 presents the results of GD-OES analysis in the case of a thin - film, CrNiAl type, deposited on a super-alloy used for turbine blade manufacturing.

Figure 6 presents a wire spectral analysis, using an USU adaptor for wires, which offers an easy sample exchange, a defined sample position and is flexible in sample diameter. Next figure (7) shows the analysis results for a semiconductor layer (GaN) on a saphir base containing a Mg enriched zone of some nm. The maximum Mg-concentration is 250ppm.

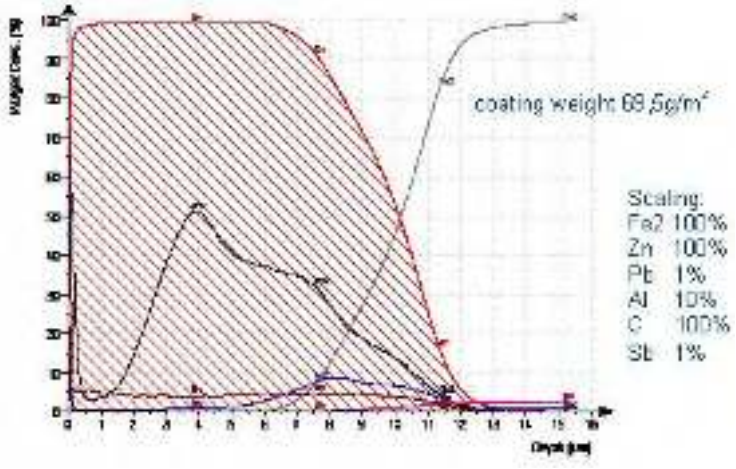

Fig. 4. Zn coating GD-OES analysis results (including the coating weight)

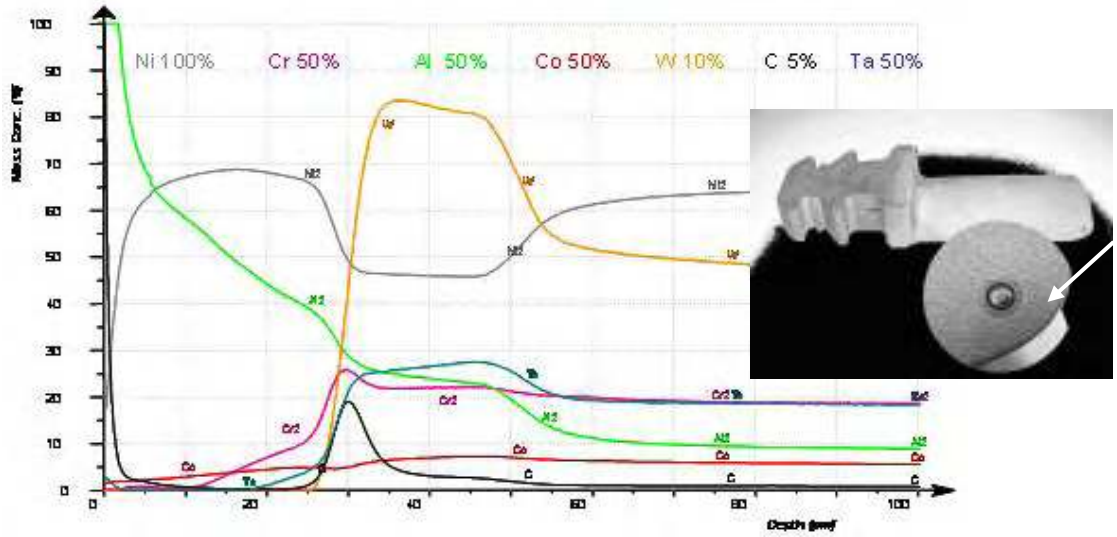

Fig. 5. CrNiAl thin-film GD-OES analysis results (substrate-turbine blade)

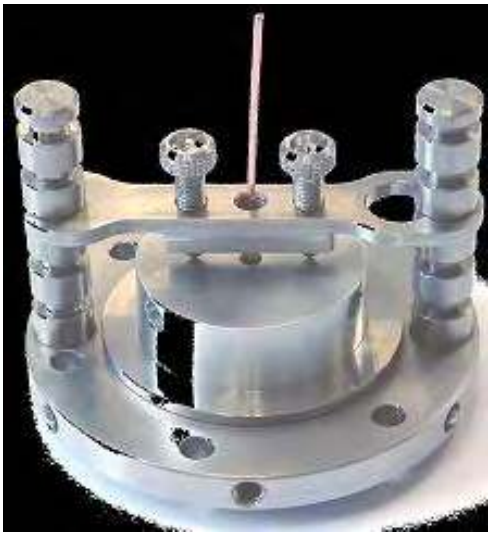

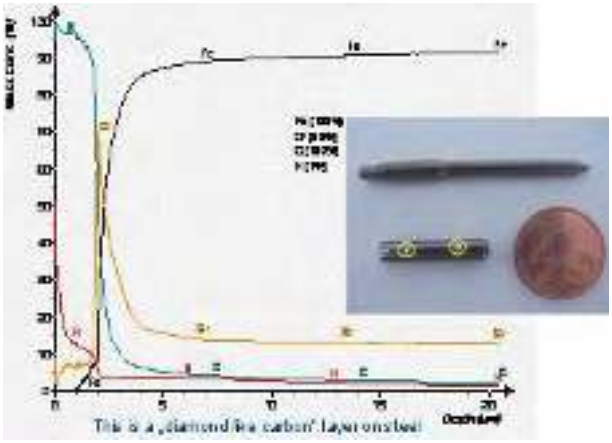

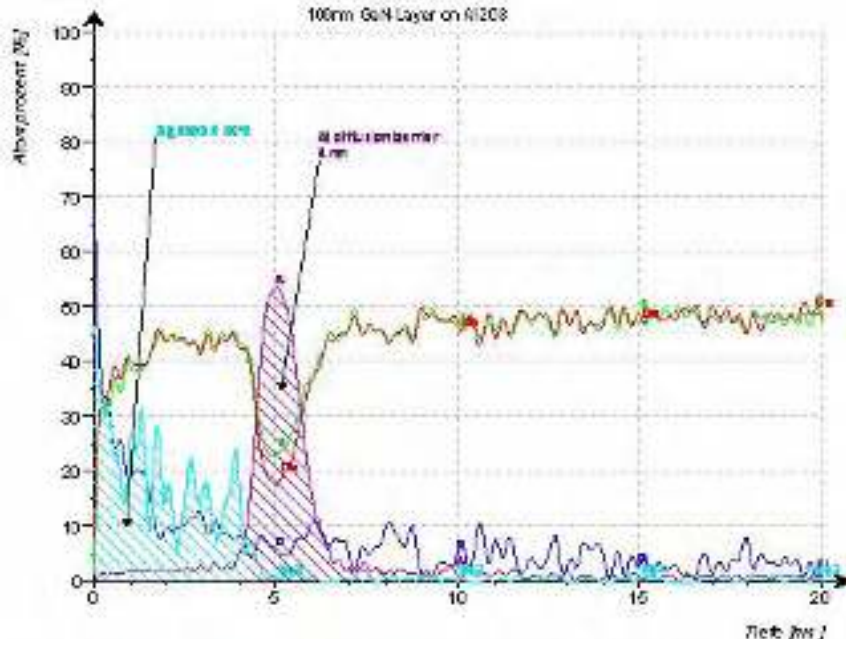

Fig. 7. GD-OES analysis of a GaN semiconductor layer

Table 1. Comparative economical analysis on different spectral techniques

Instrument	Estimative acquisition cost	Costs for consumables /month	Manpower
GDOES	130.000,-€	approx.150,-€	Laboratory assistant / engineer
REM/EDX	250.000,-€	approx.250,-€	Laboratory assistant / engineer
AUGER	500.000,-€	approx.3.000,-€	Engineer /doctor´s degree
SIMS	500.000,-€	approx.3.000,-€	Engineer /doctor´s degree
ESCA	500.000,-€	approx.3.000,-€	Engineer /doctor´s degree

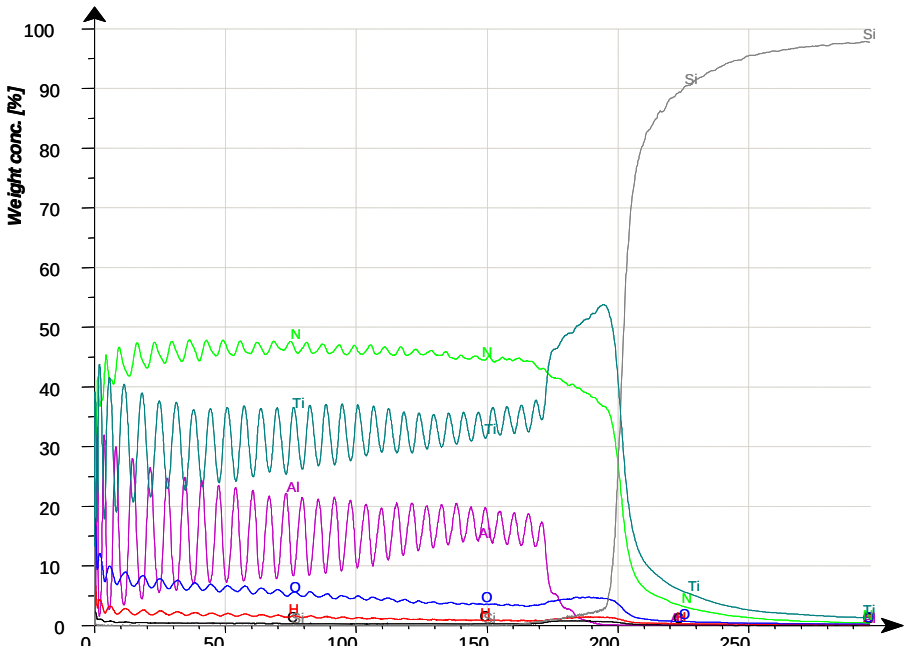

Fig. 8. The RF GD-OES TiN/TiAlN/.../TiAlN/TiN/Si thin - film

Referring on the RF-GDOES analytical possibilities, figure 8 presents the depth concentration profiles of a succession of 60 layers, TiN/TiAlN/.../TiAlN/TiN/Si types, with approx. 3nm per layer.

In terms of prices, sustenance costs, consumables and the necessary manpower, table 1 presents a comparative analysis.

5. Conclusions

In the field of metal analysis, the GDA is ideal for concentration profile analysis and surface analysis. All kinds of surface treatment processes as well as surface coating processes can be monitored by analyzing the surface and near-surface areas of the treated material. Coating thickness and chemical composition can be accurately measured using the technique of depth profile analysis.

Glow Discharge Spectroscopy is the preferred method of analysis for materials that were previously impossible to analyze by traditional methods. Non-conductive materials and coatings such as glass, ceramics, varnish and paint layers can be analyzed using the optional Radio Frequency source (GDA 750 spectrometer – Spectruma Analytik GmbH).

References

[1]. Spectruma Analytic GmbH Catalog 2007, Fabrikzeile 21, D – 95028 Hof Germany.

[2]. Munteanu, D., 2002, ***Ph.D. Thesis,*** Transilvania University of Brasov,

[3]. Munteanu, D., Munteanu, A., 2001, ***Proceedings of International Conference on Materials Science and Engineering***, Bramat Section – Materials Science.

[4]. ***Glow discharge spectroscopies***, 1995, edited by R.K. Marcus-Clemson, University-Plenum Press, N.Y and London.

THE ANNALS OF "DUNAREA DE JOS" UNIVERSITY OF GALATI.
FASCICLE IX. METALLURGY AND MATERIALS SCIENCE
N^0. 2 – 2008, ISSN 1453 – 083X

MECHANO-EROSION: A NOVEL TEST METHODOLOGY TO ACCELERATE EROSION IN ROLLING CONTACT FATIGUE EXPERIMENTS

Balamurugan KARUNAMURTHY, Mark HADFIELD
Tribology and Sustainable Design Research Centre, School of Design, Engineering and Computing,
Bournemouth University, Poole House 238, Bournemouth BH12 5BB, UK
e-mail: bkarunamurthy@bournemouth.ac.uk

ABSTRACT

Rolling contact fatigue testing of rolling elements with low saturation temperature lubricants result, in several difficulties. Mainly, uncontrolled phase changes due to flow dynamics often cause difficulties in assessing the lubricant effect on fatigue life. This work simulates these conditions for testing in a controlled environment to understand the mechanism of material wear. A rotary tribometer was modified to allow an ultrasonic transducer. This modification made it possible to bring the two different phenomena Rolling contact fatigue and Erosion together. With this novel testing method, erosion was created on the contact track within a short period of time. Moreover, Erosion characteristics and its effects on rolling contact fatigue testing were monitored and these preliminary results are presented in this paper.

KEYWORDS: Rolling contact fatigue, Rotary tribometer, Ultrasonic transducer, Erosion, Lubrication.

1. Introduction

Hybrid bearings made of silicon nitride rolling elements with steel races have shown several advantages over all steel bearings [1, 2, 3]. Particularly in refrigeration and air-conditioning units, the ability to run in working fluid eliminates the necessity for a separate oil lubrication system and offer many advantages [9, 11]. This concept of oil-free lubrication opened up huge potential applications in compressors and pumps used in refrigeration and air-conditioning units, high speed and light weight turbo pumps used in space applications. In employing refrigerant as pure lubricant, careful measures are made to ensure that the refrigerant stays in the liquid state for lubrication purposes. However, phase changes due to pressure variations at high speeds cannot be avoided which result in cavitation, a primary concern for material wear in this area of oil-free lubrication. Also, due to high speeds and loads rolling contact fatigue plays a part in material damage along with cavitation. Wear characteristics in this application is not clearly understood. Any further advancement in this field largely depends on understanding this wear mechanism which limits the bearing speed and life. Wear of mechanical systems with refrigerants and Rolling contact fatigue testing of these materials in refrigerant lubrication was reported [4, 10]. The gas/liquid phase transition has a significant influence on the wear mechanisms of traditional lubricants and need to be investigated [4]. Hence a controlled level of gas/liquid phase in lubricant whilst testing is necessary to perform this study. Rolling contact test machines alone are not suitable to perform this testing. A new test machine or an available test machine should be modified for this task. This work presents a novel test methodology to address this issue by modifying a rotary tribometer.

2. Testing methodology

A rotary tribometer and an ultrasonic vibratory system are utilized for this testing. Different types of rolling contact fatigue test machines are used to study material wear and lubrication characteristics in rolling contact. These are (1) Four-ball machine, (2) Five-ball machine, (3) Ball-on-rod machine, (4) Ball-on-plate machine, (5) Disc-on-rod machine and (6) Contacting ring machine. The major difference between these test machines are the contact geometry and loading configuration of test materials. Laboratory cavitation erosion experiments can be broadly divided into hydrodynamic and acoustic cavitation. Acoustic cavitation is a process of creating cavitation by applying high intensity ultrasound to liquids. This is advantageous over hydrodynamic method, with a small test rig size, consumes less

power and creates erosion in a short duration of test time. Acoustic cavitation uses either a piezoelectric or magnetostrictive transducer.

2.1. Ultrasonic vibratory system

This work utilizes a commercially available ultrasonic vibratory system, which has an ultrasonic generator and a piezoelectric transducer as main components. This high power intensity system can generate acoustic power in the order of 400 -600 watts. This piezoelectric transducer end is coupled with a horn by a screw. The purpose of the horn is to amplify the vibration generated by the transducer. The transducer-horn assembly design is a stepped structure and is made of titanium alloy to provide superior resistance to cavitation.

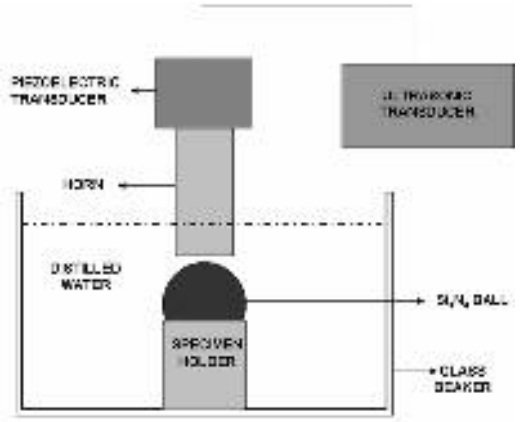

Fig.1. Cavitation erosion test setup

This system operates at a fixed frequency of 20 KHz. Amplitude of vibration of the horn can be adjusted from 0 – 60 μm peak-to-peak and continuously monitored during the tests. The horn design was carefully selected to couple with the test chamber of the rotary tribometer.

A horn diameter of 5 mm and the total length of the transducer horn assembly of 95 mm are selected for this purpose. Initially, cavitation erosion experiments on silicon nitride are conducted to test this system and also for later comparison to the results obtained from the new testing methodology. Fig.1 shows the schematic of cavitation erosion test setup. These experiments were conducted in distilled water.

Commercially available silicon nitride rolling elements were used as test materials. A low form beaker was used as testing system with distilled water in it. This test method was carried out in accordance with the ASTM standard [14]. Test specimens are generally machined to a threaded form which is then attached to the horn tip. For materials with machining difficulties, stationary specimen approach is used.

This approach allows holding the test specimen stationary in a holder close to the transducer horn. Because it is difficult to machine a silicon nitride ball, the stationary specimen approach was selected for this testing. Before testing, test specimens were visually examined using a light microscope to make sure they were free from any surface defects. The distance between the horn tip and the test specimen was determined by a feeler gauge. The piezoelectric transducer was excited at full power and a magnitude of vibration of 60 microns. Erosion initiation was noted in a very short duration of time of three minutes. These initial stages showed surface roughening, which accelerated the rate of material removal. Tests were continued for a maximum duration of 30 minutes and severe erosion was observed as shown in fig. 2 and 3. Material removal was largely due to the formation of pits resulting from grain pull outs. In later stages, pits joined together and appeared to be larger ones. This resulted in huge loss of material. These experiments are vital for understanding the erosion behaviour in the new test method. Moreover, this erosion test system was satisfactory to be utilized for this study.

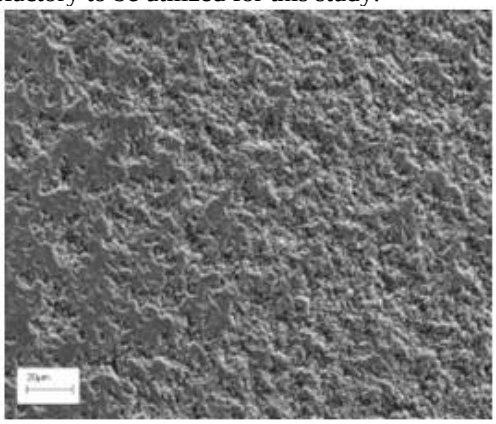

Fig.2. SEM image of eroded surface

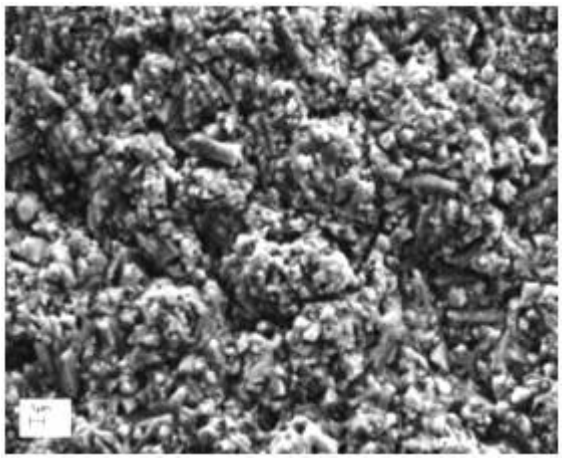

Fig.3. High magnification of erosion

2.2. Mechano-Erosion testing

The four-ball machine presented in this paper is a TE92 Microprocessor Controlled Rotary Tribometer. Advanced control and instrumentation in this machine makes it possible to conduct tests in a wide range of speeds and loads. The test chamber consists of a steel cup, oil bath, lower balls, and an upper ball for applying load and transferring motion effectively as shown in fig.4. The cup, lower three balls and the upper ball represents the outer, rolling elements and inner race of a bearing respectively. This test chamber simulates an angular contact ball bearing configuration.

This test machine is very useful for rolling contact fatigue study of materials under different conditions [5-7, 12–13] and hence selected for this work.

The upper ball is fixed to a drive spindle and its accurate positing is achieved by two rigid vertical columns of the machine. Load is applied by a pneumatic actuator; this actuator assembly includes an in-line force transducer to get the direct feedback control. Direct friction and torque measurements are also possible by a strain gauge transducer attached to the test adapters, which are mounted on a cross beam, guided by linear bearings on the machine columns. Tests can be conducted at high temperatures up to 200 ^{0}C which is continuously monitored by a thermocouple attached to the test chamber. A computer connected to the machine, provides a graphical user interface to run, control and record tests. A test is a set of series of steps, each with load, speed and temperature, data recording and alarm information. In order to combine erosion testing to this rotary tribometer, the four ball machine test chamber had to be modified. The best way to achieve this is to include the erosion setup in the test chamber as shown in fig 4. From the erosion bench testing, it was found that the rate of erosion was proportional to the distance between the transducer horn and the sample. The closer the horn tip to the test specimen would increase the erosion rate and therefore reduce the test time.

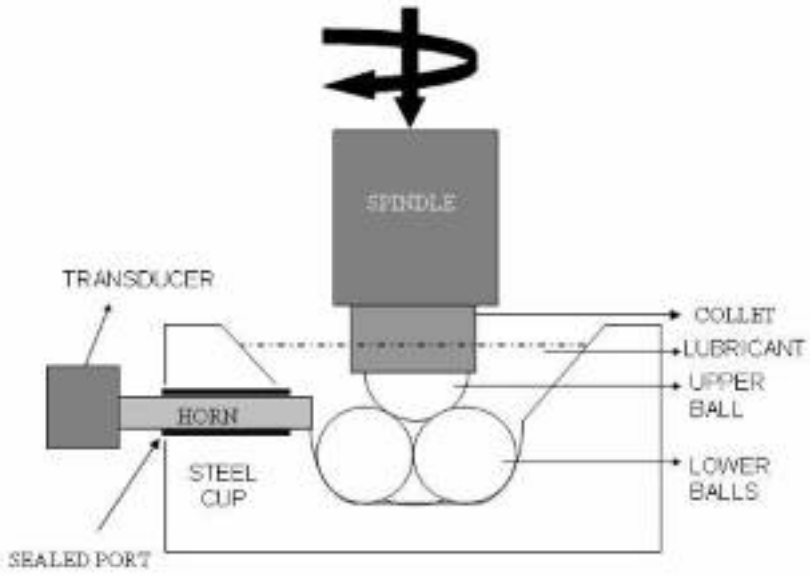

Fig. 4. Schematic of Mechano-erosion test configuration

A port had to be designed and made in the steel test cup to fix the piezoelectric transducer. The location of the port was carefully designed to allow the horn tip to be held close to the rolling elements and ensured no disturbance to their dynamics by contact. A high carbide drill bit was used to create the port of 6 mm diameter on the steel cup. Major challenge rose when a proper sealant had to be found to seal the transducer in the port. The purposes of the sealant are as follows:

1. To hold the piezoelectric transducer in the test chamber
2. To seal off the port to prevent any lubrication leakage
3. To allow the transducer horn to vibrate freely without constraining, and thereby eliminating any heat generation due to sliding contact.

This eliminates the possibility of using any mechanical seals. A high temperature adhesive sealant was selected for this purpose. The female part or the port on the steel cup was filled with this sealant and was allowed to set for a time period of 24 hrs. The centre point of the port was carefully marked and a hole of 4 mm was drilled. This helped the piezoelectric transducer to fit tight enough into the port as shown in fig. 4. The distance between horn tip and the rolling elements was fixed for all tests. One other important design alteration was to create a

support for the piezoelectric transducer in the rotary tribometer. This is because when testing starts, the two rigid vertical columns guide the test chamber to move vertically upwards to apply load and rotation by the drive spindle. When test specimen fails eventually, the test chamber moves back to its initial position. Any external support to hold the transducer in the test chamber would cause damage to the transducer and break the sealing during this test cycle. An aluminium block with a conical cut at the middle was clamped with the tribometer test chamber beam. This conical cut ensured a safe design to fix the transducer, and moreover this whole setup can be moved horizontally giving more freedom for increasing or decreasing the distance between the horn tip and the rolling elements. Test chamber was cleaned with acetone before each test to ensure no debris presence to avoid any abrasion. For preliminary tests, a low viscosity paraffinic hydrocarbon lubricant was used mainly to increase the erosion rate. These tests were carried out at different speeds and loads as shown in the table 1. Tests were run for a specified duration of time to understand the erosive wear progression at different stages of material wear under this condition. All the test samples were smooth silicon nitride balls of 12.67 mm diameter. A forced air cooling system was employed to cool the transducer horn. After each test, samples were cleaned in acetone for 20 minutes in an ultrasonic bath and then dried using a dryer before set for surface analysis. A light and a scanning electron microscope were utilized for this purpose.

4. Preliminary results and discussion

For testing, the piezoelectric transducer was inserted in the test chamber of the high speed tribometer as mentioned in the testing method. The test specimen, silicon nitride smooth ball was held by means of a collet in the drive spindle. The average surface roughness of the test specimens was 0.01 um. For hybrid contacts, lower balls of carbon chromium steel was used, which are of same diameter of the test specimen. Hardness of silicon nitride and lower balls was 1650 and 840 Hv. The transducer was excited at the maximum power, and amplitude of 60 µm peak-to- peak.

Table 1 Preliminary experiments test programme

Test	Contact stress (GPa)	Shaft speed (Rpm)	Lubricant 2.4 mm^2/s at 40^{0}C	Vibration Amplitude (µm)	Stress cycles	Test time (Hrs)
A	3	2000	Macron 110	60	2.53 x 10^5	2
B	3	3000	Macron 110	60	7.63 x 10^5	4
C	5.1	2000	Macron 110	60	5.07 x 10^5	4
D	5.1	5000	Macron 110	60	1.17 x 10^6	4
E	5.1	5000	Macron 110	60	1.76 x 10^6	6

3.1 Surface Analysis

Results obtained from these tests are promising. Erosion was formed on the contact track in a short duration of time of 30 minutes at a speed of 5000 rpm. Rolling contact fatigue testing for few hours under similar loads and speeds with same lubricant was also examined.

No sign of material damage was noticed.

A light microscope image of the contact track with erosion pits is shown in fig 5.

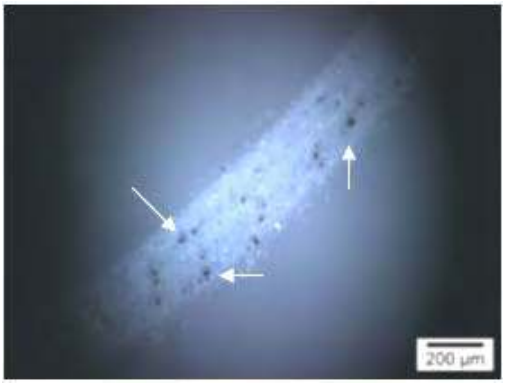

Fig.5. Light Microscope image of the ball showing erosion pits on track.

This is test A, with a maximum contact pressure of 3 GPa and with the spindle speed of 2000 rpm. Apart from the tiny pits, few number of large erosion pits were noted on this test specimen. The surface away from the contact track remained smooth as before the test. This is very much evident that both cavitation erosion and rolling contact fatigue played a role in material wear process under this testing condition.

The initial stage of material wear showed increase in surface roughness on the contact track, which became the primary factor for erosion acceleration. As the roughness of the test balls increased during the course of testing, it formed a more favourable condition for bubble nucleation. This helped in rapid cavity growth and collapse; this violent collapse increased the erosion rate. This initial stage was then followed by formation of tiny erosion pits. These pits were formed by removal of material which was encapsulated by a weakened boundary due to erosion as shown in fig 6. This was observed in the test B. Because of rolling with contact stresses these pits appeared with a unique geometry in a crescent shape as in fig 7. This is of test C with a maximum contact pressure of 5.1GPa and a spindle speed of 2000 rpm.

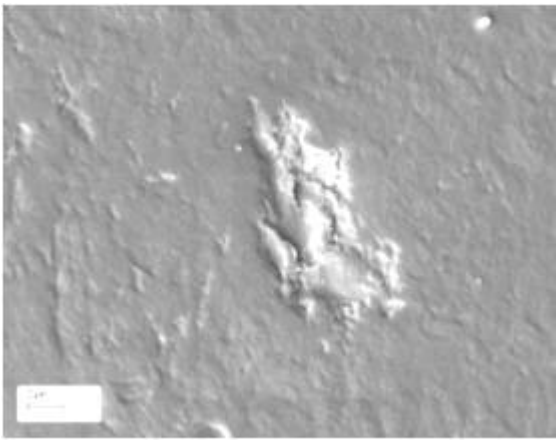

Fig.6. Erosion pit initiation from roughened surface

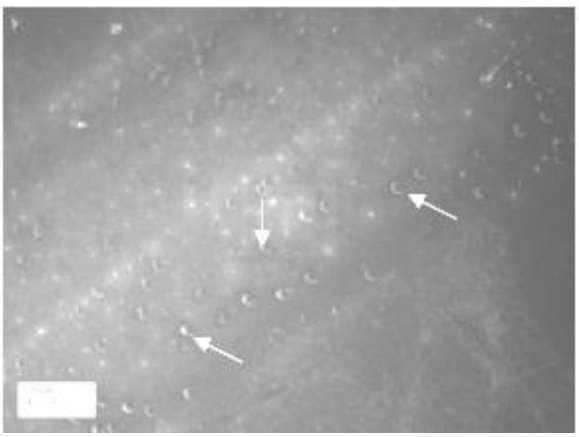

Fig.7. Crescent shaped erosion pits

These crescent shaped pits enlarged further by opening up their mouth during the course of wear process, which is shown in fig 8. This part of the wear needs further investigation.

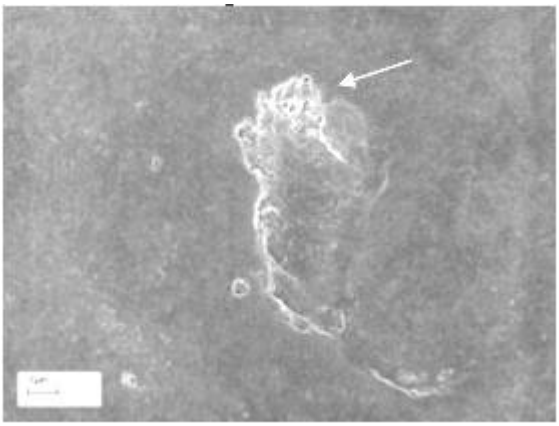

Fig.8. Close up of crescent pit showing mouth opening

When both load and speed were increased as in test D, a maximum contact pressure of 5.1 GPa and 5000 rpm. Erosion pits showed clear directionality in their growth and were joined together with the adjacent pits in a process called pit bridging as shown in fig 9.

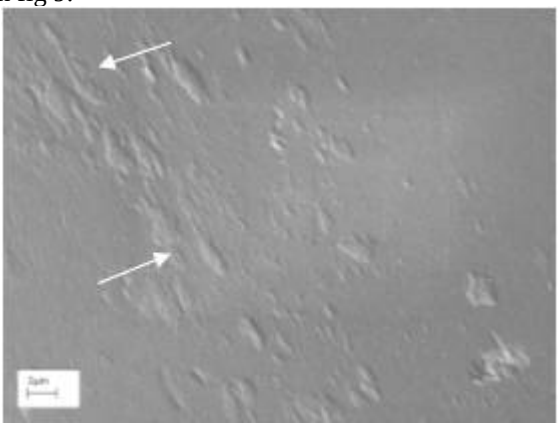

Fig.9. Directionality of erosion pit growth

The closer look of an erosion pit is shown in fig 10 which was from the same test D. Almost all erosion pits appeared in the similar shape and size. Erosion pits didn't grow deeper, because of lubricant squeezing into the pits and acting as a cushion for any further cavity collapse. This will also retard the rate of erosion, but will result in a minimum loss of material as the process continues. The final stages of this wear process ended up with the signs of more erosion on the contact track. As more pits formation leads to a dense area of pits on the track, the test specimen will eventually fail due to spalling. Test E

with more test time of 6 hrs at a maximum contact pressure of 5.1 GPa and a spindle speed of 5000 rpm resulted in enormous density of erosion pits and is shown in fig. 11.

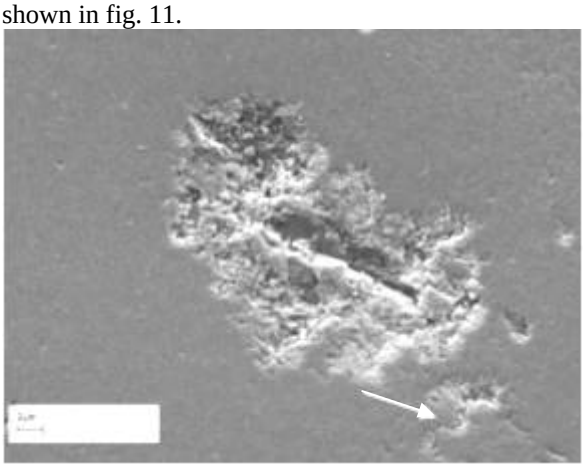

Fig.10. Large erosion pit surrounded by tiny pits bridging

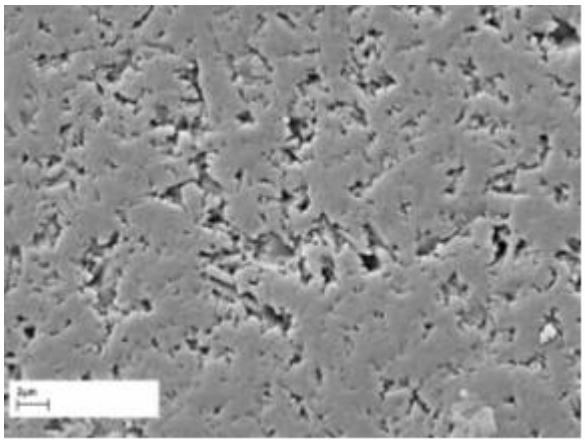

Fig.11. Final stage of wear – showing high concentration of erosion pits on track

Most of the tests conducted were Ceramic balls with steel contacts, that is upper ball was silicon nitride and the lower three balls were steel. Ceramic to ceramic contact was also investigated for initial study. The rate of material removal was found to be faster in ceramic to ceramic contact than steel contact. This is mainly because of bearing steel provides high resistant to erosion compared to ceramics.

4. Conclusions

The primary aim of this work is to accelerate erosion in rolling contact experiments, which was achieved using this test methodology. Modifications made to a rotary tribometer were successful in controlling the level of turbulence or pressure drop in the lubricating medium. The preliminary results obtained from this testing were presented. Erosion was created on the contact track and was monitored at different stages to understand the wear mechanism. Increase in contact stresses resulted in crescent shaped pits, which were not noted at low loads. Furthermore, at high loads, pit growth was dominated by widening than deepening. Due to increase in the number of stress cycles corresponding to higher spindle speeds, pits concentration were higher than at low speeds of 2000 rpm. Laboratory testing of material wear which involves both erosion and rolling contact fatigue can be studied using this test method. The liquid/gas phase changes and its influence on the wear mechanism are important and often considered to be difficult for experimental study. This work addressed this problem by presenting a novel testing methodology.

Acknowledgements

The authors would like to thank SKF Engineering and Research Centre, The Netherlands for financial support to carry out this work and permitting to publish this paper.

References

[1]. Aramaki et.al, 1988, ***The performance of ball bearings with silicon nitride ceramic balls in high speed spindles for machine tools***, Journal of Tribology, 110: 693-698.

[2]. **Bhusan, B.,** 2002, ***Introduction to tribology***, Columbus: John Willey & Sons Inc,.

[3]. Bhusan B and Sibley L.B., 1981, ***Silicon nitride rolling bearings for extreme operating conditions***, ASLE Transactions, Vol.25(4), p. 417-428.

[4]. **Cinatar, C.,** 2001, ***Sustainable development of mechanical systems using replacement environmentally acceptable refrigerants***, PhD thesis, Bournemouth University, UK.

[5]. Hadfield M., 1998, ***Failure of silicon nitride rolling elements with ring crack defects***. Ceram Int, Vol 24 (5), pp. 379-386.

[6]. Hadfield M, Stolarski TA, et al., 1993, ***Failure modes of ceramics in rolling contact***, Proceedings: Mathematical and Physical Sciences, R Soc, Lond, Vol 443 (1919), pp. 607-621.

[7]. Hadfield M, Stolarski TA, et al., 1993, ***Failure modes of ceramic elements with ring-crack defects***. Tribol Int, Vol 26:157–64.

[8]. Hamburg G, C.P.a.V.R., 1981, ***Operation of an all-ceramic mainshaft roller bearing*** in J-402 gas turbine engine. J ASME, Lubrication Engineering, Vol 37(7), pp. 407-415.

[9]. Hans H Wallin, G.M.E., 2002., ***Hybrid bearings in oil-free air conditioning and refrigeration compressors***, in SKF Evolution magazine, pp. 28-30.

[10]. Khan, Z.A., 2006, ***Rolling contact wear of hybrid ceramic bearings with refrigerant lubrication***, PhD thesis, Bournemouth University, UK.

[11]. SKF, USA., 2003, ***New Hybrid bearings enable maximum pump performance with minimum lubrication***, in Worldpumps, issue 441, pp. 37-39.

[12]. Scott D, Blackwell J., 1973, ***Hot pressed silicon nitride as a rolling bearing material – a preliminary assessment***. Wear, Vol 24 (1), pp.61-67.

[13]. Scott D, Blackwell J, et al., 1971, ***Silicon nitride as a rolling bearing material – a preliminary assessment***, Wear, Vol 17(1) 73–82.

[14]. Standard method of vibratory cavitation erosion test. ASTM G32–85, pp. 116–121.

THE ANNALS OF "DUNAREA DE JOS" UNIVERSITY OF GALATI.
FASCICLE IX. METALLURGY AND MATERIALS SCIENCE
N^0. 2 – 2008, ISSN 1453 – 083X

NANOSTRUCTURED SURFACE FOR 38MoCrAl09 STEEL BY NITRIDING IN NITROGEN ATMOSPHERE AND YAG:Nd PULSE LASER ACTIVATION

Nelu CAZACU[1], Cătălin PINTILIE[2], Sorin DOBROVICI[1], Adolf BACLEA[3]

[1]Dept.of Metallurgy and Materials Science, Dunărea de Jos University of Galaţi, Romania,
[2]S.C. Trefo S.A. Galaţi, Romania,
[3]Socomar SRL, Sorento, Italy
e-mail: Nelu.Cazacu@ugal.ro, Sorin.Dobrovici@ugal.ro

ABSTRACT

YAG:Nd pulse laser is usually used for cutting and welding. The paper is based by experiments using YAG:Nd pulse laser (KVANT 17-CIS made). Technological modules were assembled for laser beam deviation and for relative sample moving to manual controlled focused laser beam. In experiments was used a personal computer with adequate program for x-y sample moving (stepper system) and correlation with laser pulse. Steel sample (nitralloy steel) was fixed in nitriding chamber in a nitrogen flow. Defocused, laser beam energy and nitrogen pressure were modified. Hardness (HV5), macrostructure and microstructure were used for surface properties investigations.

KEYWORDS***: pulse laser, YAG:Nd, nitriding, steel***

1. Introduction

Thermo chemical treatment is based an surface chemical compositions changes under specific thermodynamic conditions only for surface layer. A duplex treatment CVD and diffusion are usually used for increasing surface concentration with one or more alloying elements. Processes activation (CVD and diffusion) are energetically made. Heating in a chemical active media is a common procedure. Laser radiation interaction with surface is a complex process in that thermal effect is important. Usual laser applications are based on intense thermal effect characterised by higher heating speed and lower heated surface. Laser cutting and welding describe these local and intense energetic interactions. This interaction may be converted in large surface interactions through additive procedure that represents a successive and relative moving of laser beam over material surface.

2. Experimental conditions

Nitriding experiments were based on KVANT 17 YAG:Nd pulse laser (CIS designed for cutting in oxygen plasma and point to point welding). Some important characteristics are: two units with solid dopped glass YAG:Nd (6.3 mm diameter, 100 mm long), homogeneus and heterogeneous metallic cutting up to 0.8 mm thickness, total power 12kW, double cooling system, 0...1000V voltage for optical pumping system, variable pulse frequency system, max. 0.5% pulse to pulse energy difference, interactions trace 0. 2...1.2 mm, circular deviations on trace max. 20%, inert gas (Ar, He) adding system, efficiency 2...5%. Laser energy was controlled by dc suply voltage in range 0...1000 V. An additional technological module (Fig. 1) was manufactured for x-y sample moving in range 20x20 mm and total interaction surface 400 mm^2. For KVANT 17 YAG:Nd pulse laser different pulse regime is valuable: variable frequency (fixed preset values), giant pulse and external command pulse. The technological unit was designed and manufactured by Dept. of Metallurgy and Materials Science, Dunărea de Jos University of Galaţi, for surface engeneering aplications, other like cutting and welding (Fig. 2). The technological unit was designed for: laser beam deviation (45^o), manual focused and step by step sample moving in Ox or Oy axes. The result of samples moves is a large surface of interactions. For

nitriding a lower weight chamber was designed for local interactions media (air, nitrogen and other gases and gas mixture.

Laser beam is focused to sample surface through glass window.

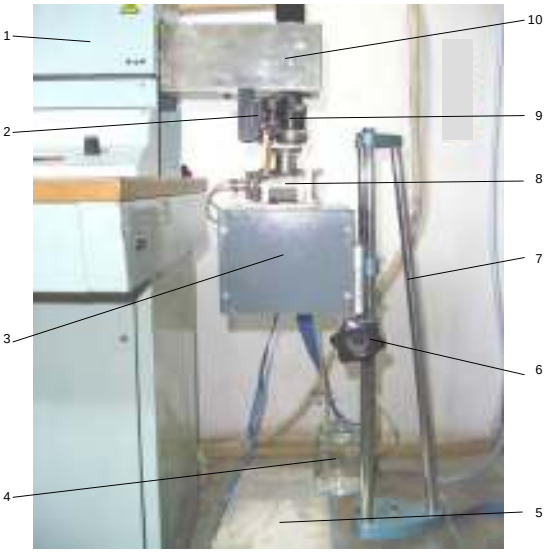

Fig. 1. Technological unit: 1 - laser; 2 – screw defocused; 3 – x/y plate; 4 - water; 5 – concrete block; 6 – screw x-y gross control ; 7 - support; 8 – nitriding space; 9 - objective; 10 – laser beam deviation mirror.

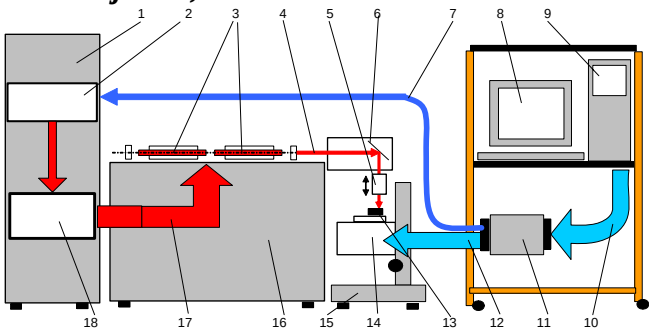

Fig. 2. PC controlled sample x-y moving a laser pulse: 1-SPIK force module, 2-Pulse control module, 3-laser units, 4-laser beam, 5-objective, 6-45^{o}deflection mirror, 7-frequency pulse control line, 8-display-9-PC, 10-parralel port communication, 11-optoisolator, 12-stepper line impulse, 13-x-y table, 14-steppers module, 15-concrete block, 16-laser module, 17-optical pumping connection, 18-high voltage optical pumping supply

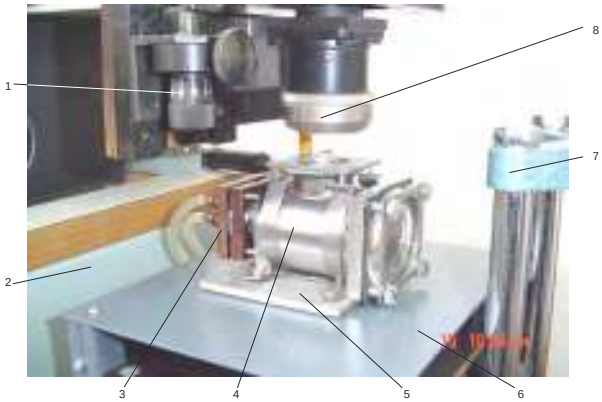

Fig. 3. Nitriding in nitrogen chamber and pulse laser activation: 1 – screw defocused control; 2 – laser module; 3 – nitrogen inlet and outlet; 4 – nitriding chamber; 5 – x-y table; 6 – x-y stepper module; 7 - support; 8 – IR objective

Table 1. Nitralloy steel (38MoCrNi Al09) chemical composition (mass%)

C	Mn	Si	Cr	Ni	Mo	Al
0,35--0,42	0,30--0,6	0,17--0,37	1,35--1,65	-	0,15--0,3	Al=0,70…1,

Another window is present for visual control of interactions. A computer program was designed for scanning sample surface through correlated pulses for x-y table and laser pulse command.

For experiments were used samples from 38MoCrAl09 (nitralloy steel class). This steel having and excelent behavior over gas nitriding treatment for part machine steel (850…1050, HV after nitriding at 500…600°C). Surface properties like hardness, fatigue and corrosion increasing and that induces good properties and performances (hardness, fatigue and corrosion).

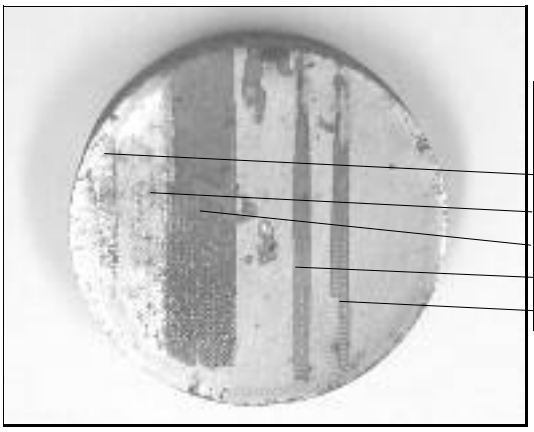

experiment	tensiune de acumulare	presiune N2
um	V	bar
1	700	-
2	750	-
3	750	0,5
4	800	0,5
5	850	-

Fig. 4 Interaction surfaces for Disk 1- side 1 (experiments no.1 to no.5)

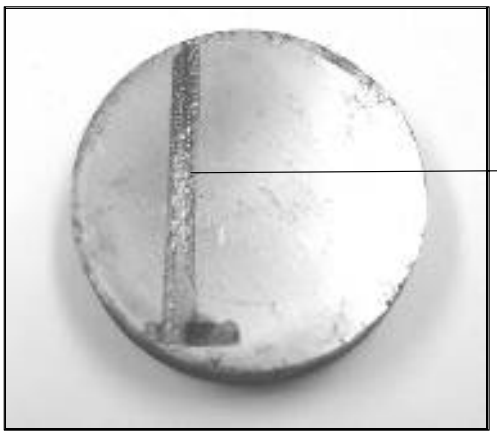

experiment	tensiune de acumulare	presiune N2
um	V	bar
6	700	-

Fig. 5 Interaction surfaces for Disk 1- side 2 (experiment no.6)

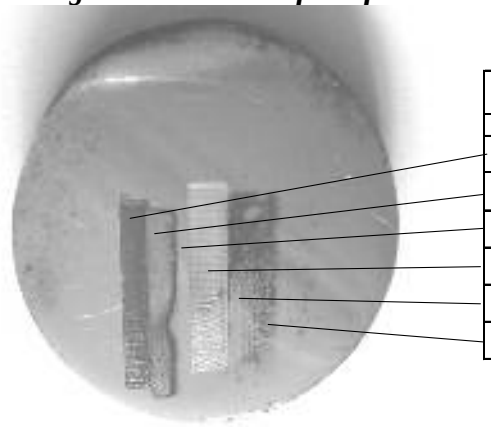

experiment	tensiune de acumulare	defocalizare	presiune N2
um	V	mm	bar
1	700	0	0,5
2	700	5	0,5
3	700	10	0,5
4	800	0	0,5
5	800	5	0,5
6	800	10	0,5

Fig. 6 Interaction surfaces for Disk 2- side 2 (experiment no.1 to no.6)

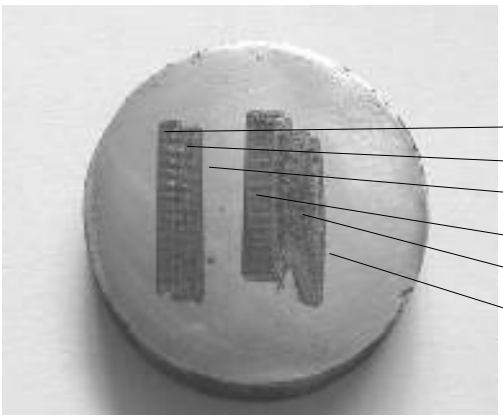

experiment	tensiune de acumulare	defocalizare	presiune N2
um	V	mm	bar
7	700	0	aer
8	700	5	aer
9	700	10	aer
10	800	0	aer
11	800	5	aer
12	800	10	aer

Fig. 7. Interaction surfaces for Disk 2- side 2 (experiment no.6 to no.12)

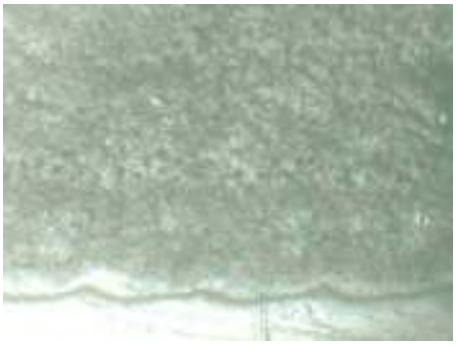

Fig. 8. Macrograph samples surface for experiment 3-disk 1, magnitude 100x

Fig. 9. Macrograph samples surface for experiment 4-disk 1, magnitude 100x

Fig. 10. Macrograph samples surface for experiment 5-disk 1, magnitude 100x

Fig. 11. Macrograph samples surface for (experiment 6- disk 1), magnitude 100x

Fig. 12. Micrograph samples surface for experiment 1, disk 1, and magnitude 300x.

Fig. 13. Micrograph samples surface for experiment 10, disk 2 and magnitude 100x.

Table 2. Experimental conditions and surface hardness after experiments

Sample		Experiment	Charging voltage	Defocused	N_2 pressure/ air	Hardness (HV_5)	Observation
		um	V	mm	Pa	daN/mm^2	-
disk 1	surface 1	1	700	0	$1,013x10^5$	381	
		2	750	0	$1,013x10^5$	532	
		3	750	0	$1,513x10^5$	303	no interaction
		4	800	0	$1,513x10^5$	418	
		5	850	0	$1,013x10^5$	441	
	surface 2	6	700	0	$1,013x10^5$	303	
disk 2	surface 1	1	700	0	$1,513x10^5$	381	
		2	700	5	$1,513x10^5$	532	
		3	700	10	$1,513x10^5$	303	no interaction
		4	800	0	$1,513x10^5$	289	
		5	800	5	$1,513x10^5$	441	
		6	800	10	$1,513x10^5$	303	no interaction
	surface 2	7	700	0	$1,013x10^5$	429	
		8	700	5	$1,013x10^5$	391	
		9	700	10	$1,013x10^5$	303	no interaction
		10	800	0	$1,013x10^5$	623	
		11	800	5	$1,013x10^5$	325	
		12	800	10	$1,013x10^5$	303	no interaction

Chemical composition for steel samples is shown in Table 1. Samples surface after nitriding treatments in nitrogen and laser pulse activation is shown in Fig.4...Fig.7.

2. Results

After ***laser/samples surface interactions***, superficial morphologies have different changes depending on values of control factors. For each experiment, interaction conditions and results are shown in ***Table 2.*** Superficial properties changes after nitriding experiments were go through Vickers hardness (HV_5, load 5kgf) and results are shown in Fig 14 and Fig 15. Micrographs of 38MoCrAl0 steel after nitriding in nitrogen atmosphere activated by YAG:Nd are shown in Fig.12 and Fig.13. A specific superposition structure is present as a result of intense laser beam surface interactions, bigger than 10% (recommended value).

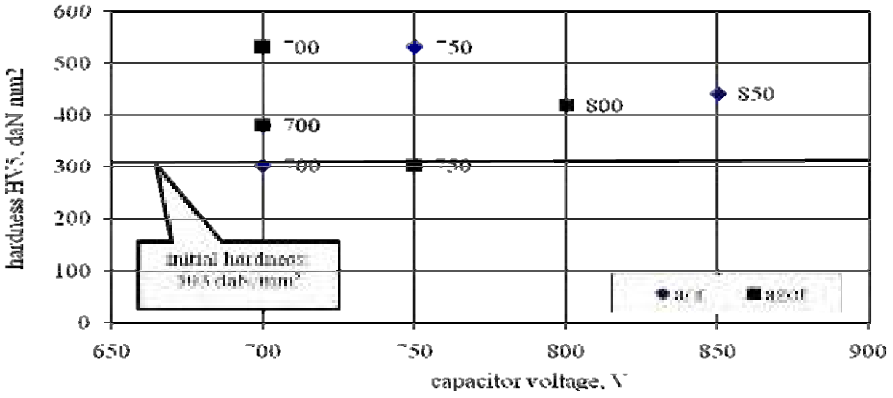

Fig 14. Surface hardness HV_5 after nitriding experiments no.1 to no.6 (disk1)

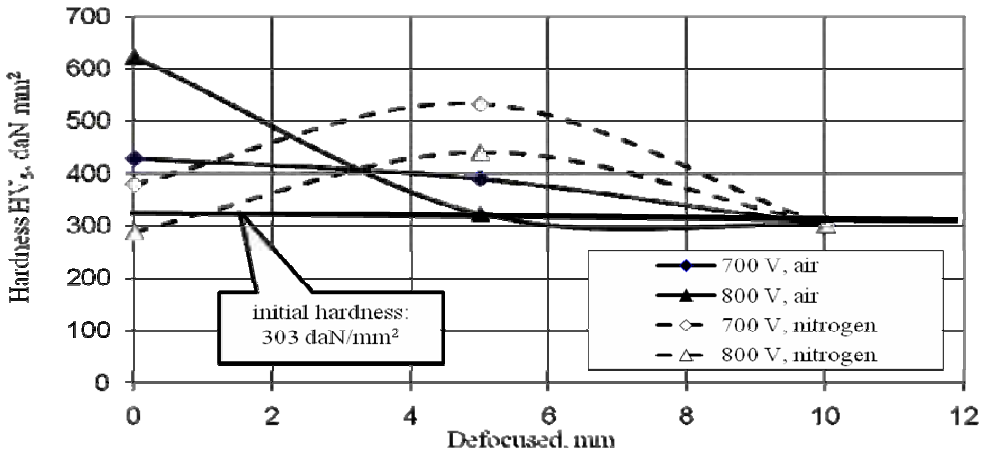

Fig.15. Surface hardness HV_5 for experiments no.1 to no.12 (disk 2).

A white nanostructured layer was formed by fine dispersed martensite (Fig 12 and Fig 12). Heating and cooling processes with high speed in layer determined higher nucleation speed and lower increasing speed.

Conclusions

Laser beam interactions with 38MoCrAl09 depend on pulse radiation energy (indirect measurement from optical pumping high voltage), defocused, chemical composition of chamber atmosphere, atmosphere pressure and optical surface properties of sample steel.

For identical values of influence factors, less chemical composition of chamber atmosphere, an increasing surface hardness were obtained because nitrogen atmosphere was activated locally in interactions volume and nitriding treatment was present (experiments 2, 5, 8 and 11, disk 2). For a higher defocused the specific local density of energy was lower and interactions are lower (surface hardness is comparable with initial values (303 daN/mm^2). PC control of scanning and laser pulse determined a higher surface uniformity after local nitriding treatment. Interactions magnitude was influenced by laser energy and defocused laser beam. For 5 mm defocused and e laser energy in correspondence with 700V …800 V condensator voltages a maximum were obtained. The hardness difference was determined by nitrogen pressure that implied a complex ***carbone-nitrogen- alloying elements*** formations.

The nitriding process in nitrogen atmosphere may be applied for small surface treatments designed for over demand values in exploitation of machine parts.

References

[1]. Ganeev R.E, 2002, Low power hardening of steels, Journal of Materials Processing Technology 121 414-419
[2]. Popescu N, 1990, Tratamente termice neconvenţionale, Editura tehnică, Bucureşti pag.223…245
[3]. Samoila C, Ionescu M.S, Drugă L, 1986, Tehnologii şi utilaje moderne de încălzire, Editura Tehnică, Bucureşti, pag.291…360
[4]. Ursu I, Mihăilescu I.N, Prokhorov A.M, Konov V.I, 1986, Interacţiunea radiaţiei laser cu materialele, Editura Academiei, Bucureşti
[5]. Donţu O, 1985, Tehnologii de prelucrare cu laser, Editura Tehnică, Bucureşti
[6]. De Kock J, 2001, Lasers Offer Unique Heat Treating Capabilities, Industrial Heating, oct. Laser Machining Inc., Somerset, Wis.

THE ANNALS OF "DUNAREA DE JOS" UNIVERSITY OF GALATI.
FASCICLE IX. METALLURGY AND MATERIALS SCIENCE
N^0. 2 – 2008, ISSN 1453 – 083X

THE MODERN STATE OF WORKS IN FIELD OF ELECTRON-BEAM TECHNOLOGY OF MELTING AND EVAPORATION OF METALS AND NON-METALS IN A VACUUM

I.N. GRECHANYUK[1], N.I. GRECHANYUK[1], G. CROITORU[2]
[1]SPC «Gekont». Vinnitsa, Ukraine
[2]«Dunarea de Jos» University, Galati, Romania
email: lucia_orac@yahoo.com

ABSTRACT

In developing of new processes for growing metal (composite) films, the main attention is given to controlling the metal vapour flows: through energy state of the condensing particles, their molecular composition, intensity, spatial distribution of the flow, etc. It is known that the widely accepted open-type evaporators, including quasi-closed ones, are characterized by instability of the directivity diagram of the vapour flow in time, even at constant temperature. Radiation load on the film growth surface from these sources is sometimes comparable to the energy of vapour flow condensation. Therefore, when they are used, it is quite difficult to produce reproducible film structures with controllable parameters. Particular difficulties arise at high evaporation rates, when micro-drops are usually present in the vapour flow.

KEYWORDS: metal (composite) films, electron beam technology, layer coating

1. Introduction

Electron beam impact on the metals leading to their heating, melting and evaporation, as a new technological path in the field of material processing has been intensively developed starting from the middle of XX century [1, 2].

Development of electron beam technology runs along three main paths:

- melting and evaporation in vacuum to produce materials, films, coatings; powerful (up to 1 MW and higher) electron beam units at the accelerating voltage of 20-30 kV are used; power concentration is relatively low (not more than 10^5 W/cm^2);

- welding of metals; equipment of three classes has been developed: low-, medium- and high-voltage covering the accelerating voltage range from 20 to 150 kV; unit power is from 1 to 120 kW and higher at maximum power concentration of 10^5-lO^6 W/cm^2;

- precision treatment of materials (drilling, milling, cutting); high-voltage (80-150 kV) low power (up to 1 kW) units are used, providing the specific power of $5\cdot10^8$ W/cm^2.

Improvement of equipment [3, 4], heat sources [5], metal vapour sources [6] and development of equipment for observation, monitoring and control of the process of electron beam impact are performed simultaneously.

SPC «Gekont» is intensively developing the first of the above areas. Special attention is given to development and manufacturing of laboratory and production electron beam equipment for implementation of a number of new technological processes:

- deposition of thermal barrier coatings on gas turbine blades;

- producing composite materials of dispersion-strengthened, micro-laminate and micro-porous type from the vapour phase;

- producing pure refractory metals, special alloys, ferroalloys, polycrystalline silicon for the needs of aerospace and power engineering, and aircraft construction;

- producing complex-alloyed powders of metallic and ceramic types for plasma deposition of coatings.

Protective coatings on gas turbine blades and equipment for their deposition. At SPC «Gekont» protective coatings on gas turbine blades are produced by electron beam evaporation of MeCrAlY (where Me is Ni,Co,Fe), MeCrAlYHfSiZr alloys and ZrO_2 based ceramics stabilized by Y_2O_3.

Alongside the traditional single-layer metallic materials of MeCrAlY, MeCrAl-YHf SiZr type and two-layer metal/ceramic materials, three variants of three-layer thermal barrier coatings have been developed, the schematics of which are given in Figure 1. The simplest coating is a three-layer coating with an inner metallic (damping) MeCrAlY, MeCrAl-YHfSiZr (where Me is Ni, Co, Fe or alloys on their base), intermediate composite MeCrAlY, MeCrAl-YHfSiZr-MeO (where MeO is Al_2O_3, ZrO_2-Y_2O_3), dispersion-strengthened or micro-laminate type and outer ZrO_2-Y_2O_3 ceramic layers (Figure 1, ***a***) [7].

The second variant is similar to the first one with the only difference that the outer ceramic layer is made in the form of a zigzag (Figure 1, ***c).***

The most interesting is the third variant of the coating, where dispersed particles of refractory borides are added to the outer ceramic layer (ZrO_2-Y_2O_3), which is also made in the form of a zigzag. In operation of products with such a coating, when the outer ceramic layer develops cracks, the boride particles, while oxidizing, form the respective oxides, which heal the developing mi-croc-racks. Thus, such a coating has the effect of «self-healing» or «self-restoration».

Outer ceramic layer with a columnar structure	Outer ceramic layer of zigzag type	Outer ceramic layer of zigzag type with «self-regulation» elements
Intermediate high-temperature layer of dispersion-strengthened or micro-laminate type	Intermediate high-temperature layer of dispersion-strengthened or micro-laminate type	Intermediate high-temperature layer of dispersion-strengthened or micro-laminate type
Inner metallic damping layer	Inner metallic damping layer	Inner metallic damping layer
Base	Base	Base
a	***b***	***c***

Fig. 1. Schematics of thermal-barrier coatings (see the text)

2. Technology and equipment presentation

Two types of production electron beam equipment were developed for implementation of the technological processes of thermal barrier coating deposition on turbine blades [3, 4, 7-10].

Figure 2 shows the general view of a production electron beam unit L-l, which is successfully operated in the science-engineering complex «Zorya-Mashproekt», Nikolaev, Ukraine. When the unit design was developed, a traditional three-chamber schematics of equipment layout was used [7, 9]. The unit working chamber is used for coating deposition proper, and the two auxiliary chambers — for loading-unloading of cassettes with blades. The unit is fitted with eight electron guns of 60 kW power each, of «Gekont» design [7].

Fig. 2. Electron beam unit L-l.

Four guns are designed for evaporation of initial materials of 70 mm diameter arranged in a row, the other four guns — for heating the coated items from below or from the top. Maximum overall dimensions of the coated items are as follows: up to 700 mm length, up to 350 mm diameter.

A feature by which the unit differs from those developed earlier [1] is the possibility of conducting not only the technological process of deposition of all the types of thermal barrier coatings, but also obtaining composition materials of the dispersion-strengthened, micro-laminate and micro-porous types in the form of sheet blanks of up to 800 mm diameter and up to 5 mm thickness. The above equipment can be also used for deposition of super-hard wear-resistant coatings on the dies, moulds, special optical coatings (for instance, mirrors from silicon carbide), etc.

At present SPC «Gekont» developed design documentation on fundamentally new electron beam equipment for deposition of protective coatings [3, 4].

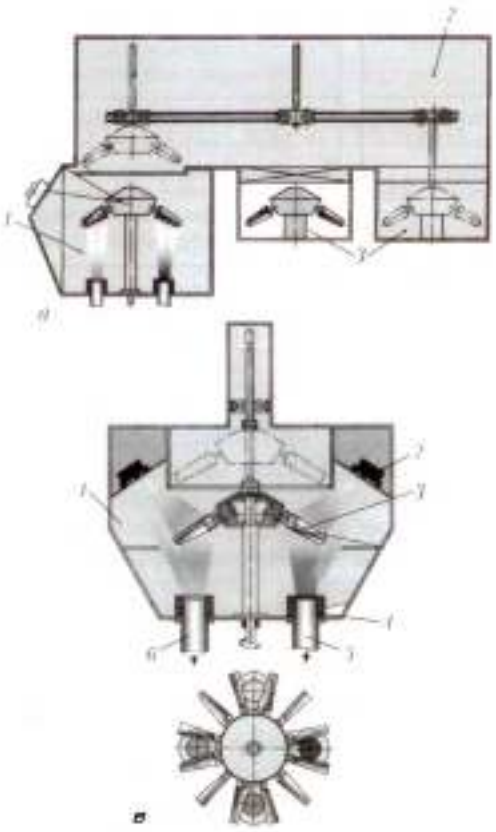

Fig. 3. Unit for protective coating deposition (for designations see the text)

The machine (Figure 3) is a vacuum unit consisting of four vacuum chambers (Figure 3, ***a***) connected to each other: main process chamber proper 1, transition chamber 2 and two load chambers (fore chambers) 3. Mounted inside process chamber 1 (Figure 3, b) are water-cooled crucibles 4, which accommodate ingots 5) 6 of evaporation materials. Beams of electron guns 2 evaporate the ingot material, which is condensed on items 3 in the form of vapour. The quantity of the used crucibles can vary, depending on the required composition and design (two-, three-layer, microplajni-nate) coating. The unit design is fundamentally new [3, 4]. This unit enables deposition of all types of protective coatings, including new types of silicide coatings of micro-laminate type.

It should be noted that the Company implemented a closed cycle of coating deposition on turbine blades, including melting of all types of ingots on nickel, cobalt and iron bases in keeping with TU U 27.4-20113410-002-2003, and using ceramic ingots according to TU U 13.2-20113410-004-2003. Production of Ni(Co)CrAlYSi powders of 40-100 μm fraction for plasma deposition of coatings has also been mastered.

2.1. Composite materials for electric contacts and equipment for their production

Despite the wide application of the processes of evaporation and condensation for deposition of protective coatings, the unique capabilities of the zonal method for producing fundamentally new materials of dispersion-strengthened, micro-laminate and micro-porous types, functionally-graded materials, etc., did not find application. Development of scientific principles of producing micro-laminate materials with less than 0.5 um thickness of alternating layers at deposition temperatures higher than 0.3 of the melting temperature of the most low-melting of the evaporation materials, is a substantial scientific achievement [11].

Fig. 4. Fine structure of (Cu-Zr-Y)/Mo micro-laminate materials

It is known that until recently such materials were produced by the method of electron beam evaporation

and subsequent condensation of metals and non-metals in vacuum at substrate temperature not higher than 300 °C [12]. These data were the basis for development for the first time in the world practice of a production electron beam technology of producing thick (up to 5 mm) micro-laminate materials (Cu-Zr-Y)/Mo (Figure 4) for electric contacts [13].

Condensed materials Cu-(0.08-0.2) % Zr-(0.08-0.2) % Y-(8-12) % Mo are produced in a production electron beam unit L-5 (Figure 5).

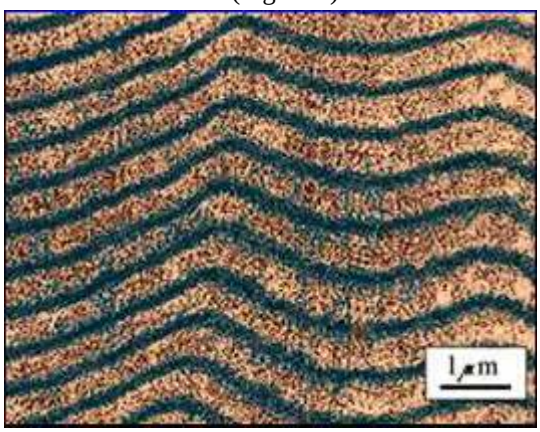

Fig. 5. Electron beam unit L-5

Technological schematic of producing this material is shown in Figure 6.

Condensed materials (Cu-Zr-Y)/Mo are sheets of 1000 mm diameter and up to 5 mm thickness, which are cut up into blanks and soldered onto the contact-holder. Tensile strength and proof stress, depending on the technological condition of production can vary between 645 and 1200 MPa and from 596 to 1000 MPa, respectively, relative elongation — from 2.0 to 8.7 % [14].

New composites, which were named dispersion-strengthened materials for electric contacts (DSMC), are certified and are produced in keeping with the technical conditions [15].

The main advantages of DSMC materials are as follows:

- absence of silver in their composition, so that they are 1.8-3 times less expensive compared to powder electric contact materials and in terms of operating reliability are 1.5-3 times superior to the existing electrical engineering materials;
- they do not maintain arcing;
- completely replace beryllium bronze;
- can stand switching current of up to 1000 A.

The most effective areas of DSMC application are as follows:

- city and long-distance electric transport (contacts used in trams, trolleybuses, trains, metro);
- lift services (passenger and freight lifts);
- port, ship cranes and other hoisting mechanisms;
- electric trolleys of all types;
- mining equipment;
- production and household electrical engineering devices, containing relays, starters, contactors, knife switches, etc.;
- tips for plasma cutting of metals and alloys;
- electrodes of resistance welding machines.

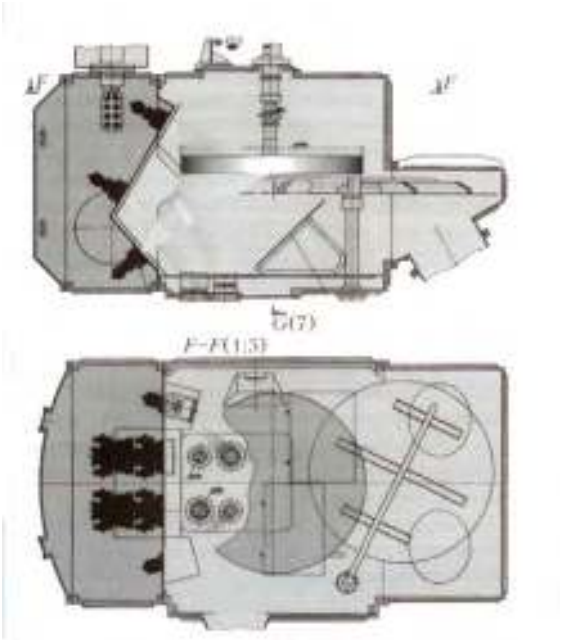

Fig. 6. Technological schematic of producing micro-laminate materials (Cu-Zr-Y)/Mo

So far according to [16], more than 1.5 mm electric contacts of 370 names have been produced (Figure 7) which are successfully operating in CIS countries, Czech and Romania.

Fig. 7. Appearance of a range of electric contacts

Simultaneously with introduction of materials for interrupting electric contacts into industry, the company in co-operation with Institute for Materials Science Problems, of NASU, «Generator» Plant (Kiev), Wroclaw Polytechnic Institute (Poland) is working to develop composite materials based on

copper, chromium, tungsten, carbon, applied in production of slide contacts, contacts for vacuum blowout chambers (Figure 8).

Fig. 8. Appearance of contacts for vacuum blowout chambers

2.2. Production technologies of electron beam re-melting of metals and alloys and equipment for their implementation

The Company has mastered the industrial technology of electron beam remelting of wastes of high-speed steels and producing finished ingots for subsequent manufacturing of tools from them [17, 18]. The used equipment allows remelting in vacuum the wastes of high-speed steel (used tools, tool production wastes) and producing cylindrical ingots of 60 to 130 mm diameter and ingots of 140-160 mm cross-section and up to 2000 mm length.

Technological and cost advantages are as follows:

- process of ingot remelting and forming occurs in one technological cycle without subsequent the mechanical treatment (forging, squeezing);
- possibility of remelting lump charge;
- rapid replacement of fixtures for producing ingots of the required dimensions;
- high quality of the produced ingots after vacuum remelting;
- producing small batches of finished ingots;
- cost of finished ingots is approximately 2-3 times lower than that of ingots produced by the traditional technology.

A number of specialized production electron beam units have been developed recently for melting super alloys, refractory metals, titanium and producing finished ingots of the diameter from 60 to 300 mm and up to 2500 mm length.

The appearance of a unit of such a type is shown in Figure 9. New high-voltage power sources of SPC «Gekont» design and electron beam gas-discharge guns with a cold cathode developed under the guidance of V.I. Melnik were used in these units for the first time [19].

Fig. 9. Specialized electron beam unit for melting metals and alloys

Special attention is given today to development of new technologies and equipment for melting silicon and ferroalloys. The Company supplied to Japan three electron beam units of 10, 20, 500 kW power for electron beam remelting of silicon (Figure 10).

Fig. 10. 500 kW electron beam unit for silicon remelting

The above examples of practical application of the processes of melting and evaporation of metals and non-metals in vacuum are a convincing proof of an ever wider application of special electrometallurgy for development of new materials and coatings.

References

[1]. Movchan, B.A., Malashenko, I.S.,1983, ***Vacuum-deposited heat-resistant coatings***. Kiev: Naukova Dumka.

[2]. Zuev, I.V.,1998 ***Treatment of materials by concentrated energy flows***. Moscow: MEI.

[3]. Grechanyuk, M., Kucherenko, P.,2005, ***Installation for electron-ray coatication of coatings***. Pat. US 6,923,868 BZ. Publ. 02.08.2005.

[4]. Grechanyuk, N.I., Kucherenko, P.P. 2005, ***Installation for electron beam deposition of coating***s. Pat. 2265078 RF. Publ. 12.27.2005.

[5]. Novikov, A.A.,2003, ***Gas-discharge gun and method of its control.*** Pat. 60377 Ukraine.

[6]. Zolkin, A.S.,1992, ***Sources of metal vapors for research and technologies***. Novosibirsk: ITF.

[7]. Grechanyuk, N.I., Kucherenko, P.P., Osokin, V.A. et al.,2000***, State-of-the-art and prospects of development of thremal barrier coatings (TBC) for gas turbine blade units and equipment for their deposition.*** Novyny Energetyky, 9, 32-37.

[8]. Grechanyuk, N.I., Dyatlova, E.K., Kucherenko, P.P. et al.,2001***, Electron gun with linear thermocathode for electron beam heating.*** Pat. 40664 Ukraine. Publ. 2001.

[9]. Grechanyuk, N.I., Kucherenko, P.P., Osokin, V.A. et al.,2001, ***Protective coating for gas turbine blades.*** Pat. 42052 Ukraine.

[10]. Grechanyuk, N.I., Osokin, V.A., Shpak, P.A. et al., 2005, ***Influence of technological parameters on structure of external ceramic layer in two-layer metal-ceramic coatings produced by electron beam deposition in one technological cycle***. Poroshk. Metallurgiya, 3/4, 41-48.

[11]. Grechanyuk, N.I., 2006, ***Method of production of microlayer thermostable materials.*** Pat. 2271404 RF.

[12]. Iliinsky, A.I.,1986, ***Structure and strength of lamellar and dispersion-strengthened films.*** Moscow: Metallurgiya.

[13]. Grechanyuk, N.I., Osokin, V.A., Afanasiev, I.B. et al., 2001, Composite material for electric contacts. Pat. 34875 Ukraine.

[14]. Borisenko, V.A., Bukhanovsky, V.V., Grechanyuk, N.I. et al., 2005, ***Temperature dependences of statistical mechanical properties of microlayer composite material MDK-3***. Proble-my Prochnosti, 4, 113-120.

[15]. TU U 20113410.001-98: Dispersion-strengthened materials for electric contacts.

[16]. TU U 31.2-20113410-003-2002: Electric contacts on the base of dispersion-strengthened materials.

[17]. Shpak, P.A., Grechanyuk, V.G., Osokin, V.A.,2002, ***Effect of electron beam remelting on structure and properties of high-speed steel R6M5.*** Advances in Electrometallurgy, 3, 12-14.

[18]. Grechanyuk, N.I., Afanasiev, I.Yu., Shpak, P.A. et al., 2003, Method of production of blanks for tools from high-speed steel. Pat. 37658 Ukraine.

[19]. Melnik, V.I., Melnik, I.V., Tugay, B.A. et al., 2006, ***Technological equipment for electron beam refusing on the base of glow discharge electron guns***. Elektrotekhnika and Elek-tronika, 5/6**,** 119-121.

THE ANNALS OF "DUNAREA DE JOS" UNIVERSITY OF GALATI.
FASCICLE IX. METALLURGY AND MATERIALS SCIENCE
N^0. 2 – 2008, ISSN 1453 – 083X

LASER SURFACE ALLOYING OF SOME STEELS FROM SiC PREDEPOSITED POWDERS

S.M.LEVCOVICI[1], D.T.LEVCOVICI[2]
[1]"Dunarea de Jos" University of Galati
[2]The Research and Design Institute for Steel "UZINSIDER ENGINEERING"-S.A
e-mail: sandalevcovici@hotmail.com

ABSTRACT

For the purpose of studying the possibilities of increasing the wear resistance, specimens of three steels with 0.2%C, 0.46%C and 1%C were surface alloyed with reinforcement from overlapping pastes with green SiC hard particles with the granulation 800 and 320. The melting of surface layer was performed by CO_2 continous wave laser on a numerical x-y table. On these specimens the micro structural characteristics, geometry of molten zone, micro hardness variation in the alloyed layer depth and the HV5 hardness on a laser processed surface were determined, which allowed defining the added material with the best hardening effect. The conditions to obtain compact surface layers with 2-3 time higher hardness than the base material were determined.

KEYWORDS: laser alloying, SiC, microstructure, micro hardness.

1. Introduction

Improved durability of tools and machine parts subject to intense wear led to the promotion of unconventional technologies of surface treatments to the active zones under the action of concentrated energy beams, such as laser and electron beams. The laser processing provides an ultrafast thermal cycle into the ambient atmosphere, on small and difficult to access areas, of complex geometry, with accuracy and high productivity. The results of the interaction between the laser beam and the processed material are off balance structural states, impossible to make by traditional treatment methods. They results in a strong hardness, increased resistance to plastic deformation, resistance to fatigue and corrosion, less wear, improved lubrication, etc.

The interaction of the laser radiation with the material surface can take place in the presence or absence of an additional material injected or pre deposited. Depending on the desired thermal effect, the structural modification procedures can be divided into [1, 2]:

-procedures without additional material, which do not modify the chemical composition of the base material, such as: hardening from the solid or liquid state, granulation finishing, glazing or vitrification, shock hardening.

-procedures with additional materials which do modify the chemical composition of the base material, such as: deposition, alloying, hard particles reinforcement.

There are various additional materials used for surface hardening and increasing the wear resistance, such as [3]:

-Hard materials of metal atom bonds: carbides (WC, W_2C, Cr_3C_2, $Cr_{23}C_6$, TiC, MoC, TaC) [4], [5], [6], [7], carbides mixtures (WC-TiC; TaC-Nb), nitrides (TiN, ZrN, TaN) [8], borides (TiB_2, ZrB_2, LaB_6) [8];

-Hard materials of non metallic atom bonds: oxides (Al_2O_3-Cr_2O_3; Al_2O_3-MgO; Al_2O_3-TiO_2; TiO_2; ZrO_2-CaO) [9], carbides (SiC, B_4C) [9, 10] nitrides (Si_3N_4, AlN), borides (AlB_{12}, SiB_6);

-Hard alloys: Fe-Cr-W-Mo-V-C-Si; Co-Cr-W-Mo-C-Si; Ni-Cr-B-Si [10, 11, 12].

The paper shows the researches on surface alloying and SiC hard particles reinforcement from overlapping pastes of the low alloyed steels having various carbon contents. Special attention was paid to the effect of the carbon content, the additional material granulation, as well as the laser processing parameters on the structure and hardness of the SiC alloyed and/or reinforced layers.

2. Experimental materials and working method

To investigate the sensitivity of the alloying process to the carbon contained in the steel base, three

low alloyed steels were selected for the experiment purpose. Chemical composition is given in Table 1. The samples were cut as 40x15x15mm.

Table 1.Chemical composition of the experimental samples

Base material code	Grade of steel	Condition	Chemical composition [%]						
			C	Mn	Si	Cr	V	S	P
1	16MnCr5 SR EN 10084:2000	annealed	0.20	1.15	0.37	1.12	-	0.032	0.028
2	51CrV4 SR EN 10083-1:1994	annealed	0.46	0.85	0.32	1.08	0.17	0.027	0.031
3	16MnCr5 SR EN 10084:2000	carburized	0.98	1.15	0.37	1.12	-	0.032	0.028

Table 2. Additional materials

Additional material code	Additional material	Chemical composition [13] [%]	Granulation mesh/″linear
AM1	Green SiC	97-98.8%SiC, 0.6%Si	800
AM2			320

Table 3.Physical properties of the silicon carbide [13]

State	Crystalline structure	Density	Tm[1]	Tv[2]	α[3]	λ[4]	HV
		[kg/m^3]	[°C]		[kJ/kgK]	[W/mK]	[GPa]
SiC α	diamond	3170	-	2830	1,80	45-450	26-37
SiC β	hexagonal	3210	2150	2780	1,76	45-450	21-29

Note: 1- melting temperature, 2-boiling temperature, 3-linear dilatation coefficient, 4-thermal conductivity.

The additional material consisted of green SiC particles; their chemical composition and granulation are presented in Table 2. The silicon carbide is polymorphous. Less than 2100°C the SiCα modification is stable as it has a diamond type structure. Above 2100°C in the SiCβ changes, as this has up to eight structural types in hexagonal and tetragonal systems. In green SiC technical powders there is a mixture of SiCα and SiCβ with hexagonal system [12]. A number of physical properties of these modifications are given in Table 3. Before the laser processing, the sample surface was degreased and covered by a paste resulting by mixing a part of hydroxiethylcellulose with tree parts of SiC powder. After drying, the thickness of the additional material was calibrated by grinding to 0.15 mm. The laser processing was made by marking single strips in an inert argon atmosphere on a LASER GT 1200W (Romania) system, by numerically controlling on a computer the working table according to direction x-y. The surface covered with the additional material has been processed by CO_2 continuous wave laser with different energy factors $K = P / d \cdot v$ [J/mm^2], obtained by keeping constant the emission power P = 950 W and the variation of the laser beam diameter d = 2.18 and 2.84 mm and of the scanning speed, v = 1…2.5 mm/s. The samples were subject to metallographic investigations on the surface and the laser strip cross section. The sensitivity to vaporization and fissuring, the geometry of the laser strip, structural modification to SiC alloying under various regimes of heat transfer, determination of the micro hardness HV0,1 (load 100gf) variation in the alloyed layer depth and the hardness HV5 (load 5kgf) on a laser processed surface.

3. Experimental results and discussions

The analysis of the cross section microstructure of the laser processed strip reveals an alloyed layer on a steel base quenched to martensite from solid phase (fig.1a). The alloyed layer was obtained from very fast melting of a thin base material layer, including the predeposited SiC particles by thermal capillary convection, followed by fast solidification and martensitic hardening. The structure of the alloyed layer is a dendritic columnar and contains martensite, residual austenite and SiC particles in an interdendritic arrangement, in amount that depend on the amount of carbon to be found in the steel, the granulation of the SiC particles, and the laser processing operation.

In the case of alloying steel of SiC powders of 320 granulation, the new structure consists of SiC particles among the branches of the martensite dendrite and residual austenite increasing with the extent of the austenite alloying. Partial dissolving of the SiC takes place even when processed under very high energies (fig.1b). In the case of steel alloying with SiC powder

of 800 granulation, is found that the SiC particles have been completely dissolved (fig.1c).

The structure is made up of austenite dendrite which, when cooled, get into high alloyed martensite and an increased amount of residual austenite.

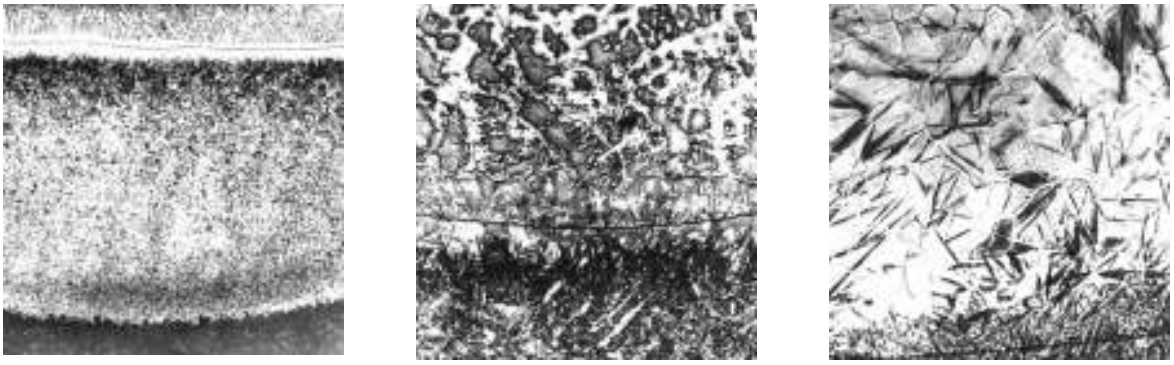

a). b). c).

Fig. 1. Microstructure of alloyed layers: a). steel code 2, AM2, K=407.3 J/mm^2, x100; b). steel code 2, AM2, K=407.3 J/mm^2, x500; c). steel code 3, AM1, K=227.6 J/mm^2, x500; Nital2%.

Table 4. Strip geometry and macro hardness HV$_5$ (d_1 = 2.84mm; *d_2 = 2.18mm)

Added material	K [J/mm^2]/ [mm/s]	Strip geometry					HV$_5$ [MPa]	Observation
		Δh	ha	hq	la	lq		
1 - 16MnCr5								
AM2	133.8	-0.05	0.11	0.97	1.60	3.06	9800	N
	167.2	-0.05	0.14	1.19	2.20	4	8420	N
	230.7	0.03	0.30	1.39	2.40	3.60	9470	**R**
	283.4	0.00	0.14	1.44	2.60	3.73	6870	N
	369.3*	0.05	0.42	1.42	2.60	4.13	7270	N
2 - 50CrV4								
AM1	217.9*	0.00	0.14	0.50	1.11	1.61	10000	N
	290.5*	0.01	0.10	0.44	1.08	1.55	8470	N
	407.3*	0.01	0.11	0.54	1.28	1.80	8380	N,V
AM2	217.9*	0.01	0.13	0.55	1.22	1.86	9800	N
	290.5*	0.05	0.19	0.55	1.22	1.83	9580	**R**
	407.3*	0.01	0.13	0.61	1.47	1.97	9410	N, V
3 - 16MnCr5 carburized								
AM1	172.4	-0.01	0.17	0.94	1.97	2.83	6120	N
	227.6	0.03	0.18	1.00	1.94	2.92	8520	N
	334.4	0.04	0.18	0.94	1.54	2.78	6590	N
	217.9*	0.03	0.06	0.58	1.39	1.94	7770	N
	296.5*	-0.05	0.14	0.61	1.31	1.97	8000	N
	435.8*	-0.05	0.14	0.67	1.50	2.11	7590	N
AM2	172.4	0.03	0.17	0.80	1.86	2.55	9490	P
	227.6	0.05	0.19	0.89	1.83	2.61	9170	-
	334.4	0.00	0.15	0.78	1.83	2.55	9170	P
	217.9*	0.03	0.19	0.61	1.31	1.92	9930	**R**
	296.5*	0.03	0.17	0.58	1.36	1.97	9720	**R**
	435.8*	0.03	0.17	0.64	1.44	2.03	9420	N, F

Note: **R** – recommended; N – None recommended; P – pores; V –vaporizations; F- fissures.

The extent of the carbide dissolving is affected by the content of carbon in the steel and the operation conditions. An increased amount of carbon limits the carbides dissolving and favors the composite structures. The increased scanning speed reduces the distance between the dendrites axes and increases the amount of SiC not dissolved. At steel of code 1 processed by maximum energy density, the advanced silicon alloying makes the lamellar graphite to appear in the structure as well. At the fusion limit it can be seen a lighter color area of high inter-diffusion in the alloyed layer which is free of SiC particles and has a

martensitic structure. Under the fusion limit the layer hardened from solid phase has an increased granulation and a higher amount of residual austenite, with softening effect. Table 4 shows a number of results on the dimensions of the laser processed strip (Δh - the deviation from the processed surface; ha, hq - the depth; la, lq - the width of the alloyed layers and quenched to martensite layers) and the hardness HV5 measured on the laser processed surface. The irregularities of the laser processed surface are highlighted by the sign and size of the deviation Δh from the level of the initial surface. It can be seen that an over height generally appears due to the inclusion of the addition material and the higher volume at the martensitic transformation. There is a negative deviation especially at the alloying of steel code 1 which exhibits a higher melting interval and a lower viscosity of the melting bath. Also the low energy density regime, which provides a lower surface temperature as well as the additional material of rough granulation which remains in suspension in the melt bath, reduces its fluidity and causes specific irregularities.

Fig. 2 shows the dependence of the alloying and quenching and from the solid phase depth according to the energy density.

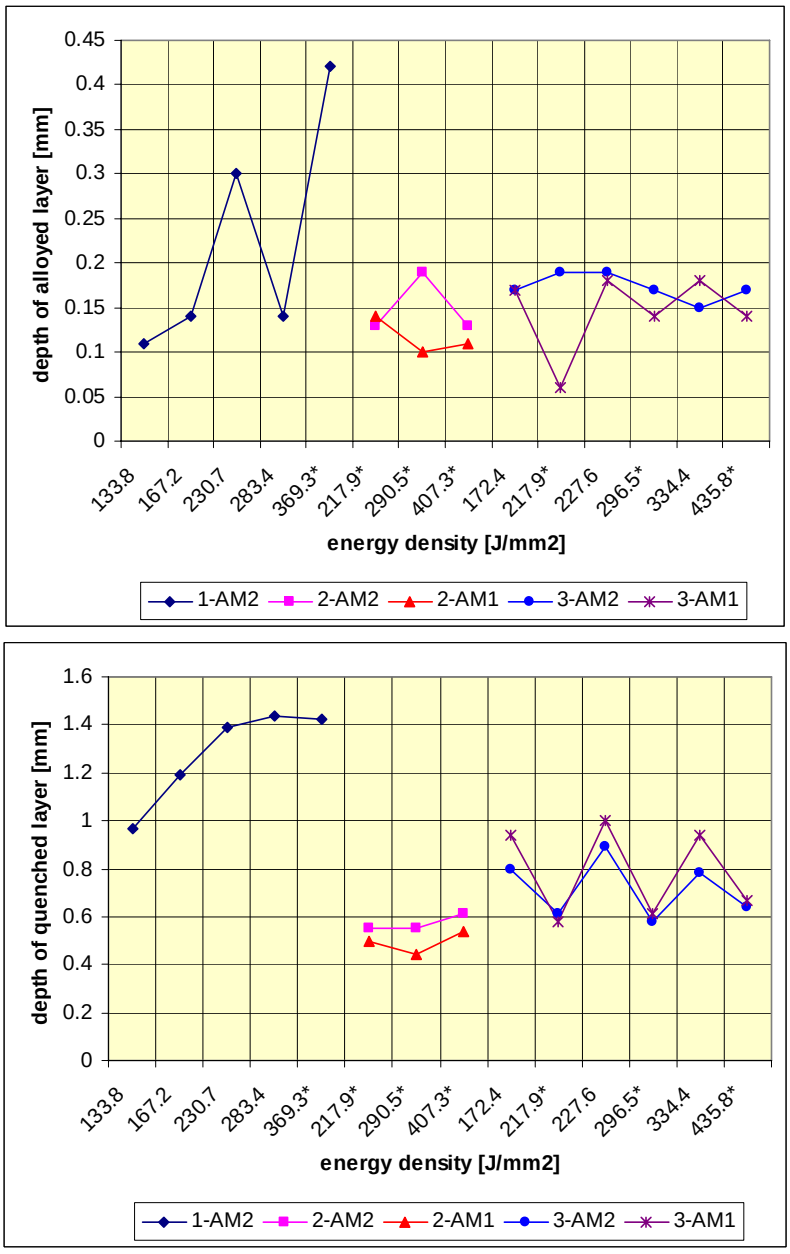

Fig. 2 Dependence of alloying and quenching depth versus energy density K. 1, 2, 3 – code of steel; AM1- 800 granulation SiC particles; AM2- 320 granulation SiC particles; *d_2=2.18mm.

When is used AM2 additional material, the maximum depths are encountered with steels code 1 of minimum carbon content and they increase with the energy density. This may be due to the fact that when the carbon in the steel increases, the carbides in the steel increase as well and the thermal conductivity of steel decreases. Particles SiC with 320 granulation are dissolved in melted bath with high density energy and this generally determines, in the same condition of laser processing, an alloying and depth better than 800 granulation SiC particles (AM1). The micro hardness analysis (Fig.3) in the depth of the laser processed strip shows a higher hardening of the alloyed layer as compared with the steel sub layer hardened from solid phase. The micro hardness of these zones increases with the steel carbon concentration. It should be noted the softening occurring in the transition zone from alloyed layer to quenched layer, which is more intensive with the amount of carbon in the steel. The HV_5 hardness is strongly affected by the additional material, the carbon in the steel and the beam diameter. With steel code 3 the strongest hardness is caused by the alloying with AM2 - green SiC of granulation 320 (Fig.4), as a result of obtaining some composite phase structures. The minimum hardness is caused by the additional material AM1 of granulation 800, when the additional material is dissolved. The hardness of the alloyed layer increases with the carbon in the steel which provides higher reinforcement to the composite layer. At the same time it decreases with higher energy densities due to the high amount of residual austenite in the matrix. The steel code 1 of minimum carbon content shows the most drastic decrease in hardness due to the additional capacity of alloying its matrix and also due to the high depth of the alloyed layer which makes that the amount of additional material be distributed in higher volumes. The maximum hardness appears when the process is performed by concentrated beams of lower diameters.

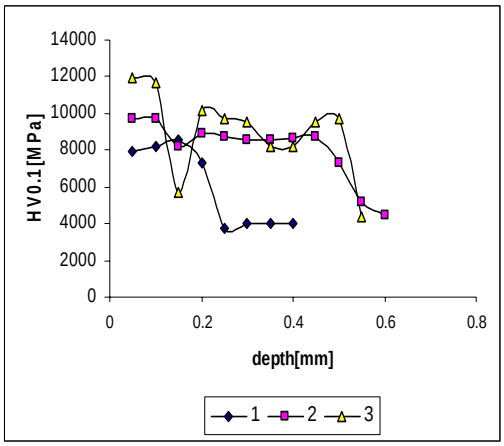

Fig.3. The variation of micro hardness in the depth of alloyed layer for AM2: steel code 1 - 230.7 J/mm^2; steel code 2 - 217.9 J/mm^2; steel code 3 - 296.5 J/mm^2.

4. Conclusions

The laser alloying of low alloyed steels from pre deposited pastes containing SiC particles leads to the steels more alloyed with carbon and silica than the base material or to the composite structures with SiC reinforcing elements, featuring higher hardness than the laser quenching from the solid phase layers of base material.

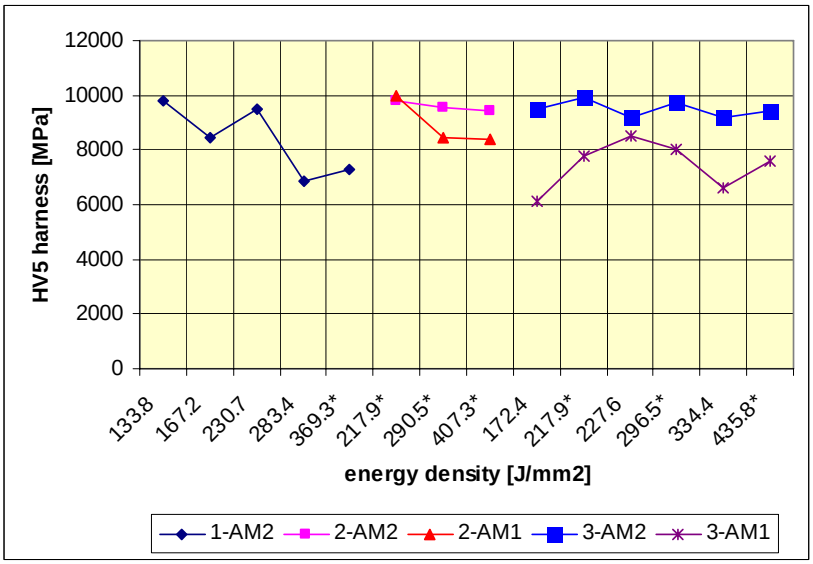

Fig.4. Dependence of hardness HV5 by additional material and carbon content of steel; 1, 2, 3 – code of steel; AM1- 800 granulation SiC particles; AM2 - 320 granulation SiC particles; *d_2=2.18mm

Improved alloyed layers may be obtained when using green SiC of 320 mesh/"linear granulation. Hardness is improved when the concentration of the carbon in steel is higher under laser processing. This process results in partial dissolving of the SiC particles and employing concentrated beams. For alloying purpose it is convenient to use steel code 2 and 3 of medium or high carbon content, which provides a hard under layer quenched from the solid.

From these experiments results that, the optimum condition for steel code 2 consists in laser alloying with 320 granulation green SiC particles, with P = 950W; d = 2.18mm; v = 1.5mm/s. This condition ensure a 0.19mm adequate depth of alloyed layer and a high hardness HV5 = 9580MPa.

For steel code 3 is recommended laser alloying with 320 granulation SiC green particles, P = 950W, d = 2.18mm, v = 2…1.5 mm/s. The depth of alloyed layer is 0.19…0.17mm with a high hardness HV5 = 9930…9720MPa.

References

[1]. Breinan E.M., Kear K.H, 1983, ***Laser Material Processing***, North Holland Publ., pp. 235.

[2]. Takacs J., Buza C.T., Bakoni K., 1984, Procedings Euromat'94, Ungaria, pp. 492.

[3]. Guo Qiang Song, 1995, ***Thèse pour docteur de l'Université Louis Pasteur***, Strasbourg,

[4]**. Levcovici S.M., Oprea F., Levcovici D.T., Paraschiv M.M.,** 1994, Procedings SMT VIII, pp. 378-382.

[5]. Levcovici S.M., Levcovici D.T., Gologan V., Farkaş L., 1997, Procedings of EUROMAT'97, vol.III, pp.131-134.

[6]. D.T.Levcovici, V.Munteanu, M.M.Paraschiv, S.M.Levcovici, A.Preda, E.Constantin, B.Levcovici, 2002, ***Laser Surface Alloying of Steel with Tungsten and Cobalt***, Materials and Manufacturing Processes, Vol.17, No.1, pp. 23 – 36.

[7]. Nagarathnam K., Komvopoulos K., 1995, Metallurgical and Materials Transaction A vol.26A, aug. p. 2131

[8]. S.M.Levcovici, V.Munteanu, D.T.Levcovici, M.M.Paraschiv, A. Preda, 2000, ***Laser Surface Hardening of Austenitic Stainless Steel***, MATERIALS ENGINEERING AND PERFORMANCE, Vol.9 No.5 pp.536-540.

[9]. Spiridonov N.V, Kobiakov I.L, Kupriakov I.C., 1988, ***Plazmennâe I lazernâe metodâ uprocinenia detalei masin***, Vîşaia şcola, Minsk, Bielarus.

[10]. Pantelis D., Manilatis P, Pantazopoulos G., 1994, Revue de Métallurgie-CIT/Génie de Matériaux, mai, p.745

[11]. Levcovici D.T., Munteanu V., Levcovici S.M., Mitoseriu O, Benea L., Paraschiv M.M., 1999, ***Laser Processing of MMC Layers on the Metal Base***, "Materials and Manufacturing Processes", vol.14, nr.4, pp. 475-487.

[12]. Levcovici Dan T., Levcovici Sanda M., Preda Adriana, Boiciuc R., 2007, ***Fe-Ni-Cu-Al-Ti-Cr Alloy Layers Obtained by Laser Processing of Predeposited Powders on Steel Base***, Revista de tehnologii neconvenţionale/ Nonconventional Technologies Review, nr.3, ARTN, pp. 44-52.

[13]. Saifulin R.S., 1983, ***Neorganiceskie kompoziţionnâe materialâ***, Moskva, Himia.

THE ANNALS OF "DUNAREA DE JOS" UNIVERSITY OF GALATI.
FASCICLE IX. METALLURGY AND MATERIALS SCIENCE
N^0. 2 – 2008, ISSN 1453 – 083X

ELECTRODEPOSITION OBTAINING AND CORROSION BEHAVIOUR OF PHENOL FORMALDEHYDE RESIN/ZINC COMPOSITE COATINGS

Olga MITOŞERIU[1], Alina CIUBOTARIU[1], Lidia BENEA[1], Pierre PONTHIAUX[2], Francois WENGER[2]

[1]Dunarea de Jos University of Galati,
[2]Ecole Centrale Paris, Laboratoire Genie de Procedées Matériaux
Grand Voie des Vignes, France
e-mail: Alina.Ciubotariu@ugal.ro

ABSTRACT

The present work has the purpose of obtaining composite coatings in zinc matrix by using phenol - formaldehyde resin type NOVOLAC (RESITAL 6358/1) in the electrodeposition process of zinc. The PF resin/Zn composite coatings were electrodeposited from a suspension of PF resin particles (diameter < 56 µm) in aqueous zinc sulphate electrolyte. Suspension was prepared by adding 10g/L and 25g/L PF resin particles into solution. The pure zinc coating has a rather regular surface, whereas the composite coatings surface has fine surface structure. For layers obtained at 3A/dm^2 the polarization resistance is higher for composite coatings with 10 g/L PF resin (R_p = 238.75 Ω cm^2) than pure zinc (R_p = 34.54 Ω cm^2). For layers obtained at 5A/dm^2 the polarization resistance is higher for composite coatings with 25 g/L PF resin (R_p = 430.19 Ω cm^2) than pure zinc (R_p = 127.34Ω cm^2). As test solution 0.5M sodium chloride was used, it was observed that by adding PF resin particles in zinc electrolyte for electrodeposition it was obtained a very good distribution of resin particles on zinc surface and PF resin/Zn composite coatings obtained are most resistant at corrosive attack than pure zinc obtained from electrodeposition under the same conditions.

KEYWORDS: PF resin particles, electrodeposition, PF resin/Zn composite coatings, thickness layers, polarization resistance

1. Introduction

Metal composite materials have found application in many areas of daily life for quite some time. Often it is not realized that the application makes use of composite materials. These materials are produced in situ from the conventional production and processing of metals. For many researchers the term metal matrix composites is often equated with the term light metal matrix composites (MMCs). Substantial progress in the development of light metal matrix composites has been achieved in recent decades, so that they could be introduced into the most important applications. These innovative materials open up unlimited possibilities for modern material science and development; the characteristics of MMCs can be designed into the material, custom-made, dependent on the application. From this potential, metal matrix composites fulfill all the desired conceptions of the designer [1]. However, the technology of MMCs is in competition with other modern material technologies, for example powder metallurgy. The advantages of the composite materials are only realized when there is a reasonable cost – performance relationship in the component production. The use of a composite material is obligatory if a special property profile can only be achieved by application of these materials [2].

To summarize, an improvement in the weight specific properties can result, offering the possibilities of extending the application area, substitution of common materials and optimization of component properties. With functional materials there is another objective, the precondition of maintaining the appropriate function of the material.

Objectives are for example: increase in strength of conducting materials while maintaining the high conductivity, improvement in low temperature creep resistance (reactionless materials), improvement of

burnout behavior (switching contact), improvement of wear behavior (sliding contact), increase in operating time of spot welding electrodes by reduction of burn outs, production of layer composite materials for electronic components, production of ductile composite superconductors, production of magnetic materials with special properties. For other applications, different development objectives are given, which differ from those mentioned before. For example, in medical technology, mechanical properties, like extreme corrosion resistance and low degradation as well as biocompatibility are expected [3]. For all these reasons metal matrix composites are only at the beginning of the evolution curve of modern materials (see Fig. 1) [4].

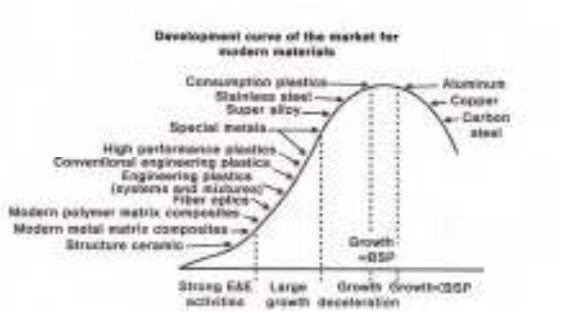

Fig. 1. Development curve of the market for modern materials

Zinc is the most widely used material for protection of steel against corrosion. The success of using zinc as a steel coating can be attributed to its sacrificial nature, low cost and ease of application (hot – dipping or electroplating) [5]. Zinc is more corrosion resistant than steel in most natural atmospheres, the exceptions being ventilated indoor atmospheres where the corrosion of both steel and zinc is extremely low and certain highly corrosive industrial atmospheres. The major drawback of thick coatings is poor weldability and difficulty to achieve a specular finish after painting. This provides the need to develop thinner electrodeposited coatings with improved properties such as hardness, ductility, corrosion, etc [6].

Electrodeposition offers rigid control of film thickness, uniformity and deposition rate and is especially attractive owing to its low equipment cost and starting materials. Due to the use of an electric field, electrodeposition is particularly suited for the formation of uniform films on substrates of complicated shape, impregnation of porous substrates and deposition on selected areas of the substrates [7].

The use of zinc-plated articles is increasing due to its sacrificial protection of steel from corrosion.

This sacrificial protection is due to the fact that the zinc is a less noble metal and catholically protects the steeleven in places where the deposit is damaged. Zinc coatings are obtained either from cyanide, non-cyanide, alkaline or acid solutions [8 - 12]. Because of the pollution and high cost associated with cyanide, deposition from other baths such as sulphate, chloride and mixed sulphate-chloride baths are gaining importance.

Good deposition depends mainly on the nature of bath constituents. Generally, a plating bath contains conducting salts, buffering agents, complexing agents and metal ions. Among these the complexing agents effectively influence the deposition process, solution properties and structure of the deposit. The action of these complexing agents is specific and depends on pH, nature of anion, temperature and other ingredients of the medium. Too many ingredients cause difficulties in maintaining the operating parameters of the bath solution during the plating process. Some of these agents smoothen the deposit over a wide current density range and the other addition agents influence the production of bright deposits [13].

In the present work, efforts have been made to develop a bath solution without additive because they could give reactions with PF resin particles and the results could not be interpreted properly.

Phenol and formaldehyde are among the most basic building blocks in polymer chemistry. The condensation reaction may be initiated by a number of alkali or acidic catalysts, resulting in a polymer. This polymer, in conjunction with various organic and inorganic reinforcing systems, offers a variety of unique properties and characteristics. The polymer acts as a matrix for binding together a number of substrates such as wood, paper: fibbers (e.g., fibreglass), or particles (e.g. wood flour, foundry sand) to form a highly crossed-linked composite. The phenolic based products have some characteristics: dimensional stability at elevated temperatures; creep resistant, excellent fire performance, cost effective, outstanding durability, excellent strength-to-weight ratio, excellent thermal insulation properties, excellent sound-damping properties, corrosion resistant, water-resistant.

The present work has the purpose of realization of composite coatings obtained by using PF resin type NOVOLAC with commercial name RESITAL 6358/1 (for the first time) synthesised by HÜTTENES - ALBERTUS Germany electrodeposited with zinc. It is necessary to note that by involving the particles of PF resin in a zinc matrix we can obtain materials with properties differing from those of the individual materials.

2. Experiment

For electrodeposition we used a cell shown in Fig. 2. Zinc plate of 99.9% purity was used as anode.

As cathode we used steel plates DC04 (chemical composition and mechanical properties are presented in Table 1) which were degreased with alkaline solution (Na_2HPO_4 x $12H_2O$ 50 – 60g/L, Na_2SiO_2 x $5H_2O$ 25 – 30g/L, liquid soap 2 – 3g/L, temperature 80 – 90^{0}C, time 10min), after etching with HCl15% for 1 - 2min and washing with distilled water.

Table 1. Chemical composition and mechanical properties for steel DC04

Steel	Chemical composition,%						Yield strength N mm^{-2}	Max tensile strength N mm^{-2}	Min % total elongation 80mm GL
	C	Mn	Si	P	S	Al			
DC04	0.04	0.20	0.02	0.018	0.012	0.060	210	270 – 350	38.00

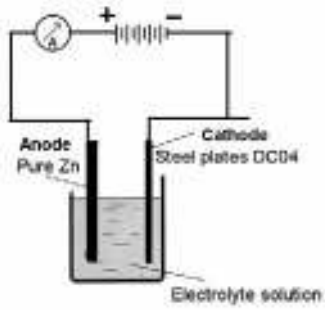

Fig. 2. Cell for electrodeposition

The PF resin/Zn composite coatings were obtained from a suspension of PF resin particles (diameter < 56 μm) in aqueous zinc sulphate electrolyte (Table 2).

Table 2. Composition and operating conditions for electrodeposition

$ZnSO_4$ x $7H_2O$	310g/L
Na_2SO_4 x $10H_2O$	75g/L
$Al_2(SO_4)_3$ x $18H_2O$	30g/L
PF resin particles	10g/L and 25g/L
Temperature	25^{0}C
pH	3.5 – 4.0
Current density	3A/dm^2 and 5A/dm^2
U	1V
Time	1h
Stirred	1000 rpm

Zinc sulphate electrolyte has cathodic polarization bigger than zinc chloride electrolyte so that we used sulphate electrolyte for electrodeposition. Sodium sulphate increase the conductibility and ability to disperse and aluminum sulphate was used as buffering agent which stabilized the acidity of electrolyte. Concomitantly we obtain more shining layers.

Phenol-Formaldehyde resin is a highly crosslinked thermosetting material that is produced by the poly-condensation of phenol and formaldehyde in the presence of either acidic or basic catalyst. An acid catalyst is usually used in preparing NOVOLAC type of resin. A novolac resin is produced if the mole ratio of formaldehyde to phenol (F/P) is greater than one [14]. This procedure produces relatively linear chains with typical molecular weights between 500 and 1000g/mol (see Fig. 3).

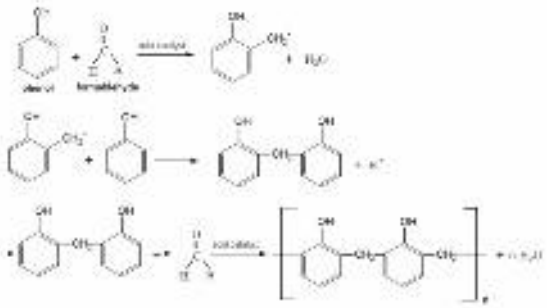

Fig. 3. Schematic illustrating the formation of the novolac type structures

The properties of PF resin type NOVOLAC with commercial name RESITAL 6358/1 synthesised by HÜTTENES – ALBERTUS Germany are presented in Table 3.

Table 3. Properties for RESITAL 6358/1

Melting point	70 – 80 º C
Sliminess at 120^{0}C	35 – 55 Pa s
Flow length	40 – 50 mm
Phenol	< 1 %
Water	**<** 0,5 %

For electrochemical corrosion measurements we used a three-electrode open cell with pure zinc and PF resin/Zn composite coatings as working electrode (WE), a platinum gauze as counter electrode (CE) and an Hg/Hg_2SO_4/saturated K_2SO_4 solution electrode as reference electrode (SSE = +670mV/NHE). As test solution 0.5 M sodium chloride was used.

The morphology of deposits was examined by scanning electron microscopy (SEM).

3. Results and discussions

Figures 4 – 7 compare a pure zinc coating and PF resin/Zn composite coating obtained at 3A/dm^2 and 5A/dm^2 current density, 1h stirred at 1000 rpm with different concentration of PF resin particles 10g/L and 25g/L (2000x magnification).

The surface morphology of layers is different compared with pure zinc coated. The pure zinc coating has a rather regular surface, whereas the composite coatings surface has fine surface structure. By increasing the PF resin concentration in the zinc electrolyte the surface structure of composite coating is changed more to finer crystallites. The PF resin acts as reducing the crystals size of electrodeposited zinc during co-deposition. The PF resin could have an inhibition effect of zinc crystals growth and a catalytic effect in increasing nucleation sites.

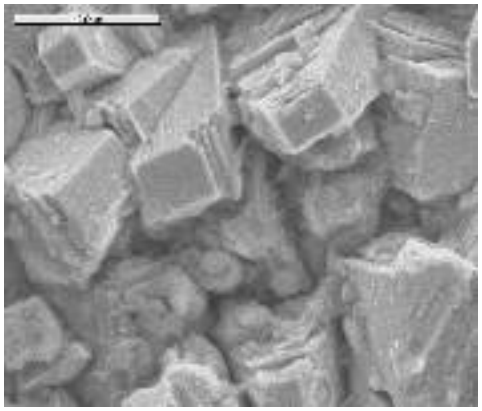

Fig. 4. SEM surface morphology of pure zinc electroplating obtained at 3A/dm^2 (2000x)

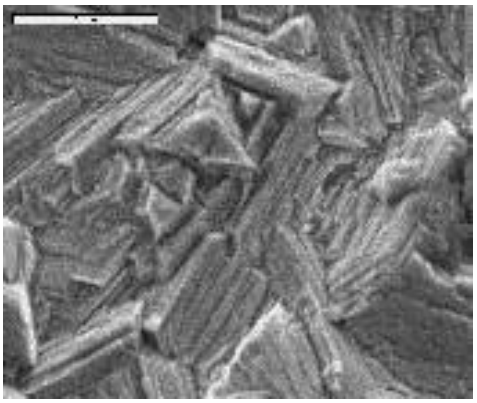

Fig. 5. SEM surface morphology of pure zinc electroplating obtained at 5A/dm^2 (2000x)

The thickness of pure zinc layers obtained at 3A/dm^2 and 5A/dm^2 current density, 1h stirred with 1000 rpm is 38.86 μm, respectively 58.24 μm.

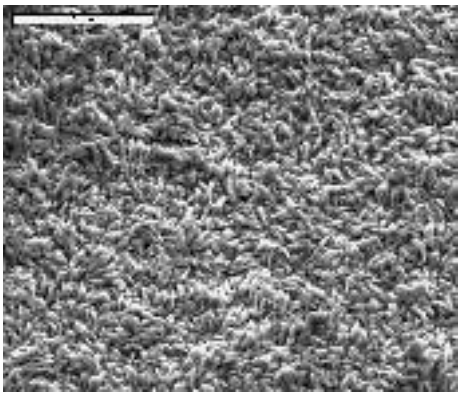

Fig. 6. SEM surface morphology of PF resin/Zn composite coatings (10g/L PF resin) obtained at 3A/dm^2 (2000x)

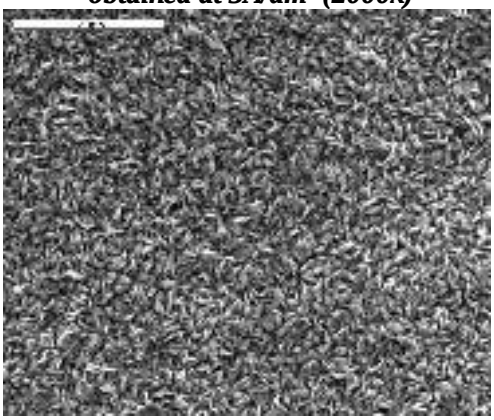

Fig. 7. SEM surface morphology of PF resin/Zn composite coatings (25g/L PF resin) obtained at 5A/dm^2 (2000x)

By adding PF resin particles the thickness of layers obtained in same conditions is a little smaller 34.27 μm for layers obtained by electrodeposition process with 10g/L PF resin at 3A/dm^2 and 55.19 μm for layers with 25g/L PF resin at 5A/dm^2 (Figure 8).

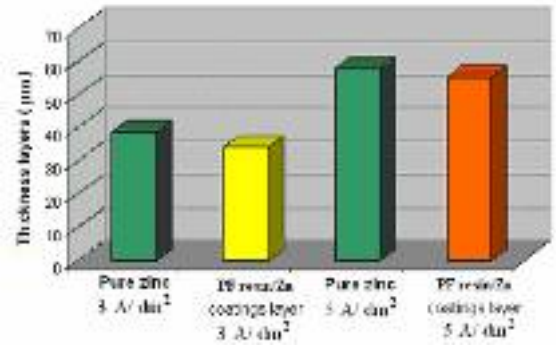

Fig. 8. Comparative thickness of pure zinc and PF resin /Zn layers obtained by electrodeposition at 3A/dm^2 and 5A/dm^2 with 10g/L, respectively 25g/L PF resin in electrolyte solution

We could observe that if we increase the current density the thickness of pure zinc and coatings layers increase. By adding PF resin particles in electrolyte solution the thickness of layers obtained is lesser, but not too much than pure zinc obtained under same conditions for electrodeposition. The decreases of layers obtained with resin particles may be explained by fine structure of composite particles.

The electrochemical investigation of each sample began with monitoring of the OCP change immediately after the immersion into the testing solutions till reaching a relatively stable stationary value. The performed potentiodynamic diagrams for pure zinc and PF resin/Zn composite coatings in 0.5M sodium chloride are presented in Figure 9.

In corrosion, quantitative information on corrosion currents and corrosion potentials can be extracted from the slope of the curves, using the Stern-Geary equation, as follows [15]:

$$i_{corr} = \frac{1}{2.303 R_p} \frac{\beta_a \beta_c}{\beta_a + \beta_c} \qquad (1)$$

- i_{corr} is the corrosion current density in Amps/cm^2;
- R_p is the corrosion resistance in ohms·cm^2;
- β_a is the anodic Tafel slope in Volts/decade or mV/decade of current density;
- β_c is the cathodic Tafel slope in Volts/decade or mV/decade of current density;
- the quantity, $(\beta_a \beta_c)/(\beta_a + \beta_c)$, is referred to as the Tafel constant.

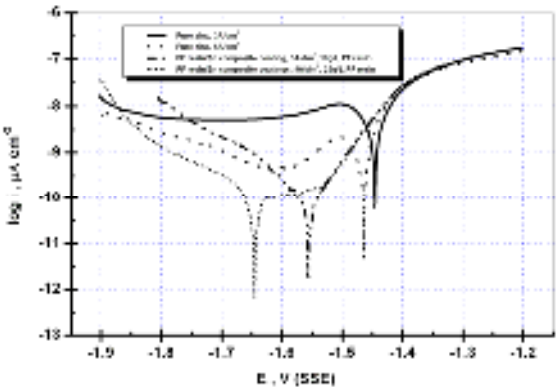

Fig. 9. Comparative polarization potentiodynamic curves for pure zinc and PF resin/Zn composite coatings in 0.5M sodium chloride solution obtained after 30 min from immersion time (log scale).

The corrosion potential (E_{corr}), corrosion current density (i_{corr}) and polarisation resistance (R_p), which were obtained from the potentiodynamic polarisation curves are summarized in Table 4.

Table 4. Polarization resistances values of pure zinc and PF resin/Zn composite coatings calculated from polarization potentiodynamic curves obtained after 30 min from immersion in 0.5M sodium chloride solution

Type of coatings	**E_{corr}, V;** Hg/Hg_2SO_4	**i_{corr},** $\mu A/cm^2$	**β_a,** mV/ decade	**β_c,** mV/ decade	**R_p from Tafel,** $\Omega\ cm^2$	**v_{corr},** µm/year
Pure zinc coating 3A/dm^2	- 1.45	239.98	47.70	31.74	34.54	360.54
Pure zinc coating 5A/dm^2	- 1.47	65.32	40.64	17.50	127.34	89.84
PF resin/Zn composite coating 3A/dm^2, 10g/L resin in electrolyte solution	- 1.53	3.32	32.83	29.30	238.75	34.13
PF resin/Zn composite coating 5A/dm^2, 25g/L resin in electrolyte solution	- 1.64	0.87	26.31	26.93	430.19	5.17

The corrosion potential is shifted to more negative values for PF resin/Zn composite coatings (- 1.64V for coatings obtained at 5A/dm^2 with 25g/L resin in electrolyte solution, respectively - 1.53V for coatings obtained at 3A/dm^2 with 10g/L resin in electrolyte solution) than pure zinc coatings (- 1.47V for coating obtained at 5A/dm^2 and - 1.45V for coating obtained at 3A/dm^2). From potentiodynamic polarization curves the polarization resistance of pure zinc coating obtained at 3A/dm^2 is 34.54Ω cm^2 and for pure zinc coating obtained at 5A/dm^2 is 127.34Ω cm^2 in 0.5M sodium chloride. The polarization resistance of PF resin/Zn coatings are bigger and the values is 238.75Ω cm^2 for coatings obtained at 3A/dm^2 with 10g/L Pf resin in electrolyte solution, respectively 430.19Ω cm^2 for coatings obtained at 5A/dm^2 with 25g/L Pf resin in electrolyte solution in 0.5M sodium chloride solution.

From experimental data was observed that corrosion rate has a big value for pure zinc coatings obtained at 3A/dm^2 (360.54μm/year) and small value for PF resin/Zn composite coatings obtained at 5A/dm^2 with 25g/L PF resin in electrolyte solution (5.17μm/year). It was observed that by adding PF resin particles in zinc electrolyte for electrodeposition it was obtained PF resin/Zn composite coatings most resistant at corrosive attack at 0.5M sodium chloride solution than pure zinc obtained from electrodeposition where the same conditions.

4. Conclusions

Our work proved that PF resin particles type NOVOLAC with commercial name RESITAL 6358/1 could be codeposited with zinc to obtain composite coatings.

The surface morphology of composite coatings layers is different compared with pure zinc coated. The regular crystal structure characteristic of electroplated zinc coatings was disturbed by PF resin particles that perturb the zinc growth during electrodeposition. By adding PF resin in zinc electrolyte for electrodeposition we obtained a very good distribution of PF resin particles on zinc surface.

The corrosion potential is shifted to more negative values for PF resin/Zn composite coatings comparative with corrosion potential for pure zinc coatings.

From potentiodynamic polarization curves the polarization resistance of pure zinc coating obtained at 3A/dm^2 and 5A/dm^2 is smaller than polarization resistance of PF resin/Zn composite coatings obtained under the conditions for electrodeposition. The biggest value of polarisation resistance (430.19Ω cm^2) was obtained for coatings obtained at 5A/dm^2 with 25g/L Pf resin in electrolyte solution in 0.5M sodium chloride

By adding PF resin particles in sulphate zinc electrolyte for electrodeposition we obtain a very fine surface structure of composite coatings, consideredas a method of obtaining nanocomposite coatings and the layers obtained are most resistant at corrosive attack in 0.5M sodium chloride solution than pure zinc obtained from electrodeposition under the same conditions.

References

[1]. Karl U. Kainer, 2006, ***Metal matrix composite***, ISBN 3-527-31360-5, Publisher Wiley

[2]. T. W. Clyne, P. J. Withers, 1993, ***An Introduction to Metal Matrix Composites,*** Cambridge University Press, Cambridge

[3]. K. K. Chawla, 1998, ***Composite Materials: Science and Engineering***, Springer-Verlag, New York

[4]. TechTrends, 1990, ***International Reports on Advanced Technologies: Metal Matrix Composites***: ***Technology and Industrial Application***, Innovation 128, Paris

[5]. A. M. Alfantazi, U. Erb, 1996, ***Corrosion properties of pulse-plated zinc-nickel alloy coatings,*** Corrosion, Volume 52 , Number 11, p. 880-888

[6]. Kh. M. S. Youssef, C. C. Koch, P. S. Fedkiw, 2004, ***Improved corrosion behaviour of nanocrystalline zinc produced by pulse-current electrodeposition***, Corrosion Science, Volume 46, Number 1, p. 51-64

[7]. I. Zhitomirsky, L. Gal-Or, A. Kohn and H. W. Hennicke, 1995, ***Electrodeposition of ceramic films from non-aqueous and mixed solutions***, Journal of Materials Science, Volume 30, Number 20, p. 5307-5312

[8]. G.N.K. Bapu, G. Devaraj and J. Ayyapparaj, 1998, ***Studies on non-cyanide alkaline zinc electrolytes***, Journal of Solid State Electrochemistry, Volume 3, Number 1, p. 48-51

[9]. Edward Budman, 1995, ***Alkaline Noncyanide Zinc Plating,*** Metal Finishing, Volume 93, Number 2, p. 60-63

[10]. J. M. Degorre, 1993, ***Electrolytic zinc coating development,*** Galvano organo, Volume 62, Number 639, p. 845-846

[11]. Wang Ruixiang, 1992, ***Cailiao Baohu***, Volume 25, Number 11, p. 33-35

[12]. Ma Chong, 1991, ***Cailiao Baohu***, Volume 24, Number 7, p. 22-24

[13]. Yanjerappa Arthoba Naik, Thimmappa Venkatarangaiah Venkatesha, Perdur Vasudeva Nayak, 2002, ***Electrodeposition of Zinc from Chloride Solution***, Turk J Chem, Volume 26, p. 725 – 733

[14]. W. Wei, H. Hu, L. You, G. Chen, 2002, ***Preparation of carbon molecular sieve membrane from phenol-formaldehyde Novolac resin***, Carbon, Volume 40, Number 3, p. 465-467

[15]. M. Stern, A. Geary, 1958, ***Journal Electrochemical Soc***iety, 105, 638

[16]. W. Wei, H. Hu, L. You, G. Chen, 2002, ***Preparation of carbon molecular sieve membrane from phenol-formaldehyde Novolac resin***, Carbon, Volume 40, Number 3, p. 465-467

[17]. M. Stern, A. Geary, 1958, ***Journal Electrochemical Soc***iety, 105, 638

THE ANNALS OF "DUNAREA DE JOS" UNIVERSITY OF GALATI.
FASCICLE IX. METALLURGY AND MATERIALS SCIENCE
N^0. 2 – 2008, ISSN 1453 – 083X

SURFACE HARDENING OVER 38MoCrAl09 STEEL BY YAG:Nd PULSE LASER

Sorin DOBROVICI[1], Nelu CAZACU[1], Liliana SAVA[2], Adolf BACLEA[3]

[1]Dept.of Metallurgy and Materials Science, Dunarea de Jos University of Galati, Romania,
[2]Unita VIG, Bucuresti, Romania,
[3]Socomar SRL, Sorento, Italy
e-mail: Nelu.Cazacu@ugal.ro, Sorin.Dobrovici@ugal.ro

ABSTRACT

Laser offers unique capabilities for high energy concentrations at small surfaces. Factors that have influences over interactions between laser beam and steel surfaces have very high control. Pulse laser YAG:Nd is usually used for cutting and welding. Paper is based on hardening experiments using KVANT 17 (YAG:Nd) pulse laser over 38MoCrAl09 steel. Results were investigated by hardness (HV5) macrographic and micrographic method.

KEYWORDS***:*** laser, YAG:Nd, hardening, steel

1. Introduction

Lasers have progressed from a laboratory curiosity to an industrial tool. Most of today's industrial lasers output infrared light in the form of a beam that is converted to heat energy when it interacts with a material being processed. Cutting and welding laser systems use highly focused beams having power densities in excess of 106W/cm^2 to quickly melt and vaporize metals. Because these two industrial applications total nearly 95% of all laser systems sold, the use of lasers for surface modification is often overlooked, [6]. Superficial hardness is obtaining through beam energy distribution with low intensity for superficial heating of surface between melting points. The principal condition for process is energy uniform distribution over metallic material surface. That conduces to a uniform heating layer depth. Heating by power laser is characterized by high heating speed (pulse laser beam) from ambient temperature to austenitic domain.

After heating laser beam is stopped (pause), heat from superficial layer is transmitted by material diffusivity to adjacent volumes with very high speed and a local quenching is realized. Cooling speed is higher by critical quenching speed that means an auto quenching process and an exterior quenching mediun is unnecessary. The heat is lost by thermal conductivity from heating layer to material core and cooling speed is approaching to 1000°C/s.

Maximal temperature (°C) in superficial layer is given by relation:

$$T_{max} = \frac{2F_0\sqrt{at}}{\lambda\sqrt{\pi}} \quad (1)$$

where: F_0 – power density, W/cm^2, a – thermal diffusivity, cm^2/s, λ – thermal conductivity, W/°C·cm; t – time, s. After surface heating by pulse laser it is possible to obtain martensitic total transformations, but a quantity of residual austenite is normally present in microstructure. A cooling process is preferable to continue under 0°C.

Laser hardening is characterized by:

- Laser beam power increasing for a constant speed of part moving conduces to decreasing hardness
- Speed and beam power are control factor for depth hardening layer and for incident interaction surface
- Hardness obtained by laser quenching is higher by furnace heating and liquid quenching
- Laser hardening is easily optically controlled and depth of quenching layer is uniform
- Hardness is depending on thermal conductivity of material

Superficial hardening by YAG:Nd pulse laser is influenced by: steel hardenability (chemical composition), laser beam energy measured through accumulator supply of optical pumping system (at capacity battery connector), pulse frequency; focalization of laser beam at material surface (defocused).

2. Experimental conditions

Pulse laser KVANT 17 (made CIS) has solid active media by YAG:Nd ($Y_3Al_5O_{12}$).

Some important characteristics are: active media dimensions diameter 6.3 mm and length 100 mm; wave length 1.06 μm (IR); pulse time 2…5ms; pulse frequency 1…20 Hz; objective focal length 50 mm; surface diameter of interaction 0.3…1.3mm; pulse energy, min. 8J.

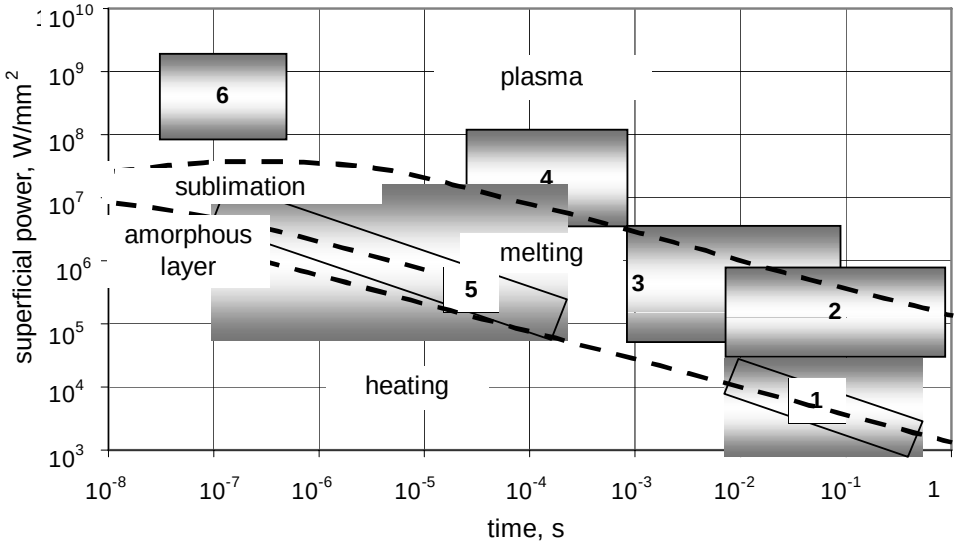

Fig.1. Basic processes and laser thermal applications in function of specific power and irradiation time: 1- superficial hardening, 2- alloying, 3- cutting and welding, 4-drilling, 5-glazing (amorphous layer) and superficial melting, 6- thermal pulse hardening, 0.

Table 1. Relative comparison of different lasers used for heat treatments

Laser type	Wave length	Absorption efficiency	Initial cost	Operating cost	Expectede life
	nm				
CO2	10,6	Low	Low	Moderate	High
YAG:Nd	1,06	Moderate/High	High	High	High
HPDD	800	High	Moderate	Low	Low

Table 2. Chemical composition for 38MoCrAlO9 (mass %)

Steel	Chemical compositon								
	C	Mn	P	S	Si	Mo	Cr	Ni	Al
38MoCrAl09	0,410	0,530	0,022	0,011	0,330	0,180	1,350	0,110	0,860

For experiments was used 38MoCrAl09 steel with final heat treatments (quenching and tempering). Chemical composition is shown in Table 2. The experimental hardening regimes using YAG:Nd pulse laser are showing in Table 3. No used additional sample surface painting and no additional cooling system for quenching.

3. Results and discussion

Hardening surface was investigated macroscopically, micrographically and by surface hardness. In Fig. 2 and Fig. 3 are shown macrographs with typical surface after laser hardening. A local melting is present and surface craters were formed because a high local energy was concentrated at the material surfaces (Fig. 2). A normal surface hardening by laser beam is presented (Fig. 3) when oxidizing surfaces appear at interactions surfaces with oxygen because the temperature is in austenitic domain.

Macrographs for different samples are shown in Fig.4. Hardness increased for all experimental regimes (Fig.5). For 0 mm defocused hardness is higher over initial hardness 300 daN/mm^2 from 520 daN/mm^2 (550V) to 650 daN/mm^2 (900V). Hardness variation had a decreased zone and a increased zone. In the decreased zone hardness has a linear decrease with capacitor voltage from 520 daN/mm^2 to 380 daN/mm^2. The decreased is a result of high energy

localized on a minimum surface at focal distance of objective (50mm) and practical defocused is zero. The minimum surface is 0.00785mm^2. Cooling capacity of material has a finite value and is determined by thermal conductivity of material.

In a second stage hardness is increasing because a cooling process from melt is present. A similar situation appears for 7.5mm defocused. For 5mm defocused and 550V…700V surface hardness have a linear increasing from 320daN/mm^2 to 650daN/mm^2.

Table 3. Pulse laser (YAG:Nd) hardening experimental regimes

Experiment (sample)	Acumulator supply	Defocalization	Total pulse number	Pulse Frequency	Discharge current	Total time	Hardness HV_5 final
u.m.	V	mm	-	Hz	10^{-6}A	minute	daN/mm^2
1	550	0	410	0,3	34-58	22	520
2	600	0	430	0,3	34-60	23	425
3	650	0	460	0,3	34-60	25	388
4	700	0	406	0,3	34-60	20	466
5	750	0	411	0,3	40-70	23	477
6	550	2,5	415	0,3	30-48	22	466
7	600	2,5	420	0,3	32-52	23	603
8	650	2,5	430	0,3	36-58	17	435
9	700	2,5	440	0,3	38-64	32	441
10	750	2,5	420	0,3	42-70	20	376
11	550	5	410	0,3	28-48	22	332
12	600	5	365	0,3	30-52	20	473
13	650	5	410	0,3	34-60	25	549
14	700	5	410	0,3	38-64	20	644
15	750	5	410	0,3	40-68	23	460
16	550	7,5	410	0,3	24-46	22	487
17							-
18	600	7,5	466	0,3	30-52	20	412
19	650	7,5	410	0,3	42-64	22	325
20	700	7,5	430	0,3	14-38	21	412
21	750	7,5	436	0,3	38-66	23	376
22	800	7,5	440	0,3	38-66	20	441
23	850	7,5	450	0,3	38-66	22	566
24	900	7,5	460	0,3	38-66	21	540
25	950	7,5	465	0,3	38-70	23	549
26	650	10	406	0,3	38-70	23	283
27	700	10	411	0,3	38-70	23	310
28	750	10	415	0,3	38-70	23	306
29	800	10	420	0,3	38-70	23	391
30	850	10	430	0,3	38-70	23	418
31	850	10	440	0,3	38-76	23	325
32	850	10	420	0,3	38-76	23	401
33	900	10	430	0,3	38-76	23	367
34	950	10	445	0,3	38-76	23	453
c1	800	5	440	0,3	40-76	26	418
c2	850	5	436	0,3	50-82	22	575
c3	900	5	422	0,3	54-88	21	371
c4	950	5	430	0,3	58-96	23	401
35							
36	800	0	410	0,3	44-74	20	603
37	850	0	430	0,3	48-80	22	644
38	900	0	460	0,3	52-86	23	655
39	950	0	406	0,3	52-86	21	-
40	800	2,5	415	0,3	44-76	24	-
41	850	2,5	420	0,3	46-80	20	441
42	900	2,5	430	0,3	50-92	23	353
43	950	2,5	440	0,3	64-100	24	623

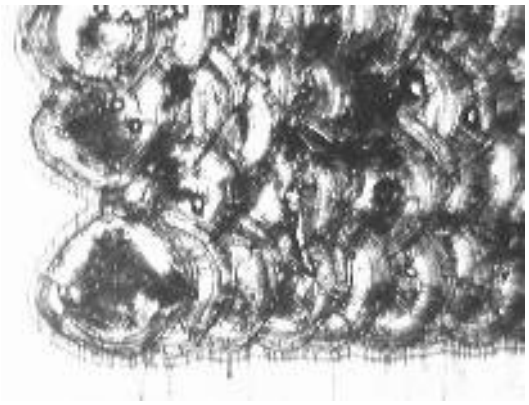

Fig. 2. Surface sample 3 (magnitude 350x).

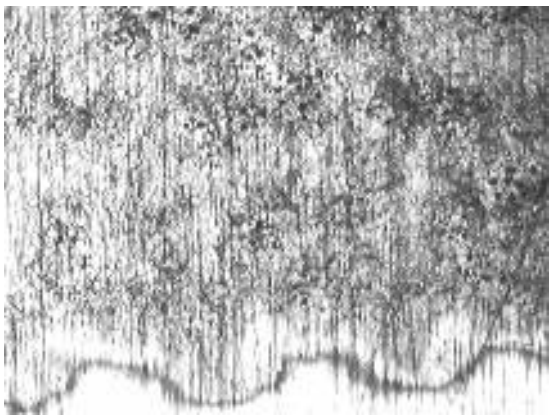

Fig. 3. Surface sample 11 (magnitude 350x).

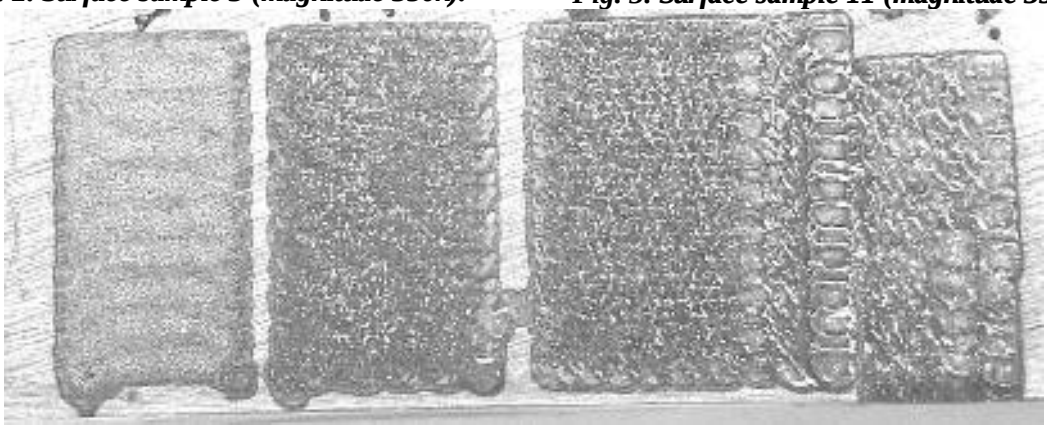

Fig. 4. Surface macrograph (samples 18, 19, 20, 21). Magnitude 10x

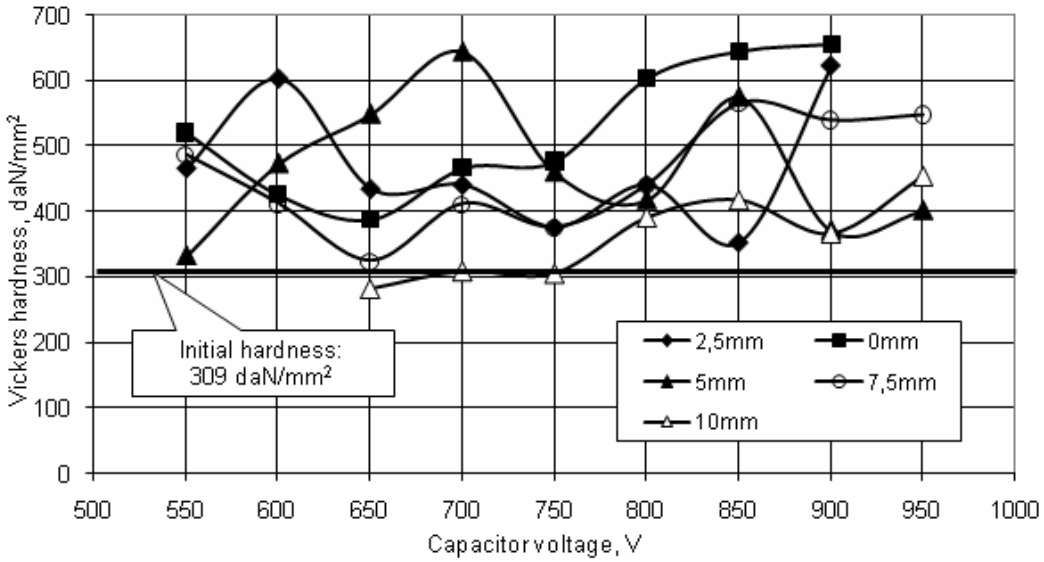

Fig.5. Hardness variations after pulse laser hardening for experimental regimes.

For 700V capacitor voltage, a maximum of hardness was obtained, approx. 650daN/mm^2.

If accumulator supply is increasing over 700V, the energy of laser pulse beam is increasing and hardness is decreasing because local heating energy is higher and auto quenching time is too short.

Over 800V local melting is present and hardness is difficult to measure (Fig.2).

Surfaces are hardened by cooling from melt. A similar situation is for 2.5mm defocused. For 10mm defocused, hardness is increasing only for 750V… 850V capacitor voltage.

4. Conclusions

The KVANT 17 pulse laser with solid active media (YAG:Nd) is normally used for cutting and welding. By adapting a xy plotter controlled by computer, small pieces (samples) is moving relatively to laser beam. Interaction energy was controlled by defocused and indirect measurement of energy (capacitor voltage).

Hardening surfaces by pulse laser YAG:Nd is possible to realize for small surfaces. For 38MoCrAl09 steel an increasing of hardness from 309 daN/mm^2 to 650 daN/mm^2 was obtained under the presented experimental condition.

References

[1]. Ganeev R.A, 2002, ***Low-power laser hardening of steels***, Materials Processing Technology, Elsevier Pbs. No.121 pg. 414-419

[2]. Popescu N, Gheorghe C, Popescu O, 1990, ***Tratamente termice neconvenţionale***, Editura tehnică, Bucureşti (pag.223…245)

[3]. Samoila C, Ionescu M.S, Drugă L, 1986, Tehnologii şi utilaje moderne de încălzire, Editura Tehnică, Bucureşti, (pag.291…360)

[4]. Ursu I, Mihăilescu I.N, Prokhorov A.M, Konov V.I, 1986, ***Interacţiunea readiaţiei laser cu materialele***, Editura Acadamiei, Bucureşti

[**5]. Donţu O**, 1985, ***Tehnologii de prelucrare cu laser***, Editura tehnică, Bucureşti

[6]. Joel De Kock, 2001, ***Laser Machining Inc***., Somerset, Wis, Lasers Offer Unique Heat Treating Capabilities Industrial Heating, Oct 2001.

THE ANNALS OF "DUNAREA DE JOS" UNIVERSITY OF GALATI.
FASCICLE IX. METALLURGY AND MATERIALS SCIENCE
N^0. 2 – 2008, ISSN 1453 – 083X

RESEARCH FOR REALIZE THE CONFIGURATION OF WIND ENERGY TURBINE

Viorel DRAGAN, Madalina Cristina DRAGAN, Stefan BALTA
Universitatea"Dunărea de Jos" din Galaţi
e-mail: stefan.balta@ugal.ro

ABSTRACT

For already quite some time, the word energy has received a somewhat negative connotation. Some circles want to make us believe that energy is something that one should have disgust for; a necessary evil that should be avoided at any price. With such unqualified negative thinking that omits recognition of the positive contributions, and that focuses only on the side effects and shadow sides, without paying attention to the technological solutions that can "neutralize" the disadvantages, mankind will not be served well. Such attitudes will have a rather lethargic effect on a healthy development of society.

KEYWORDS: energy source, wind power, global warming

1. Introduction

For the next 20-40 years, there is an ample physical availability of primary energy sources. The current estimations for oil and gas reserves are about 40 and 60 years, respectively. For coal, the estimations are 200 to 300 years, whereas for uranium it depends whether one opts for reprocessing and breeding or not: these reserves vary between 50 and 3000 years depending on the option chosen. If one takes into account the non-conventional fossil sources such as tar sand and oil shale, if one counts on the availability of the massive resources of methane hydrates in the deep ocean, on the uranium concentration in the seas or on the thorium cycle, or even on nuclear fusion from deuterium and tritium, it is obvious that the physical presence of primary energy is not really a concern. In any case, we could still continue to use it for quite a while, at least from the point of view availability. [1]

Today there are many investments made in research on new and cheaper ways of producing electricity in which wind power systems and solar panels play an important role. A great concern is raised over the environmental aspects of how electric energy is being produced varying from pollution by gases or toxic waste up to the visual aspect. However, next to the environmental issues mentioned above, there is one major problem for which there is no easy and cheap solution: the greenhouse effect.

This problem is indeed of a global nature. It has such far reaching consequences, that it is appropriate to spend some time on it.

At first sight, it is simple. The presence of gasses such as water vapour and carbon-dioxide (CO_2) in the atmosphere, guarantees that we know mild temperatures on the earth. Without these gasses, the temperature on earth would be about 30^{0}C lower. An increase of those gasses would therefore lead to a global temperature increase on earth (figure 1). This effect is called the greenhouse effect (IPCC, 1996; Houghton, 1997)

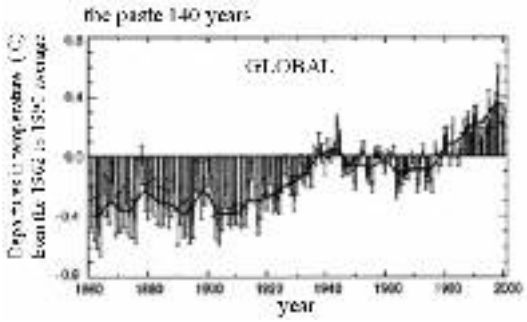

Fig. 1. The Earth's surface temperature increases

The lack of fossil fuel, that thermo plants use, is predicted to end in the near future. A bigger problem when using fossil fuel are the nooses resulted from combustion. This can be solved by developing filters for the nooses and to find cheaper ways to get rid of nuclear waste. Therefore the industry reoriented its interest to more environmentally friendly solutions.

[2]. The most common used alternatives, to provide energy for home use purposes, are residential micro-grid built using both wind power system and solar panels.

The direct proportionality between energy (power) produced by a solar panel and the area exposed to the sun has a great influence over the price of this type of equipment. The technology of fabrication for photovoltaic cell system has been under development for quite a while now but still expensive reciprocal of its power production. [3]

Denmark was the first country to use wind for generation of electricity. The history of wind turbines goes back to the 19th century. In 1890 there was already a fully operational working wind turbine to generate electricity. At the beginning of the 20th century, several hundred units with capacities up to 25 kW were in operation in Denmark [1]. In America, commercial types of wind-electric plants started to appear in the interbelic period.

2. What is and how does the wind power generation system work

Wind power generation consists of electric energy creation, usually at grid parameters, by using different types of rotary systems which harness the power of the wind. These rotary systems may have the main shaft horizontally or vertically. The horizontal position of the shaft is found in the most wind turbines when the vertical position of the shaft can be located only in a few applications and they are usually of low power (under 5 kW).

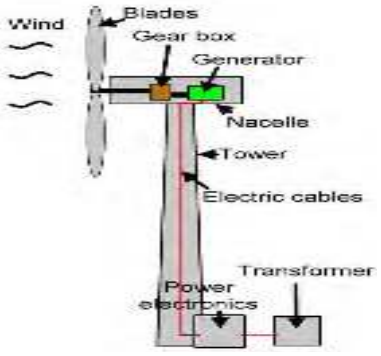

Fig. 2. Wind turbine – Basic configuration

A wind turbine uses the horizontal moving of air because this movement is the most powerful type of air current that can be used to rotate a propeller (a rotor in our case). The ascendant, or vertical, flow of air is found only in small regions and it is rarely detected nor it presents any powerful force. [4] The basic idea of how a wind turbine works can be seen in Figure 2 and described in the following paragraphs.

The horizontal flow of air blows over the rotary system on the wind turbine causing it to rotate in a certain direction. Because the rotor is a big component it needs a certain wind speed to put it on motion (usually above 5 m/s). Some wind turbines allow adjustments to be made to the blades attack angle. In this case the blades can be adjusted to a maximum efficiency level. By doing this, it allows the rotor to turn at an optimum level. Not all the time the blades adjustment can give an optimum performance, to reach it, the nacelle must also turn.

The maximum efficiency is reached when wind direction is parallel with the nacelle and the blades are configured for the actual wind speed.

If the wind turbine needs to be shut down, for various reasons including maintenance, it uses both a mechanical and electrical breaking system to turn the rotor off.

The mechanical breaking system can be mounted on the main shaft before or after the gear box. The electrical breaking system is made by turning the generator into a motor. This type of breaking cannot stop the rotor completely. Therefore there is also a mechanical breaking system.

The mechanical breaking system uses hydraulic or air pressure for locking the rotor in a fixed position.

The propeller, in our case is named a rotor because it converts mechanical energy into torque rather than torque into mechanical energy as a propeller is doing in cases of airplanes, ships or other machines. The rotor received its mechanical energy from the wind and converts the horizontal flow of air into torque at its main shaft. This torque is then converted into electric energy by the generator itself.

The generator mounted in the nacelle needs to turn at certain speeds much higher than the rotor speed. For this purpose many wind generators are using a gear box to amplify the movement of the rotor (eg. 20 rpm) up to the speed needed by generator (eg. 1500 rpm).

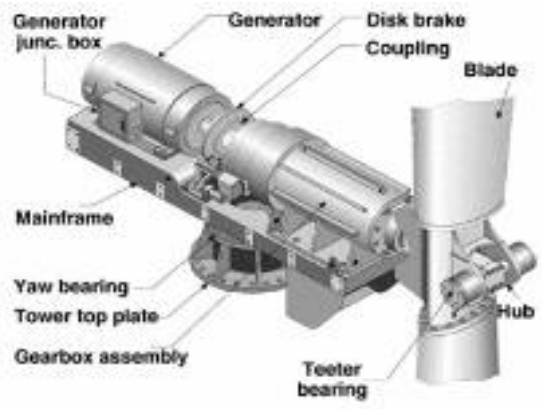

Fig. 3. Wind turbine – Main components

The main component of every wind generator system, figure 3, is the generator itself.

It is an important element because it generates electric energy by converting the mechanical energy received from the rotor.

The power, that a wind turbine generates, needs to have the appropriate parameters so it could be used successfully. To create a sinusoidal wave, that has the frequency and the voltage level compatible to the grid, a power converter is needed. This power converter will convert the energy received from the generator either DC or AC into an AC wave shape with the correct frequency and voltage level. To do that, it uses some commutation devices IGBTs or MOSFETs that need to be commanded by a DSP or other device so that the output voltage will meet its requirements.

After the AC voltage was created, it can be used in homes or if it is connected to power grid it needs to be prepared for transport, this being done by a transformer which raises the voltage to some high levels (20 kV or more).

3. Configuration of wind system

Currently, there are several main wind turbine (WT) configurations: fixed speed and directly grid connected wind turbine, variable speed WT with squirrel cage induction generator, variable-speed WT with double fed induction generator or variable speed, direct-driven synchronous generator. For every configuration presented bellow there could be several variations.

3.1 Configuration 1

The first configuration, figure 4, consists of several components connected in series to one another. In this configuration the rotor is connected directly to the synchronous generator. The power transfer from the generator to the grid is made by using a bidirectional converter. This converter allows full control to both active and reactive power. Because of using a synchronous generator the power converter should be designed to handle full power. The full power zone is reached when the wind has the potential of turning the rotor at generator nominal speed.

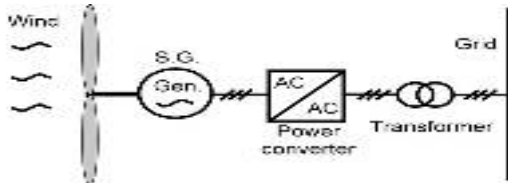

Fig. 4. Wind turbine – configuration 1

This could be considered as an advantage, because it assures that sometimes it could function at nominal parameters.

This configuration also has its disadvantage by using a big and heavy generator. Also, because the generator has permanent magnets (PM), it is an expensive apparatus.

Because it doesn't use a gear box it could be considered a simple wind turbine from a mechanical point of view but the power converter control system is a little bit more complicated than the other configurations.

3.2 Configuration 2

As seen in Figure 5, the configuration involves using a gear box for transferring the power from the rotor to the generator. This allows a smooth control of the power that is produced. The generator is not so expensive in this case because it doesn't have PM or other components that are expensive. The gear box and the induction machine generator allow the system to work at variable speed.

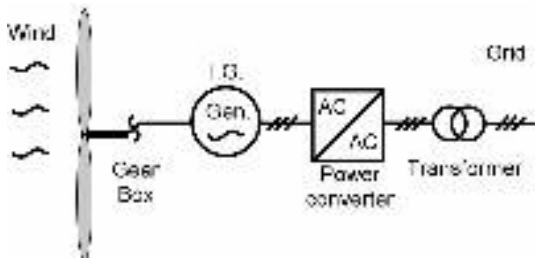

Fig. 5. Wind turbine – configuration 2

The squirrel cage induction generator must receive a certain amount of power from the grid to generate electric current. This is done by using a bidirectional converter between the generator and the grid.

The converter allows a flow of current in both directions through controlling both active and reactive power. It has to be designed to withstand full load because there are cases where the generator could generate power at nominal ratings. This configuration can be used for both grid-connected or standalone applications because of the flexibility allowed in its control. Also a big advantage is the variable speed that it can operate though not depending on the wind speed.

3.3 Configuration 3

The 3rd configuration differs from the other 2 because of the design and the components that it uses. In this case the power converter is only designed to withstand 25 % of nominal power.

The transformer has tertiary windings.

The generator, figure 6, is constructed to allow access to both rotor and stator windings. The stator windings are used for grid connection and the rotor windings are connected to the power converter.

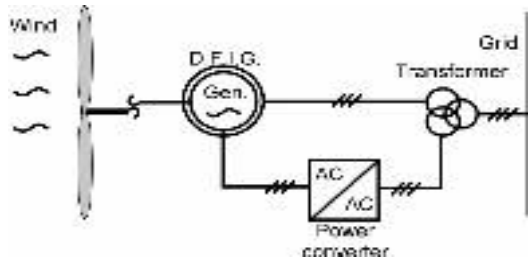

Fig. 6. Wind turbine – configuration 3

As in the above two cases, the power converter is also bidirectional. The bidirectional power converter is used especially because it allows a smooth control of active and reactive power.

For all power converters that are bidirectional, a great care should be taken to assure correct firing of the IGBTs or MOSFETs used in the high power section of the converter. The command part for this type of power converter is a little more complicated like the one used for 2 quadrant converter because it must check the power flow and control 2 inverters instead of one.

3.4 Configuration 4

This configuration is different from the other configurations because it uses a softstarter to allow the generator to start slowly (softly). This type of configuration is a more robust solution.

The soft-starter is not such an expensive component but the mechanical construction raises some difficulties because it has to support a certain amount of stress. Its major disadvantage is that it operates at constant speed with only 1-2% speed variation.

Also the system is very sensitive to the wind and, because of this, it gives certain power pulsations.

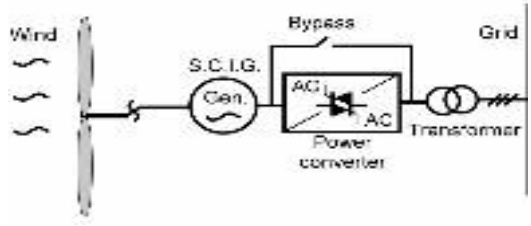

Fig. 7. Wind turbine – configuration 4

3.5 Chosen Configuration

Taking into consideration the above possible configurations, number 2 has been selected. In this configuration the gear box has been eliminated. The bidirectional converter will have to control the generator energy flow more rigorously as a normal converter will do because it has to provide power to and from the generator in the same time. Also the cost for the induction generator is very small compared with a synchronous machine or other type of machine for that matter. We consider this configuration to be easier to implement from a mechanical point of view. Also, for this system, the components are not so expensive and can be easily found. The only problem will be the power converter where the control system is a little more complex then the one used for a simple inverter.

4. Influence of wind speed over electricity generation

The amount of wind at a certain site is critical as it determines the amount of energy the turbine will produce. The best site for a wind turbine is where the wind speeds exceeds 5 m/s as higher the average wind speed for a region is, the better is for a wind turbine farm to be constructed. For example, a 10 kW turbine with an average annual wind speed of 4.47 meters per second produces about 7 700 kWh per year. The same turbine produces about 12500kWh per year at a site with an average annual wind speed of 5.36 meters per second. If the wind exceeds a critical speed limit the turbine is shut down. But in nowadays most of the wind turbines have a braking system, electrical one or mechanical one so most off wind speed problems are solved by mechanical brake or electrical brake. [5]

The wind resource can vary significantly over an area of just a few kilometers because of local terrain influences on the wind flow. There are resources that can be used to help determine the wind resources in your area:

• wind resource maps can be used to estimate the wind resource in your area;

• observation of an area's vegetation is an indicator of the wind resources in an area, for example trees can be permanently deformed by strong winds;

• the most accurate measurement is done through direct monitoring by a wind resource measurement system; however, this can be very expensive

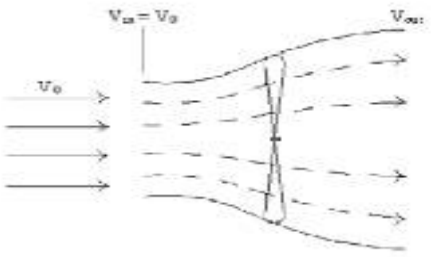

Fig. 8. Wind Speeds Increase with Height

Equation 1 formula illustrates factors that are important to the performance of a wind turbine. Notice that the wind speed, V, has an exponent of 3 applied to it. This means that even a small increase in wind speed results in a large increase in power. That is why a taller tower will increase the productivity of any wind turbine by giving it access to higher wind speeds. The formula for calculating the power from a wind turbine is:

$$P = k\ C_p\ \frac{1}{2}\ \rho\ A\ V^3 \qquad (1)$$

Where: P - Power output, kilowatts;

Cp – Maximum power coefficient, ranging from 0.25 to 0.45, dimension less (theoretical maximum = 0.59)

ρ – Air density, is about 1.25 Kg/m3 in normal conditions of temperature, pressure, see level etc.

A – Rotor swept area, m2 or π D2/4 (D is the rotor diameter in m, π = 3.1416)

V – Wind speed, m/s

k – 0.000133 A constant to yield power in kilowatts. (Multiplying the above kilowatt answer by 1.340 converts it to horsepower – i.e., 1 kW = 1.340 horsepower).

Speed variation take-in consideration the height of the tower as seen in equation 2:

$$\frac{V}{V_0} = \frac{h}{h_0}^{\alpha} \qquad (2)$$

Where: V0 – is wind speed in m/s at the ground level h = 0

a – coefficient characteristic to a location, α=0.1÷0.4

5. Conclusions

The future energy policy should not be based on an attitude "either", "or". Because of the serious challenges that we have to face, and taking into account the dynamics and its consequences due to the liberalization of the markets, we cannot afford that "luxury". The energy policy will have to be based on "this and that". All possible routes must be considered. For the time being, the energy world manages to get by. But, in the long run, one will have to "intervene" drastically. We hope that our current generation will take up its responsibility and that it invests in as many realistic long term options as possible. Only then, we will sufficiently pay back for our "consuming" of the fossil sources.

Wind energy is an ideal renewable energy because:

1. it is a pollution-free, infinitely sustainable form of energy
2. it doesn't require fuel
3. it doesn't create greenhouse gasses
4. it doesn't produce toxic or radioactive waste.

Wind energy is quiet and does not present any significant hazard to birds or other wildlife. When large arrays of wind turbines are installed on farmland, only about 2% of the land area is required for the wind turbines. The rest is available for farming, livestock, and other uses. Landowners often receive payment for the use of their land, which enhances their income and increases the value of the land. Ownership of wind turbine generators by individuals and the community allows people to participate directly in the preservation of our environment. Each megawatt-hour of electricity that is generated by wind energy helps to reduce the 0.8 to 0.9 tones of greenhouse gas emissions that are produced by coal or diesel fuel generation each year.

References

[1]. K. Voorspools en W. D'haeseleer, ***"De energetische en ecolgische impact van de implementatie van WKK in de Begische energetische context"***, TME raport #TME/WDH/99-07/FIN, K.U.Leuven, Afdeling Toegepaste Mechanica en Energiecnversie, Leuven, december 1999.

[2]. Australian Greenhouse office. Australian Greenhouse office website. [Online] [Cited: September 19, 2007.] www.greenhouse.gov.au.

[3]. Rashid, Muhammad H., 2001, Power Electronics Handbook. s.l.: Academic Press

[4]. A. Martes, *"Technische evaluatie van WKK in grote genbouwen", studiedag "REG in grote genbouwen",* Antwerpen 25 september 1997

[5]. U.S. Department of Energy, 2003, ***Small Wind Electric Systems***. s.l.: U.S. Department of Energy, National Renewable Energy Laboratory, a DOE national laboratory, June. DOE/GO-102005-2095.

[6]. Grigsby, Leonard L., 2000, ***The Electric Power Engineering Handbook*** (Electrical Engineering Handbook). s.l. CRC, September 28, ISBN13: 978-0849385780.

THE ANNALS OF "DUNAREA DE JOS" UNIVERSITY OF GALATI.
FASCICLE IX. METALLURGY AND MATERIALS SCIENCE
N^0. 2 – 2008, ISSN 1453 – 083X

VAPORISATION OF THE METALLIC BATH COMPONENT DURING REFINING IN OXYGEN CONVERTER

Lilica IVANESCU, Alexandru IVANESCU
Elisabeta VASILESCU
"Dunărea de Jos" University of Galati
e-mail: ivanescu1944@yahoo.ca

ABSTRACT

The paper presents a series of researches regarding the vaporization of the component elements of the metallic bath and slag during refining in LD converter. Also, the main factors which influence the vaporization process during steel making in LD converter are studied: the converter atmosphere; the carbon content of the metallic bath; the speed of the oxygen jet; the temperature of the metallic bath; the blowing diagram. Based on these researches we sought to obtain a technology of steel made in LD converter so that the percentage of losses by vaporization is minimum.

KEYWORDS: oxygen converter, vaporization, sludge, slag, oxygen jet speed, critical carbon content.

1. Introduction

During steelmaking in oxygen converters, in the impact zone of oxygen jet with the metallic bath, a local temperature of 3000^{o}C is created. As a result, the boiling points of the metallic bath components are exceeded, so that a part (0.6-1.2%) of the metallic charge is volatilized as a red smoke made of fine particles having a size of approximately 1μm [1-3].

1. 1.Vaporisation of the elements from the metallic bath

In Fig. 1 it is presented the variation of vapor pressure with temperature, for some metals.

The greater is the temperature of the metallic bath in the impact zone of the jet, the greater are the vapor pressures of the component elements Mn, Cr, Cu, Si, Fe, Ni, Co, Ti and the stronger the emission of gases and metallic vapors.

These vapors are entrained by the relaxing of the CO bubbles resulted from the metallic bath decarburization. Also, as a result of the bubbles action and of the oxygen jet impact with the slag-metal emulsion surface, an entrainment of the flux fine particles is achieved, especially during slag formation. At the level of the oxygen jet impact zone, the ascending gas flow has the pressure P_t corresponding to a temperature T_1 with which the gas-vapor mixture enters the recovery unit (approx. 1923 K):

$$P_t = P_{t_1} + P_{t_2} \quad , \tag{1}$$

$$P_{t_1} = P_{Fe} + P_{Si} + P_{Mn} + P_{Al} + ... \tag{2}$$

$$P_{t_2} = P_{CO} + P_{CO_2} + P_{O_2} + P_{H_2O} + P_{H_2} \tag{3}$$

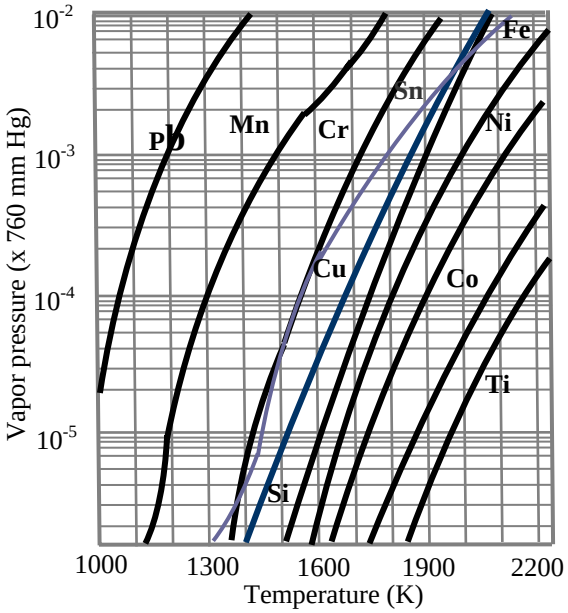

Fig. 1. Variation of the vapor pressure with temperature

Because of the oxidizing conditions in the recovery unit (false air excess) the elements vapors are oxidized and condensed at the temperature T_2

corresponding to the dew point (Fig. 2), being recovered in a proportion of 98% in the resulted sludge from the wet cleaning unit. T_3 is the temperature of condensation of the Fe, Mn and Al vapors, which were cooled with the aid of cooling water in Venturi tubes. Of the evaporated elements, Fe has an important weight and influences the level of the steel taking out [4]. The iron vaporization is influenced by the converter atmosphere, the carbon content of the iron bath; the speed of the oxygen jet, the decarburizing rate.

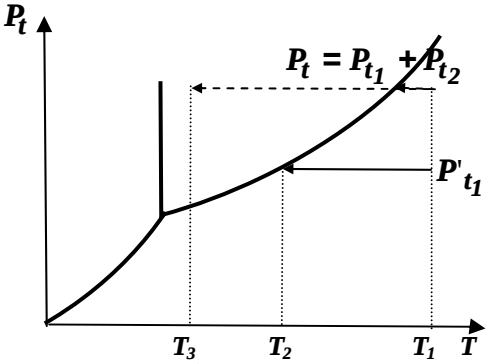

Fig. 2: Diagram of the vapors condensation of a gaseous mixture

2. The influence of the converter atmosphere upon the elements vaporization

For example it is considered the iron vaporization because Fe is quantitatively predominant in the heterogeneous system subjected to the process. As a result of the oxygen blowing, a Fe vapors counter-flow appears and determines at a distance δ from the surface of the metallic bath the formation of a fog layer of FeO, the following reaction being produced:

$$\{Fe\}+\frac{1}{2}\{O_2\}\rightarrow\{FeO\}$$

resulting for the fluxes of the Fe vapors, F_{Fe}, and of oxygen, F_{O_2}:

$$F_{Fe} = -2F_{O_2} \quad (4)$$

In conformity with Fick's law, the flux of the Fe vapors is given by the relation

$$F_{Fe} = -CD_{Fe}\frac{\partial X_{Fe}}{\partial y} + X_{Fe}(F_{Fe}+F_{O_2}) \quad (5)$$

From the relations (4) and (5) are obtained the following relations:

$$F_{Fe}(2+X_{Fe}) = -2CD_{Fe}\frac{\partial X_{Fe}}{\partial y} \quad (6)$$

$$\int_0^{\delta} F_{Fe}\,dy = -2CD_{Fe}\int_{X^0_{Fe}}^{X'_{Fe}}\frac{dX_{Fe}}{2+X_{Fe}} \quad (7)$$

$$F_{Fe} = -\frac{2CD_{Fe}}{\delta}\ln\frac{2+X'_{Fe}}{2+X^0_{Fe}} \quad (8)$$

where: F_{Fe} the flux of the Fe vapors, in mol/m^2.s; D_{Fe} – the diffusion coefficient of Fe in oxygen, in m/s; X^0_{Fe} – the molar fraction of Fe at the distance $y=0$;

X'_{Fe} – the molar fraction of Fe at the distance $y=\delta$; C – the molar concentration of the Fe vapors, in mol/m^3,

$$C = \frac{n}{V_{Fe}} = \frac{P_{Fe}}{RT} \quad (9)$$

n – the number of moles of Fe which vaporize; V_{Fe} – the molar volume of Fe;

P_{Fe} – the pressure of Fe vapors. In conclusion, the flux of the Fe vapors is twice the flux of oxygen and it is determined by the oxygen partial pressure P_{O_2} which characterizes the converter atmosphere.

3. The influence of the carbon content from the bath subjected to the vaporization

It is observed that during the decarburizing of a metallic bath with upper oxygen jet, the carbon content has a strong influence upon the decarburizing process. Thus, for a carbon content of less than 2% C (Fig. 3), the Fe vaporization becomes much weaker and tends to zero as the carbon content decreases.

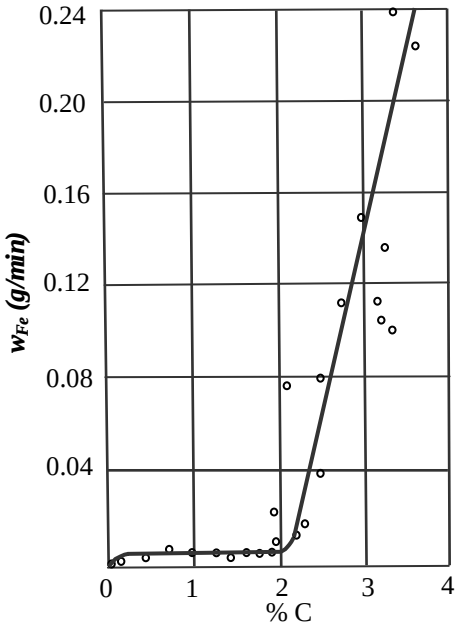

Fig.3. Variation of Fe vaporization speed with the carbon content [C]

In industrial practice the medium decarburizing rate in LD converter is 10% C/h, at a bath depth of 100 mm. The disappearance of the flame at the converter mouth and the observation of the lance are realized at a carbon content of approximately 0.05% in the metallic bath, when the vaporization is minim. It is important to determine the critical content of carbon from which the vaporization begins to decrease.

The Fick's first law is applied to the carbon transport through a thin diffusion layer at the metal-gas interface:

$$-\frac{d[C]}{dt}=\frac{1}{L}\frac{D_C}{g_0}(C_0-C_{cr}) \qquad (10)$$

where: L – the depth along which the boiling of the metallic bath takes place (~ 100 mm); D_C – carbon diffusion coefficient in iron [3.10^{-8} m^2/s]; g_0 – the thickness of the limit diffusion layer [3.10^{-5} m]; C_0 – the carbon content at the interface (~ 0.03%); C_{cr} – the critical carbon content when the vaporization is reduced.

From the relation (10) it results the value $C_{cr}=0.31\%$ which corresponds to the practical values: 0.20-0.40 %C.

4. The influence of the oxygen jet speed upon the elements vaporization

In Fig. 4 is presented the variation of the oxygen jet speed as a function of the carbon content of the metallic bath. If the oxygen jet speed is bigger than the value given by this curve for all the carbon contents, the vapors emission is weak.

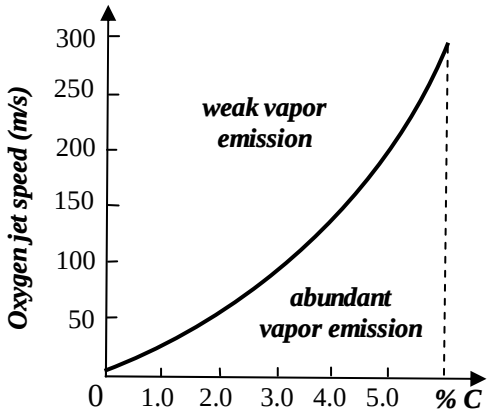

Fig. 4. Variation of oxygen jet speed with [C]

If the oxygen jet speed is smaller than the critical value, Fe is vaporized at a rate close to its maximum value:

$$w_{O_2}=K[C]^2 \qquad (11)$$

where: w_{O_2} – the oxygen jet speed; $[C]$ – the carbon concentration in the metallic bath; K – proportionality constant. The relation (11) is established on the base of the relation:

$$2F_{O_2}=F_{CO_2}>F_C \qquad (12)$$

obtained when the vapors release ends, from the reaction:

$$\{CO\}+\frac{1}{2}\{O_2\}\rightarrow\{CO_2\}$$

with F_{O_2}, F_{CO_2} and F_C – the oxygen, CO_2 and carbon fluxes. The domain upon the curve from the Fig. 4 corresponds to the case in which the steel making takes place with minimum emissions of red gases and the domain under the curve corresponds to the case in which the steel making takes place with maximum emissions.

It is concluded that during iron decarburization by oxygen blowing through the upper side, in order to obtain a reduced vaporization, the oxygen speed at the lance nozzle exit must be as great as possible in the case that the metallic bath has great carbon contents. As the decarburization advances, the iron oxidation must be maintained to a minimum value in order to suppress the smoke formation.

5. Experimental researches

The sludge samples were taken from the sludge funnel every two minutes of blowing from nine charges. The chemical composition of the converter dust (dry sludge) is presented in Tab. 1 from which some aspects concerning the vaporization process in the LD converter can be highlighted:

- the Fe content from the red smokes has a maxim in the minute 4 of blowing and corresponds to the maximum content of Fe_2O_3;
- the SiO_2 content has a maxim in the minutes 8-10 of blowing;
- the Al_2O_3 content variation has a maxim in the minute 4 of blowing, as the Fe content;
- the CaO content variation has a maxim in the minute 14 of blowing;
- the MgO content variation has a minim in the first two minutes of blowing and a maxim in the last minutes;
- the Mn content variation presents a loop in the minute 20 of blowing;
- the calcination losses (PC) variation has a maxim in the minute 14 of blowing, as CaO;
- the dry substance (SU) variation has a maxim concentration in the minute 12 of blowing.

Using a statistical program, there were obtained the histograms of the main parameters of the

vaporization process as well as the simple and multiple correlations between them [5]. Of these, we have selected the Fe content histogram (Fig.5). From the histograms the following conclusions can be drawn:

- the Fe content in the red smokes varies in the range 20-60% and the maximum frequency of 40% is obtained for a 42-50% Fe content (fig. 5);
- the FeO content in the dry sludge varies in the range 6-27% and the maximum frequency of 28% is obtained for a 18-20% FeO content;
- the CaO content in the in the dry sludge varies in the range 10-30% and the maximum frequency of 43% is obtained for a 15-20% CaO content;
- the quantity of dry substance SU varies between 5 and 35 g/l and has a maximum frequency of 40% for a concentration of 17-23 g/l;
- the calcinations losses PC vary in the range 5-28% and the maximum frequency of 28% is obtained for a 17-20% PC;
- the vaporized elements Ca, Si, Al, Mg pass as oxides CaO, SiO_2, Al_2O_3 and MgO, respectively;
- the SiO_2 content in the dry sludge varies in the range 0-2.4% and the maximum frequency of 37% is obtained for a 1.3-1.5% SiO_2 content;
- the Al_2O_3 content in the dry sludge varies in the range 0-3.8% and the maximum frequency of 42% is obtained for a 0.7-1.2% Al_2O_3 content;
- the MgO content in the dry sludge varies in the range 0-4.2% and the maximum frequency of 38% is obtained for a 0-0.8% MgO content;
- the Mn content in the in the dry sludge varies in the range 0.5-2.5% and the maximum frequency of 42% is obtained for a 1.3-1.5% Mn content.

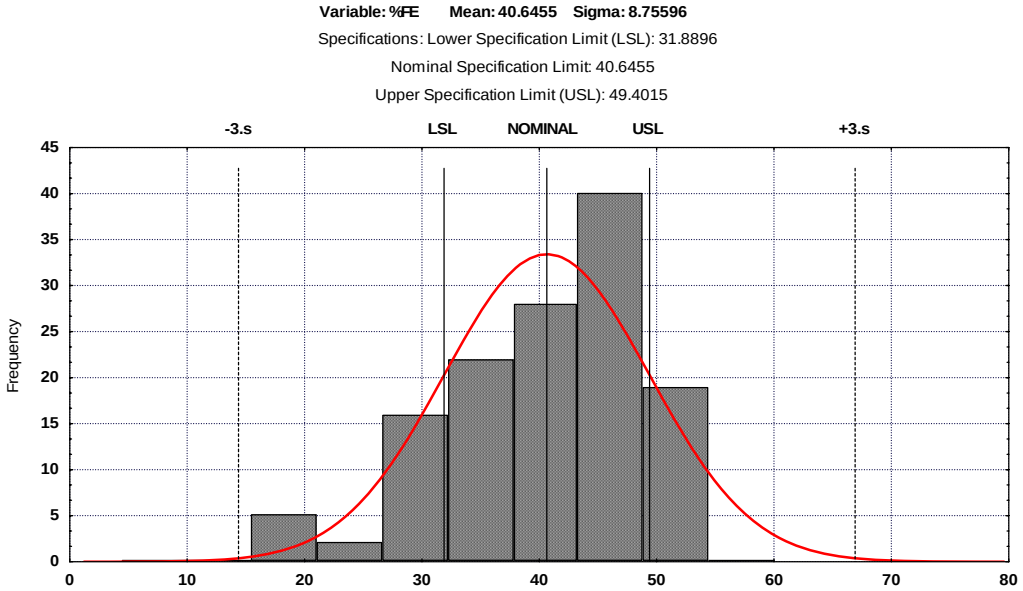

Fig. 5. The histogram of the absolute frequencies of % Fe

From the ten simple correlations we have selected for presentation the regression curves of % FeO (Fig. 6a), and of SU (Fig. 6b), in g/l, as function of the blowing time, ***t***. From the regression curves the following conclusions can be drawn:

- the FeO content presents two maxims in the minutes 8 and 20 and between them a minim corresponding to the minute 14 when the decarburization is advanced (Fig. 6a);
- the quantity of dry substance SU presents a parabolic variation, presenting a maxim of 25 g/l in the minute 12 of blowing (Fig. 6b);
- the MgO content in the dry sludge presents a parabolic variation, presenting a minim of 0.2% in the minute 12 of blowing;
- the Fe content presents a linear variation, descending from a maxim value of approx. 55% in the minute 4 of blowing to a value of approx. 30% in the minute 22 of blowing;
- the SiO_2 content variation is linear, descending from a maximum value of 1.8% in the first two minutes of blowing to a value of 0.2% in the minute 22 of blowing;
- the Al_2O_3 content variation is linear, ascending from a 0.5% minimum value in the minute 2 of blowing to a maximum value of 2.5% in the minute 22.

	% FeO = 5.121 – 1.53 t + 1.53 t^2 - 0.219 t^3 + 0. 012 t^4 ; correlation : 0.1116470 ; N=132	
% FeO	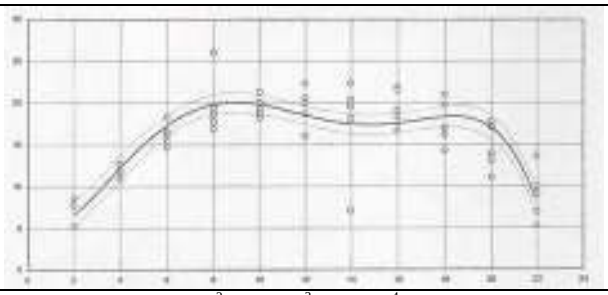	a
	SU (g/l) = 2.062 + 8. 622 t - 1.73 t^2 + 0.178 t^3 – 0.009 t^4 ; correlation : -0.303229; N=132	
SU (g/l)	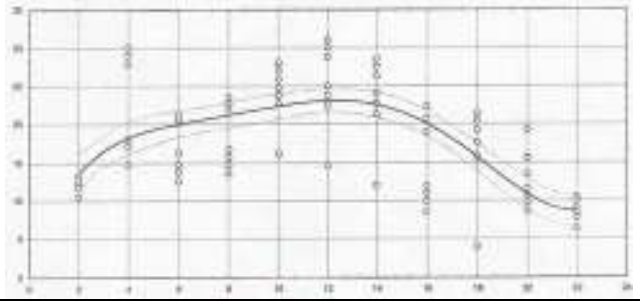	b

Fig. 6. Regression curves for % FeO and dry substance SU (g/l)

From the multiple correlations we have selected for presentation the regression surfaces of % Fe=f(%CaO, %SiO_2) (Fig. 7) and of SU=f(%Fe, %CaO) (Fig. 8) and the following technological aspects can be detached:

- the Fe content in the red smokes depends to a great extent on the CaO and SiO_2 contents from the sludge obtained by the vaporization of Ca and Si and by the lime dust training in the converter. A maxim of 54-55% Fe is registered for a 15% CaO and 2.2% SiO_2 content. The greater the CaO content in the sludge, the smaller the Fe content. This fact conducts to the conclusion that the iron vaporization can be diminished with a great CaO content in slag;
- the quantity of dry substance is determined by an intense Fe and Ca vaporization, obtaining a maximum of 35% SU for 55% Fe and 35% CaO and a minimum of 2% SU for 10% Fe and 6% CaO;
- the calcination losses are influenced by the Fe and Si vaporization, obtaining a maximum of 28% PC for 8% Fe and 2.2% SiO_2 and a minimum of 6% PC for 55% Fe and 0.2% SiO_2.

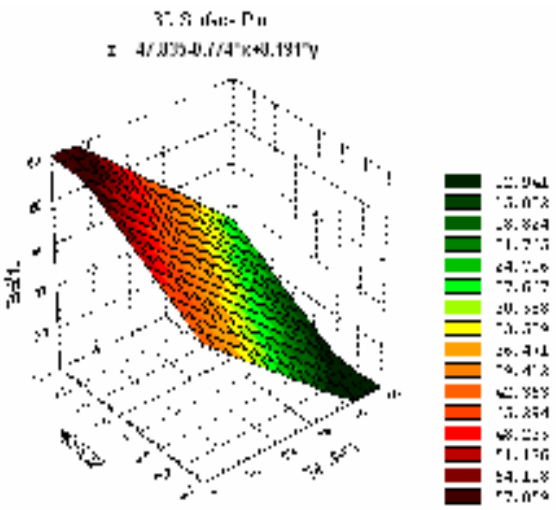

Fig.7. Correlation of %Fe as function of %CaO şi %SiO_2

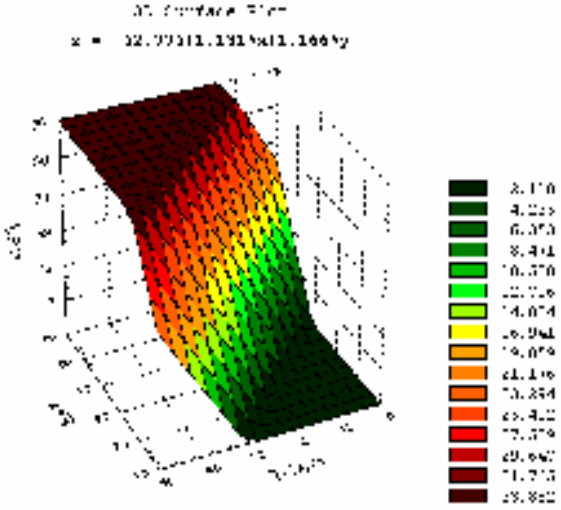

Fig.8. Correlation of %SU as function of %Fe şi %CaO

6. Conclusions

The iron volatilization in the LD converters with oxygen blowing at top through lance is important because great iron quantities (0.6-1.2%) from the metallic charge are lost as fine particles having a size of approximately 1μm, mainly made of iron oxides. In order to diminish this loss it is necessary to achieve an intense oxygen blowing regime being able to assure as greater oxygen jet speeds as the carbon content in the metallic bath is higher. The sludge obtained from the LD converter gases' purging represents an ore enriched in iron (approx. 50-55% Fe). The maintaining of a quantity of liquid slag from the previous charge determines, on one hand the faster formation of slag and, on the other hand, helps to obtain poorer emissions of vapors of Fe, Mn, Si, Mg, Al, Ca, etc at high carbon contents in the metallic bath. At small carbon contents (less than the critical one) the oxygen speed at the lance nozzle exit is the factor whose size influences the emission of metallic vapors: the greater the speed, the poorer emission of metallic vapors.

References

[1]. R. Alberny, P. Birat, 1962, "***Iron volatilization***", Circulaires d'Informations Techniques 11p. 66-70.
[2]. F. Oprea, D. Taloi, A. Ivanescu, 1984, ***"Theory of the metallurgical processes***", Editura Didactica si Pedagogica, Bucharest
[3]. W. Ackermann, 1979, "***Mass and energy transfer between the gaseous and liquid phase in oxygen converter***", Stahl und Eisen 9, p. 36-41.
[4]. A. Ivanescu, A. Ene, L. Ivanescu, C. Catana, 2005, "***Researches regarding the vaporization process of the existing elements in the metallic bath during steel making in LD converter***", International Conference METAL, Hradec nad Moravici, Czech Republic, paper A6P.
[5]. C. Mustata, V. Munteanu, D. Zorlescu, 2002, "***Mathematical modelling of the steel making in oxygen converter***", Editura Tehnica, Bucharest.

THE ANNALS OF "DUNAREA DE JOS" UNIVERSITY OF GALATI.
FASCICLE IX. METALLURGY AND MATERIALS SCIENCE
N^0. 2 – 2008, ISSN 1453 – 083X

THE STUDY OF METAL-OLD WOOD INTERACTIONS UNDER THE INFLUENCE OF PEDOLOGICAL FACTORS

Ion SANDU[1], Mikiko HAYASHI[2], Marta QUARANTA[3], Costică BEJINARIU[4] Constantin STANCIU[5], Irina Crina Anca SANDU[6], Viorica VASILACHE[1]

[1] "Al.I.Cuza" University of Iasi, Arheoinvest Platform,
Laboratory of Scientific Investigation and Cultural Heritage Conservation
[2] Ochanomizu University of Tokyo, Institute of Environmental Science for Human Life
[3] Universita degli studi di Bologna
[4] "Gh. Asachi" Technical University of Iasi
[5] "Dunărea de Jos" University of Galaţi, Faculty of Engineering Brăila,
[6] CNR-ICVBC, Firenze, Italia
email: ion.sandu@mail.dntis.ro

ABSTRACT

In the manufacture of wood objects, for binding and strengthening were used nails, cramps and other metallic elements, which in the archaeological site suffered degradation and deterioration processes, specific to metal-wood interface. The chemical and physical-structural characteristics of the products resulted from metal-old wood interactions can set up a database that can be used in authentication. For the study were taken wood samples from the Roman and Byzantine era, from Dobrogea and Moldova areas, resulted from the archaeological excavations, after year 2000, which presented in their structure metallic elements. The samples were analyzed with scanning electron microscope coupled with energy dispersion X-ray (SEM-EDX).

KEYWORDS: old wood, degradation, deterioration, corrosion, SEM-EDX.

1.Introduction

One knows the fact that the inorganic materials are much more resistant to exogenous factors as compared to the organic ones. The latest are attacked firstly by the microbiological agents which transform them, by biochemical processes, into humus while the inorganic materials are attacked by erosion and corrosion processes, thus passing into a mineral phase [1-4].

Even from the manufacturing/creation of objects, in the case of complex structures containing organic and inorganic materials, these suffer reciprocal interactions. One also knows that wood, a frequently used material, both in the structure of engineering constructions and for the manufacturing of domestic or art objects, undergoes degradation processes under the influence of some other nature materials with which it chemically interacts. Among these materials we have to mention mortars, concretes and metals. The wood interaction with metals has been very little studied [1-6].

That is why, this paper points out some cases connected to the wood-metal interaction, studied by direct analysis or with magnifying equipment (optical and electronical microscopes) as well as by the SEM-EDX technique.

2. Experimental Part

2.1. Samples

The samples taken for study are pieces of oak-tree wood fixed in iron nails from a Church floor (Zamostea, Suceava County, 1832 A.D.), which had an excessive humidity content and also bronze objects (Nufărul site, Tulcea County, IX-Xth Century and Novium Dunum, Tulcea County, XIIth Century) with monolithised wood on them.

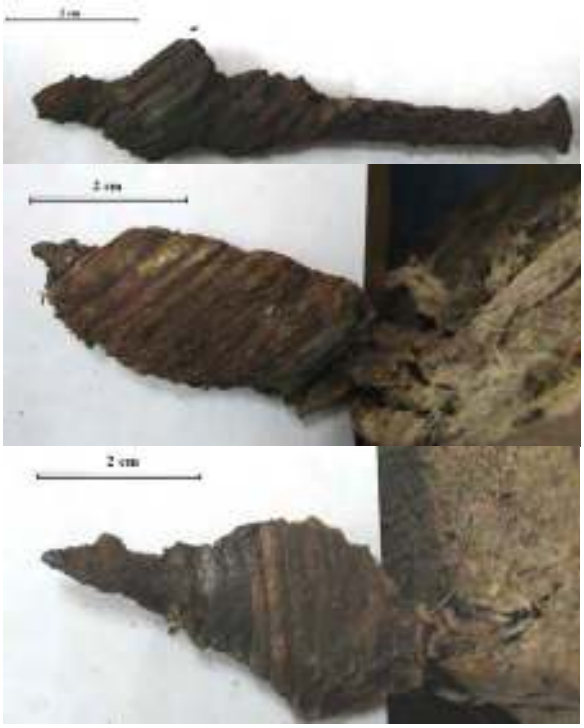

Fig. 1. Oak-tree wood samples with iron nails (Zamostea Church, Suceava County, 1832 A.D.)

Fig.2. Bronze plates (Novium Dunum, Tulcea County) with monolithised wood.

Fig.3. Bronze Coins with monolithised wood (Nufărul site, Tulcea County, IX-Xth Century)

2.2. Optical Microscopy

The samples were optically analyzed with a Motic Microscope with digital camera, having magnifying orders of 10 - 40X.

2.3. Scanning Electron Microscopy and X-ray Spectrometry (SEM-EDX)

The Scanning Electron Microscopy has been done with a TESCAN Vega II LSH electron microscope with a Bruker EDX spectrometer, with two functions:

-The image analysis with secondary electron detector (SE): resolution: up to 4.0 nm;

-The element mapping with energy dispersive X-ray spectrometer (EDX): all elements are simultaneously displayed and automatically overlaid.

-The present study has been done at an accelerating power of 30.0 kV, in the field of magnifying orders of 75-300X, with the distribution mapping of 6 elements from the surface of the old wood.

3. Results and Discussions

Fig. 4 presents the section of the wood – metal interaction zone, with the analysed longitudinal section, from which there appears that the part from the floor oak beam placed in the damp soil of the treading level has been preserved under the shape of a lens in a totally rotted beam. The longitudinal section of the lens along the iron nail shows that, on the direction of the fibre, the thickness of the preserved wood is greater than perpendicular on the fibre. The rotting of the beam and partially of the floor (on the beam intrados) has been caused by the ***Merulius Lacrimans*** mushroom which has attacked extensively all the wooden elements from the respective church.

Therefore, we speak about a preservation process of the wood under the form of a lens due to the different degree of penetration of the Fe oxidihydroxides (II, III) on the two directions along the fibre and perpendicular on it. The test proves that the Fe oxidihydroxides (II, III) have had an antimycotic effect, preserving very well the wood only in the penetration area.

Fig. 4. Longitudinal section of the wood-metal interaction area: A – the floor; b – joist

Fig. 5 presents the morphology of the surface from the contact wood – metal area in which one can notice thin traces of iron oxidihydroxides which have represented the impregnation source.

The nails have been better preserved in this area due to the inhibitor components from the oak wood such as, for instance, the tannin, than in the connection beam – floor area which has been directly exposed to the corrosive agents from the soil.

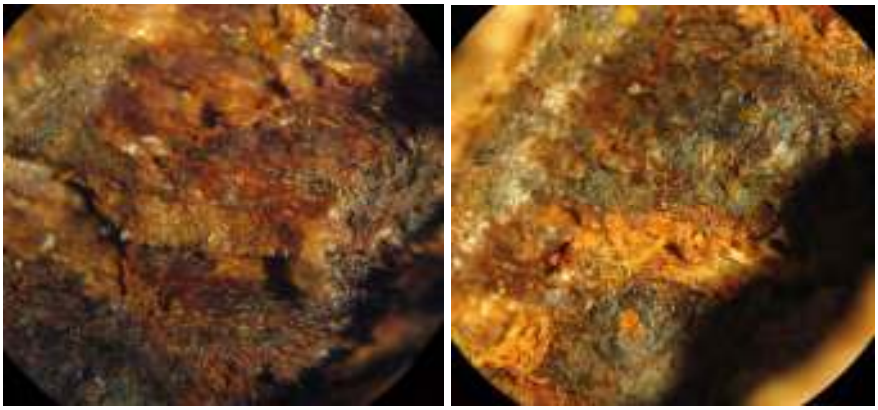

Fig. 5. Images taken with optical microscope of wood with iron traces non-uniformly distributed

Table 1 presents the composition of the alloy from which the nail has been manufactured (OL37).

Table 1. Composition of the iron nail

Element	Weight percent [%]	Atomic percent [%]	Error in %
Iron	95.849774	87.917083	2.664899
Carbon	0.353141	1.417842	0.558082
Silicon	0.247112	0.424298	0.059891
Phosphorus	0.186209	0.289913	0.051035
Sulfur	0.124372	0.187042	0.043107
Oxygen	3.239392	9.763822	0.884542
	100	100	

Fig. 6 presents the SEM microphotography with the two positions of the vector chosen by the analysis of the variation of the main components from the wood – metal interaction area.

From the EDX spectrum one can point out the continuous and uniform variation of the penetration effect of the Fe oxidihydroxide (II, III) on the two directions in the preservation area of the wood.

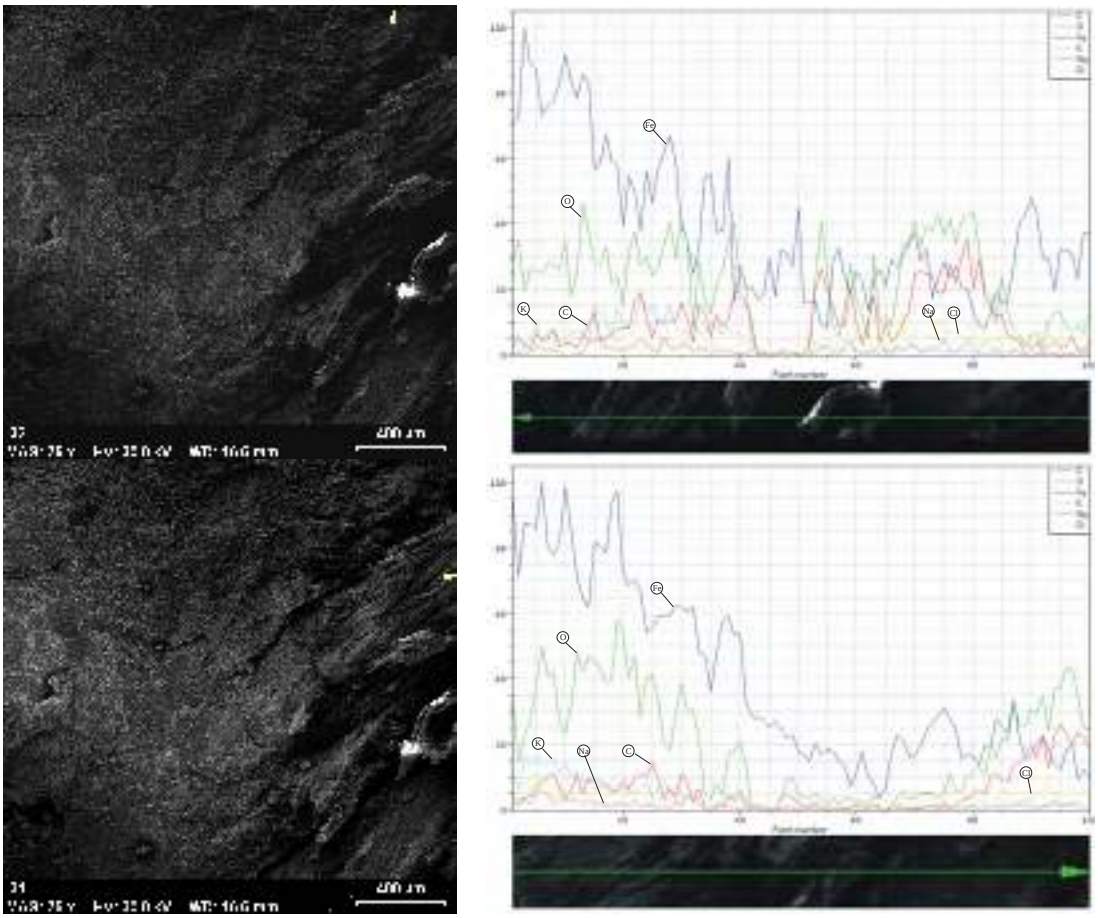

Fig. 6. SEM Image with EDX spectra of distribution along a line on the sample from wood with iron

Fig. 7 presents the mapping of the atoms for the area from the microphotography of Fig. 6 which demonstrates the uniformity of the distribution both of the components of the wood (C, O) and of the iron corrosion products (Fe, Cl and K).

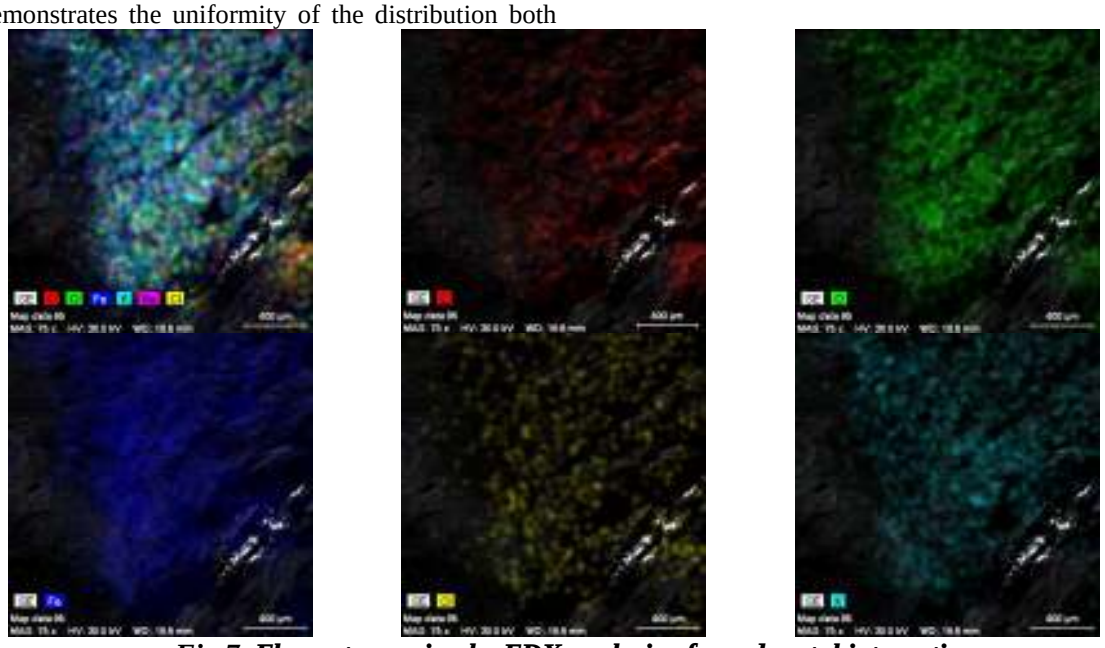

Fig.7. Element mapping by EDX analyzis of wood-metal interaction.

Table 2. Composition of diffused structure surface: wood-iron

Element	Weight percent [%]	Atomic percent [%]	Error in %
Iron	48.50823	21.5885	1.315599
Carbon	3.876974	8.0227	1.491539
Potassium	2.508171	1.594433	0.121529
Chlorine	0.301288	0.211222	0.046833
Sodium	2.160776	2.33605	0.238743
Oxygen	42.64456	66.24709	5.868803
	100	100	

Table 2 presents the average composition for the surface of the preserved area of the wood by impregnation with the Fe oxidihydroxides. One can notice a very high concentration of the Fe ions (II, III). In spite of the fact that in the structure we can find the chloride anion (the main corrosion agent of iron and the most active one, a real catalyst) due to the inhibitor components from the oak wood, the iron nail has been pretty well preserved. Fig. 8 presents a cross-section through the coin from Fig. 3 which preserves well a small wooden area from a box in which the coins have been once kept, an area which is now rotted. This trace of the preserved wood allows the archaeologists to establish the method of keeping the coins at abandon, the type of the abandon (hiding and forgetting) and their preservation state.

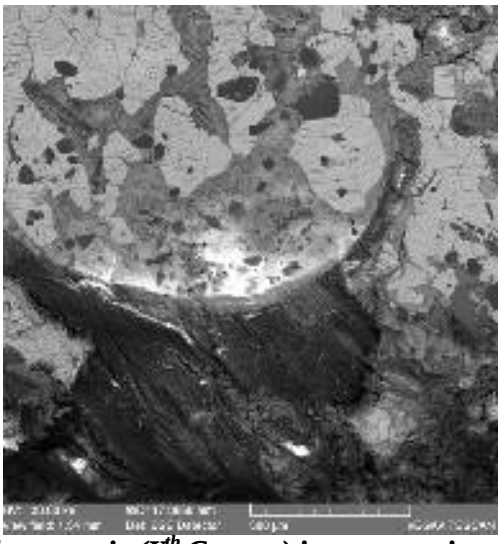

Fig. 8. SEM image of a bronze coin (Xth Century) in cross-section: on first line is visible the Liesegang Effect in a non-disturbed archaeological site; on the second line there are complex monolith structures with wood

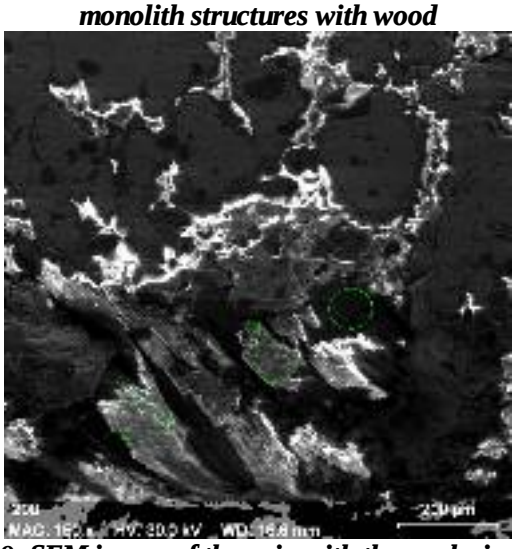

Fig. 9. SEM image of the coin with the analysis areas

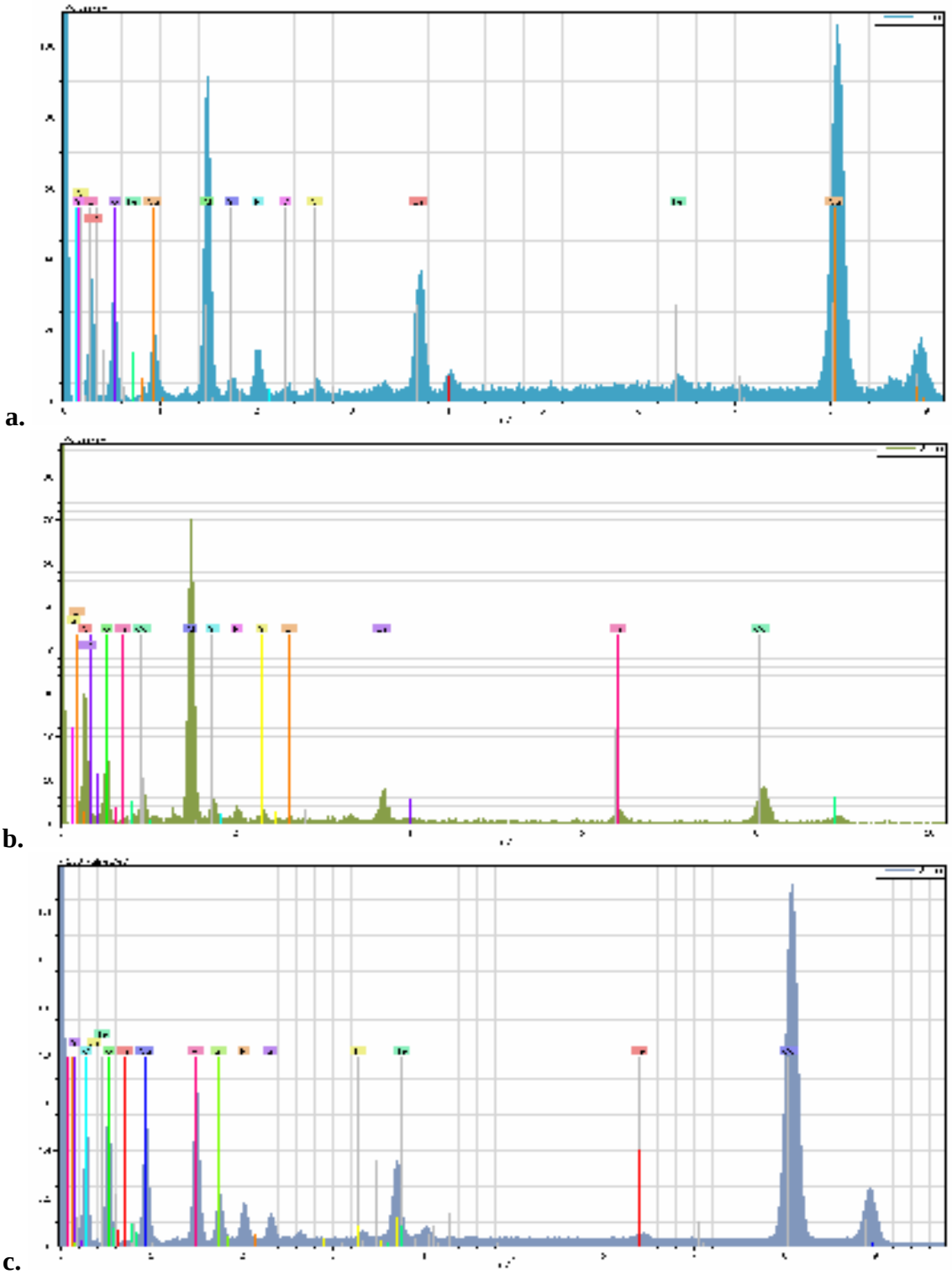

Fig. 10. Composition of area 1 (a), 2 (b) and 3 (c)

The data from table 3 confirms the presence of the wood partially carbonized with visible dendrological elements (micro-fiber, annual rings). The wood was conserved by the copper compounds.

Table 3. Composition of area 1, 2 and 3

Area	**1**		**2**		**3**	
Element	Weight percent [%]	Error in %	Weight percent [%]	Error in %	Weight percent [%]	Error in %
Carbon	6.389193	1.814477	12.18501	3.529135	7.733482	1.041857
Oxygen	35.33253	4.72851	38.85173	9.277283	30.78189	4.009206
Copper	29.53714	0.570017	11.50144	0.487489	43.06152	1.164948
Aluminium	18.78719	0.742615	26.78328	1.655008	9.274744	0.529978
Calcium	6.117853	0.176049	2.901968	0.185975	3.847487	0.154689
Iron	0.689548	0.048993	1.934821	0.149728	0.592968	0.043224
Silicon	0.864429	0.075672	2.991724	0.267102	2.065661	0.127574
Chlorine	0.155296	0.037845	0.477909	0.080947	0.627806	0.050521
Sulfur	0.110234	0.036185	0.87741	0.11058	0.668576	0.053926
Phosphorus	2.016597	0.108595	1.494708	0.159937	1.345867	0.086249

Conclusions

The paper deals which two important aspects in the field of artifacts conservation, which have wood and metal elements in contact and had been interacting in time, offering reciprocal conservability.

Therefore, in the case iron – oak-tree wood interaction, the Fe (II, III) ions conserved very well (for a long time - 200 years) the wood where they diffused. At the same time, the tannin from wood conserved the iron nail, in condition of an aggressive environment with chlorine ions.

Regarding the role of copper ions which protected the pieces of ancient wood for a very long time (1000 years).

References

[1]. **R. Sierra-Alvarez,** 2007, Process Biochemistry, 42, 5, p. 798-804;
[2]. **M.S. Rakotonirainy, L. Caillat, C. Heraud, J.B. Memet, Q.K. Tran**, 2007, Journal of Cultural Heritage, 8, 2, p. 160-169;
[3]. **X.S. Li, P**. **Englezos,** 2005, Journal of Colloid and Interface Science, 281, 2, p. 267-274;
[4]. **Z.Dominkovics, L. Danyadi, B. Pukanszky,** 2007, Composites Part A: Applied Science and Manufacturing, 38, 8, p. 1893-1901;
[5]. **C.G. Bjordal, T. Nilsson, R. Petterson,** 2007, Journal of Archaeological Science, 34, 7, p. 1169-1177;
[6]. **L.S. Selwyn, D.A. Rennie-Bisuillion**, 1993, Studies in Conservation, 38, p. 180-197.

THE ANNALS OF "DUNAREA DE JOS" UNIVERSITY OF GALATI.
FASCICLE IX. METALLURGY AND MATERIALS SCIENCE
N^0. 2 – 2008, ISSN 1453 – 083X

STRUCTURE EFFECTS OVER BEHAVIOR OF GRAPHITE GRAY IRON IN RUNNING

Adriana PREDA[1], Minodora RÎPĂ[2], Florin MICULESCU[3], Gabriela DULEA[1]
[1] UZINSIDER ENGINEERING S.A. GALATI, [2] University "Dunărea de Jos" of GALATI
[3]POLITEHNICA- BUCHAREST
e-mail: research@uzineng.ro

ABSTRACT

The work aims at emphasizing the structure changes of graphite gray iron, as a result of make-casting conditions and their effects over behavior in running of several cast items. Researches consisted of complex characterization of several gray iron specimens sampled from damaged items comparatively to other suitable ones. Chemical composition, crack aspect, tensile strength, structure, kind, micro hardness of structural constituent were analyzed. Laboratory researches made by optical and electronic microscopy emphasized the showing up of some unsuitable structures with fragile structural constituents and areas unpurified by exogenous inclusions as well as degenerated graphite. All of these steady structural changes had a powerful fragility effect over the material. This fact was confirmed by mechanical characteristics and analysis of cracking area.

Results corroborating allowed finding the causes of graphite gray iron cast items damage as a result of a faulty make-casting technological management and incomplete heating treatment.

KEYWORD: gray iron, nodule graphite, dendrites.

1. Introduction

Graphite gray iron is an alloy of iron with more than 2.11% carbon used to make, by casting procedure, a large amount of items subject to wear and vibrations. This alloy is part of antifriction category materials. Its structure has to fulfill two basic running requirements like the favorable sliding behavior and the wear resistance [9]. Based on this aspect the antifriction materials have heterogeneous structure made of two or more constituents with different properties. Basic structure – the matrix has to have a fine granulation and phases uniformly spread in order to provide the hardness and resistance suitable for the running conditions. Graphite gray iron matrix may be made of ferrite (constituent with high plasticity), pearlite (constituent with low hardness and high breaking resistance) or ferrite and pearlite where the graphite formations are dispersed. [2].

Graphite is the phase with lubricating action and vibration damping capacity that provides the favorable behavior in running. It is the structural constituent with low density, very ductile that flows plastically and makes a cover that covers the harder phases from the matrix over the contact surface.

Therefore it is avoided the breaking and pulling away of hard grains from cavities which are able to act like abrasive particles, [5]. Graphite separations shape differs depending on the kind of wear and demand: vermicular, lamellar, rosette or nodular. Dimensions, shape and distribution of graphite separations have an important influence over the mechanic characteristics of gray irons as well as the behavior in running, [3].

Acting over the chemical composition, casting parameters and heating treatment result in getting the aimed characteristics. A categorical bill has the graphitizing elements like silica and magnesium that allow the alloy to solidify after the steady iron-graphite system. Kinds of wear where the graphite gray iron may be preponderantly involved are: the abrasive wear (bill crushers, rollers, grinding disks, crusher jaws); braking slide wear (with or without lubrication) characteristic for brake blocks, clutches, wheels on rails; rolling slide wear in case of traveling parts in engineering and passenger cars [8].

The items that are the subject of this research are "supporting arms of car wheels" cast in gray iron with nodular graphite. Such item is subject to brake sliding wear and powerful vibrations. Ferrite - pearlite gray

iron with nodular graphite is suitable for this kind of loads: the matrix made of ferrite and pearlite dispersed in max. 15% lamellar shape, [8] provides the structural stability, good heating conductibility, good friction properties and average wear resistance taking into consideration the parts replacing requirement [8]. Nodular graphite with average compactness, uniformly spread, has a very good capacity in vibrations absorption.

2. Laboratory Experiments

Based on the theoretical considerations submitted, the herewith work intends to investigate three nodular graphite gray irons, apparently identical, but which stated a different behavior of cast items (fig. 1). From those specimens code 1, 2 and 3 tension specimens and metallography micro sections sampled. In case of damaged items code 2 and 3 the specimens were sampled from the cracking areas.

Fig.1. „Arm – wheel support" - cracked piece.

In order to find out the damage causes the following tests are performed: chemical and metallographical analysis, tensile test, cracking characterization, chemical composition over micro-areas by X rays as well as micro-hardness measurements on the structural constituents [1, 4, 6, 7].

Chemical composition analysis made by the DV-6 spectrometer with atomic emission (table 1) frames the materials in graphite gray nodular iron category.

Relatively large differences were found between contents of C and Si, the graphitizing element, as it follows: amount close to the bottom line of Si in case of sample code 1, a little bit over the upper limit of carbon of code 2 and over the upper limit of silica, in case of sample code 3. Tensile test performed as per SR EN 10.002/1/2002, in order to find out mechanical characteristics (table 2) emphasized the following observations: code **1** recorded high amounts of yield limit and crack resistance and a suitable elongation amount, fact confirmed by the small amount of Si and graphite as well; code **2** recorded an extremely high crack resistance (confirmed by the large content of C), yielding to permissible limit and a very low elongation. Against the high content of Si that had to provide a large quantity of graphite, therefore a high plasticity, code 3 acted very fragilly. Cracking section of probe code 3 (fig. 2) showed compactness defaults over more than 30% of surface.

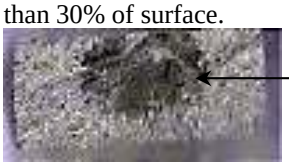

Fig. 2. Crack section appearance of sample code 3.

Table 1. Chemical composition

Sample code	Chemical composition, [%]				
	C	**Mn**	**Si**	**S**	**P**
1	3.13	0.31	2.14	0.016	0.019
2	3.78	0.18	2.24	0.016	0.044
3	3.34	0.20	2.80	0.016	0.050
Nodular graphite iron 450	3.1–3.7	0.15–0.30	2.0–2.7	Max. 0.02	Max. 0.12

Table 2. Mechanical characteristics

Sample code	Average amounts found		
	R_m [N/mm^2]	$R_{p0,2}$ [N/mm^2]	A_5 [%]
1	506	433	11.6
2	556	311	4.9
3	496	290	**7**
SR EN 1563-1999 for type EN-GJS-450-10	Min. 450	Min. 310	Min. 10

Metallographical analysis was performed by OLYMPUS optic microscope with automatic data acquisition as per SR EN ISO 945/2002.

Specimen microstructures analyzed (x100) sizes, are given in figures 3-a, b, c.

Specimen code 1 with suitable mechanical characteristics has an appropriate structure: matrix made by polyhedral grains, fine of ferrite and pearlite 10% percentage, dispersed like isles; nodular graphite with regular geometric shape, Gf6 standard scale, with variable diameter up to 25 μm, GNd1 scale and between 40-60 μm, GNd3 scale.

In case of specimens code 2 and 3 metallographical analysis emphasized several negative aspects concerning material cleanness and structure.

Specimen code 2 shows a brittle structure made of: ferrite-pearlite basic mass sintered by inter-dendrite area overlapped in exogenous inclusions, secondary cementite shows up dispersed (very hard constituent) in acicular shape and graphite is completely nodulized. On the specimen sampled from the damaged area of item code 2, several micro-crakes were found around which there are the exogenous inclusions crowds resulted from slag (fig.4).

Sample code 3 (fig. 3c) has per assembly a suitable structure (ferrite with fine polyhedral grains and 10% pearlite, nodular graphite with regular geometric shape, Gf6 standard of reference, with variable diameter over the part thickness between 25-40μm to GNd2 scale and 40-60 μm to GNd3 scale where isle area with contaminants (oxides and slag) show up.

For example (fig. 5) the macrostructure analysis of one sample from the damaged area was shown. In the thickness average of sample code 3, a powerful unpurified area, which caused the material fragilizing (fact confirmed by values of yelling and elongation limits) was found and constituted prime propagation of crakes during erection.

Results of mechanical characteristics and metallographical analysis were fulfilled by electronic microscope analysis and micro hardness measurements that confirmed the submitted data.

By ESEM-XL 30- PHILIPS electronic microscope the cracks of samples code 1, 2, 3, (figures 6-a, b, c) were analyzed and by X ray the chemical composition on the micro-areas with ferrite, graphite and impurities were found out.

In specimen code 1, cracking was ductile with a dark colored crack and inter-crystalline cleavage. Specific aspects of this crack may be seen (fig. 6a): curve lines and ferrite inter-crystalline detachment crests, as well as the black color bowls generated by graphite.

Specimen code 2 (fig. 6b) had a fragile cracking with a light color crack, silver and trans-crystalline cleavage. On the dendrites may be seen the material pulling out stages.

In case of specimen code 3 cracking has a mixed ductile-fragile character. In the inclusions area it was found out that dendrite arrangement in layers as well as evulsions generated by fragile inclusions framed by bowl type crests, was made by ferrite inter-crystalline detaching.

a) Specimen code 1 b) Specimen code 2 c) Specimen code 3

Fig.3. Nodular graphite gray iron microstructure investigated. 2% Nittal attack.

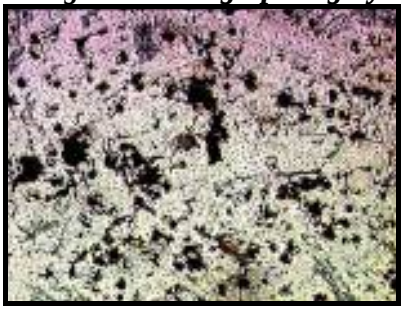

Fig. 4. Unattacked specimen code 2(×100).

Fig. 5. Specimen code 3- 2% macro Nittal attack.

a) Specimen code 1 b) Specimen code 2 c) Specimen code 3

Fig.6. Iron cracking surfaces micrographically investigated. (x200)

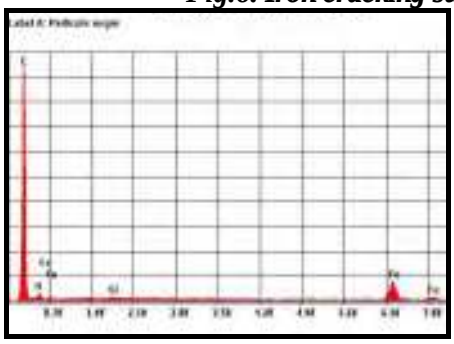

Fig.7. EDX spectrum- Specimen code 2.

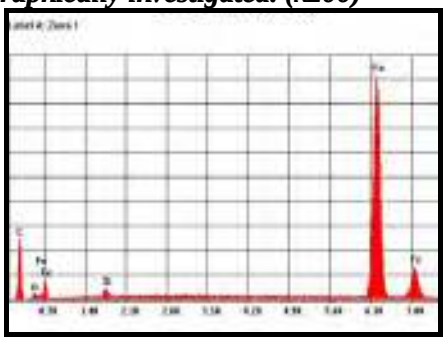

Fig.8. EDX spectrum- Specimen code 3, area 1

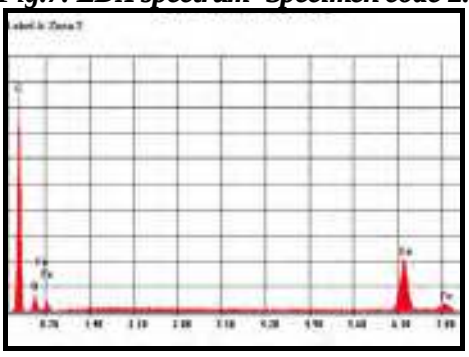

Fig.9. EDX spectrum- Specimen code 3, area 2.

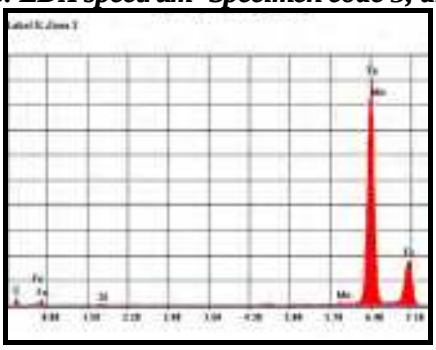

Fig.10. EDX spectrum- Specimen code 3, area 3.

In figures 7, 8, 9, 10 are shown the EDX specters of chemical elements in inter-dendrite areas oversaturated by impurities, for specimens code 2 and code 3.

Local distribution of chemical elements emphasizes several oxides and silicates present into the unpurified inter-dendrite areas of specimen code 2 and code 3(fig. 7, 8, 9). It is noticed that crowds of oxides and exogenous inclusions (silicates) caused several lacks of composition (confirmed by the presence of antigrafitizant element Mn) that led to interrupting the grafitizing process over those areas (fig. 10).

Micro hardness values given by CV-400DAT2 micro-hardness testing machine may be found in table 3. They confirmed the existence and the nature of constituents identified in structure: plastic phase ferrite, harder phase pearlite, very smooth constituent graphite, cementite-Fe_3C very hard inter-metallic compound and areas with oxides, silicates and Mn which have variable hardness depending on local distribution of impurities.

Table 3. Micro hardness values

Sample code	Average values of micro hardness [HV] recorded on each structural constituent; 50gf pressing force; 25 sec.				
	Ferrite	Pearlite	Graphite	Cementite	Zone with impurities
1	224	425	71	-	-
2	245	495	79	726	187
3	226	395	65	-	182^1; 299^2 ; 495^3 ;

Note: Exponents 1, 2, 3, are suitable for the areas where the local chemical composition was determined.

3. Conclusions

Structural modifications recorded in gray irons analyzed (cast dendrites, acicular cementite, incompletely nodulized graphite, oxides and exogenous impurities overcrowded areas) generated an extremely fragile behavior of materials code 2 and 3, fact confirmed by the mechanical characteristics values.

According to the results, the mechanical characteristics and behavior in running of nodular graphite gray iron are more powerful influenced by technological make-casting management and heating treatment than the chemical composition of the material.

At the same chemical composition, the crowds of oxides and exogenous inclusions (silicates) caused structural inhomogeneities and the showing up of composition gaps (confirmed by the antigrafitizant element Mn presence) that get to interrupt the grafitizing process over those areas.

The submitted issues are the consequence of legal nonconformities connected to the conditions and technological parameters applied:

- bubbling and unsuitable protection of metallic bath during elaboration, as well as the incompletely slag exhausting, explain the oxides and exogenous existence in the iron;

- the too large speed when parts solidifying in mold allowed the secondary cementite precipitating;

- Insufficient treatment holding temperature and time led to the cast dendrite structure keeping.

Unsuitable structures and mechanical characteristics found in nodular graphite gray iron codes 2 and 3, resulted because of the deficient technological make-casting management, neglected and incomplete heating treatment. They caused the items cracking even during assembly.

References

[1]. Dulea G. Preda A, Levcovici D. T., –*"Characterization of materials, items code PA11800.00, code PA12134.01, code PA12135.01, code PA13208.00"*. Technical report, S.C. Uzinsider Engineering, June 2007, Galati, Romania.

[2]. Geru N. - *"Metalurgie fizică"*. Edit. Tehnica si Pedagogica, Bucuresti, 1981

[3]. Lahtin Y. – *"Metalurgie fizică şi tratamente termice"* The Metallurgy Publishing House, Moscow, 1984.

[4]. Levcovici D.T, Dulea G. Preda A. –*"Characterization of materials, items code PA13205.00, code PA13207.00, code PA13308.00, code PA13308.00"*. Technical report, S.C. Uzinsider Engineering, Nov. 2007, Galati, Romania.

[5]. Nardin M. - *"Behaviour of special ferrous materials in woking conditions"*. Editura academiei, Bucuresti, 1998.

[6]. Preda A., Levcovici D.T, Dulea G. – *"Characterization of materials, items code PA 13216.00".* cod PA 13208.00 Technical report, S.C. Uzinsider Engineering, Jan. 2008, Galati, Romania.

[7]. Preda A., Levcovici D.T, Dulea G. – *"Characterization of materials, items code PA 13208.00"*. Technical report, S.C. Uzinsider Engineering, February, 2008, Galati, Romania.

[8]. Sofroni I, Ştefănescu D.M. - *"Graphite grey iron nodular"* Editura Tehnica, Bucuresti, 1978.

[9]. Stiven Schmidt – *"Dynamic concentration theory for metal rolling"*. Tribology Transactions. Vol. nr. 38/1995.

MANUSCRISELE, CĂRŢILE ŞI REVISTELE PENTRU SCHIMB, PRECUM ŞI ORICE CORESPONDENŢE SE VOR TRIMITE PE ADRESA:

MANUSCRIPTS, REVIEWS AND BOOKS FOR EXCHANGE COOPERATION, AS WELL AS ANY CORRESPONDANCE WILL BE MAILED TO:

LES MANUSCRIPTS, LES REVUES ET LES LIVRES POUR L'ECHANGE, TOUT AUSSI QUE LA CORRESPONDANCE SERONT ENVOYES A L'ADRESSE:

MANUSCKRIPTEN, ZIETSCHRITFTEN UND BUCHER FUR AUSTAUCH SOWIE DIE KORRESPONDENZ SID AN FOLGENDE ANSCHRIFT ZU SEDEN:

UNIVERSITATEA "DUNĂREA DE JOS" DIN GALAŢI
REDACŢIA ANALELOR
Str. Domnească nr. 47 – 800036 Galaţi, ROMÂNIA
E-mail: mbordei@ugal.ro

After the latest evaluation of the journals achieved by National Center for the Science and Scientometry Politics (**CENAPOSS**), as recognition of its quality and impact at national level, the journal is included in B category, 215 code (http://www.cncsis.ro/2006_evaluare_rev.php).

The journal is indexed in Cambridge Scientific Abstract (http://www.csa.com/ids70/serials_source_list.php?db=materials-set-c).

The papers published in this journal can be visualized on the "Dunarea de Jos" University of Galati site, the Faculty of Metallurgy and Material Science page: www.fmsm.ugal.ro.

AFFILIATED WITH:

- *ROMANIAN SOCIETY FOR METALLURGY*
- *ROMANIAN SOCIETY FOR CHEMISTRY*
- *ROMANIAN SOCIETY FOR BIOMATERIALS*
- *ROMANIAN TECHNICAL FOUNDRY SOCIETY*
- *THE MATERIALS INFORMATION SOCIETY (ASM INTERNATIONAL)*

Annual subscription (2 issues per year)

Edited under the care of
Faculty of
METALLURGY AND MATERIALS SCIENCE
and Research Center
QUALITY OF MATERIALS AND ENVIRONMENT

Edited date: 15.11.2008
Issues number: 200
Printed by
Galati University Press
accredited CNCSIS
47 Domneasca Street, 800036 Galati,
Romania